

RADIATIVE PROCESSES IN RELATIVISTIC ASTROPHYSICAL PLASMAS

A Dissertation

Submitted to the Faculty

of

Purdue University

by

Yonggang Luo

In Partial Fulfillment of the

Requirements for the Degree

of

Doctor of Philosophy

May 2020

Purdue University

West Lafayette, Indiana

THE PURDUE UNIVERSITY GRADUATE SCHOOL
STATEMENT OF DISSERTATION APPROVAL

Dr. Maxim Lyutikov, Chair

Department of Physics and Astronomy

Dr. Dimitrios Giannios

Department of Physics and Astronomy

Dr. Matthew Lister

Department of Physics and Astronomy

Dr. Christopher Greene

Department of Physics and Astronomy

Approved by:

Dr. John Finley

Head of the School Graduate Program

To my grandfather, Guozhen Luo, who passed away on July 17, 2019. My love for him will always be alive. All precious memories with him will be treasured in my heart forever.

ACKNOWLEDGMENTS

I am deeply indebted to many people who supported me during my Ph.D. studies. Without their help, my work for Ph.D. never would have been done. Firstly, I would like to thank my supervisor, Maxim Lyutikov. I am so happy and thankful to work with him and being part of his research group. His passion for science and deep insights about science always surprise me. I have learned a lot from the discussions with him. He doesn't only teach me the knowledge of astrophysics, but also teach me how to conduct proper research. As an ESL (English as a second language) student, I need more help from him on my writing, but he always happy to help me and correct my grammar mistakes. I want to give a big thanks to Dimitrios Giannios, whose knowledge shared with me and advise given to me are always helpful. I want to thank my great committee members: Maxim Lyutikov, Dimitrios Giannios, Matthew Lister, and Christopher Greene, who are keen to spend their amount of time with me and give me help whenever I need.

I would also like to thank my collaborators: Maxim Lyutikov, Dimitrios Giannios, Maxim Barkov, Adithan Kathirgamaraju, Tea Temim, and Luca Comisso. During the time we were working together and contributing our novel ideas, I learned different ways of thinking from them. Without their contribution, I would never have completed the projects. I am also thankful to all (former) Purdue astrophysics group faculties: Maxim Lyutikov, Dimitrios Giannios, Matthew Lister, John Finley, John Peterson, Dan Milisavljevic, Kyoung-soo Lee, Wei Cui. I appreciate their efforts to improve our weekly astrophysics journal club, and I grew my knowledge every time from the weekly astrophysics journal club.

Most importantly, I would like to thank my family for their support and encouragement. I want to thank my grandparents, Guozhen Luo and Jinlian Zhu, my parents Qingbo Luo and Xiaoying Li, and my cousin Qianyun Luo. It was a super

heart-broken time for me when my grandfather passed away on July 17, 2019. My family was not only spending a significant amount of time accompanying my grandfather and taking care of him in his last three months, but also trying to comfort me and get me out of sadness. Without their works, I can not imagine a way to overcome this hard period.

Lastly, I would like to thank my girlfriend, Hongxi Li, who keeps providing me joys in my life. And I also would like to thank all my friends at Purdue. I would never forget all stories with them at Purdue.

I want to acknowledge the Purdue Research Foundation for supporting my last year at Purdue University.

TABLE OF CONTENTS

	Page
LIST OF TABLES	viii
LIST OF FIGURES	ix
ABSTRACT	xvii
1 INTRODUCTION	1
1.1 Properties of plasma and radiation processes	2
1.1.1 Particle motion in an electromagnetic field and adiabatic invariants	2
1.1.2 Shock waves	3
1.1.3 Acceleration mechanisms	5
1.1.4 Synchrotron and IC emission	8
1.2 Observational properties and theories of the Crab nebula	10
1.2.1 Observational properties of the Crab nebula	10
1.2.2 Kennel-Coroniti prescription	12
1.3 Observational properties and theories of GRBs	12
1.3.1 Observational properties of GRBs	12
1.3.2 Hot fireball model	16
1.3.3 The external shock model of afterglows	18
1.4 The Outline of the Dissertation	22
2 SYNCHROTRON EMISSION IN AN EVOLVING MAGNETIC FIELD	24
2.1 Introduction	24
2.2 Synchrotron Emission in a constant magnetic field	24
2.3 Synchrotron emission taking into account adiabatic and radiative losses	31
2.4 Synchrotron emission from relativistically expanding sources	41
2.5 Conclusions	47
3 TURBULENT MODEL OF CRAB NEBULA RADIATION	51
3.1 Introduction	51
3.2 The sigma-problem - the problem of the magnetic flux	53
3.3 Confinement of the turbulent Crab Nebula PWN by its supernova remnant	55
3.3.1 Overall expansion	55
3.3.2 Internal velocity structure of turbulent PWN flow	58
3.3.3 Magnetic field within the shell	59
3.4 Particle distribution within the nebula	60
3.4.1 Evolution of the particle distribution in a changing magnetic field	60
3.4.2 The overall particle distribution in the Crab Nebula	64

	Page	
3.5	Acceleration in relativistic turbulent reconnection	65
3.6	The turbulent model of the Crab Nebula radiation	68
3.6.1	Model parameters	68
3.6.2	The fitting procedure	71
3.7	Spectral maps in the optical and IR	82
3.8	Conclusions	84
4	WIND-POWERED AFTERGLOWS OF GAMMA-RAY BURSTS: FLARES, PLATEAUS AND STEEP DECAYS	89
4.1	Introduction	89
4.2	Emission from relativistic termination shock	92
4.2.1	Wind dynamics	92
4.2.2	Evolution of the particles' spectrum	93
4.2.3	Observed luminosity	94
4.3	Results	101
4.3.1	Plateaus and sudden intensity drops in afterglow light curves .	101
4.3.2	Afterglow flares	104
4.4	Discussion	107
5	PREDICTION OF THE SECOND PEAK IN THE AFTERGLOW OF GW170817	111
5.1	Introduction	111
5.2	Model	113
5.3	Results	114
5.3.1	The fiducial parameters	115
5.3.2	Analytic estimates for detectability of the second peak	116
5.3.3	Second peak light curves using the "Afterglow library"	118
5.3.4	Emission from off-axis forward shock: numerical calculation of synchrotron emission	123
5.4	Conclusions	127
6	SUMMARY	128
	REFERENCES	130
A	THE DERIVATION OF THE LIGHT CURVE FUNCTION OF THE REL- ATIVISTICALLY EXPANSION AT HARD X-RAY AND ABOVE	156
	VITA	159

LIST OF TABLES

Table	Page
3.1 Summary of parameter values. In this table, B_{now} is the magnetic field now. $\gamma_{I_{max}}$ is the maximum Lorentz factor of injected electrons of component-I. $\gamma_{II_{max}}$ is the maximum Lorentz factor of injected electrons of Component-II. $\gamma_{II_{break}}$ is the middle break Lorentz factor of Component-II, where power law indices are $p_{II1} = 1.6$ below the $\gamma_{II_{break}}$ and p_{II2} above the $\gamma_{II_{break}}$. $\gamma_{I_{min}}$ is the minimum Lorentz factor of injected electrons of component-I. E_I is the energy of component-I, E_{II} is the energy of Component-II, and E_{total} is the sum of the energy of Component-I and Component-II.	79

LIST OF FIGURES

Figure	Page
1.1 A cartoon of the magnetic reconnection event. Initially, the magnetic field lines are running in the opposite direction. Then, the magnetic field lines and fluid are moving inward, and the two opposite magnetic field lines get closer to each other. Finally, the magnetic field line reconnect and change its configuration.	7
1.2 The broad-band spectrum of the Crab nebula via multi-wavelength observations, taken from [23].	11
1.3 RS-FS structure as viewed from the observer frame. RS and FS are produced from the interaction between a relativistic jet and ISM. The shocked jet and shocked ejecta are on the different sides of CD and move with the same velocity, and they have the same pressure but different density. . . .	19
1.4 Synchrotron spectrum of fast cooling and slow cooling with a power law electron distribution. Taken from [110].	21
1.5 The relation between lab time and observe time in 1-dimension condition. Firstly, the emission source emit a photon at location 1 at time t_1 . At time $t_2 = t_1 + \delta t$, the emission source move to the location 2, and emit a photon. At the same time, the first photon has travelled $c\delta t$. So the distance between these two photon is $(c - v)\delta t$, and the time interval that observer will see these two photons is $\frac{c-v}{c}\delta t$	22
2.1 The typical evolution of the Lorentz factors in radiation-only energy loss processes. The initial Lorentz factor are 5×10^5 , 1×10^6 , 2×10^6 from red to orange. The initial time is $1 \times 10^5 s$	26
2.2 The typical evolution of the Lorentz factor in radiation-only energy loss processes. Two curves have same initial Lorentz factor but correspond to two different initial time $1 \times 10^5 s$ and $2 \times 10^5 s$	26
2.3 The evolution of the typical Green's Function for instantaneous injection at $t = t_0$. We use $\gamma_{\min} = 5 \times 10^5$, $B = 5.5 G$, $t_0 = 10^5 s$, time = t_0 , $1.0001 \times t_0$, $1.0001^2 \times t_0$ from blue to green.	27

Figure	Page
2.4 The evolution of the distribution function for radiation-only energy loss processes. We use $\gamma_{\min} = 5 \times 10^5$, $B = 5.5G$, $t_0 = 10^5s$. Time increase 12s, 25s, 38s, 91s, 143s, 195s after t_0 from blue to brown. The red circle are cooling break and the grey circle are injection break due to γ_{\min} . We can see the transition when cooling break cross the injection break from yellow curve to red curve.	30
2.5 The evolution of the spectra in the radiation-only energy loss processes with the full integration. We use $\gamma_{\min} = 5 \times 10^5$, magnetic field $B = 5.5G$, power law index $p=2.2$, distance $d=3.35 \times 10^9pc$, initial time $t_0 = 10^5s$, the time in fluid are $t' = 2 \times 10^5s, 10^6s, 5 \times 10^6s, 2.5 \times 10^7s$ from red to purple.	32
2.6 The evolution of the Green's function for adiabatic expansion without radiation losses. We use $\gamma'_{\min} = 1440$, $t'_0 = 10^5s$. They correspond to time $t_0s, t_0 + 1.00 \times 10^4s, t_0 + 2.1 \times 10^4s$ from red to yellow.	34
2.7 The evolution of the distribution function for adiabatic expansion without radiation losses. We use $\gamma'_{\min} = 1440$, $t'_0 = 10^5s$. They correspond to time $t_0+5.00 \times 10^2s, t_0+5.53 \times 10^3s, t_0+1.08 \times 10^4s, t_0+1.64 \times 10^4s, t_0+2.22 \times 10^4s, t_0 + 2.83 \times 10^4s$ from red to brown.	34
2.8 The evolution of the typical Green's function for adiabatic and radiative losses with an instantaneous injection at $t = t_0$. We use $\gamma_{\min} = 1440$, $B = 5.5 G$, $t'_0 = 10^5s$, time = $t'_0, 1.1 \times t'_0, 1.1^2 \times t'_0$ from blue to green.	36
2.9 The evolution of the Lorentz factor for adiabatic and radiative losses. The initial Lorentz factor are $1.44 \times 10^3s, 2.88 \times 10^3s, 5.76 \times 10^3s, 1.15 \times 10^4s, 2.30 \times 10^4s$ from orange to blue for above curves with the initial time is 2×10^5s , and from red to purple for below curves with the initial time 1×10^5s .	37
2.10 The evolution of the distribution function for adiabatic expansion without dynamic process. We use $\gamma'_{\min} = 1440$, $B' = 5.5G$, $t'_0 = 10^5s$. The time increase $7.18 \times 10^3s, 1.25 \times 10^4s, 1.82 \times 10^4s, 2.41 \times 10^4s, 3.03 \times 10^4s, 3.68 \times 10^6s$ after t_0 from red to brown. The red circle are cooling break and the grey circle are injection break due to γ'_{\min} . We can see the transition when cooling break cross the injection break from yellow to red.	40
2.11 The evolution of the synchrotron spectrum in the case of the viewing angle is 0, and the Lorentz factor of RS is about 90, $\gamma_{\min}=5557$, initial magnetic field $B_0=2.14G$, power law index $p=2.2$, redshift $z=1$. The observe time is $t_{ob} = 1 \times 10^3s, 2 \times 10^3s, 4 \times 10^3s, 8 \times 10^3s$ from red to purple.	41
2.12 The evolution of the typical Green's function for a self-similar dynamic expansion. Consider the instantaneous injection at time $t'_0 = 10^5s$. $\gamma'_{\min}=1440$, $B'_0=5.5 G$, $p=2.2$. The time in fluid frame are $t'_0, 1.05t'_0, 1.05^2t'_0$ from red to orange.	45

Figure	Page
2.13 The evolution of the distribution function for the adiabatic expansion with dynamic process. In our model, the luminosity of wind is 10^{48} erg/s . $\gamma'_{\min}=1440$, $B'_0=5.5 \text{ G}$, $p=2.2$, $t'_0 = 10^5 \text{ s}$. The time in fluid frame increase 500s, $5.52 \times 10^3 \text{ s}$, $1.08 \times 10^4 \text{ s}$, $1.63 \times 10^4 \text{ s}$, $2.27 \times 10^4 \text{ s}$, $2.88 \times 10^4 \text{ s}$ after initial time t'_0 from red to brown. The red circle are cooling break and the grey circle are injection break due to γ'_{\min} . We can see the transition when cooling break cross injection break from yellow curve to green curve.	48
2.14 The evolution of the synchrotron spectrum in a self-similar dynamic expansion. Consider the viewing angle is 0, and the luminosity of wind is 10^{48} erg/s . $\gamma'_{\min}=1440$, $B'_0=5.5 \text{ G}$, $p=2.2$, $z=1$. The observe time is $t_{ob} = 200 \text{ s}$, 1000 s , 5000 s , 25000 s from red to purple.	49
2.15 The light curve of synchrotron emission in a self-similar expansion $m = \frac{39}{58}$ at 1 eV. Consider the viewing angle is 0, and the luminosity of wind is 10^{48} erg/s . $\gamma'_{\min}=1440$, $B'_0=5.5 \text{ G}$, $p=2.2$, $z=1$	49
2.16 The light curve of synchrotron emission in a self-similar expansion $m = \frac{39}{58}$ at 100 keV. Consider the viewing angle is 0, and the luminosity of wind is 10^{48} erg/s . $\gamma'_{\min}=1440$, $B'_0=5.5 \text{ G}$, $p=2.2$, $z=1$. The light curve is power-law and scale as $\propto t_{ob}^{\frac{mp-\frac{p}{2}-3m+1}{1+2m}}$	50
3.1 Evolution of the distribution function within one shell. Each line has injection time t_{inj} as $t_{now}/t_{inj} = 1.1, 1.2, 1.3, 1.4, 1.5$ (from green to red) with the same minimum injection Lorentz factor $\gamma_{inj,min}$ and normalization factor. As the particle distribution function evolves with time, particles are cooled due to synchrotron emission and shifted to lower energy. Here power-law index $p = 2.2$ and the minimum injection Lorentz factor $\gamma_{inj,min} = 1.9 \times 10^5$.	63
3.2 Total particle distribution function within the Nebular for different present-time magnetic fields: $2.0 \times 10^{-4} \text{ G}$ (red), $2.5 \times 10^{-4} \text{ G}$ (blue), $3.0 \times 10^{-4} \text{ G}$ (orange), $3.5 \times 10^{-4} \text{ G}$ (purple) and $4.0 \times 10^{-4} \text{ G}$ (green) at t_{now} . We keep injecting power-law particle distribution from injection time $t_{inj} = 0.1 \times t_{now}$ with $p = 2.2$ and same minimum Lorentz factor $\gamma_{inj,min} = 1.9 \times 10^5$ and let all particles evolve with time. All curves are normalized to unity at the injection break.	64
3.3 Illustration of parameters in component-I and component-II. Component-I is represented by red solid curve and component-II is represented by blue dashed curve. All parameters values are taken from Table ??, and we normalized the curve of component-II to unity at its corresponding minimum injection Lorentz factor $\gamma_{II,min}$	69

Figure	Page
3.4 Shell model of the Crab Nebula. We calculate the synchrotron emission along different lines of sight (dashed lines.)	72
3.5 The Map of the optical spectral index calculated in the wavelength range 0.5364-0.9241 μm . Taken from [195].	74
3.6 Left: The Map of the IR spectral index calculated a difference between the 3.6m and 4.5m image. Right: Map of the spectral index calculated as a difference between 3.6 μm and 8.0 μm images. Taken from [151]	75
3.7 Comparison of observational data [197]; [198]; [199]; [200]; [201]; [202]; [203]; [204] and numerical result for the broad-band spectrum. The dots represent observational data. The red solid line represents the total emission in the model. The purple and yellow dashed line represent Component-I and Component-II.	80
3.8 Broad-band spectrum of Crab Nebula. The observational data are showed as blue dots (synchrotron data is same as Fig. 3.7 and we add more data from [205]; [206]; [207]; [22] above synchrotron limit). Component-II (curve 2) and Component-I (curve 3) synchrotron emission are taken from Fig. 3.7. SSC emission is showed as curve 5. IC on thermal dust emission (curve 4) is showed as curve 6. IC on CMB is showed as curve 7. IC on starlight are showed as curve 8 (peak energy at 0.1 eV), curve 9 (peak energy at 0.3 eV) and curve 10 (peak energy at 1.0 eV). The overall total spectrum is showed as curve 1 (here we ignore IC on starlight).	83
3.9 Comparison of observed data [195] and numerical result in the optical region. The wavelength range in the observational data is 0.5364 - 0.9241 μm . We set the Crab pulsar at 0.0. The green, blue, purple, and orange solid lines represent observational data from west, east, south, and north direction, respectively. The red dashed line represents our numerical result at 0.7 μm	84
3.10 Comparison of the observed data and numerical result in the lower-frequency IR region. The wavelength range in the observational data is 3.6 - 8.0 μm . We set the Crab pulsar at 0.0. The solid lines represent observational data along different directions. The red dashed lines represents our numerical result at 7.9 μm . The blue dashed line represents our numerical data at 5.3 μm . The orange dashed line represents our numerical data at 3.5 μm . Even though we are trying to match the innermost shell index instead of the whole index map, the trend seen in the whole index map is similar to our numerical model.	85

Figure	Page
3.11 Comparison of observed data and numerical result in the higher frequency IR region. The wavelength range in the observational data is 3.6 - 4.5 μm . We set the Crab pulsar at 0.0. The solid lines represent observational data along different directions. The red dashed lines represents our numerical result at 7.9 μm . The blue dashed line represents our numerical data at 5.3 μm . The orange dashed line represents our numerical data at 3.5 μm . Even though we are trying to match the innermost shell index instead of the whole index map, the trend seen in the whole index map is similar to our numerical model.	86
4.1 The light curve of GRB 070110 in the 0.3-10 keV band. The light curve of GRB 070110 has four stages: (I) an early decay, (II) a plateau followed by (III) a rapid drop and a later flare, then (IV) a final shallow decay. Taken from [211].	90
4.2 The illustration of N_A . We are looking for the number of particles with the angle from θ to $\theta + \delta\theta$. N_A is the number of particles within a unit surface element.	95
4.3 Illustration of the jet opening angle θ_j . The emission is produced only within the opening angle θ_j . θ_i corresponds to an arbitrary place within the opening angle θ_j . If the central engine produces an explosion, we would expect the emission from a jet front surface occurs at the same time t in the lab frame. However, in the observed frame, the emission in the jet front surface occurs at a different time (the emission at the emission angle θ_i will occur at T_i , but the emission at the emission angle θ_j will occur at T_j). We assume that the observer is looking along the symmetric axis of the jet.	96
4.4 The calculation of the relation 4.13. The first light emitted from the central point $r=0$, which observed at the observed time 0. At the time t , a photon emitted from the location $r = r_{em}$ and angle θ , which observed at T_{ob} . The distance between the central point and the observer is assumed to be D	98
4.5 The illustration of the model. For the photons observed at T_{ob} , they are emitted at different times t' in the fluid frame and different angles θ	99
4.6 The illustration of the model. For the photon observed at T_{ob} , they are not emitted from a spherical shell. The distance from the central point (i.e., the time in fluid frame) and the angle respect to the line of sight are related via equation $T_{ob} = t(1 - \beta \cos \theta) = t'(1 - \beta \cos \theta) \gamma_{RS}$	100

Figure	Page
4.7 Evolution of the distribution function. Here we take account the effect of radiation loss and adiabatic expansion. In our calculation, the opening angle $\theta_j = 1/\gamma_{RS}$, $\gamma_{RS} = 90$, and the injection is stopped at time $t'_{\text{stop}} = 1.5 \times 10^5\text{s}$, $\gamma_{\text{min}} = \gamma_w/\gamma_{RS} = 5556$, initial magnetic field $B_0 = 2.1\text{G}$. The times are measured in fluid frame at $t'_{\text{stop}}/t' = 1.2, 1.1, 1.0, 0.9, 0.8$ from red to green curves.	102
4.8 The light curve at 100 KeV for different Lorentz factors of the post-RS flow. We assume that the observer is looking along the symmetric axis of the jet. The injection is stopped at a fixed time in the fluid frame, corresponding to $t'_0 = 6 \times 10^5\text{s}$. There is a sudden drop of intensity when the injection is stopped ($T_{\text{ob}} = 10000\text{s}$ for blue curve, $T_{\text{ob}} = 5000\text{s}$ for green curve, and $T_{\text{ob}} = 3333\text{s}$ for red curve). (These cases all correspond to $6 \times 10^5\text{s}$ in fluid frame). Blue curve has $\gamma_{RS} = 30$, $\gamma_{\text{min}} = \gamma_w/\gamma_{RS} = 16667$, initial magnetic field $B_0 = 6.4\text{G}$; green curve has $\gamma_{RS} = 60$, $\gamma_{\text{min}} = \gamma_w/\gamma_{RS} = 8333$, initial magnetic field $B_0=3.2\text{G}$; red curve has $\gamma_{RS} = 90$, $\gamma_{\text{min}} = \gamma_w/\gamma_{RS} = 5556$, initial magnetic field $B_0 = 2.1\text{G}$. Here we assume $B_0 \propto \gamma_{RS}^{-1}$ for our calculations.	103
4.9 The comparison of light curves for different jet angles $1/\gamma_{RS}$ (solid lines) and $1/2\gamma_{RS}$ (dotted-dash lines). Different lines correspond to parameters in Fig. 4.8 except the jet angle. We assume the viewing angle is 0. Smaller jet angle produce sharper drop.	105
4.10 The comparison of light curves for slow cooling and fast cooling, where solid lines correspond to fast cooling and dotted-dash line correspond to slow cooling. All other parameters are the same as Fig.4.8 except the initial magnetic field, where slow cooling has a weak magnetic field but fast cooling has a strong magnetic field. Fast cooling curves are brighter than slow cooling since radiation power is proportional to B^2 . More importantly, slow cooling curves are smoother than fast cooling curves, so FS, where most likely have slow cooling, may not be able to produce a steep drop behavior.	106
4.11 Producing the flares. All parameters are same as the green curve in the FIG.4.8, but we set the ejected power are two (the red curve), four (the green curve) and eight (the blue curve) times larger for a short period from $2.4 \times 10^5\text{s}$ to $2.5 \times 10^5\text{s}$. Recall that initial injection time $t_0 = 10^5\text{s}$ and break time $t_{\text{stop}} = 6 \times 10^5\text{s}$	108

Figure	Page	
5.1	Cartoon of the model. Hot torus (left from the disrupted neutron stars) creates a dense, mildly relativistic wind (shaded region). After ~ 1 second, when enough magnetic flux is accumulated on the BH, the BH launches a Blandford-Znajek-powered jet. After the jet reaches the edge of the confining wind its head part experiences a break-out, creating a nearly spherical outflow; this generates the prompt emission. Later on, the interaction of this now nearly-spherically expanding part of the jet with the surrounding medium generates the forward shock - this leads to the production of early the early afterglow that has been observed so far. Most of the jet accelerates to high Lorentz factors; the radiation from the corresponding forward shock is beamed away from the observer. Only after the jet-driven forward shock decelerated it will become visible, and should generate the late bump in the afterglow.	112
5.2	(Top) Depiction of the three criteria required for detectability of second peak. The plot shows observed radio data (red points) and multiple power law extrapolations for the observed decline (solid lines) (data taken from [249]; [265]). Vertical dashed line marks a time of 250 days and dot-dashed horizontal line indicates a radio detectability limit of $10 \mu\text{Jy}$. The numbered arrows point to the region where the second peak must lie in order to be detectable and the numbers label the criteria described in Section 5.3.2. In short, 1) requires peak time to be greater than 250d, 2) requires peak flux be above detector sensitivity and 3) requires peak flux be larger than cocoon emission. (Bottom) A figure exploring the parameter space in isotropic equivalent energy of the jet (E_{iso}) vs. external density (n). Shaded regions mark the parameter space where the second peak will be detectable (where all 3 criteria mention in top panel and Section 5.3.2 are satisfied) assuming a t^{-2} decline for current observations. Regions above dashed black line satisfy criterion 1, above dot-dashed lines satisfy criterion 2 and above solid lines satisfy criterion 3. Colors indicate the value of ϵ_{B} used for the solid and dot-dashed lines. See section 5.3.2 for analytic expressions of the lines, shaded regions and for relevant parameters used.	119
5.3	Same parameter space plot as in Fig. 5.2 except now we fix $\epsilon_{\text{B}} = 10^{-3}$ and vary the slope of the power law decline (shown in top panel of Fig. 5.2) to investigate how different declines will affect detectability of second peak. As in Fig. 5.2, shaded regions mark regions where the second peak would be detectable.	120

Figure	Page	
5.4	Light curves in X-ray at 1 keV (Top) and Radio at 6 GHz (Bottom) using the “Afterglow library”. Red points show observations of GW170817 [249], and lines show the afterglow from a jet calculated using the afterglow library [275] for two sets of parameters (see sec. for description of parameters). In a fast jet – cocoon model, the earlier time observations (red points) can be attributed to emission from the cocoon. The afterglow from a jet will peak at later times for off-axis observers, in this scenario, this peak can cause a second bump in the overall X-ray light curve of GW170817. For parameters used here, the second peak occurs at ~500 days.	121
5.5	Radio (6 GHz) afterglow light curves, similar to bottom panel of Fig. 5.4 but with a jet of opening angle 10°	122
5.6	Light curves in X-ray at 1 keV and 6 GHz using the radiative calculations, see text for details. Red points show the observation of GW170817 at 1 KeV and 6 GHz [265]. All light curves have the same parameter value as Figure 3.	126

ABSTRACT

Luo, Yonggang. PhD, Purdue University, May 2020. Radiative Processes in Relativistic Astrophysical Plasmas. Major Professor: Maxim Lyutikov.

Synchrotron radiation and inverse Compton (IC) scattering are the two most essential radiation mechanisms in high energy astrophysics. Synchrotron radiation typically dominates lower energy emission, up to GeV, and IC scattering dominates higher energy gamma-ray emission. In this work, radiation codes are developed to calculate broadband synchrotron and IC spectra for relativistic astrophysical sources: Pulsar Wind Nebulae (PWNe) and Gamma-Ray Bursts (GRBs). Our robust radiation code takes into account varying intrinsic plasma properties (*e.g.*, magnetic field evolution), various inverse Compton processes (synchrotron self-Compton and external Compton) while accounting for Klein-Nishina effects, as well as relativistic bulk motion of the emitting plasma.

First, we develop a turbulent model of the most important higher energy astrophysical source, the Crab Nebula. The model aims to resolve several long-standing problems of (PWNe): (i) the sigma problem; (ii) the hard spectrum of radio electrons; (iii) the high peak energy of gamma-ray flares; (iv) and the spatial evolution of the infrared (IR) emission. The Nebula contains two populations of injected particles: Component-I accelerated at the wind termination shock via Fermi-I mechanism, and Component-II accelerated in reconnecting turbulence in highly magnetized ($\sigma \gg 1$) plasma in the central part of the Crab Nebula. The reconnecting turbulence Component-II extends from radio to gamma rays. In essence, it accelerates radio electrons with a hard spectrum, destroying in the process the large scale magnetic flux (and thus resolves the sigma-problem), and occasionally produces gamma-ray flares (from the largest scale reconnection events). The model reproduces the broadband

spectrum of the Crab Nebula, from low-frequency synchrotron emission in radio to inverse-Compton emission at TeV energies, as well as spatially resolved evolution of the spectral indices in IR and optical bands.

Second, we study the afterglows of GRBs, concentrating on the unusual temporal features observed in some GRBs (*e.g.*, GRB 070110): flares, plateaus, and sudden drops in intensity. These variations are hard to explain with the standard model that associates the afterglow emission with the forward shock. We advance the model of afterglows of GRBs with a dominant contribution from the reverse shock propagating in an ultra-relativistic, highly-magnetized long-lasting wind produced by the central engine, presumably a powerful pulsar. We demonstrate that mild variations in the wind luminosity can produce afterglow flares, while sudden steep decay is due to the sudden termination of wind (*e.g.*, due to the collapse of the central object into the black hole).

Finally, we study the first gravitational wave observation accompanied by the electromagnetic signal, GW/GRB 170817. In this event, the LIGO and Virgo detectors observed a gravitational wave signal followed by a short gamma-ray burst. We calculated the afterglow emission within a cocoon-jet paradigm and predicted the second bump in the afterglow of GRB 170817.

1. INTRODUCTION

Various astrophysical high energy sources, such as Pulsar Wind Nebulae (PWNe) and Gamma-Ray Bursts (GRBs), produce relativistic outflows - winds. Non-thermal particles are accelerated within the winds and eventually produce broad-band emission, observed from radio to very high energy gamma-rays. The observed properties then depend on the overall dynamics of relativistic magnetized flows, relativistic kinematics (e.g., photons' time of flight effects), and a combination of various radiative processes.

The work of the dissertation focus on the properties of astrophysical relativistic winds, with applications to Pulsar Wind Nebulae and Gamma-Ray Bursts. I develop a systematic method to calculate the synchrotron radiation and IC emission produced within the relativistic winds. In the following sections, I will first go over the properties of plasma and radiation processes in §4.13. Then the observational properties and theories of the Crab nebula and GRBs will be reviewed in §1.2 and §1.3, and finally, give the outlines of this dissertation in §1.4.

The following introduction is standard and relies heavily on existing reviews and standard textbooks [1]; [2]; [3]; [4]; [5]. The text of this dissertation includes reprints of previously publications: "Prediction of the second peak in the afterglow of GW170817" (reprints in §5) with Maxim Barkov, Adithan Kathirgamaraju, Maxim Lyutikov, and Dimitrios Giannios (arXiv: 1805.08338), "Turbulent model of Crab nebula radiation" (reprints in §3) with Maxim Lyutikov, Tea Temim, and Luca Comisso (submitted to The Astrophysical Journal), and "Wind-powered afterglows of gamma-ray bursts: flares, plateaus and steep decays" (reprints in §4) with Maxim Lyutikov (in preparation). Maxim Lyutikov has supervised these research projects used in this dissertation. Maxim Barkov, who is the first author of the publication

”Prediction of the second peak in the afterglow of GW170817” (arXiv: 1805.08338), permits the texts and the plots in this article to be reprinted here.

1.1 Properties of plasma and radiation processes

1.1.1 Particle motion in an electromagnetic field and adiabatic invariants

The simplest case of a particle moving in an electromagnetic field is that a single charged particle is moving in a uniform static magnetic field without an electric field. The motion is given by $v_{\parallel} = \text{constant}$ and $v_{\perp} = \text{constant}$, where v_{\parallel} is the parallel component of velocity to the magnetic field and v_{\perp} is the perpendicular component of velocity to the magnetic field. When an orthogonal electric field is added into the uniform static magnetic field (any parallel electric field will separate opposite charge particles, and the new electric field produced by the separation of opposite charge particles will cancel the original electric field. Thus there is no parallel electric in the plasma), the particle will experience an additional drifting motion, which is perpendicular to the plane of the electric field and the magnetic field.

More frequent and complex cases of the electromagnetic fields are slowly variable magnetic fields. Even though the trajectories of charged particles in a slowly variable magnetic field are much more complicated, three adiabatic invariants could help us better analyze the plasma system.

The first adiabatic invariant is the magnetic moment defined as $\mu = \frac{mv_{\perp}^2}{2B}$. Thus, for a slowly variable magnetic field, the perpendicular component of the velocity of a particle is proportional to the square root of the magnitude of the magnetic field.

The second adiabatic invariant is the longitudinal invariant defined as $J = \int_{s_1}^{s_2} v_{\parallel} ds$, where s_1 and s_2 are the reflection points for the parallel motion in a magnetic mirror. The longitudinal invariant plays an important role in Fermi acceleration mechanisms (I will discuss the Fermi acceleration mechanism in §1.1.3), which is used to explain the acceleration of cosmic rays.

The third adiabatic invariant is the total magnetic flux Φ enclosed by a drifting surface. Thus, for a slowing variable magnetic field, if a charged particle moves around a magnetic tube, the radius of the orbits will always be equal to the radius of the magnetic tube.

1.1.2 Shock waves

Shocks are generated by supersonic motions and can be described as a transition zone. The region of undisturbed flow is called upstream, and the region of disturbed by the action of shock is called downstream. The relation between the plasma properties on upstream and downstream of a shock (the jump conditions) can be obtained from the conservative form of the magnetohydrodynamic (MHD) equations.

Denote $[X] \equiv X_2 - X_1$, where the X_2 is the variables in the downstream, and the X_1 is the variables in the upstream. From the conservation of mass, we have the jump condition:

$$[\rho (\mathbf{U} \cdot \mathbf{n})] = 0 \quad (1.1)$$

From the conservation of momentum, we have the jump condition:

$$[\rho \mathbf{U} (\mathbf{U} \cdot \mathbf{n}) + \left(P + \frac{B^2}{8\pi}\right) \mathbf{n} - \frac{\mathbf{B}}{4\pi} (\mathbf{B} \cdot \mathbf{n})] = 0 \quad (1.2)$$

From the conservation of energy, we have the jump condition:

$$\left[\left(\frac{\rho U^2}{2} + \frac{\gamma P}{\gamma - 1}\right) (\mathbf{U} \cdot \mathbf{n}) + \frac{c}{4\pi} (\mathbf{E} \times \mathbf{B}) \cdot \mathbf{n}\right] = 0 \quad (1.3)$$

From the conservation of the normal component of the magnetic field, we have the jump condition:

$$[\mathbf{B}_n] = 0 \quad (1.4)$$

From the conservation of the tangential component of the electric field, we have the jump condition:

$$[\mathbf{E}_t] = 0 \quad (1.5)$$

Here, ρ is the mass density of the flow, \mathbf{U} is the velocity of the flow, \mathbf{n} is the unit vector normal to the surface, P is the pressure, \mathbf{B} is the magnetic field, \mathbf{E} is the electric field, and γ is the specific heat ratio. These relations above constitute the jump conditions or Rankine–Hugoniot conditions of the shocks.

In the case of $\mathbf{B} = 0$, the ratios of the values of the parameters upstream and downstream of the shock are given by

$$\frac{\rho_2}{\rho_1} = \frac{U_1}{U_2} = \frac{(\gamma + 1) M^2}{2 + (\gamma - 1) M^2} \quad (1.6)$$

and

$$\frac{P_2}{P_1} = \frac{2\gamma M^2 - (\gamma - 1)}{\gamma + 1} \quad (1.7)$$

Here, M is the Mach number, defined as $M = U_1/c_{s1}$, of the upstream flow, and c_{s1} is the sound speed, defined as $c_{s1} = (\gamma P/\rho)^{1/2}$, of the upstream flow.

For a more general case, the ratios of the values of the parameters upstream and downstream of the shock are given by

$$\frac{U_{2x}}{U_{1x}} = \frac{\rho_1}{\rho_2} = X_0^{-1} \quad (1.8)$$

$$\frac{U_{2z}}{U_{1z}} = \frac{U_1^2 - c_a^2}{U_1^2 - X_0 c_a^2} \quad (1.9)$$

$$\frac{B_{2x}}{B_{1x}} = 1 \quad (1.10)$$

$$\frac{B_{2z}}{B_{1z}} = \frac{(U_1^2 - c_a^2) X_0}{U_1^2 - X_0 c_a^2} \quad (1.11)$$

$$\frac{P_2}{P_1} = X_0 \frac{c_{s2}}{c_{s1}} = X_0 \left(1 + \frac{\gamma - 1}{2} \frac{U_1^2 - U_2^2}{c_{s1}^2} \right) \quad (1.12)$$

Here, c_a is the Alfvén speed defined as $c_a \equiv \frac{B}{\sqrt{4\pi\rho}}$, x-axis is the direction of \mathbf{n} , z-axis is the tangential direction, X_0 is a positive solution of the third degree equation

$$\begin{aligned} & \left(U_1^2 - X c_a^2 \right)^2 \left[X c_{s1}^2 + \frac{1}{2} U_1^2 \cos^2 \theta (X (\gamma - 1) - (\gamma + 1)) \right] \\ & + \frac{1}{2} c_a^2 U_1^2 X \sin^2 \theta [(\gamma + X (2 - \gamma)) U_1^2 \\ & + X (X (\gamma - 1) - (\gamma + 1))] = 0 \end{aligned} \quad (1.13)$$

and θ is the angle between \mathbf{B} and the normal to the shock plane.

1.1.3 Acceleration mechanisms

There are many types of acceleration mechanisms, such as the first-order Fermi acceleration (Fermi-I mechanism) and the second-order Fermi acceleration (Fermi-II mechanism), and the energization of particles in reconnection events.

The Fermi-II acceleration mechanism

The Fermi-II mechanism was first proposed by Enrico Fermi in 1949 [6], to explain the origin of cosmic rays. In the case of a particle collides with a magnetized cloud, the energy after collision is given by

$$\frac{E_{after}}{E_{before}} \approx 1 + 2(u/c)(v/c)\cos\theta + 2(u/c)^2 \quad (1.14)$$

Here, E_{after} is the energy of particles after the collision, E_{before} is the energy of particles before the collision, u is the speed of magnetized cloud, v is the speed of particles, and $\theta \in [0, \pi]$ is the angle between the direction of the particle trajectory and the direction of the magnetized cloud trajectory.

The intuitionistic knowledge tells us the probability of the head-on collisions ($\theta = 0$) is larger than the probability of the head-tail collisions ($\theta = \pi$). The more convective explanation is that the probability of collisions is proportional to the intensity of the relative velocity of the particles and the magnetized cloud. Thus, we can average the collision angle and express the ratio of the energy differences of the particles to the energy of particles before collisions as

$$\left\langle \frac{\Delta E}{E} \right\rangle = \frac{8}{3} \left(\frac{u}{c} \right)^2 \quad (1.15)$$

This acceleration mechanism is called the second-order Fermi acceleration because the energy gain depends on the square of the speed of the magnetized cloud u^2 .

The Fermi-I acceleration mechanism

The Fermi-I mechanism was proposed by [7]; [8]; [9]; [10] independently in 1977-1978, to make acceleration processes more efficiently. In the case of that the high energy particle crosses a shock, the particle always gains the energy, no matter which it goes to upstream from downstream or it goes to downstream from upstream. The energy of particle increased is given by $\Delta E/E = (u_1 - u_2)/c$. The particles can experience multiple crossing between the upstream and downstream. Thus, the energy gained in the Fermi-I mechanism is much higher than the energy gained in the Fermi-II mechanism. This acceleration mechanism is called the first-order Fermi acceleration because the energy gain depends on the speed of the shock u .

The energization of particles in reconnection events

Magnetic reconnection is a physical process in which the oppositely directed magnetic field is breaking and reconnecting in a plasma. In the magnetic reconnection, magnetic field energy is converted to plasma kinetic and thermal energy and particle acceleration. It is a violation of Alfvén's theorem, which states that the magnetic field is frozen and move along with the fluid. Magnetic reconnection provides a solution for many problems, such as the solar corona.

The illustration of the magnetic reconnection is showed in FIG. 1.1. When magnetic field lines of opposite directions get close together, they reconnect, and the configuration of the magnetic field lines changes and releases the magnetic energy into plasma. A current sheet is confined to a thin layer between the opposite magnetic field lines.

The first theoretical description is given by Peter Sweet and Eugene Parker in 1956, thus it's so-called Sweet-Parker model [11]. In Sweet-Parker model, the dimensionless reconnection rate R is defined as the ratio of the inward velocity v_{in} to the outward velocity v_{out} . Based on the resistive MHD, R can be derived as

$$R = S^{-1/2} \tag{1.16}$$

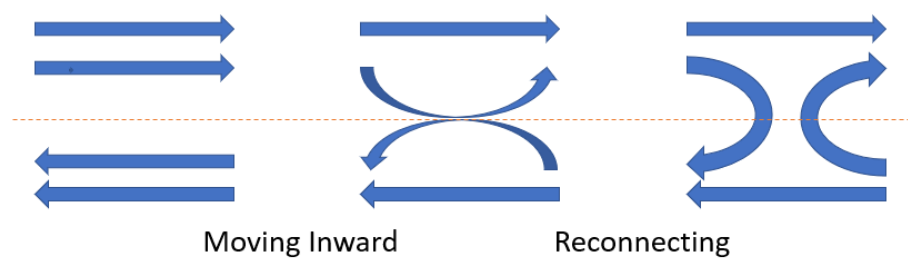


Figure 1.1. A cartoon of the magnetic reconnection event. Initially, the magnetic field lines are running in the opposite direction. Then, the magnetic field lines and fluid are moving inward, and the two opposite magnetic field lines get closer to each other. Finally, the magnetic field line reconnect and change its configuration.

where S is the dimensionless Lundquist number and is defined as $S = \frac{Lc_a}{\eta}$, L is the length of the current sheet, c_a is the speed of the Alfvén wave, and η is the plasma magnetic diffusivity.

The problem of the Sweet-Parker model is that it cannot explain the fast reconnection event, according to Eqn. 1.16. In 1964, Harry Petschek proposed an alternative model (it is a so-called Petschek model) to solve the problem [12]. In Petschek model, the fast reconnection events take place along a small fraction of the current sheet length made by slow mode shocks. The maximum reconnection rate can be estimated as

$$R_e(\text{max}) \propto (\ln S_e)^{-1} \quad (1.17)$$

which implies (1) the reconnection rate of the Petschek model is much larger than the reconnection rate of the Sweet-Parker model; (2) the reconnection rate of the Petschek model is much less sensitive to the variation of the Lundquist number S than the Sweet-Parker model.

1.1.4 Synchrotron and IC emission

Radiation emitted when charge particles are accelerated radially by a magnetic field. If the particles are non-relativistic, we call the radiation as cyclotron emission. If the particles are relativistic, we call the radiation as synchrotron emission. The total emitted power for a charge particle moving in a constant magnetic field is given by

$$P = \frac{4}{3} \sigma_T c \beta^2 \gamma^2 U_B \quad (1.18)$$

where σ_T is the Thomson cross section, and U_B is the magnetic energy density. The emitted power spectrum for a charge particle moving in a constant magnetic field is given by

$$P(\omega) = \frac{\sqrt{3}}{2\pi} \frac{q^3 B \sin \alpha}{mc^2} F\left(\frac{\omega}{\omega_c}\right) \quad (1.19)$$

where q is the charge, α is the pitch angle, and F is a dimensionless function, which we will discuss more details in §2.

In astrophysics, people often consider the particles distribution as an approximately power-law distribution $N \propto E^{-s}$. For the many charge particles system with power-law distribution accelerated by a magnetic field, the emitted power spectrum is given by

$$P(\omega) \propto B^{\frac{p+1}{2}} \nu^{-\frac{p-1}{2}} \quad (1.20)$$

Compton scattering is the scattering between photons and electrons. If the photons transfer energy to the electrons, we call the process as Compton scattering. If the electrons transfer energy to the photons, we call the process as inverse Compton scattering. A specific process called synchrotron self-Compton scattering (SSC) if the photons are produced from synchrotron emission. In astrophysics, inverse Compton scattering boosts the energy of photons and plays an essential role in producing X-ray and gamma-ray emission. For inverse Compton scattering, if the energy of photons is less than the rest energy of electrons in the rest electron frame, we call that the process is in the Thomson regime. If the energy of photons is greater than the rest energy of electrons in the rest electron frame, we call that this process is in the Klein-Nishina regime.

The Thomson cross section is given by

$$\sigma_T = \frac{8\pi}{3} r_0 = 6.65 \times 10^{25} \text{ cm}^2 \quad (1.21)$$

and the Klein-Nishina cross section is given by

$$\frac{d\sigma_{KN}}{d\Omega} = \frac{3}{16\pi} \frac{\sigma_T}{(1+x)(1-\cos\theta)} \left(x(1-\cos\theta) + \frac{1}{1+x(1-\cos\theta)} + \cos^2\theta \right) \quad (1.22)$$

Here x is the initial photon energy, and θ is the angle between the incoming photons and outgoing photons. The power spectrum of IC are derived in [13]; [14]; [15]; [16] under different treatments. More detail analysis on different aspects of synchrotron radiation and IC can be found in the reviews [17]; [18].

1.2 Observational properties and theories of the Crab nebula

1.2.1 Observational properties of the Crab nebula

Pulsars are highly magnetized rotating neutron stars, and their radiation point to the direction of the magnetic pole, so we can see pulsational signals from pulsars (we can only see the signals when the magnetic pole is pointing toward us). PWNe are nothing but a type of nebulae associated with supernovae (SNRe) explosion that are powered by pulsar winds generated by their central pulsars.

The Crab nebula is a widely known pulsar wind nebula at a distance of about 2000 pc. It is the only PWN, who was the first astronomical object identified with a historical supernova explosion. Four components constitute the Crab [19]: (1) the Crab pulsar is at the center of the Crab nebula and has a spin-down luminosity $\sim 10^5$ times larger than the Sun. (2) the shocked pulsar wind fills the Crab nebula. (3) filaments, which produce thermal emission, are around the Crab nebula. (4) the freely expanding ejecta beyond the easily visible Crab.

The first observation of Crab nebula is the observation of its progenitor SN 1054, which produced the Crab nebula, and it was first recorded on July 4th, 1054 by Chinese astronomers. The SN 1054 was so bright, so Chinese astronomers could even observe it during the daytime for 23 days. After about three more years, the SN 1054 was dim enough and disappeared in the sky due to the limitation of the observation equipment.

There is no evidence connecting Crab nebula and pulsar until David Staelin and Edward Reifstein III observed two pulsational radio sources near Crab nebula in 1968 [20]. Shortly after the discovery of two pulsational radio sources, Richard Lovelace discovered the period and location of the Crab Nebula pulsar [21].

Since then, many experiments covering multi-wavelength from radio to high energy gamma-ray have been conducted to observe Crab nebula and Crab pulsar. For example, The Spitzer Space Telescope (SST) is an infrared space telescope launched in 2003 and observes infrared emission. Fermi observes X-ray emission. Major Atmo-

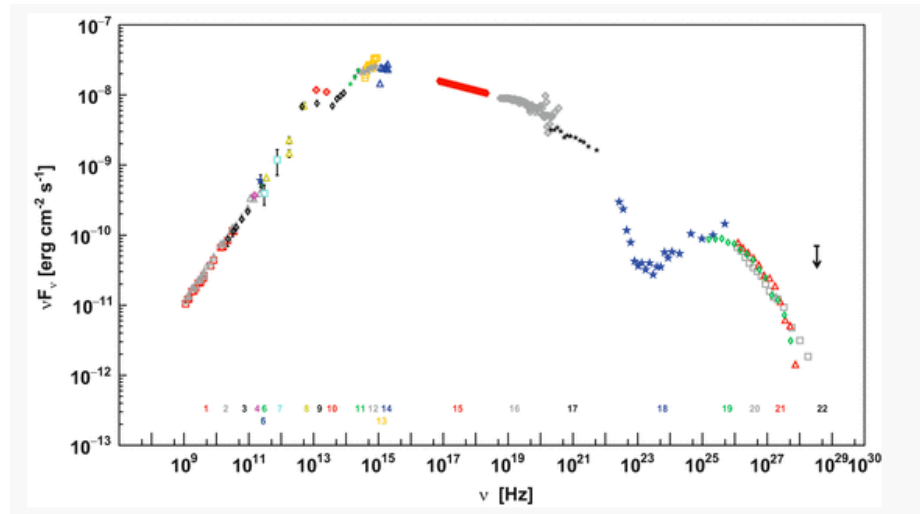


Figure 1.2. The broad-band spectrum of the Crab nebula via multi-wavelength observations, taken from [23].

spheric Gamma Imaging Cherenkov Telescopes (MAGIC), High Energy Stereoscopic System (H.E.S.S.), and Very Energetic Radiation Imaging Telescope Array System (VERITAS) are Imaging Atmospheric Cherenkov Telescopes and observes high energy gamma rays.

The most recent and surprising observation was from Tibet AS γ experiment, which is an air shower observation array located in Tibet, China. AS γ collaboration observed the gamma-ray photons over 100 TeV from Crab nebula in 2019, and it is the first detection of photons with energy beyond 100 TeV from an astrophysical source [22].

The spectrum of the Crab nebula is shown as Fig 6.7 in [23] via multi-wavelength observations. Here the result of the spectrum of the Crab nebula is reprinted as Fig. 1.2. There are two peaks in the broad-band spectrum. The one around 10^{15} Hz is a synchrotron emission peak, and the other one around 10^{26} Hz is an IC peak (I will discuss more detail about synchrotron emission and IC in §1.1.4). The little bump around 10^{13} Hz is believed as the thermal component satisfies the black body radiation formula.

1.2.2 Kennel-Coroniti prescription

Following the work of [24], Kennel-Coroniti developed a standard one-dimensional spherically symmetric steady MHD model of Crab nebula [25]; [26]. The idea of the Kennel-Coroniti model is that the pulsar generates a highly relativistic wind, and a strong shock terminates the wind.

They then assumed the particle distribution obeys power-law and followed the MHD solutions to find the best-fit result of the pulsar luminosity, L ; the shock radius, r_s ; and the ratio, σ , of the Poynting to particle energy fluxes in the upstream wind to match the flow and pressure boundary conditions at the nebula-remnant interface. The best-fit solution they found is $L = 5 \times 10^{38}$ ergs s^{-1} , $r_s = 3 \times 10^{17}$ cm, and $\sigma = 0.003$.

Fig 13 in [26] presents the comparison of the best-fit Crab nebula spectra and observation data. The parameter, which fits the hard X-ray and γ -ray, can also reproduce the observed intensity and spectra slope of the optical-UV band. Thus, they have succeeded in linking the different independent observations over the different frequency ranges by using the one MHD flow model.

However, their stead MHD model only accounts for the synchrotron spectrum from infrared to X-ray emissions, not for the radio emission. More drawbacks of the Kennel-Coroniti model and the attempt to build the model of Crab nebula radiation, which can account for a broad range of emission from radio to highest γ -ray are discussed in §3.

1.3 Observational properties and theories of GRBs

1.3.1 Observational properties of GRBs

GRBs are the most energetic astronomical events in the universe [27]; [28] with duration from few ten millisecond to several hundred seconds. The observed fluences of GRBs are from 10^{-4} to 10^{-7} erg/cm². The redshift and flux implies that GRBs

can produce isotropic luminosity from 10^{48} to 10^{55} ergs. However in reality, GRBs are narrowly beamed as a jet outflow [29]; [30], which reduces the corresponding real energy release in GRBs from 10^{48} to 10^{52} erg [31]; [32]; [33]; [34]; [35]; [36]; [37]; [38]. Even though people have observed GRBs for about sixty years, there are many puzzles people still don't understand in GRBs events.

GRBs could be detected a few times a day at the random direction in the sky [39]; [40]; [41], even though the rate of GRBs event in a galactic is estimated only from 10^{-6} to 10^{-5} yr^{-1} [42]; [43]; [44], The first GRBs signal was detected in 1967 by the Vela satellites, which were designed to detect gamma-ray emitted by nuclear weapons in early years of Cold War, and the discovery was published in 1973 when the solar origins were ruled out completely [45].

The origin of GRBs had puzzled people for a long time, and many models were proposed to explain the existence of GRBs. However, due to the GRBs' short duration, the first Vela observation was not able to provide too much information, such as redshift, distance, localization, and luminosity. Following the Vela's discovery, Compton-Gamma-Ray-Observatory (CGRO) was launched in 1991. CGRO was a space observatory detecting photons with energies from 20 KeV to 30 GeV, and it carries four instruments: The Burst and Transient Source Experiment (BATSE), The Oriented Scintillation Spectrometer Experiment (OSSE), The Imaging Compton Telescope (COMPTEL), and The Energetic Gamma Ray Experiment Telescope (EGRET). CGRO discovered that GRBs are isotropically distributed, which indicates that GRBs are located at a cosmological distance. CGRO also found that there are two classes of GRBs (see Fig.1 in [40]): short GRBs with duration less than two seconds (see Fig.1 in [46] as a typical light curve of short GRBs), and long GRBs with duration more than two seconds (see Fig.1 in [47] as a typical light curve of long GRBs).

Following CGRO, BeppoSAX was launched in 1996. BeppoSAX was a space satellite detecting photons with energies from 0.1 KeV to 300 KeV with relatively larger area and better angular resolution, and it carries five instruments: Low En-

ergy Concentrator Spectrometer (LECS), Medium Energy Concentrator Spectrometer (MECS), Medium Energy Concentrator Spectrometer (MECS), Phoswich Detector System (PDS), and Wide Field Camera (WFC). BeppoSAX made the first accurate distance measurement and determined a faint, distant host galaxy in 1997, thus convinced that GRBs are located a cosmological distance [41]; [48]; [49]; [50]; [51]; [52]; [53]; [54]; [55]; [56]. In 1997, satellites BeppoSAX, along with 4.2-m William Herschel Telescope (WHT) on La Palma, discovered the first X-ray and optical afterglow after the gamma-ray burst event GRB 970228 [53]; [54]. In 1998, [57] found that the Type Ib/c event supernova (SN) GRB 980425/SN 1998bw represents the general mechanism for GRBs by analyzing BeppoSAX data. The relationship between GRBs and SNs are confirmed later by High Energy Transient Explorer (HETE-2) via observing GRB 030329/SN 2003dh in 2003 [58]; [59]. In 1999, BeppoSAX, along with Robotic Optical Transient Search Experiment (ROTSE), observed a very bright optical flash from GBR 990123 while gamma-ray burst was still active [60]; [61], which can be explained by standard fireball model [62]; [63]; [64], see §1.3.2.

The GRBs emission themselves are usually called GRBs prompt emission. The properties of GRB prompt emission could be summarized as the following [65]: (1) GRB light curves are very diverse. (2) GRB prompt emission is non-thermal, and a band function [39] could describe most of the GRB spectra. (3) The peak energy ranges from 10 KeV to 10 MeV. (4) The prompt gamma-ray emission is linearly polarized with a large degree of polarization. The possible radiation mechanisms are synchrotron emission, Inverse Compton emission (IC), synchrotron self-Compton (SSC), and hadronic cascade. However, the origin of GRB prompt emission is still an unsolved problem, and many aspects of GRBs prompt emission are still mysteries, such as jet composition, energy dissipation mechanism, particle acceleration mechanism.

Many theoretical GRBs models predicted that GRBs are produced in relativistic explosion [66]; [1]. The observational evidences are from radio scintillation measurement for GRB 970508 [67]; [68] and superluminal motion of the radio afterglow of

GRB 030329 [69], where the blast wave was found to be relativistically for a couple of weeks after the explosion. It was expected under much theoretical consideration that a long-lasting fading emission in the X-ray, optical, and radio band, which is also called afterglow, will be produced when the highly relativistic jet interacts with the interstellar gas and should be following the GRBs prompt emission [70]; [71]; [63]. In the same year, Very Large Array (VLA) at the National Radio Astronomy Observatory observed the first radio afterglow after the gamma-ray burst event GRB 970508 [68]. The general behaviors of GRB afterglow emission could be summarized as the following: (1) GRB afterglow starts as an early time steep decay with a power-law index steeper than -2. (2) Following the early steep decay, there is a shallow decay or plateau with a power-law index -0.5 or larger. (3) In most GRBs, the plateau is followed by a normal decay with a typical power-law index -1. (4) In the end, there is a late steep decay with a power-law index -2 or steeper. (5) About half of GRBs have one or more X-ray flares.

Short GRBs are perhaps from the merger of two compact objects because (1) short GRBs were found to be associated with older stellar population and low star forming regions, (2) short GRBs were found to be on average less energetic and at a lower redshift [72]; [73]; [74]. Long GRBs are perhaps from the collapse of massive stars because (1) long GRBs were found to be on average larger energetic and larger time scale. (2) long GRBs were found to be in star forming regions of their host galaxies. (3) type Ic supernovae were detected associated with several long GRBs [57]; [28]; [75]; [76]; [77]; [78]; [79]; [80]; [81]; [82]; [83]; [84]; [85]; [86].

In 2004, The Neil Gehrels Swift Observatory (Swift) [87] was launched, and we enter the new era of studying GRBs. Swift is a multi-wavelength space observatory detecting photons with energies from 0.02 KeV to 150 KeV, and it carries three instruments: Burst Alert Telescope (BAT), X-ray Telescope (XRT), and Ultraviolet/Optical Telescope (UVOT). When BAT detects a burst, XRT and UVOT can quickly point to the GRB position within 60-100 seconds and observe its X-ray and lower frequency afterglow emission. In other words, the three instruments of Swift can

work together to observe GRBs and afterglows in the gamma-ray, X-ray, ultraviolet, and optical wavebands. Swift has several notable detections, such as the first accurate location of short GRBs was identified, and the first X-ray afterglow in a short GRB was detected on May 9, 2005 [88]; [80]; the most distant cosmic explosion ever seen GRB 090429B was observed on April 29, 2009 [89]; the most powerful observed gamma-ray burst GRB 190114C was observed on January 19, 2019 [90].

The Fermi Gamma-ray Space Telescope (Fermi) [91] was launched in 2008. Fermi is a space observatory detecting photons with energies from 8 KeV to 300 GeV, and it carries two instruments: the Large Area Telescope (LAT) and the Gamma-ray Burst Monitor (GBM). Fermi has several discoveries associated with GRBs, such as some GRBs were found having an additional spectra component in their prompt emission [92]; [93]; the maximum photon energy 94 GeV was detected from GRB 130427A on April 27, 2013 [94]; GRB 170817A was identified after its gravitational wave was detected by LIGO detector [95].

Many more new satellites, such as Ultra-Fast Flash Observatory (UFFO) [96]; [97] and Hard X-ray Modulation Telescope (HXMT) [98], and ground-based observatories, such as The Expanded Very Large Array (EVLA) [99], Atacama Large Millimeters/submillimeter Array (ALMA) [100] and Low-Frequency Array (LOFAR) [101], have been used to investigate the nature of GRBs. Some future detectors, such as Space Variable Objects Monitor (SVOM) [102], have been proposed to give us more information from the observations.

1.3.2 Hot fireball model

Since [41] found that GRBs are located in cosmological distance, the isotropic photon energies can be estimated as $E_{iso} \sim 10^{51}$ erg. Even consider the beaming effect, the jet photon energies can be estimated as $E_{jet} \sim 10^{48}$ erg. Such high energies concentrated on a scale of the size of a star will produce a fireball naturally.

The first process within the fireball is the adiabatic expansion. During the first process, the energy of photons and electrons are converted into the kinetic energies of protons, so that the fireball undergoes a relativistic expansion with Lorentz factor $\Gamma \geq 10^3$ [103].

The second process within the fireball is the deceleration when the relativistic fireball interacts with the external medium. During the second process, the kinetic energies of protons are converted into the thermal energies, which can be radiated away as photons [104]; [62]; [105]. In the meantime, a reverse shock formed and accelerated electrons, which produced non-thermal photons via synchrotron radiation and IC.

There are four critical radii in the fireball model [106]: R_i is the initial radius of the fireball, where a large amount of energy is released. $R_\eta \sim R_i \eta$ is the radius of radiation/matter dominated phase transition. Behind $R_i \eta$, all the energy is in the kinetic energy of the matter. $R_{pair} \sim \left(\frac{E}{\pi R_i^3 a}\right)^{\frac{1}{4}} \frac{R_i}{T_p}$ is the radius of optically thin to pairs. Behind R_{pair} , the pair-production become small enough, and the fireball become optically thin to pairs. $R_e \sim \left(\frac{\tau E}{4\pi m_p c^2 \eta}\right)^{\frac{1}{2}}$ is the radius of optically thin to electrons associated with protons. Behind R_e , the scattering between the photons and the electrons are sufficient small, and the fireball become optically thin to electrons associated with protons. Here we denote $\eta = \frac{E}{M c^2}$ as the ratio of the initial energy to the mass of the fireball.

Two critical values for η can be derived [106]; [103]. η_{pair} is the value of the η when $R_{pair} = R_e$

$$\eta_{pair} \sim \left(\frac{\sigma_T^2 E \alpha T_p^4}{\pi m_p^2 c^4 R_i}\right)^{\frac{1}{2}} \quad (1.23)$$

η_b is the value of the η when $R_e = R_\eta$

$$\eta_b \sim \left(\frac{\sigma_T E}{2\pi m_p c^2 R_i^2}\right)^{\frac{1}{3}} \quad (1.24)$$

Here α is the fine structure constant, and σ_T is the Thomson scattering cross section.

There are four different types of fireballs [106]. The case of $\eta_{pair} < \eta$ is called pure radiation fireball. In this case, $R_{pair} > R_e$, so the explosion energy escapes as radiation when the fireball becomes optically thin to pair-production. The case of $\eta_b < \eta < \eta_{pair}$ is called electron dominated opacity. In this case, the part of the explosion energy is converted to the kinetic energy of matter, but since the photons decouple with the electrons before the fireball enters into the matter-dominated phase, the fireball is still in radiation dominated regime. The case of $1 < \eta < \eta_b$ is called relativistic baryonic fireball. In this case, the fireball becomes matter-dominated before it becomes optical thin to electrons. So most of the explosion energy is converted into the kinetic energy of matters. This case is the most suitable situation for GRBs. The case of $\eta < 1$ is called a Newtonian fireball. In this case, the rest mass energy is larger than the radiation energy, and the explosion energy is not able to produce a relativistic fireball.

1.3.3 The external shock model of afterglows

While we are still not able to explain all the features in GRBs observation, there is a standard agreement that Reverse Shock (RS) and Forward Shock (FS) play an essential role in GRBs prompt emission and afterglow emission. The RS-FS system could be explained as follows: there are four regions, which include unshocked jet, shocked jet, shocked ejecta, and unshocked ejecta. FS, which satisfies Blandford & Mckee self-similar solution [107], separates shocked ejecta and unshocked ejecta, contact discontinuity (CD) separates shocked ejecta and shocked jet, and RS separates unshocked jet and shocked jet. Once a collimated jet is launched, the jet hits the interstellar medium (ISM) and produces a forward shock that moves outward into the ISM and a reverse shock that back into the unshocked jet. Between the shocked medium and the shocked jet, a density-discontinuity surface will be formed. This structure is shown as FIG.1.3.

Conventionally, GRBs prompt emissions and afterglow emission are explained by the standard fireball model [104]; [108]; [106]; [109]; [2], which is the following: when a

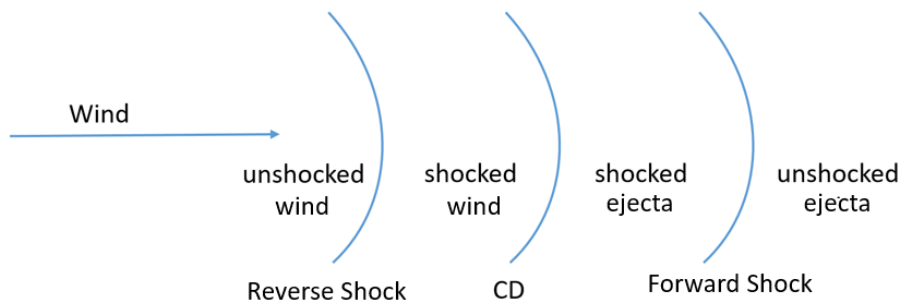


Figure 1.3. RS-FS structure as viewed from the observer frame. RS and FS are produced from the interaction between a relativistic jet and ISM. The shocked jet and shocked ejecta are on the different sides of CD and move with the same velocity, and they have the same pressure but different density.

massive star collapse, gravitational energy is transformed to thermal energy, and then most of the thermal energy is transformed to the kinetic energy of outflow jet. When the jet is slowed down by surrounding ISM, the kinetic energy of the outflow jet is dissipated in the FS and RS. Then the prompt emission is produced by the internal collision of matter-dominated shells within the flow, and afterglows are generated in the relativistic blast wave after the flow is slowed down by shocks with the surrounding circumstance medium.

For the cooling process, we introduce three characteristic frequencies: the typical synchrotron frequency of the accelerated electrons with the minimum Lorentz factor ν_0 , the typical synchrotron frequency of the cooled electrons with the minimum Lorentz factor ν_{min} , and the cooling frequency ν_c . It's for sure that ν_{min} is the lowest one among three characteristic frequencies. If $\nu_0 > \nu_c$, we call the corresponding spectrum as fast cooling. If $\nu_0 < \nu_c$, we call the corresponding spectrum as slow cooling. With a power law electrons distribution (power law index = p), for fast cooling, the flux at the observer is given by [110]

$$F_\nu = \begin{cases} (\nu/\nu_c)^{1/3} F_{\nu,\max}, & \nu_c > \nu \\ (\nu/\nu_c)^{-1/2} F_{\nu,\max}, & \nu_0 > \nu > \nu_c \\ (\nu_0/\nu_c)^{-1/2} (\nu/\nu_0)^{-p/2} F_{\nu,\max} & \nu > \nu_0 \end{cases} \quad (1.25)$$

and for slow cooling, the flux at the observer is given by [110]

$$F_\nu = \begin{cases} (\nu/\nu_0)^{1/3} F_{\nu,\max}, & \nu_0 > \nu \\ (\nu/\nu_0)^{-(p-1)/2} F_{\nu,\max}, & \nu_c > \nu > \nu_0 \\ (\nu_c/\nu_0)^{-(p-1)/2} (\nu/\nu_c)^{-p/2} F_{\nu,\max} & \nu > \nu_c \end{cases} \quad (1.26)$$

where $F_{\nu,\max}$ is the observed peak flux. The typical synchrotron spectrum of slow cooling and fast cooling are showed as Fig. 1 in [110], here I reprint the result as Fig. 1.4.

Readers should be aware of three-time variables I will use throughout this dissertation. They are fluid time, lab time, and observe time. In this dissertation, the fluid times are denoted as t' (I also denote all quantities measured in the fluid frame

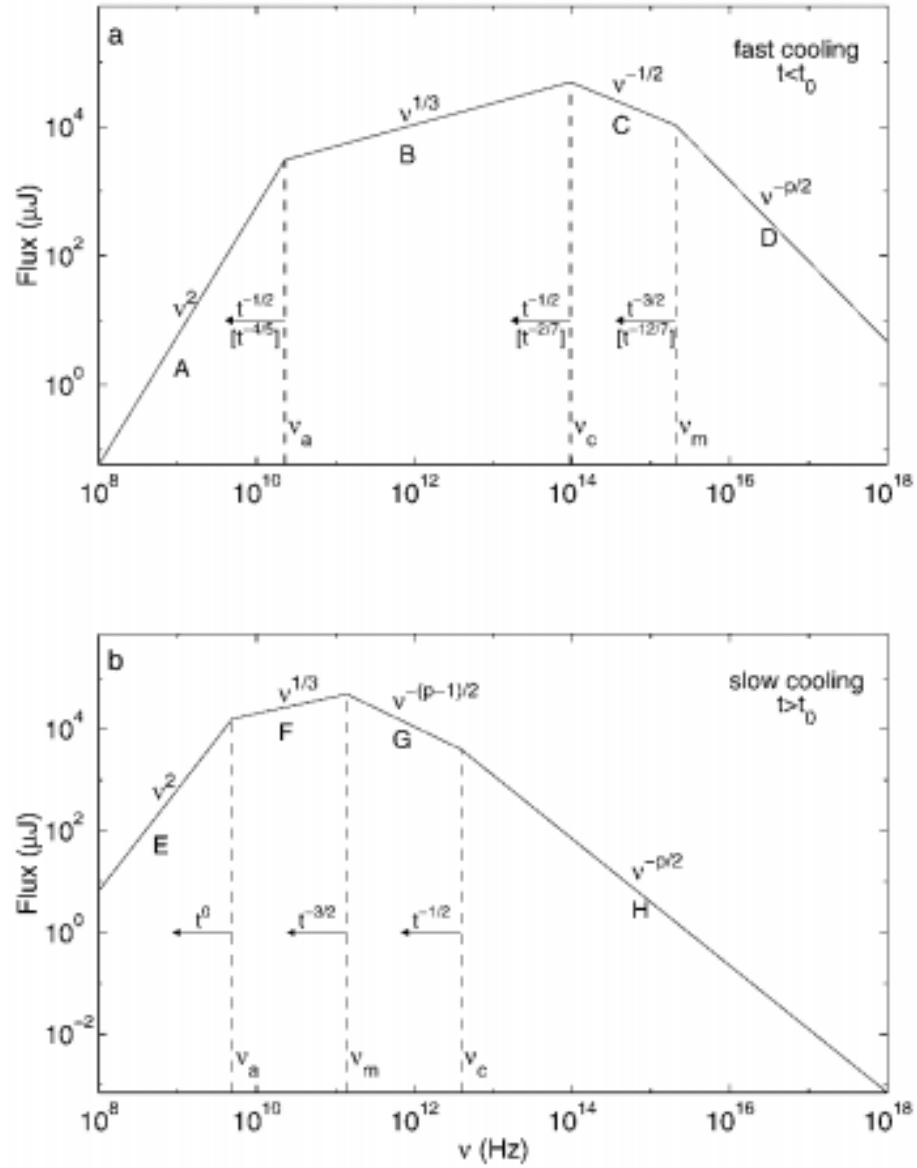


Figure 1.4. Synchrotron spectrum of fast cooling and slow cooling with a power law electron distribution. Taken from [110].

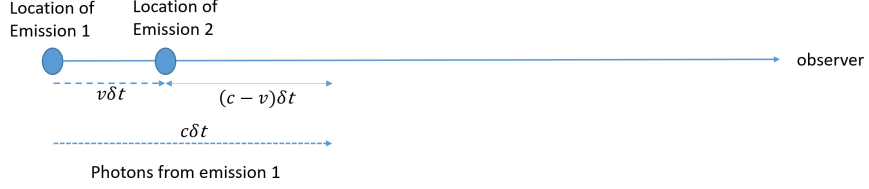


Figure 1.5. The relation between lab time and observe time in 1-dimension condition. Firstly, the emission source emit a photon at location 1 at time t_1 . At time $t_2 = t_1 + \delta t$, the emission source move to the location 2, and emit a photon. At the same time, the first photon has travelled $c\delta t$. So the distance between these two photon is $(c - v)\delta t$, and the time interval that observer will see these two photons is $\frac{c-v}{c}\delta t$.

as variable-plus-prime), lab time as t (I also denote all quantities measured in lab frame as just-variables) and observe time as T or T_{ob} . The illustration of three-time variables in 1-dimension condition is as FIG.4.20. Fluid time is the time measured in the fluid frame. Lab time is the time measured in the lab frame. According to special relativistic, $t = t'\Gamma$, where Γ is the Lorentz factor of fluid. Observe time is the time interval measured by an observer in the lab frame. From the FIG.4.20, the time interval between emission 1 and emission 2 in lab frame is $\delta t = t_2 - t_1$. But for observer, the time interval between emission 1 and emission 2 is $\delta T = \frac{c-v}{c}\delta t = (1 - \beta)\delta t = \frac{t}{2\Gamma^2}$ since the emission location move toward observer with distance $v\delta t$, where I assume the fluid has relativistic movement.

1.4 The Outline of the Dissertation

In the rest of this dissertation, I will focus on my previous works to apply a powerful program, which can calculate the synchrotron spectrum and IC spectrum for a broad range of relativistic processes, to several astrophysical objects: PWNs, GRBs, GWs. In chapter §2, I present the analytical work of calculating the synchrotron spectrum. Chapter §2 provides the calculation tool for the works in §3, §4, and §5. In

chapter §3, I calculate the broad-band spectrum and spectra index map of the two-component Crab nebula model. In chapter §4, I present an alternative GRB model in which the emission is from the long-lived terminate shock. Radiation loss, adiabatic expansion, and the effect of opening angle are considered in this section. By applying this model, I explain the steep drop, the flares, and the plateau within the GRB afterglow light curve. In chapter §5, I present a study in which FS emission is included in the GRB/GW 170817 event. I calculate the light curve of GRB/GW 170817 and predict the second bump at a later time. Finally, I summarize my dissertation and present some work I will do in the future in chapter §6.

2. SYNCHROTRON EMISSION IN AN EVOLVING MAGNETIC FIELD

2.1 Introduction

Synchrotron emission is one of the most common radiation mechanism in astrophysics. Thus, a systematic way of calculating the synchrotron spectrum is needed for a broad range of topics: such as GRBs, AGNs, and other relativistic processes.

In this chapter, I will derive the basic analytical method of calculating synchrotron emission. I will start my calculations from the case of a constant magnetic field without an expansion process in §2.2. Then, I will dive into the process of adiabatic expansion in §2.3. Both radiative losses and adiabatic expansion are considered in §2.3. Finally, I will extend my calculation into a more general situation (we consider a self-similar dynamic expansion for a demonstration, but the scope of solvable problems are any expansion processes, whose bulk Lorentz factors is the power-law of time t . Thus, the applicable power much beyond the self-similar dynamic expansion case) in §2.4.

2.2 Synchrotron Emission in a constant magnetic field

Let us consider the evolution of the distribution function of accelerated particles taking into account only radiative losses.

First, we want to find the Green's function. For a pure power-law distribution, this was done by Kardashev (1962) [111]. We will include the effect of γ_{\min} , which is the minimum Lorentz factor of the injected electrons, in my calculations.

For completeness, let us first re-derive the Green's function for synchrotron-cooling particles in a constant magnetic field. We need to solve Boltzmann's (Liouville's) equation with energy losses,

$$\frac{\partial f}{\partial t} + \frac{\partial(\dot{\gamma}f)}{\partial \gamma} = f_{inj} \quad (2.1)$$

where f is the distribution function of the injected particles, f_{inj} is the particle injection spectrum, and γ is the Lorentz factor of injected electrons.

We assume that at time $t = t_i$, a distribution $f_{inj} \propto \gamma^{-p}\Theta(\gamma - \gamma_{min})$ ($\Theta(x)$ is the Heavyside function) is injected. The Green's function is given by the solution of Eqn. (2.1) with injection $\propto \gamma^{-p}\delta(t - t_i)\Theta(\gamma - \gamma_{min})$, where p is the power law index, t_i is the injection time, and t is the time after injection, thus $t \geq t_i$.

In constant magnetic field the energy of particle experiencing synchrotron losses evolves according to

$$\begin{aligned} \frac{d\gamma}{dt} &= -C_1 B^2 \gamma^2 \\ C_1 &= \frac{\sigma_T}{6\pi mc} \end{aligned} \quad (2.2)$$

and the solution is

$$\gamma = \frac{\gamma_0}{1 + C_1 B^2 \gamma_0 (t - t_0)} \quad (2.3)$$

where σ_T is the Thomson cross section (we have separated magnetic field from the universal constants), t_0 is the initial time, B is the magnetic field, and γ_0 is the initial Lorentz factor of the particles. I plot how does Lorentz factor evolve with time as Fig.2.1 and Fig.2.2.

Thus, the Green's function becomes the solution of partial differential equation

$$\frac{\partial f}{\partial t} - C_1 B^2 \frac{\partial(f\gamma^2)}{\partial \gamma} = f_0 \gamma^{-p} \delta(t - t_i) \Theta(\gamma - \gamma_{min}) \quad (2.4)$$

with initial condition $G(\gamma, t_i, t_i) = f_0 \gamma^{-p} \Theta(\gamma - \gamma_{min})$, where f_0 is a normalization constant, which satisfies $L_{inj} = \int_{\gamma_{min}}^{\infty} f_0 \gamma^{1-p} mc^2 d\gamma$ and L_{inj} is the injection power.

The solution of (2.4) is Eqn. (5) in [111] as

$$G(\gamma, t, t_i) = \begin{cases} f_0 \frac{(1 - C_1 B^2 \gamma (t - t_i))^{p-2}}{\gamma^p}, & \frac{\gamma_{min}}{C_1 B^2 \gamma_{min} (t - t_i) + 1} < \gamma < \frac{1}{C_1 B^2 (t - t_i)} \\ 0, & \text{else} \end{cases} \quad (2.5)$$

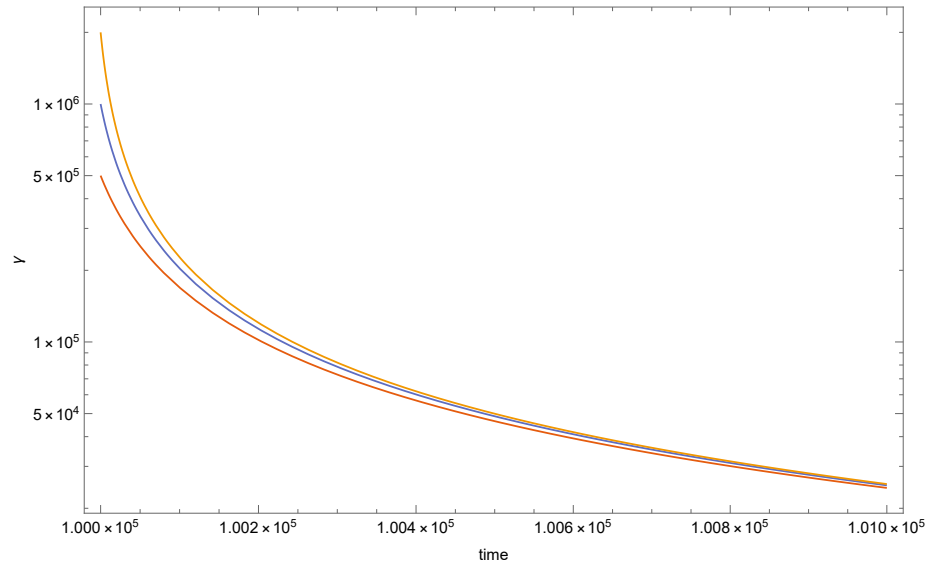


Figure 2.1. The typical evolution of the Lorentz factors in radiation-only energy loss processes. The initial Lorentz factor are 5×10^5 , 1×10^6 , 2×10^6 from red to orange. The initial time is $1 \times 10^5 s$.

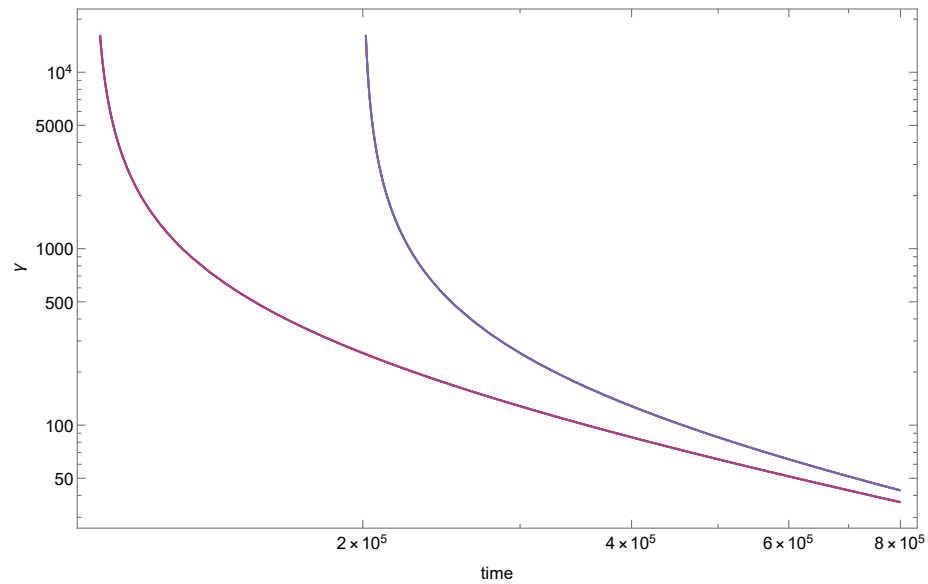


Figure 2.2. The typical evolution of the Lorentz factor in radiation-only energy loss processes. Two curves have same initial Lorentz factor but correspond to two different initial time $1 \times 10^5 s$ and $2 \times 10^5 s$

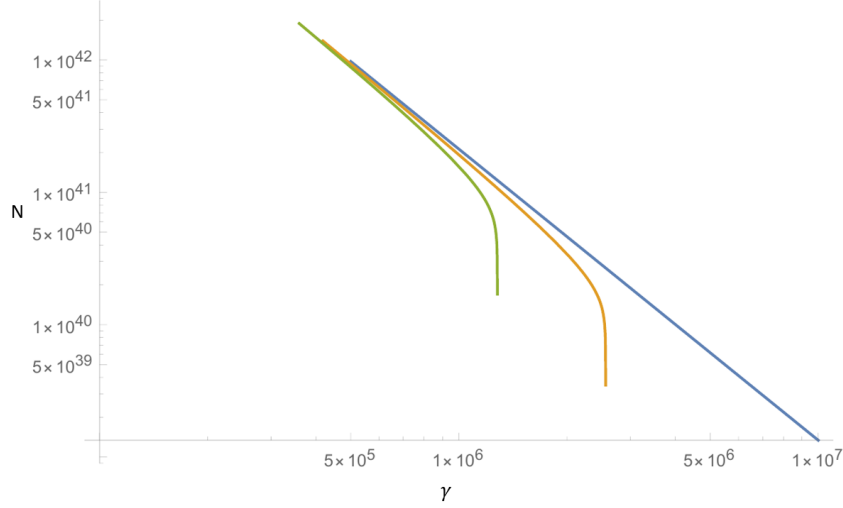


Figure 2.3. The evolution of the typical Green's Function for instantaneous injection at $t = t_0$. We use $\gamma_{\min} = 5 \times 10^5$, $B = 5.5G$, $t_0 = 10^5 s$, time = t_0 , $1.0001 \times t_0$, $1.0001^2 \times t_0$ from blue to green.

The evolution of the typical Green's function is showed as FIG. 2.3.

The Green's function is a special distribution function for instantaneous injection at time t_i . In order to find the distribution function for constant injection rate, we need to integrate over the duration of injection from the injection starting time to now, i.e. $N(\gamma, t) = \int_{t_0}^t G(\gamma, t, t_i) dt_i$, where t_0 is the initial injection time. The calculation is very tricky, as we describe below.

We consider two cases: (i) $\frac{\gamma_{\min}}{C_1 B^2 \gamma_{\min}(t-t_0)+1} < \frac{1}{C_1 B^2(t-t_0)} < \gamma_{\min}$, and (ii) $\frac{\gamma_{\min}}{C_1 B^2 \gamma_{\min}(t-t_0)+1} < \gamma_{\min} < \frac{1}{C_1 B^2(t-t_0)}$. Notice that γ_{\min} is a constant but $\frac{1}{C_1 B^2(t-t_0)}$ is decreasing as time goes, so case (ii) is at the early time of the evolution, and case (i) is at the later time of the evolution.

Let us consider about case (i) firstly. All injected particles have contribution to the distribution function. In terms of their Lorentz factor γ , we can divide the distribution function into four regions, which are $\gamma < \frac{\gamma_{\min}}{C_1 B^2 \gamma_{\min}(t-t_0)+1}$, $\frac{\gamma_{\min}}{C_1 B^2 \gamma_{\min}(t-t_0)+1} < \gamma < \frac{1}{C_1 B^2(t-t_0)}$, $\frac{1}{C_1 B^2(t-t_0)} < \gamma < \gamma_{\min}$, and $\gamma_{\min} < \gamma$. Now we can do integration over each region separately.

For the case of $\gamma < \frac{\gamma_{\min}}{C_1 B^2 \gamma_{\min}(t_0)+1}$, γ is less than $\frac{\gamma_{\min}}{C_1 B^2 \gamma_{\min}(t-t_i)+1}$ for any positive number $t_i > t_0$, so the Green's function $G(\gamma, t, t_i)$ is always zero for the all duration of injection. Thus, the contribution from this part simply becomes

$$N_1(\gamma, t) = \int_{t_0}^t G(\gamma, t, t_i) dt_i = 0 \quad (2.6)$$

For the case of $\frac{\gamma_{\min}}{C_1 B^2 \gamma_{\min}(t-t_0)+1} < \gamma < \frac{1}{C_1 B^2(t-t_0)}$, γ is less than $\frac{1}{C_1 B^2(t-t_i)}$ for any positive number $t_i > t_0$, but is not necessary larger than $\frac{\gamma_{\min}}{C_1 B^2 \gamma_{\min}(t-t_i)+1}$. More specifically, when t_i is larger than $t - \frac{\gamma_{\min}-\gamma}{C_1 B^2 \gamma \gamma_{\min}}$, γ is less than $\frac{\gamma_{\min}}{C_1 B^2 \gamma_{\min}(t-t_i)+1}$, which means the Green's function is 0. So the Green function is non-zero only for duration of injection $t_0 < t_i < t - \frac{\gamma_{\min}-\gamma}{C_1 B^2 \gamma \gamma_{\min}}$. Thus, the contribution to the distribution function from this part becomes

$$N_2(\gamma, t) = \int_{t_0}^t G(\gamma, t, t_i) dt_i = \int_{t_0}^{t - \frac{\gamma_{\min}-\gamma}{C_1 B^2 \gamma \gamma_{\min}}} G(\gamma, t, t_i) dt_i \quad (2.7)$$

For the case of $\frac{1}{C_1 B^2(t-t_0)} < \gamma < \gamma_{\min}$, γ is neither necessary less than $\frac{1}{C_1 B^2(t-t_i)}$, nor necessary larger than $\frac{\gamma_{\min}}{C_1 B^2 \gamma_{\min}(t-t_i)+1}$. More specifically, when t_i is larger than $t - \frac{\gamma_{\min}-\gamma}{C_1 B^2 \gamma \gamma_{\min}}$, γ is less than $\frac{\gamma_{\min}}{C_1 B^2 \gamma_{\min}(t-t_i)+1}$, which means the Green's function is 0. And when t_i is smaller than $t - \frac{1}{C_1 B^2 \gamma}$, γ is larger than $\gamma < \frac{1}{C_1 B^2(t-t_i)}$, which also means the Green's function is 0. So the Green function is non-zero only for duration of injection $t - \frac{1}{C_1 B^2 \gamma} < t_i < t - \frac{\gamma_{\min}-\gamma}{C_1 B^2 \gamma \gamma_{\min}}$. Thus, the contribution to the distribution function from this part becomes

$$N_3(\gamma, t) = \int_{t_0}^t G(\gamma, t, t_i) dt_i = \int_{t - \frac{1}{C_1 B^2 \gamma}}^{t - \frac{\gamma_{\min}-\gamma}{C_1 B^2 \gamma \gamma_{\min}}} G(\gamma, t, t_i) dt_i \quad (2.8)$$

Finally, for the case of $\gamma_{\min} < \gamma$, γ is not necessary less than $\frac{1}{C_1 B^2(t-t_i)}$, but γ is always larger than $\frac{\gamma_{\min}}{C_1 B^2 \gamma_{\min}(t-t_i)+1}$ for any positive number $t_i > t_0$. More specifically, when t_i is smaller than $t - \frac{1}{C_1 B^2 \gamma}$, γ is larger than $\gamma < \frac{1}{C_1 B^2(t-t_i)}$, which means the Green's function is 0. So the Green function is non-zero only for duration of injection $t - \frac{1}{C_1 B^2 \gamma} < t_i < t$. Thus, the contribution to the distribution function from this part becomes

$$N_4(\gamma, t) = \int_{t_0}^t G(\gamma, t, t_i) dt_i = \int_{t - \frac{1}{C_1 B^2 \gamma}}^t G(\gamma, t, t_i) dt_i \quad (2.9)$$

Then let us consider case (ii). we want to divide the distribution function into four regions again. But this time, the four parts are $\gamma < \frac{\gamma_{\min}}{C_1 B^2 \gamma_{\min}(t-t_0)+1}$, $\frac{\gamma_{\min}}{C_1 B^2 \gamma_{\min}(t-t_0)+1} < \gamma < \gamma_{\min}$, $\gamma_{\min} < \gamma < \frac{1}{C_1 B^2(t-t_0)}$, and $\frac{1}{C_1 B^2(t-t_0)} < \gamma$. Now we can do integration over each region separately.

For the case of $\gamma < \frac{\gamma_{\min}}{C_1 B^2 \gamma_{\min}(t-t_0)+1}$, γ is less than $\frac{\gamma_{\min}}{C_1 B^2 \gamma_{\min}(t-t_i)+1}$ for any positive number $t_i > t_0$, so the Green's function is always zero for the all duration of injection. Thus, the contribution from this part simply becomes

$$N_1(\gamma, t) = \int_{t_0}^t G(\gamma, t, t_i) dt_i = 0 \quad (2.10)$$

For the case of $\frac{\gamma_{\min}}{C_1 B^2 \gamma_{\min}(t-t_0)+1} < \gamma < \gamma_{\min}$, γ is less than $\frac{1}{C_1 B^2(t-t_i)}$ for any positive number $t_i > t_0$, but is not necessary larger than $\frac{\gamma_{\min}}{C_1 B^2 \gamma_{\min}(t-t_i)+1}$. More specifically, when t_i is larger than $t - \frac{\gamma_{\min}-\gamma}{C_1 B^2 \gamma \gamma_{\min}}$, γ is less than $\frac{\gamma_{\min}}{C_1 B^2 \gamma_{\min}(t-t_i)+1}$, which means the Green's function is 0. So the Green's function is non-zero only for duration of injection $t_0 < t_i < t - \frac{\gamma_{\min}-\gamma}{C_1 B^2 \gamma \gamma_{\min}}$. Thus, the contribution to the distribution function from this part becomes

$$N_2(\gamma, t) = \int_{t_0}^t G(\gamma, t, t_i) dt_i = \int_{t_0}^{t - \frac{\gamma_{\min}-\gamma}{C_1 B^2 \gamma \gamma_{\min}}} G(\gamma, t, t_i) dt_i \quad (2.11)$$

For the case of $\gamma_{\min} < \gamma < \frac{1}{C_1 B^2(t-t_0)}$, γ is always less than $\frac{1}{C_1 B^2(t-t_i)}$ for any positive number $t_i > t_0$, and γ is also always larger than $\frac{\gamma_{\min}}{C_1 B^2 \gamma_{\min}(t-t_i)+1}$ for any positive number $t_i > t_0$. So the Greens function is non-zero for whole duration of injection $t - \frac{1}{C_1 B^2 \gamma} < t_i < t - \frac{\gamma_{\min}-\gamma}{C_1 B^2 \gamma \gamma_{\min}}$. Thus, the contribution to the distribution function from this part is simply

$$N_3(\gamma, t) = \int_{t_0}^t G(\gamma, t, t_i) dt_i \quad (2.12)$$

Finally, for the case of $\frac{1}{C_1 B^2(t-t_0)} < \gamma$, γ is not necessary less than $\frac{1}{C_1 B^2(t-t_i)}$, but γ is always larger than $\frac{\gamma_{\min}}{C_1 B^2 \gamma_{\min}(t-t_i)+1}$ for any positive number $t_i > t_0$. More specifically, when t_i is smaller than $t - \frac{1}{C_1 B^2 \gamma}$, γ is larger than $\gamma < \frac{1}{C_1 B^2(t-t_i)}$, which means the Green's function is 0. So the Green's function is non-zero only for duration

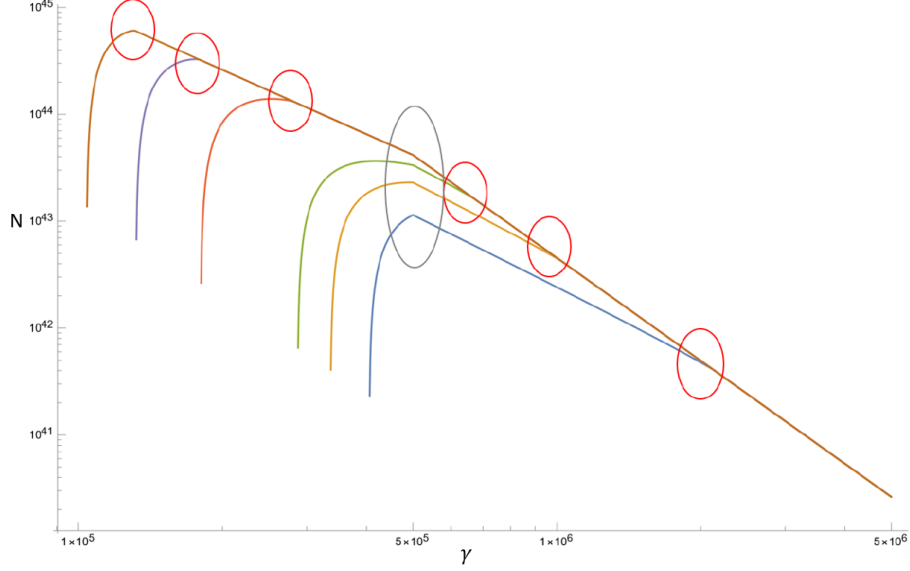


Figure 2.4. The evolution of the distribution function for radiation-only energy loss processes. We use $\gamma_{\min} = 5 \times 10^5$, $B = 5.5\text{G}$, $t_0 = 10^5\text{s}$. Time increase 12s , 25s , 38s , 91s , 143s , 195s after t_0 from blue to brown. The red circle are cooling break and the grey circle are injection break due to γ_{\min} . We can see the transition when cooling break cross the injection break from yellow curve to red curve.

of injection $t - \frac{1}{C_1 B^2 \gamma} < t_i < t$. Thus, the contribution to the distribution function from this part becomes

$$N_4(\gamma, t) = \int_{t_0}^t G(\gamma, t, t_i) dt_i = \int_{t - \frac{1}{C_1 B^2 \gamma}}^t G(\gamma, t, t_i) dt_i \quad (2.13)$$

By adding these four regions' contribution (either case (i), or case (II)), we will have the distribution function as

$$N(\gamma, t) = N_1(\gamma, t) + N_2(\gamma, t) + N_3(\gamma, t) + N_4(\gamma, t) \quad (2.14)$$

See Fig. 2.4 as a demonstration of the evolution of the distribution function for the radiation-only energy losses processes.

Next, we calculate the synchrotron spectrum. Single particle emissivity is

$$P(\omega) = \frac{\sqrt{3} B^2 e^3}{2\pi mc^2} F\left(\frac{\omega}{\omega_c}\right) \quad (2.15)$$

$$\omega_c = \frac{3B\gamma^2 e}{2mc} \quad (2.16)$$

The luminosity is

$$L(\omega, t) = \int N(\gamma, t)P(\omega) d\gamma = \int_{\gamma_{\min}}^{\infty} N(\gamma, t) \frac{\sqrt{3} B^2 e^3}{2\pi mc^2} F\left(\frac{\omega}{\omega_c}\right) d\gamma \quad (2.17)$$

where ω is the frequency of the emitted photons, and $F(x)$ is defined as:

$$F(x) \equiv x \int_x^{\infty} K_{\frac{5}{3}}(\xi) d\xi \quad (2.18)$$

where $K_{\frac{5}{3}}(\xi)$ is a Bessel function of the second kind.

So luminosity becomes

$$L(\omega) = \int_{\gamma_{\min}}^{\infty} N(\gamma, t) \frac{\sqrt{3} B^2 e^3}{2\pi mc^2} x \int_x^{\infty} K_{\frac{5}{3}}(\xi) d\xi d\gamma \quad (2.19)$$

where we define $x \equiv \frac{\omega}{\omega_c}$. By substituting equation (2.6), (2.7), (2.8), (2.9) (for the case (ii)) or (2.10), (2.11), (2.12), (2.13) (for the case (i)), and (2.14) into equation (2.19), we can calculate the luminosity from the radiation-only energy loss processes.

Also we want to calculate flux in the unit of Jy as below

$$F(\nu) = 10^{23} \frac{L(\nu)}{4\pi r^2} = 10^{23} \frac{2\pi L(\omega)}{4\pi r^2} = 10^{23} \frac{L(\omega)}{2r^2} \quad (2.20)$$

where r is the distance between the object and the observer.

FIG. 2.5 shows the evolution of the spectra in the radiation-only energy loss processes with the full integration calculation. There are clearly two breaks and three regions in the FIG. 2.5. We measure the slope of each region, and the results are $F \propto E^{0.33}$ in the low energy region, $F \propto E^{-0.52}$ in the middle energy region, and $F \propto E^{-1.04}$ in the high energy region, which are consistent with the classical analytical results, where $F \propto E^{\frac{1}{3}}$ in the low energy region, $F \propto E^{\frac{1-p}{2}}$ in the middle energy region, and $F \propto E^{\frac{p}{2}}$ in the high energy region. Here we use $p = 2.2$ for the calculations.

2.3 Synchrotron emission taking into account adiabatic and radiative losses

In the §2.2, we considered the radiation-only energy loss processes. In this section, we will add the energy losses due to adiabatic expansion, which is important for slowly

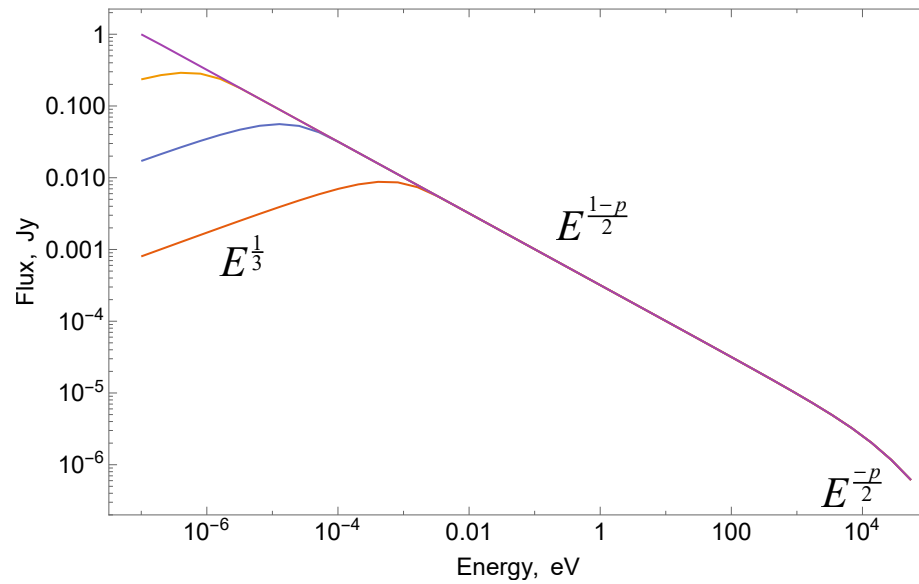


Figure 2.5. The evolution of the spectra in the radiation-only energy loss processes with the full integration. We use $\gamma_{\min} = 5 \times 10^5$, magnetic field $B = 5.5$ G, power law index $p=2.2$, distance $d=3.35 \times 10^9$ pc, initial time $t_0 = 10^5$ s, the time in fluid are $t' = 2 \times 10^5$ s, 10^6 s, 5×10^6 s, 2.5×10^7 s from red to purple.

cooled particles (*e.g.*, weak radio emission in GRBs [112]). We denote that non-primed variables are variables in the lab frame, and primed variables are in the frame of the fluid for the rest of the section.

In order to understand the effect of the adiabatic losses better, we first let magnetic field B approaches 0 (which means we consider the adiabatic-only energy loss processes), then we need to solve the partial differential equation

$$\frac{\partial f}{\partial t'} - \frac{1}{2t'} \frac{\partial(\gamma' f(\gamma', t'))}{\partial \gamma'} = f_0 \gamma'^{-p} \delta(t' - t'_i) \Theta(\gamma' - \gamma'_{\min}) \quad (2.21)$$

with the initial condition

$$f(\gamma', t'_0) = f_0 \gamma'^{-p} \Theta(\gamma' - \gamma'_{\min}) \quad (2.22)$$

where the Lorentz factor of the injected electrons satisfies

$$\frac{d\gamma'}{dt'} = -\frac{\gamma'}{2t'} \quad (2.23)$$

Then we can calculate the Green's function

$$G(\gamma', t', t'_i) = \begin{cases} f_0 \gamma'^{-p} \left(\frac{t'_i}{t'}\right)^{\frac{p-1}{2}}, & \gamma'_{\min} \sqrt{\frac{t'_i}{t'}} < \gamma' < \infty \\ 0, & \text{else} \end{cases} \quad (2.24)$$

and γ' evolves as

$$\gamma' = \gamma'_i \sqrt{\frac{t'_i}{t'}} \quad (2.25)$$

The evolution of the typical Green's function and the distribution function of the adiabatic-only energy losses processes are showed as FIG. 2.6 and FIG. 2.7

To take into account adiabatic and radiative losses together, we assume that the emitting plasma is permeated by spatially constant but temporarily slowly changing magnetic field $B_z(t)$. This adiabatic expansion will lead to two effects. First, the decreasing magnetic field will slow down radiative losses (for which $\dot{\gamma} \propto B^2$). Second, plasma expansion will lead to adiabatic losses.

Conservation of the first adiabatic invariant (constant magnetic flux though the cyclotron orbit) gives

$$\partial'_t \ln \gamma' = \frac{1}{2} \partial'_t \ln B' \quad (2.26)$$

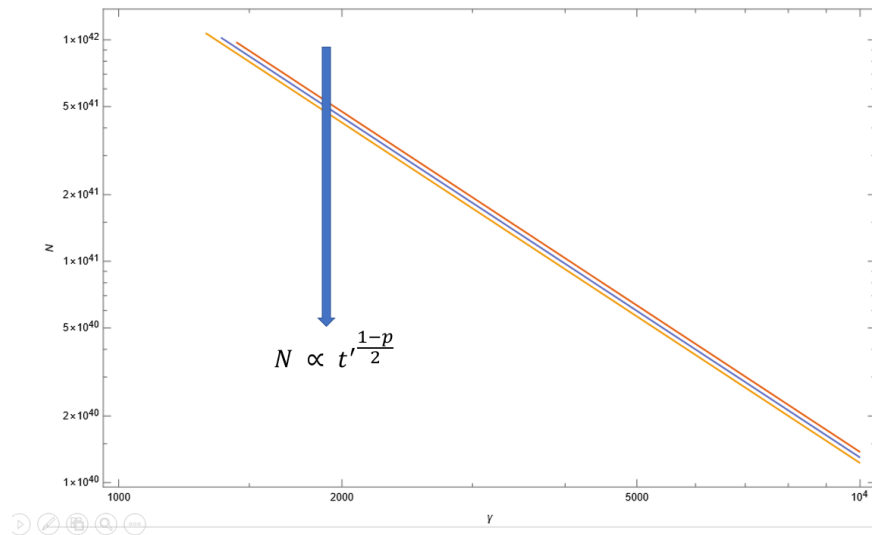


Figure 2.6. The evolution of the Green's function for adiabatic expansion without radiation losses. We use $\gamma'_{\min} = 1440$, $t'_0 = 10^5$ s. They correspond to time t_0 s, $t_0 + 1.00 \times 10^4$ s, $t_0 + 2.1 \times 10^4$ s from red to yellow.

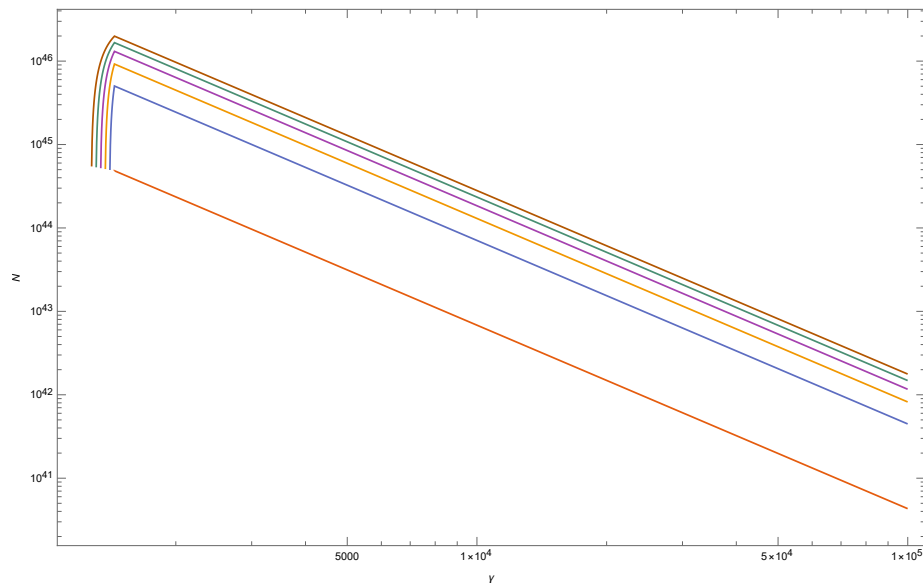


Figure 2.7. The evolution of the distribution function for adiabatic expansion without radiation losses. We use $\gamma'_{\min} = 1440$, $t'_0 = 10^5$ s. They correspond to time $t_0 + 5.00 \times 10^2$ s, $t_0 + 5.53 \times 10^3$ s, $t_0 + 1.08 \times 10^4$ s, $t_0 + 1.64 \times 10^4$ s, $t_0 + 2.22 \times 10^4$ s, $t_0 + 2.83 \times 10^4$ s from red to brown.

We assume that the magnetic field decreasing $\propto 1/t'$,

$$B' = B_0 \frac{t'_0}{t'} \quad (2.27)$$

Then, we take account adiabatic process, thus we need to solve the partial differential equation:

$$\frac{\partial f(\gamma', t')}{\partial t'} - \frac{\tilde{C}_1 B_0'^2}{t'^2} \frac{\partial (\gamma'^2 f(\gamma', t'))}{\partial \gamma'} - \frac{1}{2t'} \frac{\partial (\gamma' f(\gamma', t'))}{\partial \gamma'} = f_{\text{inj}} \quad (2.28)$$

with the injection function

$$f_{\text{inj}} = f_0 \gamma'^{-p} \delta(t' - t'_i) \Theta(\gamma' - \gamma'_{\text{min}}) \quad (2.29)$$

and the initial condition

$$f(\gamma', t'_0) = f_0 \gamma'^{-p} \Theta(\gamma' - \gamma'_{\text{min}}) \quad (2.30)$$

where the Lorentz factor of the injected electrons satisfies

$$\frac{d\gamma'}{dt'} = -\frac{\tilde{C}_1 B_0'^2 \gamma'^2}{t'^2} - \frac{\gamma'}{2t'} \quad (2.31)$$

and

$$\tilde{C}_1 = \frac{\sigma_T t_0'^2}{6\pi mc} \quad (2.32)$$

is a constant.

Then the Green's function is given by

$$G(\gamma', t', t'_i) = \begin{cases} f_0 \gamma'^{-p} \left(\frac{t'_i}{t'}\right)^{\frac{p-1}{2}} \left(1 - \frac{2}{3} \tilde{C}_1 B_0'^2 \gamma' \sqrt{t'} \left(\frac{1}{t_i'^{3/2}} - \frac{1}{t'^{3/2}}\right)\right)^{p-2}, & \gamma'_{\text{low}} < \gamma' < \gamma'_{\text{up}} \\ 0, & \text{else} \end{cases} \quad (2.33)$$

and

$$\frac{1}{\gamma'} = \frac{2\tilde{C}_1 B_0'^2}{3t'} \left(\left(\frac{t'}{t'_i}\right)^{3/2} - 1 \right) + \frac{1}{\gamma'_i} \sqrt{\frac{t'}{t'_i}} \quad (2.34)$$

where γ'_{low} is the lower bound of the Lorentz factor due to the minimum Lorentz factor of the injection and satisfies

$$\frac{1}{\gamma'_{\text{low}}} = \frac{2\tilde{C}_1 B_0'^2}{3t'} \left(\left(\frac{t'}{t'_i}\right)^{3/2} - 1 \right) + \frac{1}{\gamma'_{\text{min}}} \sqrt{\frac{t'}{t'_i}} \quad (2.35)$$

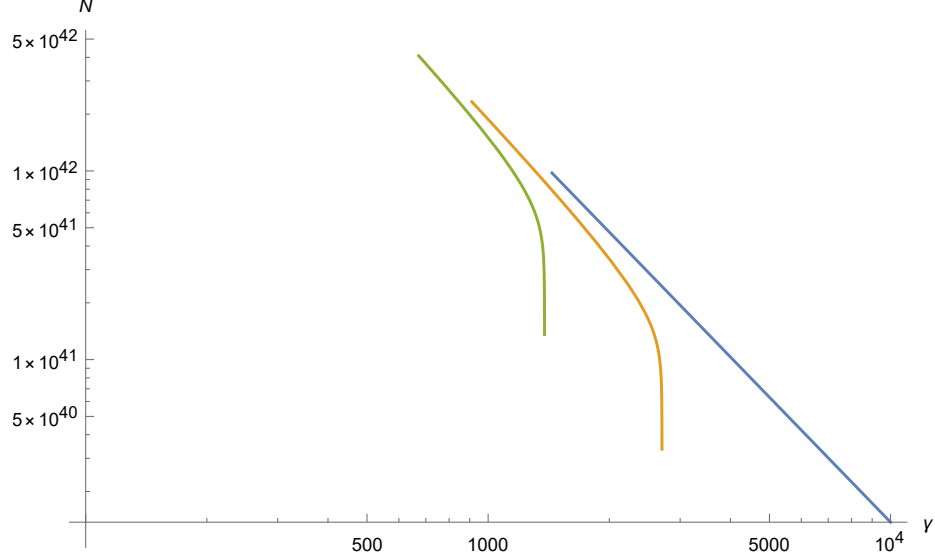


Figure 2.8. The evolution of the typical Green's function for adiabatic and radiative losses with an instantaneous injection at $t = t_0$. We use $\gamma_{\min} = 1440$, $B = 5.5$ G, $t'_0 = 10^5$ s, time = $t'_0, 1.1 \times t'_0, 1.1^2 \times t'_0$ from blue to green.

and γ'_{up} is the upper bound of the Lorentz factor due to the cooling break and satisfies

$$\frac{1}{\gamma'_{\text{up}}} = \frac{2\tilde{C}_1 B_0'^2}{3t'} \left(\left(\frac{t'}{t'_i} \right)^{3/2} - 1 \right) \quad (2.36)$$

The evolution of the typical Green's function for adiabatic and radiative losses is showed as FIG. 2.8. The evolution of the Lorentz factor for adiabatic and radiation losses is showed as FIG.2.9.

Use the similar method as before, we can divide the contribution into four parts and calculate the distribution function for each part by doing integration to the Green's function. Again, we need to find the time of period, whose the corresponding Green's function is non-zero. There are three breaks: (1) the break due to evolved minimum injection Lorentz factor γ'_m . (2) the cooling break γ'_c . (3) the minimum injection Lorentz factor γ'_0 . Thus there will be two cases: (i) fast cooling: $\gamma'_m < \gamma'_c < \gamma'_0$. (ii) slow cooling: $\gamma'_m < \gamma'_0 < \gamma'_c$. We denote t'_u as the solution of the

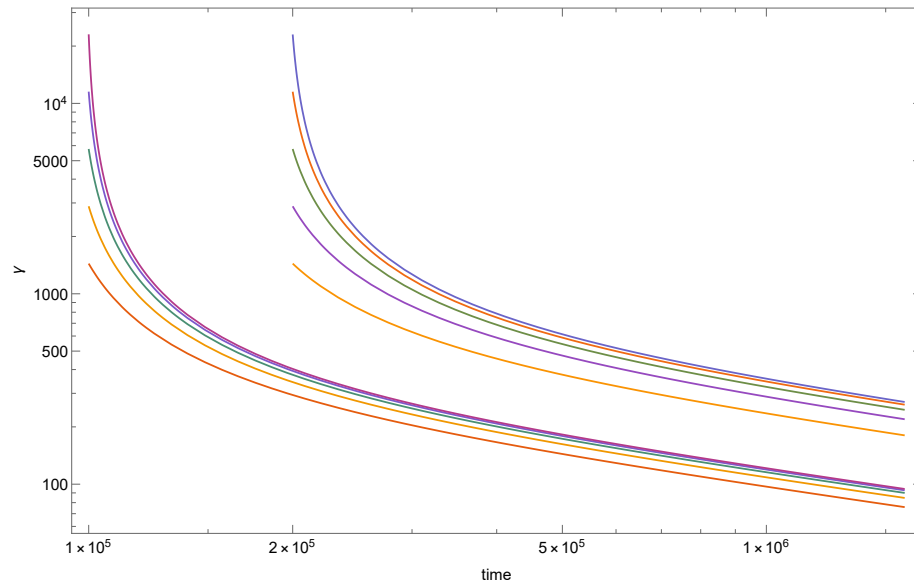


Figure 2.9. The evolution of the Lorentz factor for adiabatic and radiative losses. The initial Lorentz factor are $1.44 \times 10^3 s$, $2.88 \times 10^3 s$, $5.76 \times 10^3 s$, $1.15 \times 10^4 s$, $2.30 \times 10^4 s$ from orange to blue for above curves with the initial time is $2 \times 10^5 s$, and from red to purple for below curves with the initial time $1 \times 10^5 s$.

equation $\frac{2\tilde{C}_1 B_0'^2}{3t'} \left(\left(\frac{t'}{t'_i} \right)^{3/2} - 1 \right) + \frac{1}{\gamma'_{\min}} \sqrt{\frac{t'}{t'_i}} = \frac{1}{\gamma'}$, and t_l as the solution of the equation $\frac{1}{\gamma'} = \frac{2}{3t'} \left(\tilde{C}_1 B_0'^2 \left(\left(\frac{t'}{t'_i} \right)^{3/2} - 1 \right) \right)$.

Let's consider the case (i) firstly. In terms of the Lorentz factor of the injected electrons, We can divide the distribution function into four regions, which are $\gamma' < \gamma'_m$, $\gamma'_m < \gamma' < \gamma'_c$, $\gamma'_c < \gamma' < \gamma'_0$, and $\gamma'_0 < \gamma'$. Now we can calculate the contribution from each region by doing integration. The general idea is very similar as we discussed in radiative-only energy loss processes, so I will skip the discussion here, and only show the results of the integration.

For the case of $\gamma' < \gamma'_m$, no particles has been cooled enough to reach this region, so the Green's function is always 0. Thus the distribution function is

$$N_1(\gamma', t') = \int_{t'_0}^{t'} G(\gamma', t', t'_i) dt'_i = 0 \quad (2.37)$$

For the case of $\gamma'_m < \gamma' < \gamma'_c$, the Green's function is non-zero when $t'_0 < t'_i < t'_u$. So the distribution function is

$$N_2(\gamma', t') = \int_{t'_0}^{t'} G(\gamma', t', t'_i) dt'_i = \int_{t'_0}^{t'_u} G(\gamma', t', t'_i) dt'_i \quad (2.38)$$

For the case of $\gamma'_c < \gamma' < \gamma'_0$, the Green's function is non-zero when $t'_l < t'_i < t'_u$. So the distribution function is

$$N_3(\gamma', t') = \int_{t'_0}^{t'} G(\gamma', t', t'_i) dt'_i = \int_{t'_l}^{t'_u} G(\gamma', t', t'_i) dt'_i \quad (2.39)$$

For the case of $\gamma'_0 < \gamma'$, the Green's function is non-zero when $t'_l < t'_i$. So the distribution function is

$$N_4(\gamma', t') = \int_{t'_0}^{t'} G(\gamma', t', t'_i) dt'_i = \int_{t'_l}^{t'} G(\gamma', t', t'_i) dt'_i \quad (2.40)$$

Then Let's consider the case (ii). In terms of the Lorentz factor of the injected electrons, We can divide the distribution function into four regions, which are $\gamma' < \gamma'_m$, $\gamma'_m < \gamma' < \gamma'_0$, $\gamma'_0 < \gamma' < \gamma'_c$, and $\gamma'_c < \gamma'$. Now we can calculate the contribution from each region by doing integration. Again I will skip the discussion here, and only show the results of the integration.

For the case of $\gamma' < \gamma'_m$, no particles has been cooled enough to reach this region, so the Green's function is always 0. Thus the distribution function is

$$N_1(\gamma', t') = \int_{t'_0}^{t'} G(\gamma', t', t'_i) dt'_i = 0 \quad (2.41)$$

For the case of $\gamma'_m < \gamma' < \gamma'_0$, the Green's function is non-zero when $t'_0 < t'_i < t'_u$. So the distribution function is

$$N_2(\gamma', t') = \int_{t'_0}^{t'} G(\gamma', t', t'_i) dt'_i = \int_{t'_0}^{t'_u} G(\gamma', t', t'_i) dt'_i \quad (2.42)$$

For the case of $\gamma'_0 < \gamma' < \gamma'_c$, the Green's function is non-zero any time t'_i , which satisfies $t'_0 < t'_i$. So the distribution function is

$$N_3(\gamma', t') = \int_{t'_0}^{t'} G(\gamma', t', t'_i) dt'_i = \int_{t'_0}^{t'} G(\gamma', t', t'_i) dt'_i \quad (2.43)$$

For the case of $\gamma'_c < \gamma'$, the Green's function is non-zero when $t'_i < t'_i$. So the distribution function is

$$N_4(\gamma', t') = \int_{t'_0}^{t'} G(\gamma', t', t'_i) dt'_i = \int_{t'_i}^{t'} G(\gamma', t', t'_i) dt'_i \quad (2.44)$$

Finally, we add the contribution from these four regions $N = N_1 + N_2 + N_3 + N_4$ as our total distribution function. The evolution of the distribution function is showed as FIG.2.10.

Since we are considering an expansion process, we need to take account angle dependence, i.e., Doppler factor, which is defined as

$$\delta = \frac{1}{\Gamma (1 - \cos \theta \beta)} \quad (2.45)$$

where Γ is the Lorentz factor of the bulk motion, β is the velocity of the bulk motion, and θ is the angle respected to the line of sight.

Then we have the relation for the frequency as

$$\omega = \delta \omega' \quad (2.46)$$

and the relation for the luminosity as

$$L_\omega(\omega) = \delta^2 L'_{\omega'}(\omega') \quad (2.47)$$

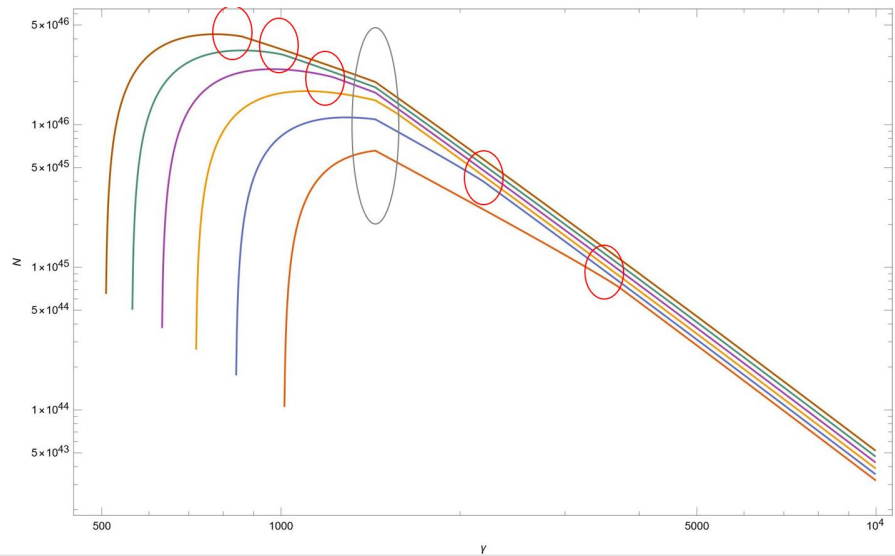


Figure 2.10. The evolution of the distribution function for adiabatic expansion without dynamic process. We use $\gamma'_{\min} = 1440$, $B' = 5.5\text{G}$, $t'_0 = 10^5\text{s}$. The time increase $7.18 \times 10^3\text{s}$, $1.25 \times 10^4\text{s}$, $1.82 \times 10^4\text{s}$, $2.41 \times 10^4\text{s}$, $3.03 \times 10^4\text{s}$, $3.68 \times 10^6\text{s}$ after t_0 from red to brown. The red circle are cooling break and the grey circle are injection break due to γ'_{\min} . We can see the transition when cooling break cross the injection break from yellow to red.

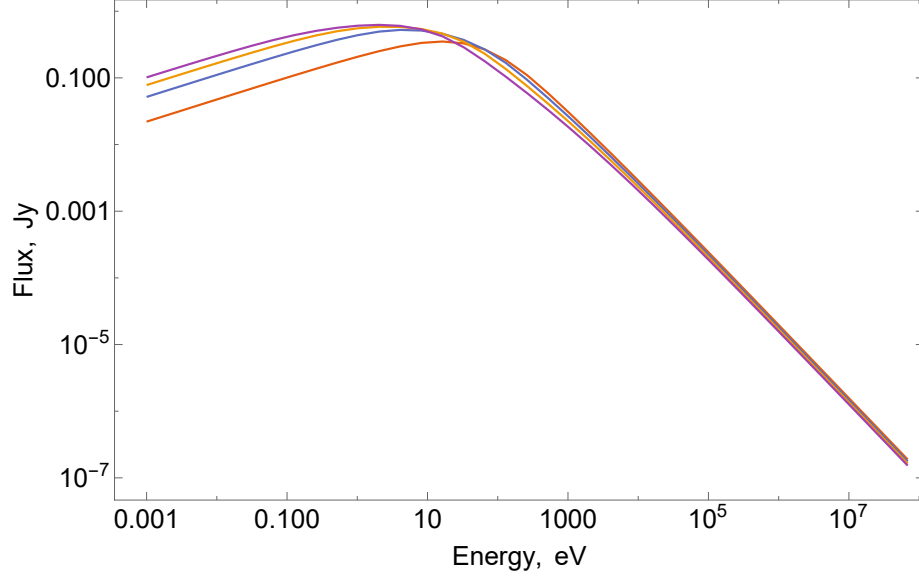


Figure 2.11. The evolution of the synchrotron spectrum in the case of the viewing angle is 0, and the Lorentz factor of RS is about 90, $\gamma_{\min}=5557$, initial magnetic field $B_0=2.14\text{G}$, power law index $p=2.2$, redshift $z=1$. The observe time is $t_{ob} = 1 \times 10^3\text{s}$, $2 \times 10^3\text{s}$, $4 \times 10^3\text{s}$, $8 \times 10^3\text{s}$ from red to purple.

Combine these two relation, the luminosity in the observer's frame is given by

$$L(\omega, \delta) = \delta^2 L' \left(\frac{\omega}{\delta} \right) \quad (2.48)$$

Consider the jet is toward us, or the viewing angle is 0, and the Lorentz factor of RS is about 90. We calculate the numerical result as FIG.2.11.

2.4 Synchrotron emission from relativistically expanding sources

Let us first consider the model with a general dynamic expansion with the power law decreasing Lorentz factor of CD, as

$$\Gamma_{RS} \propto \Gamma_{CD} \propto t^{-m} \propto t'^{-\frac{m}{1+m}} \quad (2.49)$$

and

$$r_s \propto t \propto t'^{\frac{1}{1+m}} \quad (2.50)$$

so

$$\gamma'_{\min} \propto \frac{\gamma_{wind}}{2\Gamma_{RS}} \propto t^m \propto t'^{\frac{m}{1+m}} \quad (2.51)$$

where prime is in fluid frame and un-primed is in coordinate frame.

And we also assume that the wind is magnetized with luminosity

$$L_w = 4\pi\gamma_w^2 \left(n_w m_e c^2 + \frac{b_w^2}{4\pi} \right) r^2 c \quad (2.52)$$

where n_w and b_w are density and magnetic field measured in the wind frame. So

$$b_w = \frac{\sqrt{L_w} \sqrt{\frac{\sigma_w}{\sigma_w+1}}}{\sqrt{cr}\gamma_w} \quad (2.53)$$

where σ_w is the wind magnetization parameter. In the post-RS region, the magnetic field is

$$B' = \frac{\gamma_w}{\Gamma_{CD}} b_w = \frac{\sqrt{L_w} \sqrt{\frac{\sigma_w}{\sigma_w+1}}}{\sqrt{cr}\Gamma_{CD}} \propto t^{m-1} \propto t'^{\frac{m-1}{m+1}} \quad (2.54)$$

Thus, the Green's function becomes the solution of the partial differential equation

$$\frac{\partial f(\gamma', t')}{\partial t} - \frac{\tilde{C}_2 B_0^2}{t'^{\frac{2-2m}{1+m}}} \frac{\partial (\gamma'^2 f(\gamma', t'))}{\partial \gamma'} - \frac{1-m}{2t'(1+m)} \frac{\partial (\gamma' f(\gamma', t'))}{\partial \gamma'} = f_{inj} \quad (2.55)$$

with the initial condition

$$f_{inj} = f_0 \gamma'^{-p} \Theta(\gamma' - \gamma'_{\min}) \quad (2.56)$$

where the Lorentz factor of the injected electron satisfies

$$\frac{d\gamma'}{dt'} = -\frac{\tilde{C}_2 B_0^2 \gamma'^2}{t'^{\frac{2-2m}{1+m}}} - \frac{(1-m)\gamma'}{2t'(1+m)} \quad (2.57)$$

and

$$\tilde{C}_2 = \frac{\sigma_T t_0^{\frac{2-2m}{1+m}}}{6\pi mc} \quad (2.58)$$

is a constant.

In the previous two sections, we have the injection function $f_{\text{inj}} = f_0 \gamma'^{-p} \Theta(\gamma' - \gamma'_{\text{min}})$. In this section, Γ decrease with time, and $\gamma'_{\text{min}} \propto \frac{\gamma_{\text{wind}}}{\Gamma}$ increase with time. Thus, the injection function $f_{\text{inj}} = f_0 \gamma'^{-p} \Theta(\gamma' - \gamma'_{\text{min}})$ is not a constant anymore.

In the case of that the energy rate injected is still a constant, we need to derive a new normalization parameter, which is expected to be the function of time. Consider that the power deposited by the wind in the shocked medium scale as

$$\frac{L_w}{\Gamma_{CD}^2} \propto \left(\frac{t}{t_0}\right)^{2m} \propto \left(\frac{t'}{t'_0}\right)^{\frac{2m}{1+m}} \quad (2.59)$$

and assume the injection function satisfies

$$f_{\text{inj}}(\gamma', t'_i) = K f_0 \gamma'^{-p} \Theta(\gamma' - \gamma'_{\text{min}}(t'_i)) \quad (2.60)$$

where K is the normalization parameter we are looking for. The injection at time t'_0 and t'_i have relation

$$\left(\frac{t'_i}{t'_0}\right)^{\frac{2m}{1+m}} \int_{\gamma'_{\text{min}}(0)}^{\infty} f_0 \gamma'^{1-p} d\gamma' = K f_0 \int_{\gamma'_{\text{min}}(t'_i)}^{\infty} \gamma'^{1-p} d\gamma' \quad (2.61)$$

and the definite integral gives

$$\left(\frac{t'_i}{t'_0}\right)^{\frac{2m}{1+m}} \gamma'_{\text{min}}(0)^{2-p} = K \gamma'_{\text{min}}(t')^{2-p} = K \gamma'_{\text{min}}(0)^{2-p} \left(\frac{t'_i}{t'_0}\right)^{\frac{(2-p)m}{1+m}} \quad (2.62)$$

Then we can calculate the normalization parameter

$$K = \left(\frac{t'_i}{t'_0}\right)^{\frac{mp}{1+m}} \quad (2.63)$$

and the injection function

$$f_{\text{inj}}(\gamma', t_i) = f_0 \left(\frac{t'_i}{t'_0}\right)^{\frac{mp}{1+m}} \gamma'^{-p} \Theta(\gamma' - \gamma'_{\text{min}}(t'_i)) \quad (2.64)$$

Substitute the injection function into equation (2.55) and (2.57), the Green's function can be solved, and the result is

$$G = \begin{cases} f_0 \left(\frac{t'_i}{t'_0}\right)^{\frac{mp}{1+m}} \gamma'^{-p} \left(\frac{t'_i}{t'}\right)^{\frac{(p-1)(1-m)}{2+2m}} \left(1 - \frac{2+2m}{7m-3} \tilde{C}_2 B_0^2 \gamma' t'^{\frac{1-m}{2+2m}} \left(t'^{\frac{7m-3}{2+2m}} - t_i^{\frac{7m-3}{2+2m}}\right)\right)^{p-2}, & \gamma'_{\text{low}} < \gamma' < \gamma'_{\text{up}} \\ 0, & \text{else} \end{cases} \quad (2.65)$$

and the Lorentz factor evolves with time as

$$\frac{1}{\gamma'} = t'^{\frac{1-m}{2+2m}} \left(\frac{2+2m}{7m-3} \tilde{C}_2 B_0^2 \left(t'^{\frac{7m-3}{2+2m}} - t_i'^{\frac{7m-3}{2+2m}} \right) + \frac{1}{\gamma'_i t_i'^{\frac{1-m}{2+2m}}} \right) \quad (2.66)$$

where γ'_{low} is the lower bound of the Lorentz factor due to the minimum Lorentz factor of the injection and satisfies

$$\frac{1}{\gamma'_{\text{low}}} = t'^{\frac{1-m}{2+2m}} \left(\frac{2+2m}{7m-3} \tilde{C}_2 B_0^2 \left(t'^{\frac{7m-3}{2+2m}} - t_i'^{\frac{7m-3}{2+2m}} \right) + \frac{1}{\gamma'_{\text{min}} t_i'^{\frac{1-m}{2+2m}}} \right) \quad (2.67)$$

and γ'_{up} is the upper bound of the Lorentz factor due to the cooling break and satisfies

$$\frac{1}{\gamma'_{\text{up}}} = t'^{\frac{1-m}{2+2m}} \left(\frac{2+2m}{7m-3} \tilde{C}_2 B_0^2 \left(t'^{\frac{7m-3}{2+2m}} - t_i'^{\frac{7m-3}{2+2m}} \right) \right) \quad (2.68)$$

We then adopt the value of $m = \frac{39}{58}$ from [113], where $\Gamma_{CD} \propto t'^{-\frac{38}{58}}$ by assuming the motion of the CD is expected to be self-similar before it catches up with the primary FS. Then we plot the evolution of the typical Green's function for instantaneous injection at time t'_0 as FIG.2.12

Again, we can use the same analysis before to divide the contribution into four regions with three break points: γ'_m , γ'_c , and γ'_0 . There are will be two cases, which are case (i) fast cooling: $\gamma'_m < \gamma'_c < \gamma'_0$, and case (ii) slow cooling: $\gamma'_m < \gamma'_0 < \gamma'_c$. We denote t'_u as the solution of the equation

$$t'^{\frac{1-m}{2+2m}} \left(\frac{2+2m}{7m-3} \tilde{C}_2 B_0^2 \left(t'^{\frac{7m-3}{2+2m}} - t_i'^{\frac{7m-3}{2+2m}} \right) + \frac{1}{\gamma'_{\text{min}} t_i'^{\frac{1-m}{2+2m}}} \right) = \frac{1}{\gamma'} \quad (2.69)$$

and we denote t'_l as the solution of the equation

$$t'^{\frac{1-m}{2+2m}} \left(\frac{2+2m}{7m-3} \tilde{C}_2 B_0^2 \left(t'^{\frac{7m-3}{2+2m}} - t_i'^{\frac{7m-3}{2+2m}} \right) \right) = \frac{1}{\gamma'} \quad (2.70)$$

Let us consider case (i) firstly. The four regions are: $\gamma' < \gamma'_m$, $\gamma'_m < \gamma' < \gamma'_c$, $\gamma'_c < \gamma' < \gamma'_0$ and $\gamma'_0 < \gamma'$. Now we can calculate the contribution from each region by doing integration. The general idea is very similar as we discussed in the radiative-only energy loss processes, so I will skip the discussion here, and only show the results of the integration

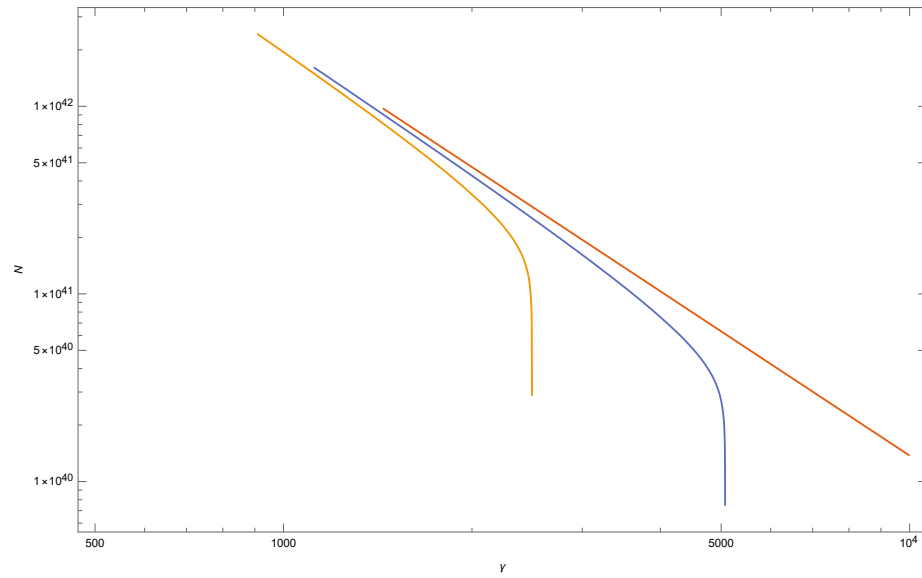


Figure 2.12. The evolution of the typical Green's function for a self-similar dynamic expansion. Consider the instantaneous injection at time $t'_0 = 10^5$ s. $\gamma'_{\min} = 1440$, $B'_0 = 5.5$ G, $p = 2.2$. The time in fluid frame are t'_0 , $1.05t'_0$, $1.05^2t'_0$ from red to orange.

For the case of $\gamma' < \gamma'_m$, no particles has been cooled enough to reach this region, so the Green's function is always 0. Thus the distribution function is

$$N_1(\gamma', t') = \int_{t'_0}^{t'} G(\gamma', t', t'_i) dt'_i = 0 \quad (2.71)$$

For the case of $\gamma'_m < \gamma' < \gamma'_c$, the Green's function is non-zero when $t'_0 < t'_i < t'_u$. So the distribution function is

$$N_2(\gamma', t') = \int_{t'_0}^{t'} G(\gamma', t', t'_i) dt'_i = \int_{t'_0}^{t'_u} G(\gamma', t', t'_i) dt'_i \quad (2.72)$$

For the case of $\gamma'_c < \gamma' < \gamma'_0$, the Green's function is non-zero when $t'_l < t'_i < t'_u$. So the distribution function is

$$N_3(\gamma', t') = \int_{t'_0}^{t'} G(\gamma', t', t'_i) dt'_i = \int_{t'_l}^{t'_u} G(\gamma', t', t'_i) dt'_i \quad (2.73)$$

For the case of $\gamma'_0 < \gamma'$, the Green function is non-zero when $t'_l < t'_i$. So the distribution function is

$$N_4(\gamma', t') = \int_{t'_0}^{t'} G(\gamma', t', t'_i) dt'_i = \int_{t'_l}^{t'} G(\gamma', t', t'_i) dt'_i \quad (2.74)$$

Then Let's consider the case (ii). In terms of the Lorentz factor of the injected electrons, We can divide the distribution function into four regions, which are $\gamma' < \gamma'_m$, $\gamma'_m < \gamma' < \gamma'_0$, $\gamma'_0 < \gamma' < \gamma'_c$, and $\gamma'_c < \gamma'$. Now we can calculate the contribution from each region by doing integration. Again I will skip the discussion here, and only show the results of the integration.

For the case of $\gamma' < \gamma'_m$, no particles has been cooled enough to reach this region, so the Green's function is always 0. Thus the distribution function is

$$N_1(\gamma', t') = \int_{t'_0}^{t'} G(\gamma', t', t'_i) dt'_i = 0 \quad (2.75)$$

For the case of $\gamma'_m < \gamma' < \gamma'_0$, the Green's function is non-zero when $t'_0 < t'_i < t'_u$. So the distribution function is

$$N_2(\gamma', t') = \int_{t'_0}^{t'} G(\gamma', t', t'_i) dt'_i = \int_{t'_0}^{t'_u} G(\gamma', t', t'_i) dt'_i \quad (2.76)$$

For the case of $\gamma'_0 < \gamma' < \gamma'_c$, the Green's function is non-zero for any t_i , which satisfies $t_i > t_0$. So the distribution function is

$$N_3(\gamma', t') = \int_{t'_0}^{t'} G(\gamma', t', t'_i) dt'_i = \int_{t'_0}^{t'} G(\gamma', t', t'_i) dt'_i \quad (2.77)$$

For the case of $\gamma'_c < \gamma'$, the Green's function is non-zero when $t'_i < t'$. So the distribution function is

$$N_4(\gamma', t') = \int_{t'_0}^{t'} G(\gamma', t', t'_i) dt'_i = \int_{t'_i}^{t'} G(\gamma', t', t'_i) dt'_i \quad (2.78)$$

Finally, we add the contribution from these four regions $N = N_1 + N_2 + N_3 + N_4$ as our total distribution function. The evolution of the distribution function is shown as FIG. 2.13. Furthermore, we calculate the luminosity by using Eqn. 2.19. See FIG. 2.14.

For dynamic process, the relation between the time in fluid frame and observe time is slightly different as below

$$t_{ob} = \frac{t' (1 + m)}{2 (1 + 2m) \Gamma_{CD}} \quad (2.79)$$

We also plot the light curve at 1 eV as FIG.2.15 and 100 KeV as FIG.2.16. We can also prove that the light curve simply satisfies the approximate relation

$$F \propto t_{ob}^{\frac{mp - \frac{p}{2} - 3m + 1}{1 + 2m}} \quad (2.80)$$

at high energy region (please see Appendix for more detail of proof). For our case at 100 KeV with parameters $m = \frac{39}{58}$, $p = 2.2$, the numerical result gives $F \propto t_{ob}^{-0.2718}$ and the approximate relation gives $F \propto t_{ob}^{-0.2721}$, which are consistent with each other.

2.5 Conclusions

In this section, we calculated synchrotron emission from a relativistically expanding magnetized wind. In the next three chapters, I will apply this calculation tool to the relevant works, such as (1) turbulent model of Crab nebula radiation, (2) Pulsar winds in GRBs afterglows: flares, plateaus, and steep decays, and (3) Prediction of the second peak in the afterglow of GW170817.

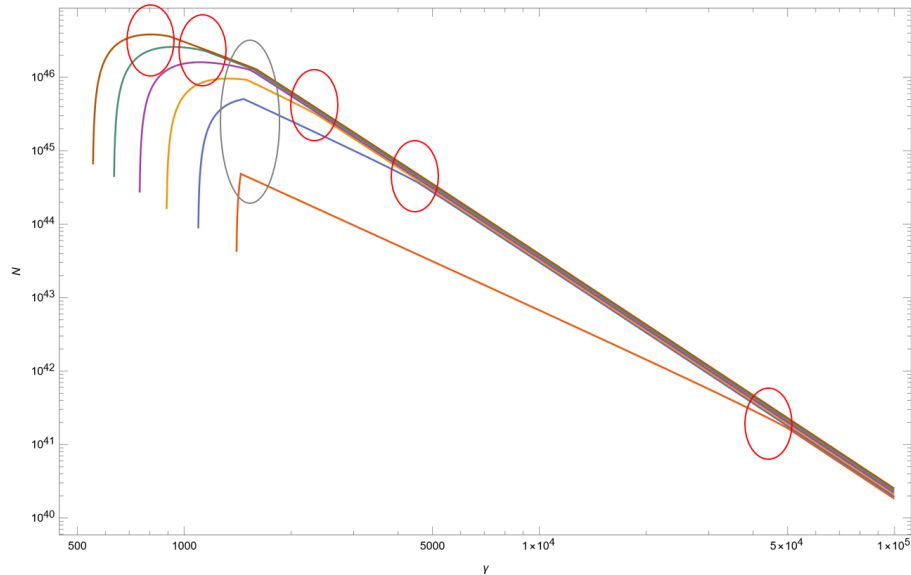


Figure 2.13. The evolution of the distribution function for the adiabatic expansion with dynamic process. In our model, the luminosity of wind is 10^{48} erg/s . $\gamma'_{\min}=1440$, $B'_0=5.5 \text{ G}$, $p=2.2$, $t'_0 = 10^5 \text{ s}$. The time in fluid frame increase 500s, $5.52 \times 10^3 \text{ s}$, $1.08 \times 10^4 \text{ s}$, $1.63 \times 10^4 \text{ s}$, $2.27 \times 10^4 \text{ s}$, $2.88 \times 10^4 \text{ s}$ after initial time t'_0 from red to brown. The red circle are cooling break and the grey circle are injection break due to γ'_{\min} . We can see the transition when cooling break cross injection break from yellow curve to green curve.

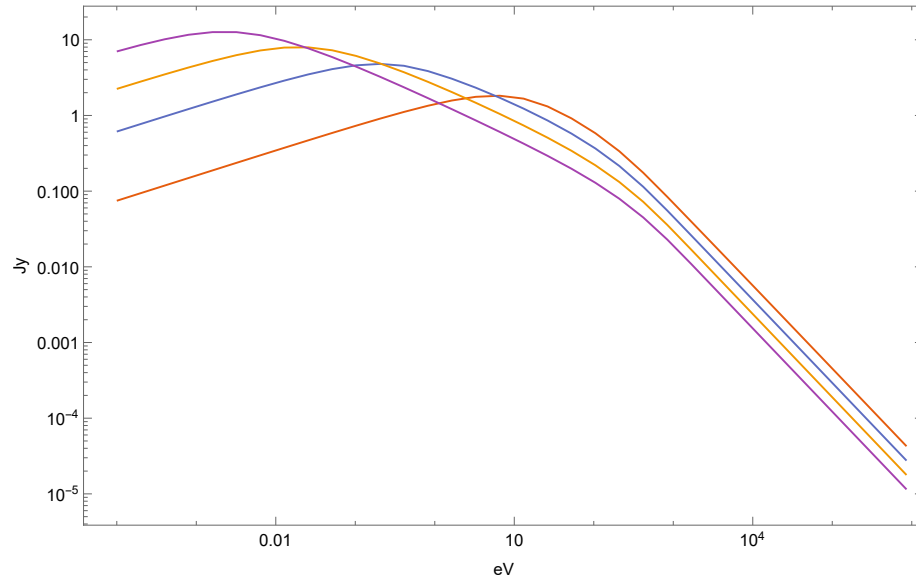


Figure 2.14. The evolution of the synchrotron spectrum in a self-similar dynamic expansion. Consider the viewing angle is 0, and the luminosity of wind is 10^{48} erg/s . $\gamma'_{\min}=1440$, $B'_0=5.5 \text{ G}$, $p=2.2$, $z=1$. The observe time is $t_{ob} = 200s, 1000s, 5000s, 25000s$ from red to purple.

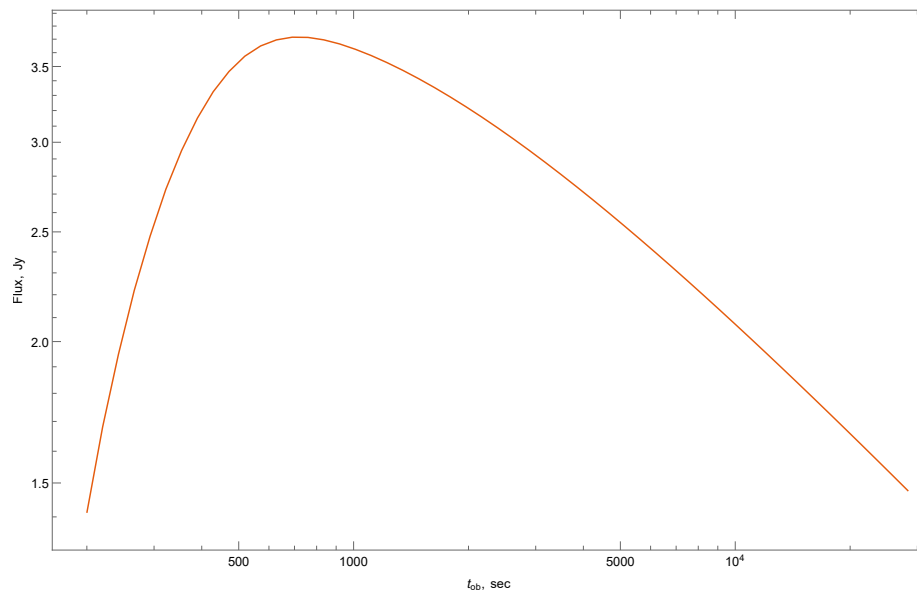


Figure 2.15. The light curve of synchrotron emission in a self-similar expansion $m = \frac{39}{58}$ at 1 eV. Consider the viewing angle is 0, and the luminosity of wind is 10^{48} erg/s . $\gamma'_{\min}=1440$, $B'_0=5.5 \text{ G}$, $p=2.2$, $z=1$.

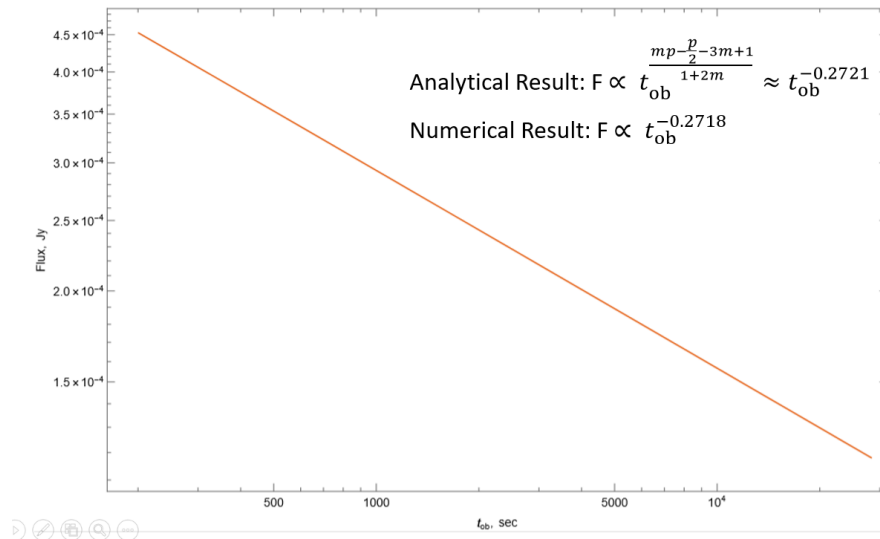


Figure 2.16. The light curve of synchrotron emission in a self-similar expansion $m = \frac{39}{58}$ at 100 keV. Consider the viewing angle is 0, and the luminosity of wind is 10^{48} erg/s . $\gamma'_{\text{min}} = 1440$, $B'_0 = 5.5 \text{ G}$, $p = 2.2$, $z = 1$. The light curve is power-law and scale as $\propto t_{\text{ob}}^{\frac{mp - \frac{p}{2} - 3m + 1}{1 + 2m}}$

3. TURBULENT MODEL OF CRAB NEBULA RADIATION

3.1 Introduction

The Crab Nebula is the paragon of high energy astrophysical sources - understanding particle acceleration in the Crab Nebula has implications for other sources, like active galactic nuclei and gamma-ray bursts. Conventionally, particles in the pulsar wind nebulae (PWNe) are assumed to be accelerated at the pulsar wind termination shock [24]; [25]; [26]; [114]. The inferred particle spectral index $p = 2.2$, derived from the non-thermal X-ray synchrotron spectrum, matches the expectations for the Fermi-I mechanism, *e.g.* [115]. In addition, numerical Magnetohydrodynamics (MHD) simulations [116]; [117]; [118]; [119], with the assumed particle acceleration at the termination shock, reproduce well the overall X-ray morphology of the PWNe.

However, there are clear drawbacks of the Kennel & Coroniti model [25]; [26]. The origin of the radio emitting particles is not addressed. The radio spectrum of Crab PWN has a spectral index $\alpha = 0.3$ [120]; [121], which implies a particle spectral index of $p = 1.6$ for an isotropic distribution of non-thermal electrons. Such hard radio emission is not consistent with the Fermi-I acceleration mechanism (assumed to be operational at the terminate shock), which typically gives $p > 2$, *e.g.* [115]. In addition, the lowest observed radio emission from the Crab Nebula, down to 100 MHz, requires Lorentz factors of only 10^2 , well below the typically expected wind Lorentz factor of $\gamma_w \sim 10^4 - 10^6$, *e.g.* [122]; [123].

The second major problem in modeling the Crab Nebula's emission, identified by [24]; [25], is the so-called sigma-problem: models of pulsar magnetospheres [124]; [125]; [126] predict $\sigma \gg 1$, where sigma is the conventional magnetization parameter, [25]. Supersonic flows with $\sigma \gg 1$ (carrying *large-scale* magnetic field) cannot be

accommodated with the non-relativistically expanding nebula. The resolution to the sigma-problem is the destruction of the large-scale magnetic flux, either in the wind [127] (but see [128]), or in the turbulent post-shock flow [129]; [130]; [131]; [132]; [133]. We accept the latter interpretation, see Section 3.2.

The third problem of the Kennel & Coroniti model [25] is related to Crab Nebula's gamma-ray flares [134]; [135]; [136]. As discussed by [137] (before the discovery of the flares) and [138] (see also [139]), the peak energy of flares - as high as 400 MeV- violates the synchrotron limit, and is inconsistent with the slow Fermi-I-type acceleration at the shock front. Reconnection in magnetically dominated plasma may accelerate particles at a much faster rate, resolving the problem of the high-peak energy of flares [140]; [141]; [142]; [137]; [138]; [143]; [144]; [145]; [146]; [147]; [148]; [149].

The fourth problem of the Kennel-Coroniti model is that it is in significant conflict with the observed radial-spectral dependence of the PWNe [150]; [121]. Models predict a drop in size of the PWN by at least a factor two between radio and X-ray wavelengths, but observed PWNe do not show this behavior.

We suggest a common resolution to all the problems mentioned above (the spectrum of radio electrons, the sigma problem, the high peak energy of gamma-ray flares, and the resolved spectral evolution). We foresee that there are two non-thermally-emitting components in the Nebula: one (Component-I) is accelerated at the termination shock, and another (Component-II) is accelerated in relativistic reconnection events in the bulk of the Nebula, as argued by [151], see also [152]. Component-I abides by the rules of the Kennel & Coroniti model [25]; [26], with low magnetization in the equatorial part of the wind. Component-II results from the highly magnetized plasma turbulence, which increase the rate of reconnection [153], in the bulk of the nebula and destroys the magnetic flux in reconnection events. The largest reconnection events result in gamma-ray flares [138].

In §3.2, we discuss the sigma-problem from the point of view of the conservation of large-scale magnetic flux. In §3.3, we construct a turbulent model of PWNe. In §3.4, we consider the evolution of particles in a changing magnetic field of the Nebula.

In §3.5, we discuss the particle acceleration mechanisms in magnetically-dominated reconnecting turbulence. In §3.6, we construct the turbulent model of the Crab Nebula radiation. In §3.7, we construct the corresponding spectral maps in the IR and optical and compare them with observational data.

3.2 The sigma-problem - the problem of the magnetic flux

To clarify the sigma-problem, and to highlight its resolution [129]; [130], let us consider a central source (a neutron star) that injects into the Crab Nebula a highly magnetized, $\sigma \sim 1$, relativistic (supersonic - hence causally disconnected from the source) flow that carries *a large-scale toroidal magnetic field*. If at the injection radius r_{in} (\sim light cylinder), the magnetic field is B_{in} , then the magnetic energy is injected with the rate

$$\frac{dE_B}{dt} \sim B_{in}^2 r_{in}^2 c \quad (3.1)$$

(for $\sigma \sim 1$, dE/dt is of the order of the spin-down luminosity). The total injected energy is then

$$E_B = B_{in}^2 r_{in}^2 ct \quad (3.2)$$

At the same time, the central source injects magnetic flux, integrated over half cross-section of the Nebula, at a rate

$$\frac{d\Phi}{dt} \sim B_{in} r_{in} c \quad (3.3)$$

(the total injected flux, integrated over the whole cross-section of the Nebula, is zero, with two opposite contributions of the value (3.4) through two east-west cross-sections.). The total flux, integrated over half cross-section, stored in the nebula is

$$\Phi_{tot} \sim B_{in} r_{in} ct \quad (3.4)$$

If the cavity expands with velocity V_{PWN} , the magnetic field and the energy in the bulk are

$$B \sim \frac{\Phi_{tot}}{(V_{PWN}t)^2} = \frac{cB_{in}r_{in}}{tV_{PWN}^2}$$

$$E_{stored} \sim B^2(V_{PWN}t)^3 = \frac{B_{in}^2 r_{in}^2 c^2 t}{V_{PWN}} \quad (3.5)$$

Comparing (3.2) and (3.5), the injected and the stored energy, it is then required that $V_{PWN} \sim c$ - only relativistically expanding nebula can accommodate the injected flux. Since PWNe expand non-relativistically, our assumption that a central source injects a highly magnetized relativistic flow leads to an inconsistency - this is the sigma paradox. Only weakly magnetized flows, with magnetic energy flux much smaller than the total wind luminosity by $\sigma \sim V_{PWN}/c$, can be matched to the non-relativistically expanding boundary [25].

This exercise also suggest a resolution of the sigma paradox: what is needed is the destruction of the large scale magnetic flux (but not necessarily of the magnetic field!). Consider a large scale magnetic loop, which has zero total toroidal flux composed of two opposite contributions in the two east-west cross-sections. If the loop is broken into small loops, the total flux remains zero, but also now the flux is zero through any east-west cross-sections. Relation (3.3) is then not valid any longer - there is then no sigma paradox.

Thus, if the magnetic field is converted into small scale structures, it would behave as a fluid with some specific equation of state. For example, if a “fluid” is composed of magnetic bubbles, then the conservation of flux within a bubble would produce magnetic pressure

$$B^2 \propto V_b^{-4/3} \quad (3.6)$$

where V_b is the volume of a bubble. This scaling is reminiscent of the relativistic fluid with adiabatic index of 4/3. [131] indeed demonstrated numerically that development of current-driven instabilities in the post-termination shock region leads to the resolution of the sigma problem.

Given the above arguments, we conclude that instead of smooth flow imagined by [25], the PWNe *must* be highly turbulent. Below we develop a magnetohydrodynamic and radiation model of a PWN, *assuming* it is dominated by turbulence. Previously, a number of models took into account turbulence and ensuing diffusion on top of the Kennel-Coroniti flow *e.g.* [154]; [155]; [156] [157]. Here we take an extreme position that magnetohydrodynamic turbulence dominates the flow. This is surely an extreme assumption: in reality the flow is partially magnetic flux conserving (as demonstrated by large-scale polarization structures that imply toroidal magnetic field [158]) and partially turbulent. Yet, as we argue, this extreme 1D model does reproduce various observational phenomena and resolve the problems of the Kennel-Coroniti model.

3.3 Confinement of the turbulent Crab Nebula PWN by its supernova remnant

As we argued above, destruction of the magnetic flux is needed to resolve the sigma-problem. This is achieved via reconnecting turbulence in the post-shock flow. In this section, we construct a turbulent model of PWNe, whereby the post-shock flow quickly becomes highly turbulent, thus losing the extra requirement of magnetic flux conservation. We consider an extreme case of complete destruction of the magnetic flux. Naturally, this is an approximation - the real PWN does keep some toroidal magnetic flux, as illustrated by polarized emission from high energy [158]; [159]; [160]; [161] to microwaves [162]; [163], to the radio [164].

3.3.1 Overall expansion

Consider a central source producing a relativistic supersonic wind with luminosity L_w , confined within a homologously expanding stellar envelope. Let us first estimate the overall dynamics of the bubble in the early stages of expansion, when the reverse shock in the ejecta has not yet reached the expanding PWN.

The stellar envelope ejected during the supernova explosion expands homologically, so that its density evolves according to

$$\begin{aligned}\rho &= \frac{3}{4\pi} \frac{M_{ej}}{(V_{ej}t)^3} \\ E_{ej} &= \frac{3}{10} M_{ej} V_{ej}^2, \\ v_r &= \frac{r}{t}, \quad r \leq V_{ej}t\end{aligned}\tag{3.7}$$

where M_{ej} is ejecta mass and V_{ej} is the maximal velocity; a more general scaling of ρ can also be used, $\rho \propto t^{-3} f(r/t)$, $v_r \propto (r/t) f(r/t)$.

Conventionally (*e.g.* [165]) the dynamics of the PWN is treated in what could be called a Sedov approximation, whereby the internal pressure of the nebular drives supersonic expansion into the supernova ejecta. (Roughly speaking, Sedov approximation is applicable if the size of the termination shock in the pulsar wind is much smaller than the size of for the PWN.) In this case the mass, momentum and energy conservation equations are

$$\begin{aligned}\partial_t M &= 4\pi R^2 \rho \left(V - \frac{R}{t} \right) \\ M \partial_t V &= 4\pi R^2 \left(p - \rho \left(V - \frac{R}{t} \right)^2 \right) \\ \partial_t (4\pi p R^3) &= L_w - 4\pi R^2 V p \\ V &= \partial_t R\end{aligned}\tag{3.8}$$

(p and ρ are pressure and density internal to the expanding PWN, L_w is wind luminosity, V is overall velocity of expansion.).

The wind luminosity is given by the pulsar spin-down power:

$$\begin{aligned}
L_w &= \frac{I_{NS}\tau\Omega_0^4}{2(1+t\tau\Omega_0^2)^2} \\
\tau &= 2\frac{B_{NS}^2R_{NS}^6}{I_{NS}c^3} \\
\Omega &= \frac{\Omega_0}{\sqrt{1+t\tau\Omega_0^2}} = \frac{\Omega_0}{\sqrt{1+t/t_0}} \\
t_0 &= \frac{c^3I_{NS}}{2B_{NS}^2R_{NS}^6\Omega_0^2}
\end{aligned} \tag{3.9}$$

where I_{NS} is the moment of inertia of the neutron star, Ω_0 is the initial spin, Ω is the current spin, $B_{NS} = 4 \times 10^{12}$ G is surface magnetic field and $R_{NS} = 10^6$ cm is radius of the neutron star.

When can we neglect Ω_0 in the evolution of Ω ? Estimating when $t_0 = t_{age}$, the current age, neglect of Ω_0 requires

$$\Omega_0 \gg \frac{c^{3/2}\sqrt{I_{NS}}}{\sqrt{2}B_{NS}R_{NS}^3\sqrt{t_{age}}} = 130\text{rads}^{-1}. \tag{3.10}$$

which corresponds to the initial period $P_0 < 46$ msec. This is just somewhat longer than the present spin period of the Crab pulsar, 34 msec. Thus, for Crab, as a first approximation we can neglect the evolution of the wind luminosity, assuming $L_w \sim$ constant.

Assuming constant wind power the corresponding scaling are

$$\begin{aligned}
R_{PWN} &= 0.38 \left(\frac{L_w V_0^5}{E_{ej}} \right)^{1/5} t^{6/5} = R_{PWN,now} \left(\frac{t}{t_{now}} \right)^{6/5} \\
M &= 22.4 \left(\frac{E_{ej}^2 L_w^3}{V_0^{10}} \right)^{1/5} t^{3/5} \\
p &= 0.064 \left(\frac{E_{ej}^3 L_w^2}{V_0^3} \right)^{1/5} t^{-13/5}
\end{aligned} \tag{3.11}$$

where R_{PWN} is the radius of the PWN, M is the swept-up mass and p is the pressure.

3.3.2 Internal velocity structure of turbulent PWN flow

Let us adopt a limiting case, where instead of smooth flow envisioned by [25] the requirement of magnetic flux destruction leads to a completely turbulent flow in the nebula. The turbulent magnetic field behaves as a fluid, with some specific equation of state, Eq.(3.6). The post-shock plasma is relativistically hot, with the sound speed $c_s \sim c/\sqrt{3}$. The post-shock evolution of the fluid (mixture of relativistic plasmas and turbulent magnetic field) will then quickly reach sub-relativistic velocities and, hence, an incompressible limit.

Consider incompressible flow within a sphere expanding according to (3.11). Looking for the flow velocity of the incompressible fluid in the form $v(r, t) = V_{ej}(t)f(x)$ with $x = r/R_{PWN}(t)$, we find

$$v = \frac{6}{5} \frac{R_{PWN,now}^3 t^{13/5}}{r^2 t_{now}^{18/5}} \quad (3.12)$$

(this satisfies the condition $\text{div } \mathbf{v} = 0$ and matches to the boundary expansion). Eq. (3.12) gives the velocity of fluid element located at time t at a distance r ; it is parameterized to the size $R_{PWN,now}$ and age t_{now} of the Crab Nebula now.

The flow should also match the post-termination-shock conditions (*e.g.*, $v_{term.shock} = c/3$ in the purely fluid regime). Clearly this cannot be done in a mathematically meaningful sense - the system becomes over-determined. Still, the estimate of the location of the termination-shock,

$$\frac{r_{term.shock}}{R_{PWN,now}} \approx \sqrt{\frac{R_{PWN,now}}{ct_{now}}} \approx 0.1 \quad (3.13)$$

is a reasonable estimate of the relative size of the termination shock with respect to the overall Nebula. Recall, that one of the effects of the sigma-problem within the model of [25] was that the size of the termination shock becomes too small for $\sigma \rightarrow 1$. The turbulent model avoids that problem. We consider this as a major advantage of the model.

Consider next a shell ejected at time t_{ej} from the termination shock of radius R_{ej} . Integrating equation of motion (3.12) with $v = dr/dt$, the location of the shell at time t is

$$\frac{r_{shell}}{R_{PWN,now}} = \left(\left(\frac{R_{ej}}{R_{PWN,now}} \right)^3 + \left(\frac{t}{t_{now}} \right)^{18/5} - \left(\frac{t_{ej}}{t_{now}} \right)^{18/5} \right)^{1/3} \rightarrow$$

$$\left(\left(\frac{R_{ej}}{R_{PWN,now}} \right)^3 + 1 - \left(\frac{t_{ej}}{t_{now}} \right)^{18/5} \right)^{1/3} \quad (3.14)$$

(As a check, for $t_{ej} = 0$ and $R_{ej} = 0$ Eq. (3.14) reproduces (3.11)). The last equality in (3.14) refers to the present time, $t = t_{now}$.)

A shell located at $r_{shell,now}$ at present time has been ejected at time

$$\frac{t_{ej}}{t_{now}} = \left(1 + \left(\frac{R_{ej}}{R_{PWN,now}} \right)^3 - \left(\frac{r_{shell,now}}{R_{PWN,now}} \right)^3 \right)^{5/18} \quad (3.15)$$

3.3.3 Magnetic field within the shell

At each moment the amount of the energy injected by the pulsar should balance nebula pressure, given by the sum of magnetic and kinetic pressures p_k . (Plasma within the Nebula is relativistically hot, hence we can neglect the energy of the bulk motion which is smaller by a factor $(v/c)^2$ than the combined enthalpy.)

Using (3.11) with total pressure given by the sum of kinetic and magnetic pressure,

$$p_{tot} = \frac{B^2}{8\pi} + p_k = \frac{B^2}{8\pi}(1 + \beta) \quad (3.16)$$

where β is the plasma beta parameter, the magnetic field within a nebula at time t is then

$$B(t) = B_{now} \left(\frac{t}{t_{now}} \right)^{-13/10}$$

$$B_{now} = 16.4 \frac{E_{ej}^{3/10} L_w^{1/5}}{V_0^{3/2} \sqrt{1 + \beta}} t_{now}^{-13/10} = \frac{\sqrt{6} L_w t_{now}}{R_{PWN,now}^{3/2}} \approx 6 \times 10^{-4} \text{ G} \quad (3.17)$$

where the last estimate assumes ejecta energy $E_{ej} = 10^{51}$ ergs, maximum velocity $V_0 = 7500 \text{ km s}^{-1}$ and $\beta = 10^2$.

Given the nature of the order-of-magnitude estimates, the above values is very close to the estimates of the magnetic field in the Nebula (*e.g.* [121]). We consider this as another major advantage of the model.

3.4 Particle distribution within the nebula

Above, we constructed a fluid-like turbulent model of PWN, composed of shells of material injected at different times. Magnetic field in each shells evolves with time according to (3.17). In this Section we calculate the radiation signatures of such turbulent PWN. In §3.4.1 we consider the evolution of the particle distribution within each injected shell, taking into account radiative losses (there are no adiabatic losses in the incompressible approximation).

In subsection 3.4.1, we find the Green's function for particles injected at some moment and an experiencing radiative decay in an evolving magnetic field. The Green's function, multiplied by the injection rate, gives the particle distribution function within each shell. Next, in subsection 3.4.2, we integrate the Green's function over the injection time to find the total particle distribution within the Nebula.

Qualitatively, the evolution of the energy of a given particle in decreasing magnetic field proceeds as follows. At high injected energies, and early times, a given particle loses most energy to synchrotron radiation. With time, efficiency of synchrotron losses decreases both due to the decrease of particles' energy and due to the decrease in the overall magnetic field.

3.4.1 Evolution of the particle distribution in a changing magnetic field

We assume that particles are injected into the inner regions of the PWN with some given distribution and seek to find the particle distribution within each injected shell,

taking into account radiative losses and a changing magnetic field within each shell. We need to solve the Boltzmann's (Liouville's) equation for the Green's function G

$$\frac{\partial G}{\partial t} = \frac{\partial(\dot{\gamma}G)}{\partial \gamma} + f_{inj}\delta(t - t_{inj}) \quad (3.18)$$

for an injected spectrum with a power-law particle distribution

$$f_{inj} \propto \gamma_{inj}^{-p}, \quad \gamma > \gamma_{inj,min}, \quad (3.19)$$

where t_{inj} is the moment of injection and $\gamma_{inj,min}$ is a minimum injection Lorentz factor.

Consider first the evolution of the Lorentz factor of the particles experiencing radiative losses in an evolving magnetic field,

$$\begin{aligned} \dot{\gamma} &= -\frac{4}{9} \frac{e^2}{m_e c^3} \gamma^2 \omega_B^2 \\ \omega_B &= \frac{eB}{m_e c} \\ B &= B_0 \left(\frac{t}{t_0} \right)^{-\delta} \end{aligned} \quad (3.20)$$

with $\delta > 1/2$. (In our case, $\delta = 13/10$, see Eq.(3.17).) For definiteness we can set $t_0 = t_{now}$, so that $t < t_0$.

Introducing

$$\begin{aligned} \tau_c &= \frac{9}{4} \frac{m_e^3 c^5}{e^4 B_{now}^2} \\ \gamma_M &= \frac{\tau_c}{t_{now}}, \end{aligned} \quad (3.21)$$

Eq. (3.20) can be written as

$$\dot{\gamma} = - \left(\frac{t_{now}}{t} \right)^{2\delta} \frac{\gamma^2}{t_{now} \gamma_M} \quad (3.22)$$

If at time t_{inj} a particle was injected with Lorentz factor γ_{inj} , then the Lorentz factor evolves according to

$$\begin{aligned} \frac{\gamma}{\gamma_{inj}} &= \left(1 + \frac{1}{2\delta - 1} \left(\left(\frac{t_{now}}{t_{inj}} \right)^{2\delta-1} - \left(\frac{t_{now}}{t} \right)^{2\delta-1} \right) \frac{\gamma_{inj}}{\gamma_M} \right)^{-1} \\ \frac{\gamma_{inj}}{\gamma} &= \left(1 - \frac{1}{2\delta - 1} \left(\left(\frac{t_{now}}{t_{inj}} \right)^{2\delta-1} - \left(\frac{t_{now}}{t} \right)^{2\delta-1} \right) \frac{\gamma}{\gamma_M} \right)^{-1} \end{aligned} \quad (3.23)$$

For a given time t the Lorentz factor must be smaller than

$$\gamma_{max}(t) = (2\delta - 1) \left(\left(\frac{t_{now}}{t_{inj}} \right)^{2\delta-1} - \left(\frac{t_{now}}{t} \right)^{2\delta-1} \right)^{-1} \gamma_M \quad (3.24)$$

and larger than

$$\gamma_{min}(t) = \left(1 + \frac{1}{2\delta - 1} \left(\left(\frac{t_{now}}{t_{inj}} \right)^{2\delta-1} - \left(\frac{t_{now}}{t} \right)^{2\delta-1} \right) \frac{\gamma_{inj,min}}{\gamma_M} \right)^{-1} \gamma_{inj,min} \quad (3.25)$$

Thus, at any time t , the distribution function for particles injected at t_{inj} is given by

$$G(t, t_{inj}) \propto \gamma^{-p} \left(1 - \frac{1}{2\delta - 1} \left(\left(\frac{t_{now}}{t_{inj}} \right)^{2\delta-1} - \left(\frac{t_{now}}{t} \right)^{2\delta-1} \right) \frac{\gamma}{\gamma_M} \right)^{p-2} \Theta(\gamma - \gamma_{min}(t)) \Theta(\gamma_{max}(t) - \gamma), \quad (3.26)$$

see Fig. 3.1. Eq. (3.26) gives the Green's function for the evolution of the particle distribution function.

There is a special injection time $t_{inj,full}$ so that now, at $t = t_{now}$, for $t_{inj} < t_{inj,full}$ the highest possible Lorentz factor becomes smaller than the minimal injection Lorentz factor $\gamma_{inj,min}$: in this regime all the particles enter the fast cooling regime:

$$\frac{t_{inj,full}}{t_{now}} = \left(1 + (2\delta - 1) \frac{\gamma_M}{\gamma_{inj,min}} \right)^{-1/(2\delta-1)} \rightarrow \left(1 + \frac{\gamma_M}{\gamma_{inj,min}} \right)^{-1} \quad (3.27)$$

If $t_{inj} < t_{inj,full}$, then all the particles within a shell cool below $\gamma_{inj,min}$. Since $\gamma_M \leq \gamma_{inj,min}$ most of the particles that have been accelerated above $\gamma_{inj,min}$ over the lifetime of the Nebula had time to cool down below $\gamma_{inj,min}$.

The ratio $\gamma_{max}/\gamma_{min}$ is

$$\frac{\gamma_{max}}{\gamma_{min}} = 1 + (2\delta - 1) \left(\left(\frac{t_{now}}{t_{inj}} \right)^{2\delta-1} - \left(\frac{t_{now}}{t} \right)^{2\delta-1} \right)^{-1} \frac{\gamma_M}{\gamma_{inj,min}} \quad (3.28)$$

For earlier $t_{inj} \rightarrow 0$ the ratio $\gamma_{max}/\gamma_{min} \rightarrow 1$. Thus, with time all the particles injected at some t_{inj} occupy a narrower and narrower range of $d\gamma$ - there is an effective pile-up of the distribution.

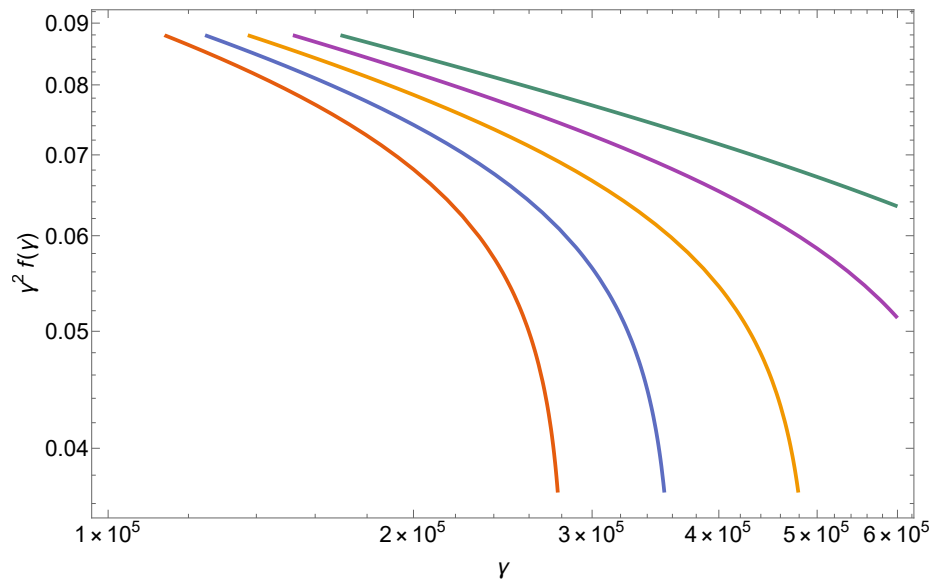


Figure 3.1. Evolution of the distribution function within one shell. Each line has injection time t_{inj} as $t_{now}/t_{inj} = 1.1, 1.2, 1.3, 1.4, 1.5$ (from green to red) with the same minimum injection Lorentz factor $\gamma_{inj,min}$ and normalization factor. As the particle distribution function evolves with time, particles are cooled due to synchrotron emission and shifted to lower energy. Here power-law index $p = 2.2$ and the minimum injection Lorentz factor $\gamma_{inj,min} = 1.9 \times 10^5$.

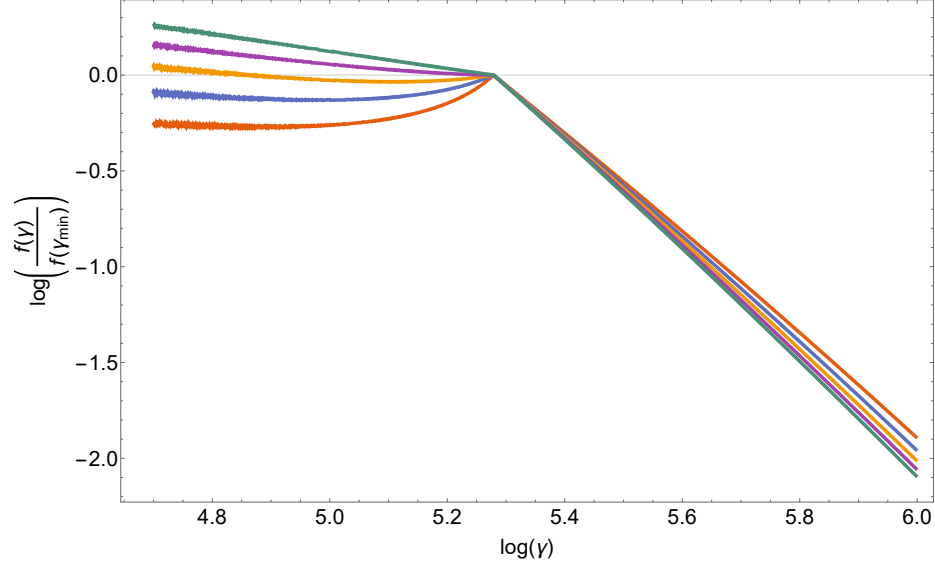


Figure 3.2. Total particle distribution function within the Nebular for different present-time magnetic fields: $2.0 \times 10^{-4} \text{G}$ (red), $2.5 \times 10^{-4} \text{G}$ (blue), $3.0 \times 10^{-4} \text{G}$ (orange), $3.5 \times 10^{-4} \text{G}$ (purple) and $4.0 \times 10^{-4} \text{G}$ (green) at t_{now} . We keep injecting power-law particle distribution from injection time $t_{inj} = 0.1 \times t_{now}$ with $p = 2.2$ and same minimum Lorentz factor $\gamma_{inj,min} = 1.9 \times 10^5$ and let all particles evolve with time. All curves are normalized to unity at the injection break.

3.4.2 The overall particle distribution in the Crab Nebula

Eqn. (3.26) describes the evolution of the distribution function for the particles injected at time t_{inj} . To find the total distribution function in the Nebula, the Green's function (3.26) should be integrated over injection times $t_{inj} \leq t_{now}$. Results of numerical integration are plotted in Fig. 3.2 (constant injection parameters are assumed).

In Fig. 3.2, there is one injection break at $\gamma_{inj,min}$ for all curves since they all have same minimum injection Lorentz factor. For large magnetic fields (e.g. purple and green curves), particles cool quickly, so that the distribution increases below the injection break towards smaller Lorentz factors and has relatively higher number of particles at lower energy. For small magnetic fields (e.g. red, blue and orange curves), the distribution is nearly constant and has a relatively lower number of particles at

lower energies, which are the particles cooled quickly early-on when the magnetic field was strong.

3.5 Acceleration in relativistic turbulent reconnection

In addition to providing a satisfactory solution of the sigma-problem, magnetized turbulence in the bulk of the Crab Nebula is expected to accelerate particles far out of thermal equilibrium.¹ Particle acceleration can occur due to a combination of turbulence fluctuations and magnetic reconnection events that are self-consistently produced by the turbulent motions in the plasma. Indeed, in magnetized turbulence, contrary to hydrodynamic turbulence, the presence of the magnetic field gives rise to turbulence eddies that becomes progressively more anisotropic towards small scales within the inertial range, producing current-sheet-like structures that are prone to magnetic reconnection [167]; [168]; [169]; [170] due to the plasmoid instability that kicks in while current sheets are forming [171]; [172]; [173].

Recent first-principle kinetic simulations [152]; [174] have shown that in a strongly magnetized plasma ($\sigma \gg 1$), such as the case for the central part of the Crab Nebula, the interplay between turbulence fluctuations and magnetic reconnection leads to the generation of a large fraction of non-thermal particles. The resulting particle energy distribution had been shown to display a power-law energy tail $dn/d\gamma \propto \gamma^{-p}$ that extends well beyond the Lorentz factor

$$\gamma \sim (1 + \sigma) \gamma_0, \quad (3.29)$$

which takes into account the fact that most of the magnetic energy is converted to particle energy by the time the particle energy spectrum has saturated [152]; [174]. The slope p of the particle energy spectrum was found to depend on the plasma magnetization σ and the amplitude of the turbulence fluctuations δB_{rms} with respect

¹To be clear, our model is different from "turbulent reconnection" of [166], in that case "turbulent reconnection" is understood as turbulence inside a reconnecting current sheet. In contrast, what we envision can be described as turbulence with reconnection occurring in various current sheets inside the turbulence itself.

to the mean magnetic field B_0 . In particular, the power-law slope p is harder for larger magnetizations and stronger turbulence fluctuations [175]; [152]; [174]. For $\sigma \gg 1$ and large turbulent fluctuations ($\delta B_{\text{rms}}^2/B_0^2 \sim 6$ in some regions of the Crab Nebula, as discussed in [151]), the power-law slope was found to be $p < 2$ [152]; [174], but generally not as hard as the slope generated by reconnection alone with the same parameters, which can approach $p \rightarrow 1$ for $\sigma \gg 1$ [140]; [176]; [177]; [178]; [148]; [147]. Therefore, it is conceivable to assume a space-averaged spectrum with a slope $p \sim 1.6$, as can be inferred from the radio spectrum of the Crab Nebula.

More specifically, [152]; [174] have shown that plasmoid-mediated reconnection controls the initial acceleration of particles from the thermal bath at γ_0 up to the Lorentz factor $\gamma_0(1 + \sigma)$. In our model, γ_0 corresponds to the wind Lorentz factor in the absence of dissipation. Then, some particles are further accelerated to much higher energies by stochastic interactions with turbulent fluctuations, with the most energetic particles reaching

$$\gamma_{\text{max}} \sim \frac{eB_{\text{rms}}\ell}{m_e c^2}, \quad (3.30)$$

where ℓ indicates the size of the largest turbulent eddies and B_{rms} is the space-averaged root-mean-square value of the magnetic field. This two-stage acceleration process is characterized by a combination of systematic (Fermi-I) and stochastic (Fermi-II) particle acceleration mechanisms.

At small scales, the non-ideal reconnection electric fields, whose magnitude is $|E_{\parallel}| \simeq \beta_R \delta B_{\text{rms}}$, accelerate particles according to

$$\frac{d\langle\gamma\rangle}{dt} = \frac{e}{m_e c} \beta_R \delta B_{\text{rms}}, \quad (3.31)$$

where β_R is the average reconnection rate, which is an $O(0.1)$ quantity for relativistic collisionless plasmas [179]; [180]; [181]; [177]; [182]; [183]; [184]; [185]; [186]; [148]. The fast reconnection rate $\beta_R \sim 0.1$ guarantees that magnetic reconnection can process large volumes of plasma in few outer-scale eddy turnover times, in addition to enabling particle acceleration on a fast timescale $t_{\text{acc}} \sim \beta_R^{-1} \rho_L/c$, where L is the particle Larmor radius.

After the initial acceleration due to plasmoid-mediated reconnection, particles are further accelerated by stochastic scattering off turbulent fluctuations in the inertial range of the turbulent energy cascade. The mean particle energy gain due to stochastic acceleration is related to the diffusion coefficient in energy space as

$$\frac{d\langle\gamma\rangle}{dt} = \frac{1}{\gamma^2} \frac{\partial}{\partial\gamma} \left(\gamma^2 D_{\gamma\gamma} \right), \quad (3.32)$$

with an energy diffusion coefficient $D_{\gamma\gamma}$ that depends on the instantaneous plasma magnetization and the particle Lorentz factor as [174]

$$D_{\gamma\gamma} \sim 0.1\sigma \left(\frac{c}{l} \right) \gamma^2, \quad (3.33)$$

akin to the original Fermi-II mechanism (*e.g.* [115]; [187]). Note that the timescale t_{acc} of the stochastic acceleration process is comparable to that of fast plasmoid-mediated reconnection in the strong turbulence scenario considered here. Indeed, the stochastic acceleration timescale is $t_{acc} \sim \gamma^2/D_{\gamma\gamma} \sim 10\ell/\sigma c$, with σ being the instantaneous magnetization. The instantaneous magnetization decreases rapidly in time as a result of magnetic dissipation and reaches $\sigma \sim 1$ in few outer-scale eddy turnover times. Then $t_{acc} \sim 10\ell/c$ as it would be in the case of fast reconnection ($\beta_R \sim 0.1$) driving particles up to the highest energies allowed by the system size (*i.e.*, with particle Larmor radius $\rho_L \sim \ell$).

Finally, we also expect that at the largest scales, magnetic reconfigurations can generate large scale current sheets whose statistic is not well described as a self-similar sequence controlled by turbulent motions. In this case, the reconnection of the large scale magnetic field might be responsible for particle acceleration up to the maximum available potential. Particle acceleration at these large-scale current sheets can extend up to the synchrotron burn-off limit of 100 MeV and beyond, thus powering the Crab Nebula gamma-ray flares [148]; [188]. Therefore, in this model of the Crab Nebula radiation, magnetized turbulence with reconnecting current sheets can accelerate both the radio electrons and also produce the Crab gamma-ray flares.

3.6 The turbulent model of the Crab Nebula radiation

3.6.1 Model parameters

Above, in Sections 3.3 and 3.4, we described the one-dimensional spacial and temporal evolution of the flow and of the distribution function of the accelerated particles as functions of injection time and the magnetic field at present time in the Nebula. In this Section, we calculate the resulting broadband spectrum: the synchrotron component and the inverse-Compton component of the non-thermal synchrotron emission, thermal dust emission, CMB, and starlight photons.

Following [151] we assume that there are two acceleration mechanisms in the Crab Nebula: those from the terminate shock (Component-I) and the reconnecting turbulent acceleration mechanism (Component-II). (The possibility of having two acceleration mechanisms in PWNe has been suggested previously by [26]; [114]; [189]; [190]; [191]; [192]; [118]; [193]; [194].)

The Component-I obeys the usual acceleration condition of Fermi-I acceleration at the equatorial part of the pulsar wind, the properties of the Component-II are discussed in §3.5. Both components are accelerated within the inner regions of the Nebula; though Component-II has more extended acceleration sites, see Fig 4 in [151]. Here we neglect the difference in the sizes of the acceleration regions. With time, both components expand hydrodynamically and experience radiative cooling. Component-I is in the fast cooling regime, meaning that particles with the minimal injected energy cool efficiently on the timescale of the PWN. Component-II is from magnetic reconnecting turbulent and is in the slow cooling regime, so that particles with minimal injected energy do not cool.

We assume that two populations of accelerated particle are injected in the inner region of the Nebula, Fig. 3.3. The Component-I's injected electron distribution has power-law index p_I , minimum and maximum injection Lorentz factors $\gamma_{I_{min}}$ and $\gamma_{I_{max}}$. The values of p_I is restricted by the observed spectral power-law indices in the X-ray range, and the value of $\gamma_{I_{min}}$ is restricted by the observed peak and spectral

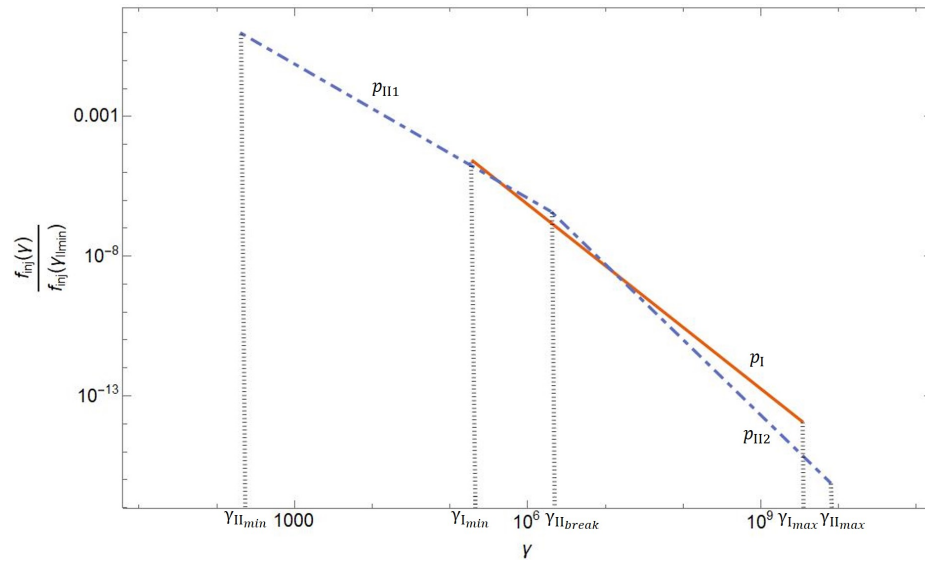


Figure 3.3. Illustration of parameters in component-I and component-II. Component-I is represented by red solid curve and component-II is represented by blue dashed curve. All parameters values are taken from Table ??, and we normalized the curve of component-II to unity at its corresponding minimum injection Lorentz factor γ_{IImin} .

power-law indices in the IR range. The maximum injection $\gamma_{I_{max}}$ is limited both by the observed break, and the theoretical limit of synchrotron acceleration/burn-off, around 100 MeV (*e.g.* [137]).

For Component-II the injected electron distribution has a broken power-law spectrum with indices p_{II1} and p_{II2} , minimum and maximum injection Lorentz factors $\gamma_{II_{min}}$ and $\gamma_{II_{max}}$, and break injection $\gamma_{II_{break}}$; p_{II1} is the power-law index below the injection break $\gamma_{II_{break}}$, p_{II2} is the power-law index above $\gamma_{II_{break}}$. The minimum injection $\gamma_{II_{min}}$ is not restricted: it should be sufficiently low, \sim few hundreds at most, to have the radio spectrum extending down to below \sim 100 MHz. The maximum injection $\gamma_{II_{max}}$ is similarly limited by the acceleration/burn-off. We illustrate these parameters in Fig. 3.3. The spectrum below the break is determined by the observed radio spectrum. The break (approximately in the IR) is required for the Component-II not to overshoot Component-I in the soft X-rays. (In the hard X-rays and gamma-rays the two components contribute similarly).

In our calculation, we fix $p_I = 2.2$ (this is derived from the X-ray spectrum of the Crab Nebula wisps), $p_{II1} = 1.6$ (which is derived from the radio spectral index $\alpha_r = 0.3$), and $\gamma_{II_{min}} = 200$ (corresponding to synchrotron frequency below few tens of MHz). There are several fit parameters: magnetic field at present time B_{now} , $\gamma_{I_{min}}$, $\gamma_{II_{break}}$, $\gamma_{I_{max}}$, p_{II2} , $\gamma_{II_{max}}$, the relative normalization factor of Component-I and Component-II and the overall normalization factors for each component. We explored these parameters and tried to fit the observational data of the IR index map, optical index map, and the broad-band spectrum.

In the following sections, we first calculate the synchrotron spectrum in §3.6.2, and then the corresponding IC signal in §3.6.2. The overall spectrum and its evolution is calculated in §3.6.2, and the spatial evolution of spectral indices in the optical and radio in §3.7.

3.6.2 The fitting procedure

Fitting the broad-band spectrum involving synchrotron and SSC components as well as other contribution for soft photons (*e.g.* dust, starlight and CMB) involves numerous parameters and data measurements over a huge range of energies. This is a complicated task, that cannot be achieved in one-go. Next we describe a novel procedures we developed to tackle this problem. It is somewhat akin to a boot-strap method, where numerous parameters are improved step-wise, trying to achieve the best fit.

Both Components produce synchrotron emission, and, in addition, there are IC emission on the synchrotron photons (SSC), thermal dust emission, external star light and CMB. A wide range of particles and photons energies requires that KN effects be taken into account for the IC component. Next we describe a novel procedure to self-consistently fit the synchrotron and IC processes due to two particle distributions.

The synchrotron component

We use the exact expression for local single particle spectral emissivity [17]

$$\begin{aligned}
 P(\omega, r, t) &= \frac{\sqrt{3}}{2\pi} \frac{Be^3}{mc^2} F\left(\frac{\omega}{\omega_c}\right) \\
 \omega_c &= \frac{3}{2} \gamma^2 \frac{eB}{m_e c} \\
 F(x) &\equiv x \int_x^\infty K_{\frac{5}{3}}(\xi) d\xi
 \end{aligned} \tag{3.34}$$

where $K_{\frac{5}{3}}(\xi)$ is a Bessel function of the second kind.

Given the temporal and the corresponding spatial evolution of the magnetic field, Eqn. (3.17) and the particles' Green's function (3.26), we calculate the spectral luminosity along a given line of sight at any moment t :

$$L(\omega, t) = \int_{r_{\min}}^{r_{\max}} dl \int N(\gamma, t, r) P(\omega, r, t) d\gamma \tag{3.35}$$

where the integration path passes through a different shell, see Fig. 3.4

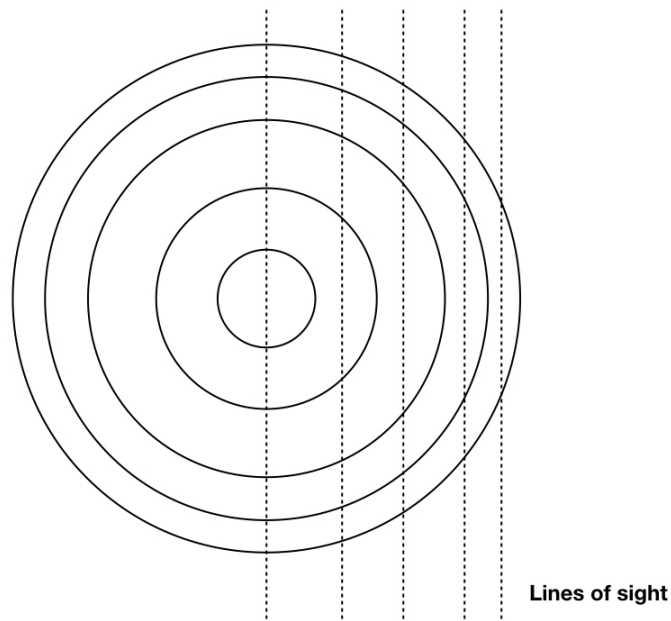


Figure 3.4. Shell model of the Crab Nebula. We calculate the synchrotron emission along different lines of sight (dashed lines.)

In practice, we break the Nebula into a number of thin shells (180 in total in our calculation), and choose shell spacing equal in observed radii. The choice of equal spacing in the observed radii is important: equal spacing in presently observed radii corresponds to *different* duration of injection time for different shells, see Eqn. (3.14). We chose the innermost shell at $0.100 R_{PWN,now}$ and each shell has a width of $0.005 R_{PWN,now}$.

The ejection time for each shell is given by Eqn. (3.15), where B_{now} represent the current magnetic field in the Nebula and is a free parameter in our model. We then chose 10 lines of sight which are equally spaced in observed radii, i.e., $0.1 R_{PWN,now}$, $0.2 R_{PWN,now}$, \dots , $1.0 R_{PWN,now}$. Using $N(t) = \int G(t, t_{inj}) dt_{inj}$, for a given injection spectrum, we know the distribution function at each point in the Nebula at any given time. We can then calculate the spatially resolved synchrotron emissivity (see §3.6.2) and the IC power (see §3.6.2).

We adopt the following step-by-step method of fitting the observed broad-band spectrum from synchrotron emission:

- We estimate p_{II2} from X-ray observations.
- We fit the optical index map to estimate B_{now} (To show the optical index map of the Crab nebula, I reprint the FIG. 2 in [195] as FIG. 3.5). Stronger B_{now} produces a sharper rise at outer shells and weaker B_{now} produces a milder rise at outer shells.
- Once we have the estimate of B_{now} , we are able to estimate $\gamma_{I_{max}}$ and $\gamma_{II_{max}}$ according to the broad-band spectrum at the synchrotron limit region, where we expect both components to disappear above 100 MeV.
- The requirement that Component-II does not overshoot Component-I in the X-ray region gives a range of allowed $\gamma_{II_{break}}$.
- We also fit the IR index map of the innermost shell, which is $\alpha \approx 0.3$ for lower frequencies and $\alpha \approx 0.5$ for higher frequencies (To show the IR index map of

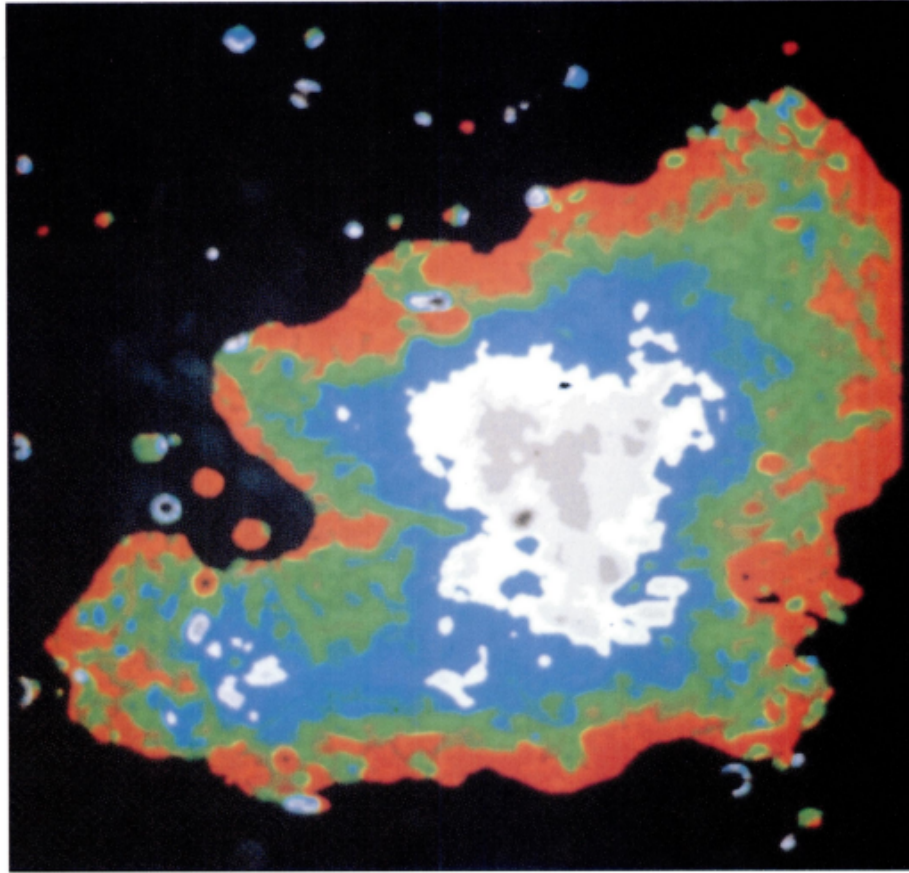


Figure 3.5. The Map of the optical spectral index calculated in the wavelength range $0.5364\text{-}0.9241 \mu\text{m}$. Taken from [195].

the Crab nebula, I reprint the FIG. 2 in [151] as FIG. 3.6). This gives $\gamma_{II_{break}}$ and $\gamma_{I_{min}}$.

- Given the above estimates, we are then able to find the best value of relative normalization factors of Component-I and Component-II.

The IC component

Both the particle and the photon distribution within the Nebula are very broad, so that for different parts of the distribution, the IC scattering occurs both in Thomson

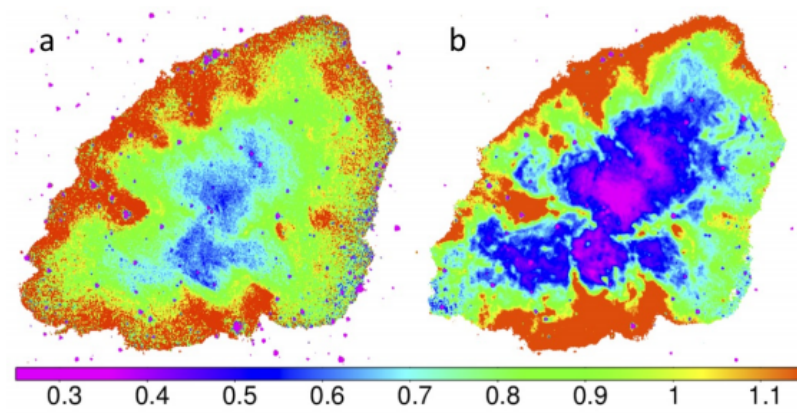


Figure 3.6. Left: The Map of the IR spectral index calculated a difference between the 3.6m and 4.5m image. Right: Map of the spectral index calculated as a difference between 3.6 μm and 8.0 μm images. Taken from [151]

and Klein-Nishina regimes. The general expression for the differential cross section is *e.g.* [196]

$$\frac{d\sigma_{KN}}{d\Omega} = \frac{3}{16\pi} \frac{\sigma_T}{(1+x(1-\cos\theta))} \left(x(1-\cos\theta) + \frac{1}{1+x(1-\cos\theta)} + \cos^2\theta \right) \quad (3.36)$$

where x is the initial photon energy in units of $m_e c^2$, and θ is the scattering angle in the frame where the electron is initially at rest.

Transformations of the directions and the energies of incoming, scattered photons and the lepton's velocity is a complicated exercise in Lorentz transformation *e.g.* [15]; [114]; [16]. In particular, [15] derived the angle-averaged scattering rate analytically, and [16] re-derived the angle-averaged scattering rate by considering some standard asymptotic forms. In our work, we derived the angle-averaged outgoing photon energy, and then calculate it numerically.

The notations are the following. In the electron comoving frame K' , x' is the energy of the incoming photon, x'_1 is the energy of the outgoing photon, ψ' is the angle between the electron velocity and incoming photon direction, ψ'_1 is the angle between the electron velocity and outgoing photon direction, δ' is the azimuthal angle and θ' is the scattering angle. In the lab frame, we define x as incoming photons energy, x_1 as outgoing photons energy, ψ as the angle between the electron velocity and incoming photon direction.

Combining Lorentz transformations

$$x' = \frac{x}{\gamma(1+\beta\cos\psi')} \quad (3.37)$$

with Compton scattering

$$x'_1 = \frac{x'}{1+x'(1-\cos\theta')}, \quad (3.38)$$

we find

$$x_1 = \frac{x\gamma(1+\beta\cos\psi'_1)}{\gamma(1+\beta\cos\psi') + x(1-\cos\theta')} \quad (3.39)$$

The geometric relation between scattering angle θ' , azimuth angle δ' , angle between incoming photon and electron ψ' and angle between outgoing photons and electron ψ'_1 is:

$$\cos\psi'_1 = \cos\theta' \cos\psi' - \sin\theta' \cos\delta' \sin\psi' \quad (3.40)$$

which gives

$$x_1 = \frac{x\gamma (1 + \beta (\cos \theta' \cos \psi' - \sin \theta' \cos \delta' \sin \psi'))}{\gamma (1 + \beta \cos \psi') + x (1 - \cos \theta')} \quad (3.41)$$

The Lorentz transformation for angle is $\cos \psi' = \frac{\cos \psi - \beta}{1 - \beta \cos \psi}$, thus

$$x_1 = \frac{x\gamma \left(1 + \beta \left(\cos \theta' \frac{\cos \psi - \beta}{1 - \beta \cos \psi} - \sin \theta' \cos \delta' \sin \psi'\right)\right)}{\gamma \left(1 + \beta \frac{\cos \psi - \beta}{1 - \beta \cos \psi}\right) + x (1 - \cos \theta')} \quad (3.42)$$

Then averaging over angle δ' and ψ , we have

$$x_1 = \frac{\csc^2 \frac{\theta'}{2} \left(\csc^2 \frac{\theta'}{2} (\gamma - \cos \theta' (\gamma + x)) + \frac{x}{2} \cos 2\theta' + \frac{x}{2} \right) \ln \left(\frac{2\gamma - x \cos \theta' + x}{4\gamma^2 \left(\frac{1}{2\gamma} - x \cos \theta' + x \right)} \right) + 4x\gamma^2 (1 - \cos \theta')}{8x\gamma} \quad (3.43)$$

In order to fit the IC component, we adopt the step-by-step procedure of fitting the observed spectrum from IC emission:

- For the sample of Lorentz factor of electrons (say $\gamma = 200, \gamma = 400, \dots$), we calculated the corresponding number density of electrons n_e , and made a table of value as n_e vs. γ .
- For the sample of incoming photon energies (say $x = 10^{-7}$ eV, $x = 2 \times 10^{-7}$ eV, ...), we calculated the corresponding number of incoming photons N_γ , and made a table of value as N_γ vs. x .
- For the sample of outgoing photon energies x_1 , we made a table of $N_{scattered}$ vs. x_1 , where $N_{scattered}$ is unknown and will be calculated in the following steps.
- We pick values of γ, x and x_1 from the tables and run the loop (e.g $\gamma = 200, x = 10^{-7}$ eV, $x_1 = 10^5$ eV), and we solve equation 3.43 to find the value of $\cos \theta'$.
- Assuming that the solution of Eqn. 3.43 is $\cos \theta' = S(x, x_1, \gamma)$, then $d(\cos \theta') = S_{max}(\tilde{x}, \tilde{x}_1, \tilde{\gamma}) - S_{min}(\tilde{x}, \tilde{x}_1, \tilde{\gamma})$, for $\tilde{x} \in \left[x - \frac{dx}{2}, x + \frac{dx}{2}\right]$, $\tilde{x}_1 \in \left[x_1 - \frac{dx_1}{2}, x_1 + \frac{dx_1}{2}\right]$, $\tilde{\gamma} \in \left[\gamma - \frac{d\gamma}{2}, \gamma + \frac{d\gamma}{2}\right]$, where dx, dx_1 and $d\gamma$ are step length in the table.
- Substitute the value of $x', \cos \theta'$ and $d \cos \theta'$ into Eqn. 3.36, we can calculate the corresponding differential cross section.

- Then we substitute the corresponding number density of electrons n_e and number particle of incoming photons N_γ (say the i^{th} row in the table is value n_{e_i} and the j^{th} row in the table is value N_{γ_j}), the collision rate would be $n_{e_i}N_{\gamma_j}c\sigma$. We need to be aware of that all variable above are in rest frame of electron. So
- The collision rate in lab frame is $N_{scattered} = n_{e_i}N_{\gamma_j}c\sigma/\gamma_i$.
- Finally, sum up over the table of value of electrons and multiply the scattered photon frequency, we will find $(\nu F(\nu))_{scattered} \propto \sum_{i,j} \nu x_1 N_{scattered} = \sum_{i,j} \nu x_1 n_{e_i} N_{\gamma_j} c\sigma / \gamma_i$.

We verified that the step-by-step procedure described here reproduces a number of analytical results (*e.g.*, IC scattering of mono-energetic seed photons and mono-energetic electrons, IC scattering of mono-energetic seed photons and power law energy distribution electrons).

The SSC component

The model has a number of parameters, §3.6.1. By adopting the step-by-step methods from section 3.6.2, we calculated the overall spectrum by adding the two synchrotron components and the SSC component.

The SSC emission is shown as curve 5 in Fig. 3.8. Given that the model is very simple, *e.g.* one-dimensional, and spans nearly 20 orders of magnitude in energy and some seven orders of magnitude in flux, the fits were done "by eye". We found the best values of all parameters are $B_{now} = 2.7 \times 10^{-4} \text{G}$, $\gamma_{I_{max}} = 3.5 \times 10^9$, $\gamma_{II_{max}} = 8.0 \times 10^9$, $p_{II2} = 2.7$, $\gamma_{I_{min}} = 1.9 \times 10^5$, and $\gamma_{II_{break}} = 2.0 \times 10^6$. Component-II constitutes about 60% of the ejection energy and Component-I constitutes about 40% of the ejection energy. The numerical fitting program may be added in further work to improve the precision of parameters value, but for now, our results have good enough precision to demonstrate our model. We summarize all parameters values in Table. ??.

Table 3.1.

Summary of parameter values. In this table, B_{now} is the magnetic field now. $\gamma_{I_{max}}$ is the maximum Lorentz factor of injected electrons of component-I. $\gamma_{II_{max}}$ is the maximum Lorentz factor of injected electrons of Component-II. $\gamma_{II_{break}}$ is the middle break Lorentz factor of Component-II, where power law indices are $p_{II1} = 1.6$ below the $\gamma_{II_{break}}$ and p_{II2} above the $\gamma_{II_{break}}$. $\gamma_{I_{min}}$ is the minimum Lorentz factor of injected electrons of component-I. E_I is the energy of component-I, E_{II} is the energy of Component-II, and E_{total} is the sum of the energy of Component-I and Component-II.

parameters	B_{now} (G)	$\gamma_{I_{max}}$	$\gamma_{II_{max}}$	p_{II2}	$\gamma_{I_{min}}$	$\gamma_{II_{break}}$	E_{II}/E_{total}	E_I/E_{total}
values	2.7×10^{-4}	3.5×10^9	8.0×10^9	2.7	1.9×10^5	2.0×10^6	0.6	0.4

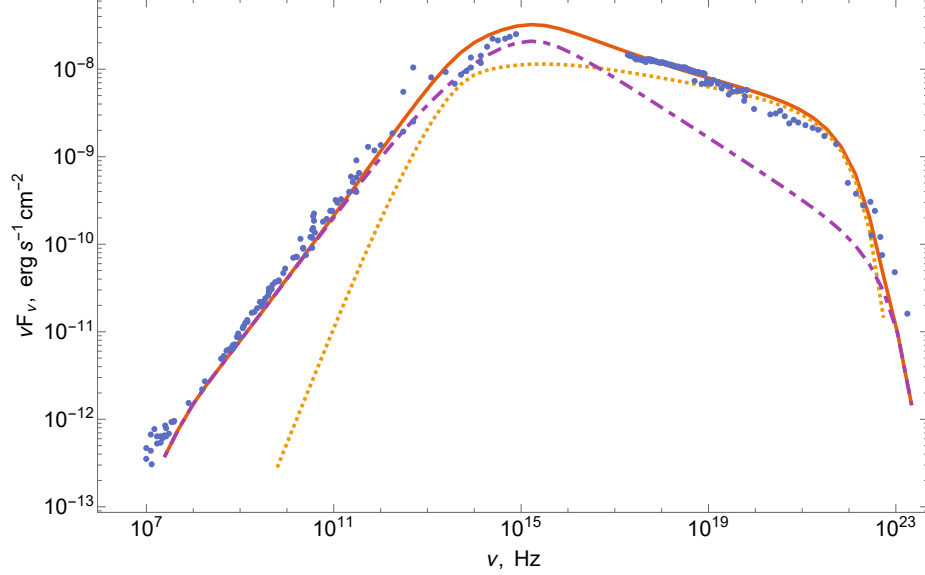


Figure 3.7. Comparison of observational data [197]; [198]; [199]; [200]; [201]; [202]; [203]; [204] and numerical result for the broad-band spectrum. The dots represent observational data. The red solid line represents the total emission in the model. The purple and yellow dashed line represent Component-I and Component-II.

We then substituted all of parameter values from Table ?? into Eqn. (4.11) and calculated the broad-band synchrotron spectrum in Fig. 3.7, where we present the synchrotron emission from component-I and component-II as yellow dotted line and purple dotted-dash line respectively, and their combined contribution as the red solid line. As we can see, the low energy synchrotron emission is dominated by component-II and high energy synchrotron emission is dominated by component-I. In the section 3.6.2, we use the broad-band synchrotron spectrum as seed photons for the IC component calculation.

As shown in Fig. 3.8, our purely SSC emission model with parameter values taken from Table ?? roughly reproduce the current broad-band spectrum. The overall spectrum consists of three parts: Part I: $10^8 - 10^{14}$ Hz is the low energy emission and is dominated by synchrotron emission from component-II, which has a peak at around 10^{14} Hz. p_{II_2} does not affect the overall spectrum significantly, however, it

will affect IR spectra index map in section 3.7. Part II: $10^{16} - 10^{22}$ Hz is the middle energy emission and is dominated by synchrotron emission from component-I. Part III: $10^{22} - 10^{28}$ Hz is the high energy emission and has a peak around 10^{26} Hz. Part III is dominated by SSC emission with taking account synchrotron emission from both component-I and component-II as seed photons.

Dust and star light contributions

There is a big gap around $10^{23} - 10^{26}$ Hz region between observational data and our numerical SSC emission. In order to fill up this big gap, we consider additional IC photons on CMB and dust. First we calculated the IC on seed photons, including CMB, component-I and component-II. The IC on CMB is showed as curve 7 in Fig. 3.8. As we can see, additional IC emission on CMB are not able to gives a apparent rise or fill up the gap around $10^{23} - 10^{26}$ Hz region. Thus, we need to add IC emission from dust.

We then consider thermal emission from dust with temperature 62K, and the normalization factor is determined by fitting a small bump in IR band around 5×10^{12} Hz. The thermal dust emission is showed as curve 4 in Fig. 3.8. The associated IC emission gives a comparable contribution and fill up the gap. See curve 6 in Fig. 3.8

Our step-by-step method does not try to fit and calculate two synchrotron components and IC emission at the same time. Fitting-to-all (two synchrotron emission mechanism and IC emission) numerical algorithm with some statistical index checking could be implemented so that we can get better fitting result. But apparently, it cost more time to fit two physical process at the same time. [13]; [14]; [15]; [16] proposed different way to calculate IC emission analytically and numerically, however, the way we adopted in this chapter is the most acceptable way by trading off time and precision.

Star light photons also have IC emission within nebula, thus we investigate the effect of IC on star light in this section. We assume that seed photons of IC are

from black body emission (for star light with different temperatures corresponding to 0.1, 0.3 and 1.0 eV). Then we adopted our step-by-step method from section 3.6.2 again and calculated the corresponding IC emission.

In Fig. 3.8, we present IC on star light photons with peak energy at 0.1 eV (curve 8), 0.3 eV (curve 9) and 1.0 eV (curve 10), which are normalized to flux 1.0 eV/cm^3 at current time. Even for the highest IC emission on starlight in the case of peak energy at 0.1 eV, IC on star light are way below the SSC. Thus in later sections, we ignore the IC emission on star light photons.

Finally, the total spectrum is showed as curve 1 in Fig. 3.8 by combining Component-I and Component-II Synchrotron, SSC, IC on thermal dust emission and IC on CMB (here we ignore IC on starlight photons).

3.7 Spectral maps in the optical and IR

The spatial variations of the non-thermal spectrum have been identified as one of the drawbacks of the Kennel & Coroniti models [150]; [121] and §3.1: Kennel-Coroniti pure-MHD spherical advection model gives a constant spectral index with a sharp steepening at the edge of the PWN. Addition of diffusion on top of Kennel-Coroniti flow [154]; [155]; [156]; [157], have been proposed to explain the spectral steepening. Yet, the diffusion model cannot predict the change of the source size with photon energy.

Our method has the ability to reproduce the observed spectral index map, which is gradually steepening from the innermost shell to the edge of the PWN. In order to calculate the spectral index map, we consider our shell model in Fig. 3.4. Each shell has the same parameters but only the injection time is different. The injection time needs be calculated by Eqn. (3.15). For any given injection time, we are able to calculate the emissivity within each shell. By summing up the emission from each shell, we are able to calculate the total emission along each line of sight.

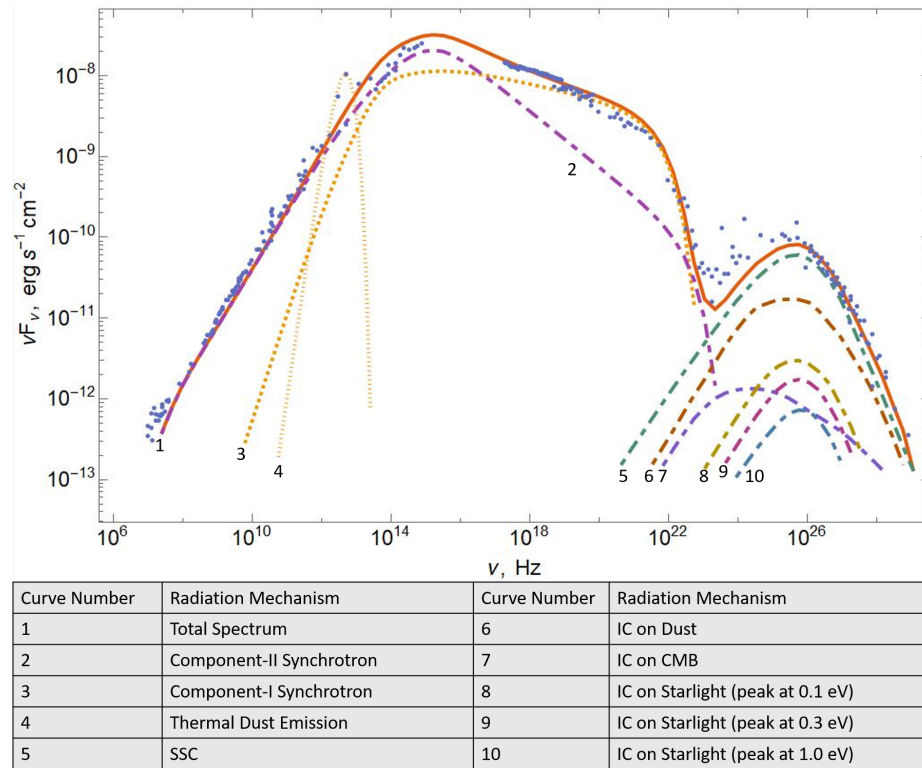


Figure 3.8. Broad-band spectrum of Crab Nebula. The observational data are showed as blue dots (synchrotron data is same as Fig. 3.7 and we add more data from [205]; [206]; [207]; [22] above synchrotron limit). Component-II (curve 2) and Component-I (curve 3) synchrotron emission are taken from Fig. 3.7. SSC emission is showed as curve 5. IC on thermal dust emission (curve 4) is showed as curve 6. IC on CMB is showed as curve 7. IC on starlight are showed as curve 8 (peak energy at 0.1 eV), curve 9 (peak energy at 0.3 eV) and curve 10 (peak energy at 1.0 eV). The overall total spectrum is showed as curve 1 (here we ignore IC on starlight).

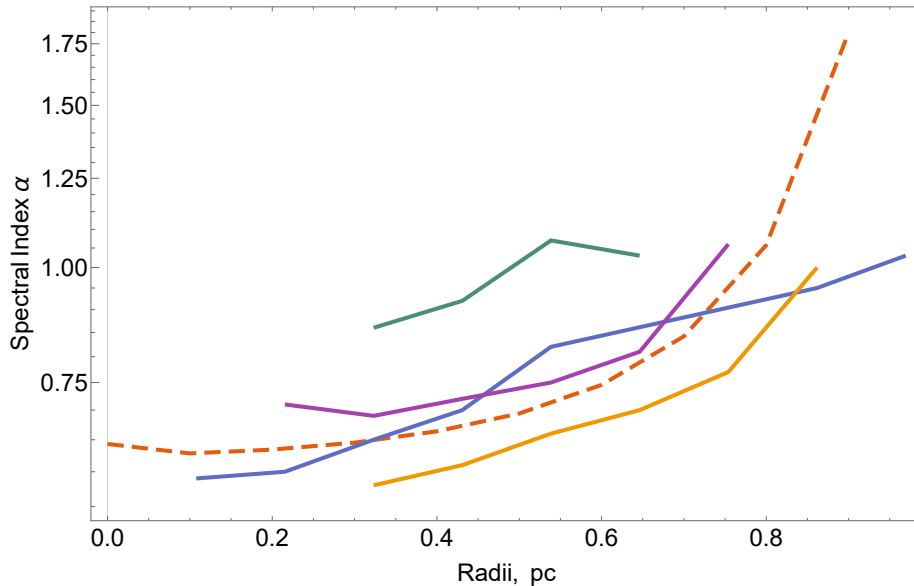


Figure 3.9. Comparison of observed data [195] and numerical result in the optical region. The wavelength range in the observational data is $0.5364 - 0.9241 \mu\text{m}$. We set the Crab pulsar at 0.0. The green, blue, purple, and orange solid lines represent observational data from west, east, south, and north direction, respectively. The red dashed line represents our numerical result at $0.7 \mu\text{m}$.

In our work, we calculate the emission along each line of sight in the IR ($7.9 \mu\text{m}$, $5.3 \mu\text{m}$, and $3.5 \mu\text{m}$) and optical wavelengths ($0.7 \mu\text{m}$), and then we use them to plot the spectral index map at each frequency. Results are presented in Figs. 3.9–3.11.

Figs. 3.9–3.11 show that the spectral index maps from radio to IR are consistent with observational results, thus demonstrating that our model can generally reproduce the evolution of the spectral indices in IR and optical.

3.8 Conclusions

In this chapter, following [151], we further develop a turbulent model of the Crab Nebula, and by extension, of PWNe in general. We demonstrate that developed turbulence in the magnetized post-shock wind can consistently resolve a number of problems of the Kennel and Coroniti model, both theoretical and observational. Tur-

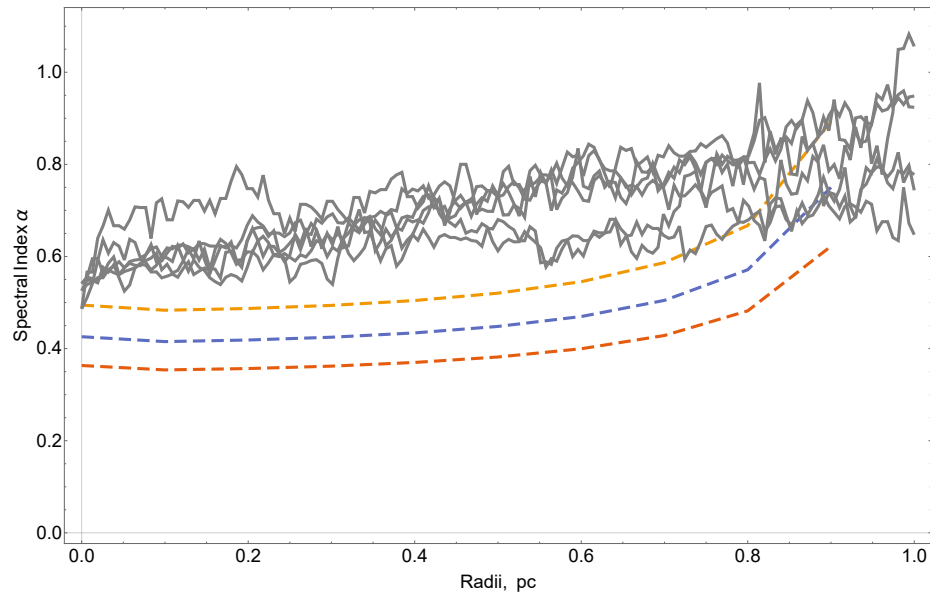


Figure 3.10. Comparison of the observed data and numerical result in the lower-frequency IR region. The wavelength range in the observational data is $3.6 - 8.0 \mu\text{m}$. We set the Crab pulsar at 0.0. The solid lines represent observational data along different directions. The red dashed lines represents our numerical result at $7.9 \mu\text{m}$. The blue dashed line represents our numerical data at $5.3 \mu\text{m}$. The orange dashed line represents our numerical data at $3.5 \mu\text{m}$. Even though we are trying to match the innermost shell index instead of the whole index map, the trend seen in the whole index map is similar to our numerical model.

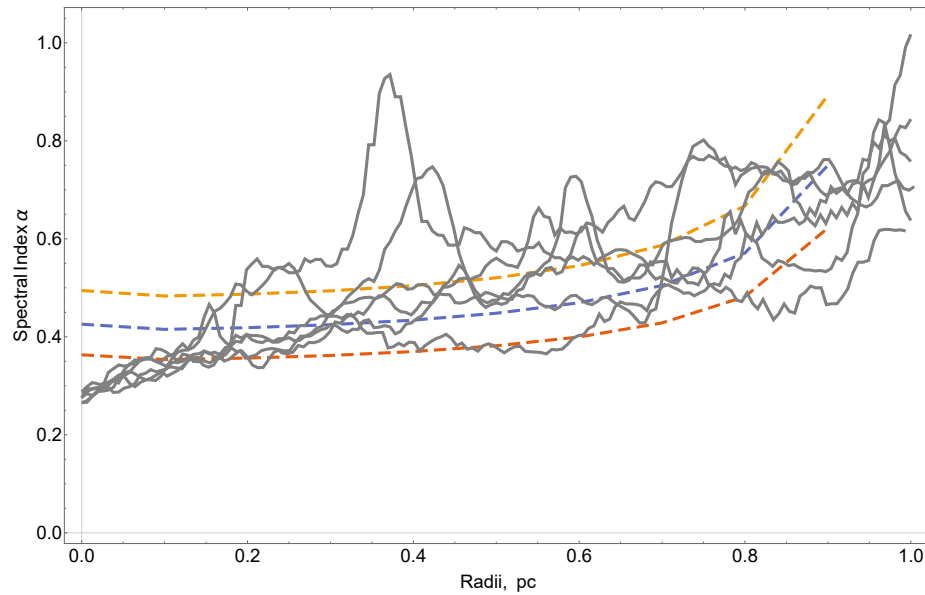


Figure 3.11. Comparison of observed data and numerical result in the higher frequency IR region. The wavelength range in the observational data is $3.6 - 4.5 \mu\text{m}$. We set the Crab pulsar at 0.0. The solid lines represent observational data along different directions. The red dashed lines represents our numerical result at $7.9 \mu\text{m}$. The blue dashed line represents our numerical data at $5.3 \mu\text{m}$. The orange dashed line represents our numerical data at $3.5 \mu\text{m}$. Even though we are trying to match the innermost shell index instead of the whole index map, the trend seen in the whole index map is similar to our numerical model.

bulence and ensuring reconnection destroys the magnetic flux, resolving the long-standing sigma-paradox, explains the origin and spectrum of radio electrons, gamma-ray flares, and the spectral evolution of the flow. With a simple 1D model, we are able to fit, within a factor of few, the broadband spectrum that stretches over 20 orders of magnitude in frequency. Importantly, the model suggests that reconnection is an important particle acceleration mechanism in a major astrophysical object - and, by extension, may be important/dominant in other astrophysical high-energy sources.

We advocate two acceleration mechanisms that produce two separate particle components: Component-I originates from particles accelerated at the terminate shock, presumably via the Fermi-I acceleration mechanism. Component-I dominates from optical to X-ray wavelengths and produces mostly the bright X-ray torus. Component-II is generated by magnetized turbulence that produces reconnecting current sheets of different sizes in the bulk of the Nebula. Particles are then accelerated by magnetic reconnection in the current layers and by scattering off turbulent fluctuations. Both the hard radio spectrum of Component-II and the requirement that rare reconnection events produce gamma-ray flares, requires regions with high magnetization, $\sigma \gg 1$.

Thus, we argue that the radio emitting leptons are accelerated by the same mechanism as GeV emitting leptons, but are different from the X-ray emitting ones. This is different from [193]; [194] where the two populations were non-overlapping in energy. One of the major advantages of our model is that it is physically motivated, and not just an *ad hoc* parametrization.

The model also explains low injection Lorentz factor for the Component-II, $\gamma_{II,min}$, (see more detailed discussion in [151]). At mid-latitudes the pulsar wind is relatively slow, $\gamma_w \sim 10^2$, and highly magnetized, $\sigma_w \sim 10^3$. Thus, the total energy per particle (in terms of $m_e c^2$) is $\gamma_p \sim \gamma_w \sigma_w \sim 10^5$. Within the striped part of the wind this total energy is given to the particles, producing the break at $\gamma_{I,min}$. At the intermediate attitudes, where the wind is not striped, only the bulk energy is thermalized, giving $\gamma_{II,min} \sim \gamma_w \sim 10^2$.

There is a number of issues that remain to be resolved. First, our 1D model naturally cannot reproduce azimuthal variations in the properties of the Crab Nebula. Presumably they originate due to intrinsic anisotropy of the wind and mildly relativistic velocities (and corresponding Doppler corrections) of the shocked flow in the innermost parts of the Nebula.

A more accurate evaluation of the particle energization near the cut-off energy would require a kinetic equation that also includes the effect of particle diffusion. In future work, we want to develop a more refined kinetic model that includes particle diffusion. Synchrotron radiation losses could also be added in Eq. (32). However, the synchrotron cooling of the radio electrons is negligible in the Crab nebula. Particle acceleration by reconnection electric fields also do not suffer significant synchrotron losses since the particle pitch angle is aligned to the magnetic field. On the other hand, the synchrotron losses in Fermi II acceleration would become significant at much higher particle energies. We intend to explore their role with particle-in-cell simulations in the next works.

The main theoretical unsolved problem, that the current model depends on is the suggestion that magnetic reconnection can indeed produce a spectrum with $p = 1.6$, §3.5. Another issue is the shear number of radio emitting electrons [208]. Applications to other PWNe also need to be explored. Some PWNe show clear signature of turbulence, *e.g.* 3C 58 [209].

4. WIND-POWERED AFTERGLOWS OF GAMMA-RAY BURSTS: FLARES, PLATEAUS AND STEEP DECAYS

4.1 Introduction

Gamma-ray bursts (GRBs) are produced in relativistic explosions [66]; [1] that generate two shocks: forward shock and reversed shock. The standard fireball model [104]; [108]; [106]; [109] postulates that the prompt emission is produced by internal dissipative processes within the flow: collisions of matter-dominated shells, [106], or reconnection events [130]. The afterglows, according to the model, are generated in the external relativistic blast wave.

One of the most surprising results of the Swift observations of the early afterglow is the presence of temporal structures not expected in the standard model: plateaus and flares [210], and sudden steep decays, *e.g.*, in GRB 070110 [211]. To show the afterglow of the GRB 070110, I reprint the FIG 2 in [211] as FIG. 4.1. These features are hardly consistent with the standard fireball model, as discussed by [212]; [113].

The origin of sudden drops in afterglow light curves is especially mysterious. As an example, GRB 070110 starts with a normal prompt emission, followed by a normal early decay phase until approximately 100 seconds, and a plateau until $\sim 10^3$ s. At about 2×10^4 s, the light curve of the afterglow of GRB 070110 drops suddenly with a temporal slope $\alpha > 7$ [213]; [214]; [215]; [211]. This abrupt steep decay is inconsistent with the standard fireball model. In essence, it implies that emission from the forward shock (FS) switches off instantaneously (though see [216]; [217]; [218]; [219]; [220]; [221]). It is hard to see how this can happen: the properties of the forward shock are “cumulative”, in a sense that its dynamics depend on the *total* swept-up mass and injected energy, which is impossible to change on a short time scale.

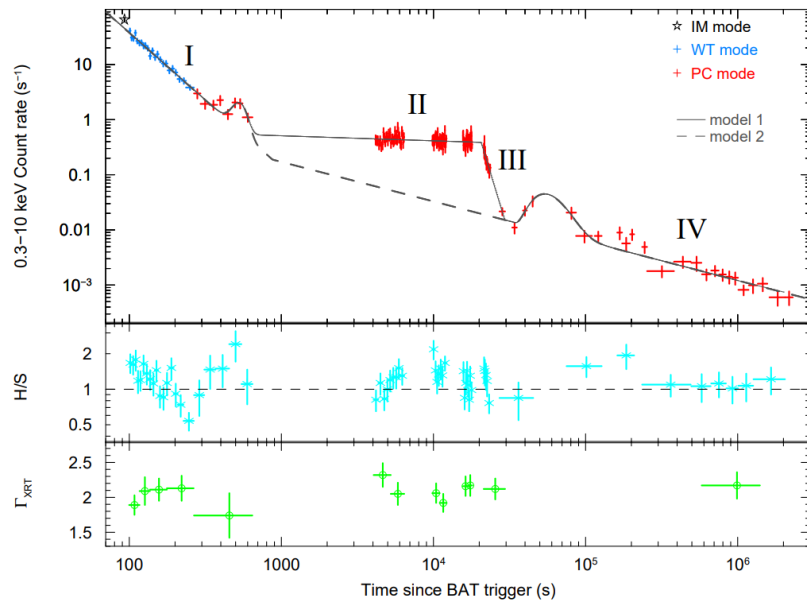


Figure 4.1. The light curve of GRB 070110 in the 0.3-10 keV band. The light curve of GRB 070110 has four stages: (I) an early decay, (II) a plateau followed by (III) a rapid drop and a later flare, then (IV) a final shallow decay. Taken from [211].

In [113] (see also [222]) developed a model of early GRB afterglows with dominant X-ray contribution from the highly magnetized ultra-relativistic reverse shock (RS), an analog of the pulsar termination shock. The critical point is that emission from the RS in highly magnetized pulsar-like wind occurs in the fast cooling regime. Thus it reflects *instantaneous* wind power, not accumulated mass/energy, as in the case of the forward shock. Thus, it is more natural to produce fast variation in the highly magnetized RS.

The model by [113] has several key features. (i) the high energy X-ray and the optical synchrotron emission from the RS particles occur in the fast cooling regime - this ensures efficient conversion of the wind power into radiation and thus can account for rapid variability due to changes in the wind properties.; (ii) plateaus – parts of afterglow light curves that show slowly decreasing spectral power – are a natural consequence of the RS emission. We study these effects in more detail in the present paper.

In this work, we explore a model that most of the early X-ray afterglow emission comes from the RS of a long-living central engine. Variations in the wind luminosity produce fast flares. As the wind is terminated, the radiation from the RS ceases instantaneously. In section 4.2, we build a spectrum evolution model for particles injected into the wind outflow at the termination shock. The radiative loss, the adiabatic expansion, and the effect of duration are included in our model. In section 4.3, we present our result, which clearly shows a plateau following by a steep drop. We also compare our results with different parameter settings (e.g., various Lorentz factors of the post-RS flow, various narrow jet angles, and fast cooling v.s. slow cooling). We also investigate the origination of flare within GRB afterglow in this section. We conclude and discuss our work in section 4.4.

4.2 Emission from relativistic termination shock

4.2.1 Wind dynamics

Following [113], we assume that a powerful pulsar is born in the initial GRB explosion. The pulsar produces highly, magnetized, and highly relativistic wind that shocks against the expanding ejecta. Thus, the system constitutes a relativistic double explosion [222].

Let the central source produce luminosity per solid angle $dL/d\Omega$ that is carried by particles and magnetic field,

$$\begin{aligned} \frac{dL}{d\Omega} &= \left(\rho' + \frac{B'^2}{4\pi}\right)r^2\gamma_{RS}^2 = (1 + \sigma)\rho'r^2\gamma_{RS}^2 \\ \sigma &= \frac{B'^2}{4\pi\rho'} \end{aligned} \quad (4.1)$$

where ρ' is plasma density, B' is the toroidal magnetic field, and γ_{RS} is the Lorentz factor of the post-RS flow; the speed of light was set to unity. In this work, we denote primed variables in the fluid frame.

In a pulsar paradigm, the wind is highly magnetized, $\sigma \gg 1$, and extremely relativistic, $\gamma_w \sim 10^4 - 10^6$ [25]; [223]; [224]. This highly magnetized wind shocks against relativistically expanding ejecta. The emission is produced in the shocked wind. The dynamics of the double relativist explosions are somewhat complicated [222]. The second shock sweeps-up the tail material from the initial explosion. Thus, the dynamics of the second shock depends on the internal structure of the post-first shock flow, and the wind power; all pressure relations are highly complicated by the relativistic and time-of-flight effects. Under certain conditions, the flow is approximately self-similar.

To avoid the mathematical complications, and to demonstrate the essential physical effects most clearly, we assume a simplified dynamics of the second shock, allowing it to propagate with constant velocity. Thus, in the frame of the shock, the decreases linearly with time,

$$B' = B'_0 \frac{t'_0}{t'} \quad (4.2)$$

where time t'_0 and magnetic field is B'_0 are some constants. In the following, we assume that the RS starts to accelerate particles at time t'_0 , and we calculate the emission properties of particles injected at the wind termination shock taking into account radiative and adiabatic losses.

4.2.2 Evolution of the particles' spectrum

As the wind generated by the long-lasting engine starts to interact with the tail part of the flow generated by the initial explosion, the RS forms in the wind, see Fig. 1.3. Let's assume that the RS accelerates particles with a power-law distribution,

$$f(\gamma', t'_i) \propto \gamma'^{-p} \Theta(\gamma' - \gamma'_{\min}) \quad (4.3)$$

where t'_i is the injection time, Θ is the step-function, γ is the Lorentz factor of the particles, and γ'_{\min} is the minimum Lorentz factor of the injected particles. γ'_{\min} can be estimated as [26]

$$\gamma'_{\min} \sim \gamma_w / 2\Gamma_{RS} \sim \gamma_w / \Gamma_{CD} \sim \gamma_w / \gamma_{RS} \quad (4.4)$$

Here, γ_w is the Lorentz factor of the wind, Γ_{RS} is the Lorentz factor of the RS, γ_{RS} is the Lorentz factor of the post-RS flow, Γ_{CD} is the Lorentz factor of the contact discontinuity (CD), and we assume $\sigma \approx 1$.

The accelerated particles produce synchrotron emission in the ever-decreasing magnetic field, while also experiencing adiabatic losses. Synchrotron losses are given by the standard relations (*e.g.*, [225]). To take account of adiabatic losses we note that the conservation of the first adiabatic invariant (constant magnetic flux through the cyclotron orbit) gives

$$\partial_{t'} \ln \gamma' = \frac{1}{2} \partial_{t'} \ln B' \quad (4.5)$$

Using Eqn. (4.2) for the evolution of the field, we find the equation for the evolution of a particles' Lorentz factor

$$\begin{aligned}\frac{d\gamma'}{dt'} &= -\frac{\tilde{C}_1 B_0'^2 \gamma'^2}{t'^2} - \frac{\gamma'}{2t'} \\ \tilde{C}_1 &= \frac{\sigma_T t_0'^2}{6\pi m_e c}\end{aligned}\quad (4.6)$$

where σ_T is the Thomson cross-section.

Solving for the evolution of the particles' energy in the flow frame,

$$\frac{1}{\gamma'} = \frac{2\tilde{C}_1 B_0'^2}{3t'} \left(\left(\frac{t'}{t_i'} \right)^{3/2} - 1 \right) + \frac{1}{\gamma_i'} \sqrt{\frac{t'}{t_i'}}, \quad (4.7)$$

we can derive the evolution of a distribution function (the Green's function) (*e.g.*, [226]; [26])

$$\begin{aligned}G(\gamma', t', t_i') &= \begin{cases} \gamma'^{-p} \left(\frac{t_i'}{t'} \right)^{\frac{p-1}{2}} \left(1 - \frac{2}{3} \tilde{C}_1 B_0'^2 \gamma_w' \sqrt{t'} \left(\frac{1}{t_i'^{3/2}} - \frac{1}{t'^{3/2}} \right) \right)^{p-2}, & \gamma'_{\text{low}} < \gamma' < \gamma'_{\text{up}} \\ 0, & \text{else} \end{cases} \\ \frac{1}{\gamma'_{\text{low}}} &= \frac{2\tilde{C}_1 B_0'^2}{3t'} \left(\left(\frac{t'}{t_i'} \right)^{3/2} - 1 \right) + \frac{1}{\gamma'_{\text{min}}} \sqrt{\frac{t'}{t_i'}} \\ \frac{1}{\gamma'_{\text{up}}} &= \frac{2\tilde{C}_1 B_0'^2}{3t'} \left(\left(\frac{t'}{t_i'} \right)^{3/2} - 1 \right)\end{aligned}\quad (4.8)$$

where γ'_{low} is a lower bound of Lorentz factor due to minimum Lorentz factor at injection and γ'_{up} is an upper bound of Lorentz factor due to cooling.

Once we know the evolution of the distribution function injected at time t_i' , we can use the Green's function to derive the total distribution function by integrating over the injection times

$$N(\gamma', t') \propto \int_{t_i'}^{t'} \dot{n}(t_i') G(\gamma', t', t_i') dt_i' \quad (4.9)$$

where $\dot{n}(t_i')$ is the injection rate (assumed to be constant below).

4.2.3 Observed luminosity

The intensity observed at each moment depends on the intrinsic luminosity, the geometry of the flow, relativistic, and time-of-flight effects (*e.g.*, [227]; [228]; [1]).

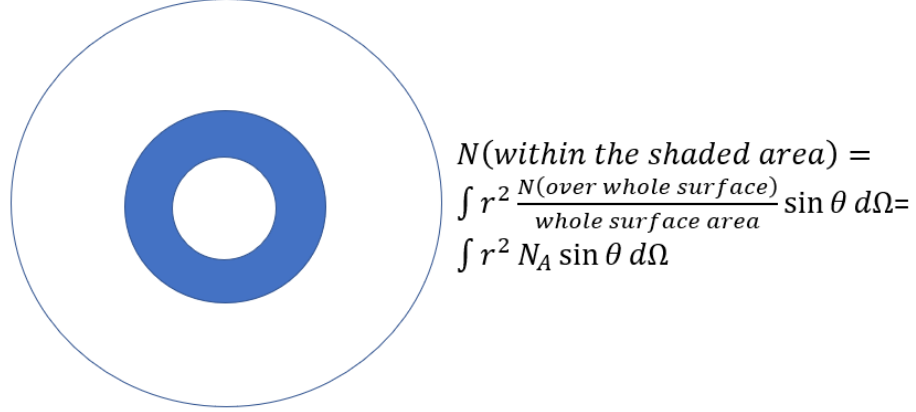


Figure 4.2. The illustration of N_A . We are looking for the number of particles with the angle from θ to $\theta + \delta\theta$. N_A is the number of particles within a unit surface element.

The intrinsic emissivity at time t' depends on the distribution function N and synchrotron power P_ω :

$$L'(\omega', t') = \int \int N_A(\gamma', t') P_\omega(\omega') d\gamma' dA' \quad (4.10)$$

where N_A , the number of particles per unit area, is defined as $N_A = N/A = N/(2\pi r'^2(1 - \cos \theta_j))$ (see Fig. 4.2), $P(\omega')$ is the power per unit frequency emitted by each electron, and dA' is the surface differential.

We assume that the observer is located on the symmetry axis and that the active part of the RS occupies angle θ_j to the line of sight, see Fig. 4.3). The emitted power is then

$$L'(\omega', t') = \int_0^{\theta_j} \int_{\gamma'_{\min}}^{\infty} N_A(\gamma', t') P(\omega') d\gamma' 2\pi r'^2 \sin(\theta) d\theta \quad (4.11)$$

Photons seen by a distant observer at times t are emitted at different radii and angles θ . To take account of the time of flight effects, we note that the distance between the initial explosion point and an emission point (r', θ) is $r' = vt' = vT_{ob}(1 - \beta \cos(\theta))^{-1} \gamma_{RS}^{-1}$, where T_{ob} is the observed time. Supposed that a photon was emitted from the distance r' and angle $\theta = 0$ at time t' , and at the same time, the other photon was emitted from the distance r' and any arbitrary angle $\theta = \theta_i < \theta_j$, see FIG

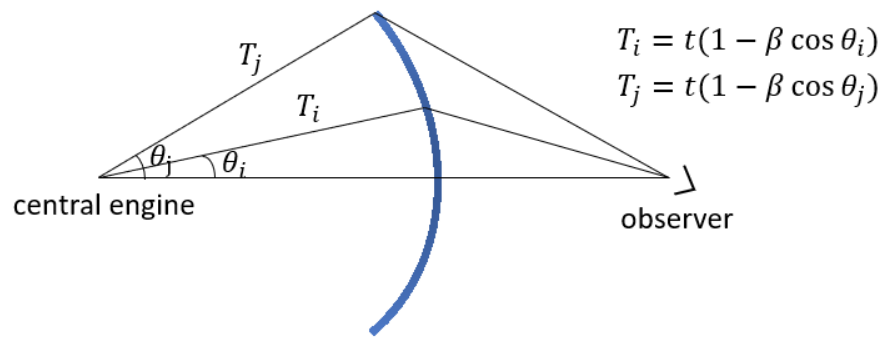


Figure 4.3. Illustration of the jet opening angle θ_j . The emission is produced only within the opening angle θ_j . θ_i corresponds to an arbitrary place within the opening angle θ_j . If the central engine produces an explosion, we would expect the emission from a jet front surface occurs at the same time t in the lab frame. However, in the observed frame, the emission in the jet front surface occurs at a different time (the emission at the emission angle θ_i will occur at T_i , but the emission at the emission angle θ_j will occur at T_j). We assume that the observer is looking along the symmetric axis of the jet.

4.3. These two photons will be observed at time T_0 and T_{θ_i} , then the relation between T_0 and T_{θ_i} is given by:

$$r' = vt' = \frac{vT_0}{(1 - \beta)\gamma_{RS}} = \frac{vT_{\theta_i}}{(1 - \beta \cos(\theta_i))\gamma_{RS}} \quad (4.12)$$

where, the time t' measured in the fluid frame, and the corresponding observe time T_{ob} , is a function of θ and t' :

$$T_{ob} = t(1 - \beta \cos \theta) = t'(1 - \beta \cos \theta) \gamma_{RS} \quad (4.13)$$

The relation above can be derived from the model shown in Fig. 4.4. In the lab frame, the first light emitted from the central point and observed at time D/c . At the time t , the ejected particle moves to the location of the radius $r = r_{em} = vt$ and the angle θ . At the same time, a photon is emitted. The time of traveling between the location of the emission and the observer is

$$\Delta t = \frac{\sqrt{(D - r_{em} \cos \theta)^2 + (r_{em} \sin \theta)^2}}{c} \quad (4.14)$$

The observed time is the difference between the observation of the first light and the light emitted at time t , which can be written as

$$T_{ob} = t + \Delta t - D/c = t + \frac{\sqrt{(D - r_{em} \cos \theta)^2 + (r_{em} \sin \theta)^2}}{c} - D/c = t(1 - \beta \cos \theta) \quad (4.15)$$

under the assumption of $r_{em} \ll D$.

Thus the derivative on both sides of Eqn. (4.13) gives

$$\sin(\theta)d\theta = -\frac{T_{ob}}{t'^2\beta\gamma_{RS}}dt' \approx -\frac{T_{ob}}{t'^2\gamma_{RS}}dt' \quad (4.16)$$

Substitute the relation (4.16) in to the equation (4.11), the luminosity function can be described as

$$L'(T_{ob}, \omega') \approx \int_{t'_{\theta'=0}}^{t'_{\theta'=\theta_j}} \int_{\gamma'_{\min}}^{\infty} \frac{-2\pi c^2 T_{ob}}{\gamma_{RS}} \times N_A(\gamma', t') P(\omega') d\gamma' dt' \quad (4.17)$$

Here, the minus sign comes from the Eqn. (4.16).

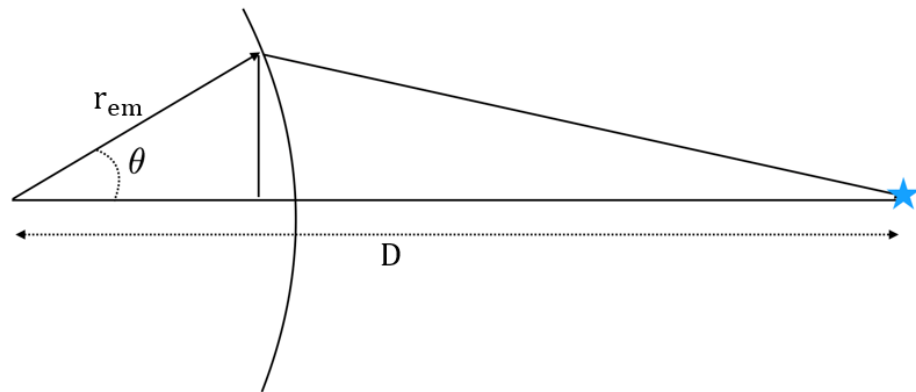


Figure 4.4. The calculation of the relation 4.13. The first light emitted from the central point $r=0$, which observed at the observed time 0. At the time t , a photon emitted from the location $r = r_{em}$ and angle θ , which observed at T_{ob} . The distance between the central point and the observer is assumed to be D .

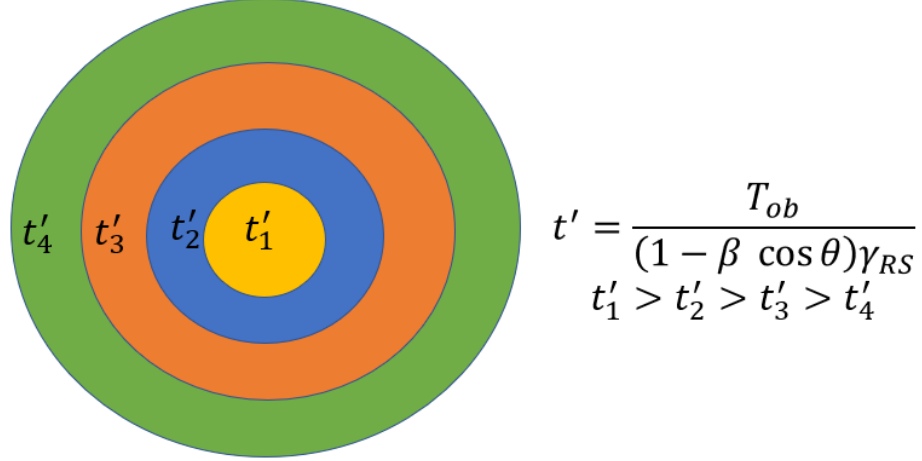


Figure 4.5. The illustration of the model. For the photons observed at T_{ob} , they are emitted at different times t' in the fluid frame and different angles θ .

To understand the Eqn. 4.17, the radiation observed at T_{ob} corresponds to the emission angle from 0 to θ_j , which also corresponds to the emission time $t'_{\theta'=0} = \frac{T_{ob}}{(1-\beta)\gamma_{RS}}$ to $t'_{\theta'=\theta_j} = \frac{T_{ob}}{(1-\beta \cos \theta_j)\gamma_{RS}}$. So we need to integrate the emissivity function over the range of the emission angle, or integrate the emissivity function over the range of the emission time from $t'_{\theta'=0} = \frac{T_{ob}}{(1-\beta)\gamma_{RS}}$ to $t'_{\theta'=\theta_j} = \frac{T_{ob}}{(1-\beta \cos \theta_j)\gamma_{RS}}$. The illustrations of the model are showed as Fig. 4.5 and Fig. 4.6.

Finally, taking into account Doppler effects (Doppler shift $\omega = \delta\omega'$ and the intensity boost $I_\omega(\omega) = \delta^3 I'_{\omega'}(\omega')$; where δ is the Doppler factor $\delta = 1/(\gamma_{RS}(1 - \beta \cos \theta))$), substitute the relation $t' = T_{ob}/(1 - \beta \cos(\theta))\gamma_{RS}$ into Eqn.(4.17) we finally arrive at the equation for the observed intensity:

$$F = \frac{L}{4\pi D^2} \approx \int_{\frac{T_{ob}}{(1-\beta \cos(\theta_j))\gamma_{RS}}}^{\frac{T_{ob}}{(1-\beta)\gamma_{RS}}} \int_{\gamma'_{\min}}^{\infty} \frac{1}{2\gamma_{RS}} c^2 D^{-2} T_{ob} \delta^3 N_A P(\omega/\delta) d\gamma' dt' \quad (4.18)$$

where D is the distance, I is the specific intensity.

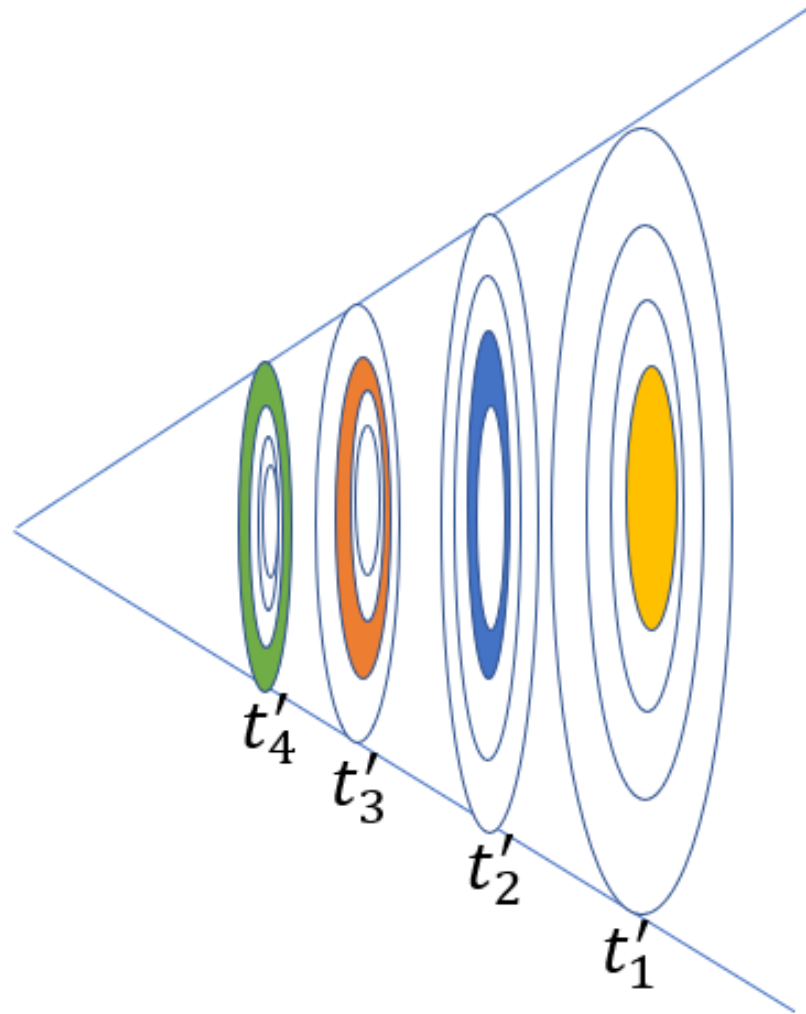


Figure 4.6. The illustration of the model. For the photon observed at T_{ob} , they are not emitted from a spherical shell. The distance from the central point (i.e., the time in fluid frame) and the angle respect to the line of sight are related via equation $T_{ob} = t(1 - \beta \cos \theta) = t'(1 - \beta \cos \theta) \gamma_{RS}$

4.3 Results

In the following we apply the general relations derived above to three specific problem: (i) origin of plateaus in afterglow light curves, §4.3.1; (ii) sudden drops in the afterglow light curves, §4.3.1, and (iii) afterglow flares, §4.3.2. For numerical estimates, we assume the redshift $z = 1$, the Lorentz factor of the wind $\gamma_w = 5 \times 10^5$, the wind luminosity $L_w = 10^{46}$ erg/s, the initial injection time $t'_0 = 10^5$ s (in jet frame), the power law index of particle distribution $p = 2.2$, and $\Gamma_{CD} \approx \gamma_{RS}$ for all calculations.

4.3.1 Plateaus and sudden intensity drops in afterglow light curves

RS particles occur in the fast cooling regime, and the resulting synchrotron luminosity L_s is approximately proportional to the wind luminosity L_w . Thus the constant wind will produce a nearly constant light curve. In other words, the plateaus are natural consequences in our model in the case of a constant long-lasting wind. FIG. 4.8 shows the light curve at 100 KeV for different Lorentz factors of the post-RS flow (more detail about parameters setting in FIG. 4.8 will be discussed later). At the early phase, all light curves experience a nearly constant evolution with time, which show the feature of plateau as we expected.

Assume the central engine suddenly stops operating. This process could be due to the collapse of a neutron star into a black hole or sudden depletion of an accretion disk. At a later time, when the “tail” of the wind reaches the termination shock, acceleration stops. Let the injection terminate at a some time t'_{stop} . The distribution functions in the shocked part of the wind then become

$$N(\gamma', t') \propto \int_{t'_0}^{\min(t', t'_{\text{stop}})} G(\gamma', t', t'_i) dt'_i \quad (4.19)$$

In FIG. 4.7, we showed the evolution of the distribution function by assuming the opening angle $\theta_j = 1/\gamma_{RS}$, $\gamma_{RS} = 90$, and the injection is stopped at time $t'_{\text{stop}} = 1.5 \times 10^5$ s (in this case, the $T_{\text{ob,stop}} = 833$ s in the observer’s frame). As we can see that

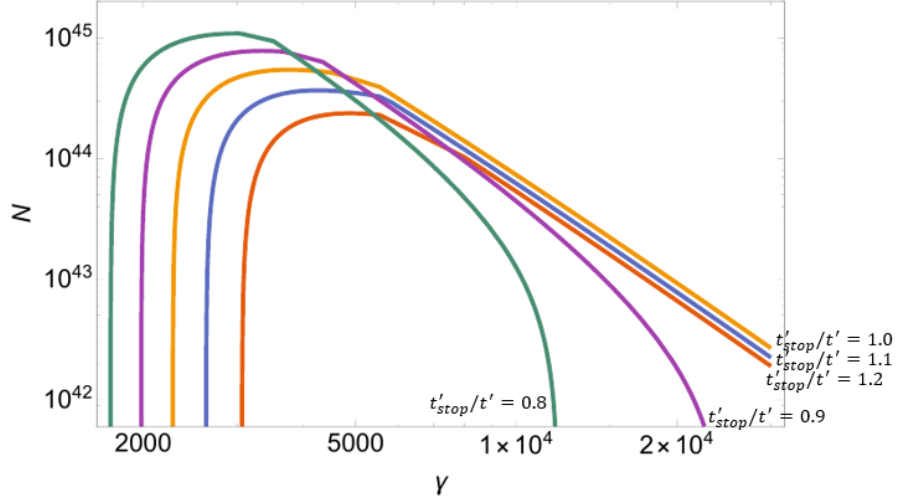


Figure 4.7. Evolution of the distribution function. Here we take account the effect of radiation loss and adiabatic expansion. In our calculation, the opening angle $\theta_j = 1/\gamma_{RS}$, $\gamma_{RS} = 90$, and the injection is stopped at time $t'_{\text{stop}} = 1.5 \times 10^5$ s, $\gamma_{\text{min}} = \gamma_w/\gamma_{RS} = 5556$, initial magnetic field $B_0 = 2.1$ G. The times are measured in fluid frame at $t'_{\text{stop}}/t' = 1.2, 1.1, 1.0, 0.9, 0.8$ from red to green curves.

the number of high energy particles dropped sharply right after we stop the injection, and this is because particles lose their energy via synchrotron radiation and adiabatic expansion in fast cooling regime.

Assume the emission at $\theta = 0$ start decay at time $T_{\text{ob}0}$, and $\theta = \theta_j$ start decay at time $T_{\text{ob}j}$. Now we could estimate the relation between $T_{\text{ob}0}$ and $T_{\text{ob}j}$ by considering Eqn. (4.12):

$$\frac{T_{\text{ob}j}}{T_{\text{ob}0}} = \frac{1 - \beta \cos(\theta_j)}{1 - \beta} \approx 2 \quad (4.20)$$

where we assume β is close to 1, and once again, we assume the opening angle θ_j is $1/\gamma_{RS}$ for the estimation of Eqn. 4.20.

In FIG. 4.8, we assume the opening angle $\theta_j = 1/\gamma_{RS}$, and combine the effect of duration and the effect of stopped injection together, and we use Eqn. (4.17) to calculate the light curve at 100 KeV for three different Lorentz factors of the post-RS flow γ_{RS} : $\gamma_{RS} = 30$, $\gamma_{RS} = 60$, and $\gamma_{RS} = 90$.

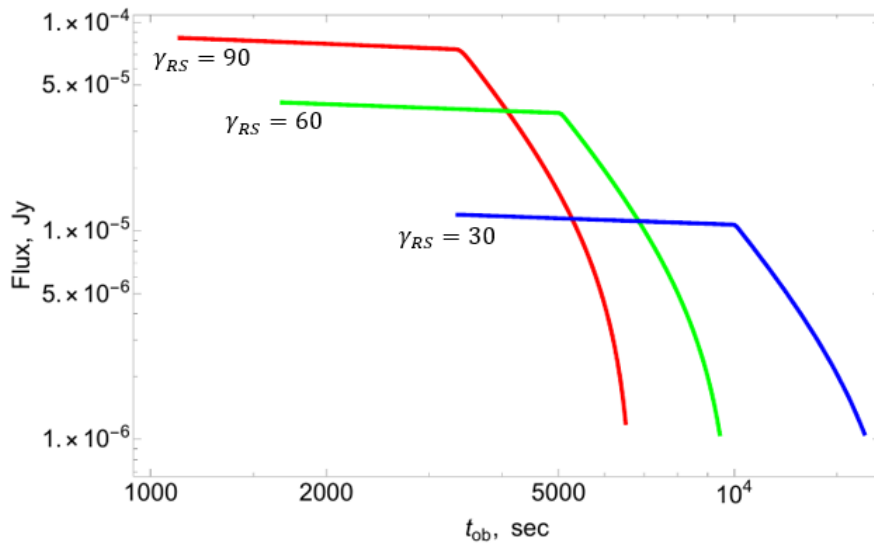


Figure 4.8. The light curve at 100 KeV for different Lorentz factors of the post-RS flow. We assume that the observer is looking along the symmetric axis of the jet. The injection is stopped at a fixed time in the fluid frame, corresponding to $t'_0 = 6 \times 10^5$ s. There is a sudden drop of intensity when the injection is stopped ($T_{\text{ob}} = 10000$ s for blue curve, $T_{\text{ob}} = 5000$ s for green curve, and $T_{\text{ob}} = 3333$ s for red curve). (These cases all correspond to 6×10^5 s in fluid frame). Blue curve has $\gamma_{RS} = 30$, $\gamma_{\text{min}} = \gamma_w/\gamma_{RS} = 16667$, initial magnetic field $B_0 = 6.4$ G; green curve has $\gamma_{RS} = 60$, $\gamma_{\text{min}} = \gamma_w/\gamma_{RS} = 8333$, initial magnetic field $B_0 = 3.2$ G; red curve has $\gamma_{RS} = 90$, $\gamma_{\text{min}} = \gamma_w/\gamma_{RS} = 5556$, initial magnetic field $B_0 = 2.1$ G. Here we assume $B_0 \propto \gamma_{RS}^{-1}$ for our calculations.

From the numerical result, we do see a very flat plateau before we stop the injection and a following sudden steep decay right after we stop the injection, which is consistent with observational results. Next, we investigated how the jet angle (the effect of duration) affects our result and what the result would be different in the slow cooling regime.

In Fig. 4.9, we compare the light curves of variate opening angles. More specifically, we keep all parameters is the same as Fig. 4.8 but use a jet angle of $\theta_j = 1/2\gamma_{RS}$ instead of $\theta_j = 1/\gamma_{RS}$, to explore the effect of duration (or opening angle). As we can see, all dash curves ($\theta_j = 1/2\gamma_{RS}$) are much sharper than their corresponding solid curves ($\theta_j = 1/\gamma_{RS}$). Thus, the narrower angle produces the steeper drop.

In Fig 4.10, we compare the light curves of fast cooling and slowing cooling. The regime of fast cooling is defined as the typical synchrotron frequency of the accelerated electrons with the minimum Lorentz factor ν_m is larger than the cooling frequency ν_c . The regime of slow cooling is defined as the typical synchrotron frequency of the accelerated electrons with the minimum Lorentz factor ν_m is less than the cooling frequency ν_c [110]. We keep all parameters the same as Fig. 4.8 but reduce the magnitude of the initial magnetic field so the emission is in the slow cooling regime, to explore the effect of cooling time. As we can see, all dashed curves (slow cooling) are flatter than their corresponding solid curves (fast cooling). Thus, the steep drop, which results from the terminated wind, will be smoothed in the slow cooling regime.

4.3.2 Afterglow flares

We do see flares in GRB from observational data. In the frame of the FS model, the synchrotron emission is proportional to the integrated total energy within the outflow, thus it requires the total energy is in the geometrical progression for many flares. In our points of view, the flare is produced from the RS due to sudden increased ejected power.

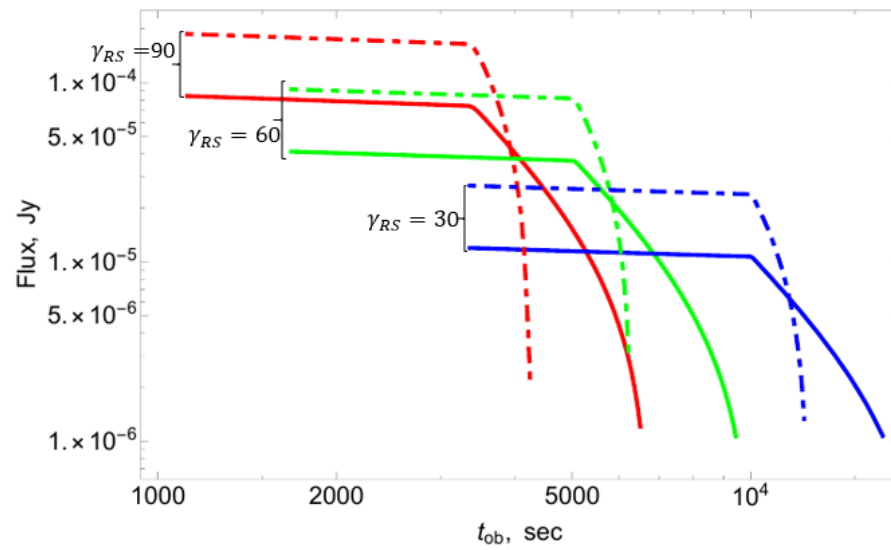


Figure 4.9. The comparison of light curves for different jet angles $1/\gamma_{RS}$ (solid lines) and $1/2\gamma_{RS}$ (dotted-dash lines). Different lines correspond to parameters in Fig. 4.8 except the jet angle. We assume the viewing angle is 0. Smaller jet angle produce sharper drop.

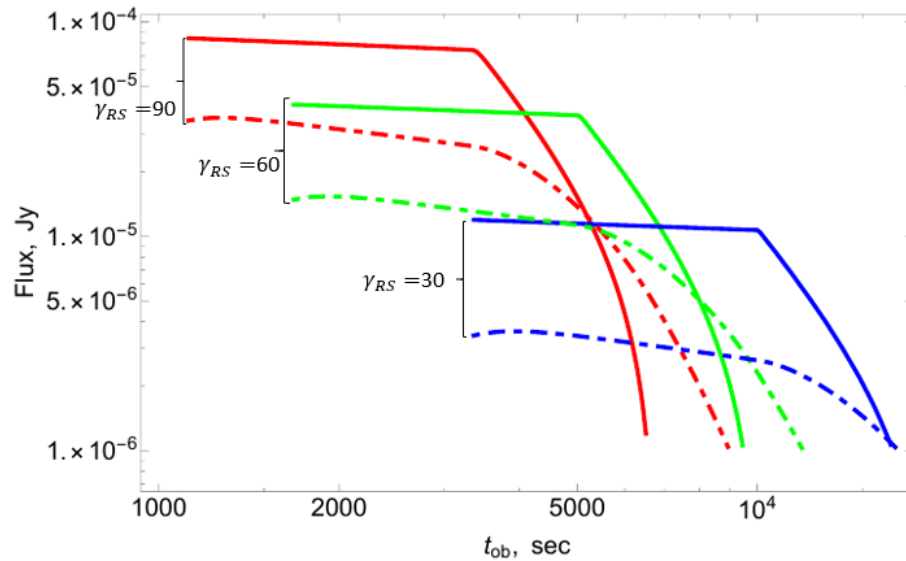


Figure 4.10. The comparison of light curves for slow cooling and fast cooling, where solid lines correspond to fast cooling and dotted-dash line correspond to slow cooling. All other parameters are the same as Fig.4.8 except the initial magnetic field, where slow cooling has a weak magnetic field but fast cooling has a strong magnetic field. Fast cooling curves are brighter than slow cooling since radiation power is proportional to B^2 . More importantly, slow cooling curves are smoother than fast cooling curves, so FS, where most likely have slow cooling, may not be able to produce a steep drop behavior.

In order to examine our idea, we re-consider the case of $\gamma_{RS} = 60$ (the green curve in FIG. 4.8). Recall that the green curve in Fig. 4.8 has initial injection time $t_0 = 10^5$ s and stop time $t_{\text{stop}} = 6 \times 10^5$ s. We keep all parameter as same as the blue curve in FIG. 4.8 but set the ejected power are two, four, and eight times larger than the normal magnitude of the ejected power for a short period of time from 2.4×10^5 s to 2.5×10^5 s. The corresponding light curves are calculated in Fig. 4.11.

In FIG. 4.11, there is a sharp rise around $T_{ob} = 2000$ s (which corresponds to the starting time of the increased ejected power $t = 2.4 \times 10^5$ s at emission angle $\theta = 0$) due to a sudden increased ejected power, and a sharp drop around $T_{ob} = 4000$ s (which corresponds to the ending time of the increased ejected power $t = 2.5 \times 10^5$ s at emission angle $\theta = \theta_j$) because the ejected power back to normal level. In our calculation, the cases of peak power increased two, four and eight times larger are considered, and the corresponding total injected energy is 1.0167, 1.05, 1.1167 times larger. The magnitude of the rise in flux is less than the magnitude of the rise in ejected power (e.g. the rise in ejected power by a factor eight only gives the rise in flux by a factor two), because of the effect of duration, in other words, the emission from the increased ejected power from a different angle cannot be observed simultaneously (e.g. in the observe frame, when the emission at emission angle $\theta = 0$ is increased to eight times larger, the emission at emission angle $\theta = \theta_j$ is still at a normal level).

4.4 Discussion

In this paper, we argue that the observed steep drop within GRBs is generally consistent with the synchrotron emission coming from particles accelerated behind an RS propagating in a long-lasting ultra-high relativistic wind. The key point is that the RS can react quickly to the changes of the wind properties, and the injection is stopped at a specific time t'_{stop} . After we stop the injection, the distribution function shows that fewer and fewer particles could survive at high energy. We could roughly treat the emission from the single-particle as a Dirac-delta function with a peak at

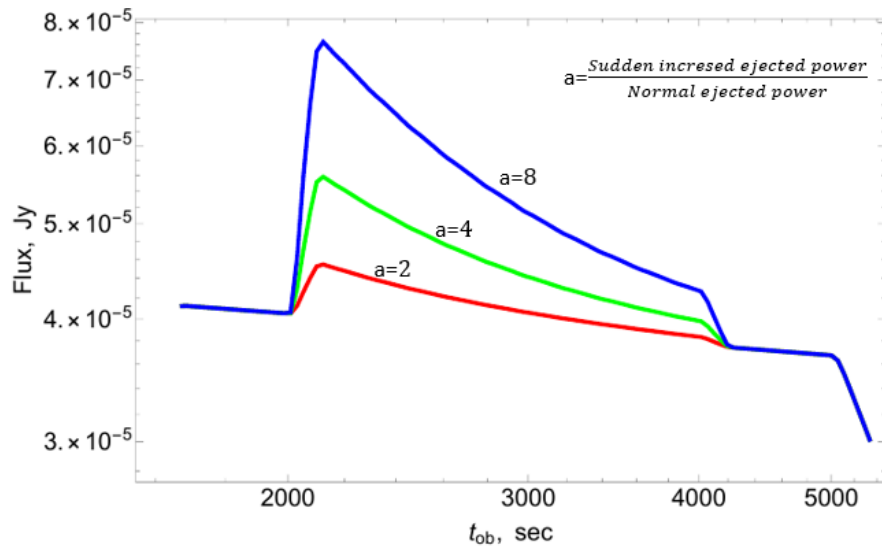


Figure 4.11. Producing the flares. All parameters are same as the green curve in the FIG.4.8, but we set the ejected power are two (the red curve), four (the green curve) and eight (the blue curve) times larger for a short period from 2.4×10^5 s to 2.5×10^5 s. Recall that initial injection time $t_0 = 10^5$ s and break time $t_{\text{stop}} = 6 \times 10^5$ s.

$\omega = 3\omega_B\gamma^2\delta/2$ or $\omega \propto \gamma^2$ (i.e., the high flux at high energy requires a large number of particles with large Lorentz factor γ). Since the number of particles drops suddenly for the particles with large γ value in the distribution function, we would not be surprised that the light curve also drops suddenly at high energy.

One may argue that we can ignore the effect of duration. To answer this question, we did calculation without the effect of duration (in our case, we calculated the emission from a narrow-angle $1/2\gamma_{RS}$), and we found out that the drop is extremely sharp without the effect of duration. See Fig. 4.9. From our point of view, the emission from the off-axis part will be observed later than the emission from the on-axis part, so the effect of stopped injection will change the on-axis emission first and the off-axis emission later, which could flatten the extremely sharp decay.

In most of our calculations, we assume the opening angle $\theta = \gamma_{RS}^{-1}$. However we may also consider other cases. For $\theta > \gamma_{RS}^{-1}$, we can barely see the emission within the angle γ_{RS}^{-1} due to Doppler boosting, so there is no huge difference with our model. For $\theta < \gamma_{RS}^{-1}$, the effect of duration has less impact on the observed emission, so the drop stage has a shorter time and sharper spectral shape than our model. See Fig. 4.9.

We also consider the case of slow cooling (e.g., in FS). By manipulating the magnitude of the magnetic field, we calculated the emission for the case where cooling time is larger than wind lifetime (i.e., slow cooling). In a slow cooling regime, the particle with large Lorentz factor γ can keep their dynamic energy for a long time because of low cooling loss, and thus we would expect there are still many particles carrying large Lorentz factor γ at a later time, even though the wind has been terminated. The result shows that slow cooling gives a much flatter curve than fast cooling. Thus the steep drop requires a fast cooling in RS.

Finally, in our model, the afterglow flares are corresponding to the variation of pulsar winds. In the fast cooling regime, these variations can be reflected in the emission immediately. So a short period of increased wind power can produce a short period of increased observed flux (i.e., a flare).

Our model might provide explanations to many other problems in GRBs. For example, if the explosion does not produce a long-lasting wind, then there will be no X-ray afterglow since RS reflects the properties of wind (naked GRBs problem) [229]. We might also apply our model to missing orphan afterglow problem, which states that we might see afterglow in X-ray and optical without seeing any prompt emission since prompt emission is collimated from RS and afterglow will be spread out later due to FS deceleration [230]. Unfortunately, we have not seen any this type of event solidly [231]; [232]. In our model, both prompt emission and afterglow emission are from RS, so they have similar collimation property.

5. PREDICTION OF THE SECOND PEAK IN THE AFTERGLOW OF GW170817

5.1 Introduction

On 14 September 2015, two experiment groups Laser Interferometer Gravitational-Wave Observatory (LIGO) and Virgo interferometer (Virgo) made the first observation of gravitational wave (GW) [233]. The gravitational wave was produced by two black holes with mass of 29 and 36 solar masses merging together. The mass of new merged black hole was 62 solar masses, and about 3 solar masses was emitted as gravitational wave.

On 2017 August 17, LIGO and Virgo detector discover the gravitational-wave (GW) transient GW170817 [234], which was consistent with the coalescence of a binary neutron star system, see Fig.1 in [235]. The time variation at the three detectors (LIGO-Hanford detector, LIGO-Livingston detector, and Virgo detector) allowed us to determine the direction of the source. Unlike the previous two black hole merger events, GW 170817 allow us to detect its electromagnetic counterpart. Two seconds later, GRB 170817A was registered by GBM/*Fermi* [95] and SPI-ACS/INTEGRAL [236] experiments. The discovery of GRB 170817 is also consistent with the classical scenario that short GRB are produced from neutron star mergers. The jet of GRB 170817 is about 30 degree to the line of sight due to its faint flux. The optical counterpart was detected by a large number of ground-based facilities [234].

GRB/GW170817 was unusual in many respects. The prompt gamma-ray emission consisted of two distinctive components - a hard short pulse delayed by ~ 2 seconds with respect to the LIGO signal followed by a weaker, softer thermal pulse with $T \sim 10$ keV lasting for another ~ 2 seconds, (see Fig. 1 in [237]). The appearance of a thermal component at the end of the burst is unusual for short GBRs. Both the hard

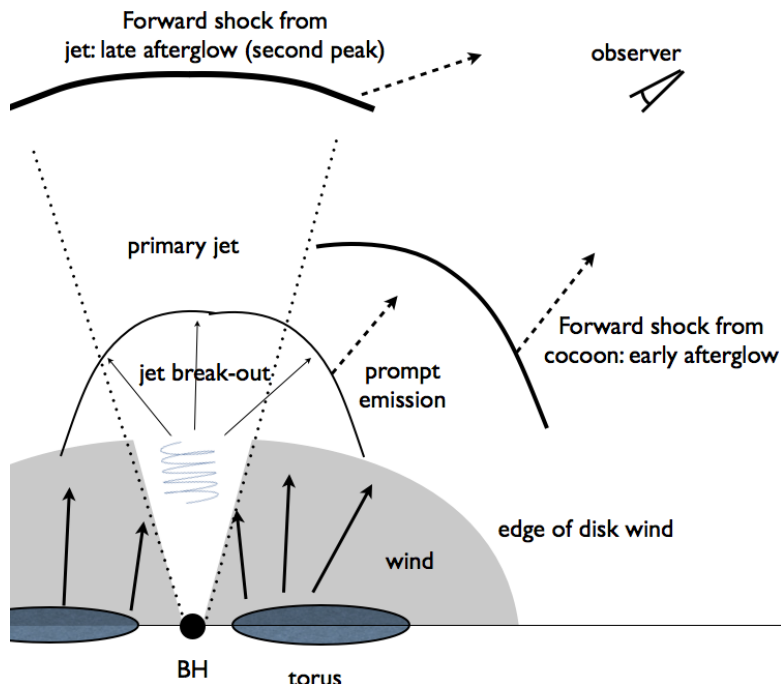


Figure 5.1. Cartoon of the model. Hot torus (left from the disrupted neutron stars) creates a dense, mildly relativistic wind (shaded region). After ~ 1 second, when enough magnetic flux is accumulated on the BH, the BH launches a Blandford-Znajek-powered jet. After the jet reaches the edge of the confining wind its head part experiences a break-out, creating a nearly spherical outflow; this generates the prompt emission. Later on, the interaction of this now nearly-spherically expanding part of the jet with the surrounding medium generates the forward shock - this leads to the production of early the early afterglow that has been observed so far. Most of the jet accelerates to high Lorentz factors; the radiation from the corresponding forward shock is beamed away from the observer. Only after the jet-driven forward shock decelerated it will become visible, and should generate the late bump in the afterglow.

and the soft components do not satisfy the Amati relation, making GRB 170817A distinctively different from other short GRBs [237]; [238].

5.2 Model

The detection of the EM signal contemporaneous with gravitational waves is consistent with the binary NS scenario for short GRB [239]; [66]; [72]; [240]; [241]. Currently, there are several competing models for the prompt and afterglow emission from GW170817: (i) radially stratified quasi-spherical ejecta (i.e. cocoon) traveling at mildly relativistic speeds (e.g., [242]; [243]; [244]); (ii) emission from off-axis collimated ejecta characterized by a narrow cone of ultra-relativistic material with slower wings extending to larger angles (i.e. structured jet) (e.g., [245]; [246]; [247]; [248]; [249]; [250]; [251]; [252]). In the structured jet scenario, the GW 170817 merger powered a normal SGRB directed away from the line of sight; (iii) fast jet – cocoon model - we describe it next in more detail.

The key points of the fast jet – cocoon model is described in [237]; also see Fig 5.1. An active stage of a merger lasts $\sim 10 - 100$ milliseconds after which the neutron stars collapse into BH. During the merger an accretion torus of $\sim 0.1M_{\odot}$ forms around the BH with a viscous time $t_d \sim 0.1$ s *e.g.* [253]; [254]. At the same time, magnetic fields are amplified within the disk to $\sim 10^{15}$ G [255]; [256]; [253] due to the development of MRI and the presence of the velocity shear. Qualitatively, as the matter is accreted onto the BH, the BH accumulates magnetic flux which was generated in the accretion disc due to dynamo process [257]; [258]; [259]; [260]. The magnetic field doubling time can be estimated as $t_{B \text{ double}} \approx t_d$ [258], so it takes about 10 doubling times for the magnetic field to grow from 10^{12} G to 10^{15} G, which is close to 1 s, a similar growth time $\sim 5 \times 10^3 GM_{\text{BH}}/c^2$ was achieved in 3D GRMHD simulations [260]. At the same time baryons slide off into the BH along magnetic field lines, leaving polar regions with low density. This creates conditions favorable for the operation of the Blandford-Znajek (BZ) mechanism [261]. As a result, the accumulation of the magnetic flux leads to a delay for the jet to switch-on. The BZ jet then propagates through a pre-existing dense wind with mildly relativistic velocity [237]; [238]. As it breaks out from the wind, it generates a nearly isotropic cocoon, Fig. 5.1. The wind

emission shocked by the breaking-out jet produces the soft tail. After the break-out the primary jet accelerates and becomes invisible to the observer. The inclination of the binary system come directly from the GWs signal $\theta_{\text{obs}} \approx 30^\circ \pm 10^\circ$ [234]; [262].

Observationally, Chandra and VLA [263]; [246]; [249]; [264]; [265] show that GRB/GW 170817 was steadily brightening with time, and has now reached its peak and starts to decay. The very simple power-law spectrum was extending for eight orders of magnitude in frequency. The measurement of the power law index $p = 2.17$ indicates that radiation should come from ejecta with $\Gamma \sim 3 - 10$.

We interpret these observations as non-thermal synchrotron emission coming from the “break-out” (nearly spherical) part of the mildly relativistic forward shock. But observations up to $t \leq 250$ days have not been able to distinguish the above scenarios, because of the observed emission will be dominated by radiation from mildly relativistic material [249] present in all the models.

Most importantly, at later times, *the models predict qualitatively different behavior*. Both the cocoon and structured jet models should produce only one bump in X-ray light curve by the jet or the cocoon. On the other hand, the fast jet – cocoon model [237] has two active components - a cocoon formed during jet breakout and an ultra-relativistic jet. The initial rise of x -ray light curve (see red dots Figure 5.4) is formed by a cocoon - a shock break-out. As we discuss in this chapter, later on (a few years after GW event) the fast jet – cocoon model predicts rebrightening of the afterglow as the primary jet slows down and becomes visible (see Fig. 5.1). The detection of second X-ray or radio bump will be a smoking gun for fast jet – cocoon model and rule out one component models. Calculations of the properties of the predicted second afterglow bump is the key point of the chapter.

5.3 Results

In this work we perform three types of calculations of the predicted second peak: (i) using analytical estimates from [266]; [267], §5.3.2 ; (ii) model light curves from the

Afterglow library [268], §5.3.3; (iii) in-house numerical calculations of the synchrotron emissivity of the relativistically expanding and synchrotron cooling plasma, §5.3.4.

5.3.1 The fiducial parameters

The accretion torus/disc after the NS-NS merger can be relatively massive $\sim 0.1M_{\odot}$ *e.g.* [254]. The disc produces a dense mildly relativistic wind with mass $\sim 0.05M_{\odot}$ [269]; [270] and also supplies the central BH with magnetic flux needed to launch the BZ jet. The accretion rate on BH horizon can be estimated as, see more details in [237]

$$\dot{M}_{\text{BH}} \approx 0.002 \frac{M_{d,-1}}{t^{5/3}} M_{\odot}/\text{s} . \quad (5.1)$$

Here $M_d = 0.1M_{d,-1}M_{\odot}$ is mass of the disc in solar mass units and time is in seconds. The BZ jet power can be [261]; [271]; [272] as high as

$$L_{\text{BZ}} \approx 5 \times 10^{50} \frac{M_{d,-1}}{t_{0.3}^{5/3}} \text{ erg/s} , \quad (5.2)$$

here we assume efficiency of BZ jet formation $C(a_{\text{BH}}) \approx a_{\text{BH}}^{2.4}$ with BH spin parameter $a_{\text{BH}} = 0.7$ [253]; [273]; [274]; [237].

The opening angle of the jet is unknown. The second bump can be detected if jet is relatively narrow and powerful. Following [237] the opening angle of the jet can be assumed $\theta_j = 0.1 \approx 5^\circ$, so the isotropic jet power can be as high as

$$E_{\text{iso,max}} \approx \frac{2}{\theta_j^2} \int_{t=2}^{\infty} L_{\text{BZ}} dt \approx 10^{53} \text{ ergs} . \quad (5.3)$$

This is the estimate of the primary jet energy that we will use in the calculations.

Initially, the primary jet emission is beamed away from the observer. As the jet-driven blast wave slows down it becomes visible. In the following, we perform calculations to address the question: What are the conditions required to produce an observable second afterglow bump from the primary jet.

5.3.2 Analytic estimates for detectability of the second peak

Let us first obtain simple analytic constraints on parameters in order for the second peak associated with the afterglow of the jet to be detectable. We consider the second peak to be detectable if the following 3 criteria are satisfied. 1) The time of the second peak (t_{peak}) must be greater than the time of current observations (~ 250 d), otherwise this peak would have been already detected or can be weaker than the cocoon component, in which case the second peak will not be detectable. 2) The peak flux must be greater than the sensitivity limit of the detector (for radio at 6 GHz we use a limit of $10 \mu\text{Jy}$). 3) The value of the peak flux must be larger than that of the cocoon at the time of the peak. To estimate the flux from the cocoon component at a late time, we use a power law extrapolation of current observations. These criteria are depicted in the top panel of Fig. 5.2 where the numbered arrows show the regions where the corresponding criteria mentioned above are satisfied. In this figure we use the radio data at 6GHz as an example, the dashed vertical line marks a time of 250 days, the dot-dashed horizontal line marks a detectability limit of $10 \mu\text{Jy}$, and the solid line shows the extrapolation of the decline in the observed emission assuming it is $\propto t^{-2}$ as estimated in [265]. Below we always assume the observing frequency $\nu_m < \nu < \nu_c$ and $(1+z) \approx 1$ which is valid for GW170817.

The peak in the afterglow occurs as the beaming angle of the emission from the core of the jet increases and reaches the line of sight of the observer ($1/\Gamma \sim \theta_{\text{obs}}$). This peak occurs at a time *e.g.* [267]

$$t_{\text{peak}} \approx 280 \left(\frac{E_{\text{iso},52}}{n_{-4}} \right)^{\frac{1}{3}} \left(\frac{\theta_{\text{obs}}}{25^\circ} \right)^{\frac{8}{3}} \text{ days.} \quad (5.4)$$

Criterion 1) requires $t_{\text{peak}} \gtrsim 250d$, using the above equation and assuming $\theta_{\text{obs}} = 25^\circ$, we get $E_{\text{iso},52} \gtrsim 0.8 n_{-4}$. This inequality is satisfied by all the regions above the dashed black line in the bottom panel of Fig. 5.2 which shows E_{iso} vs n .

The peak flux of the afterglow can be obtained by substituting t_{peak} in analytic expressions for the flux for post jet break light curves *e.g.* [266]; [267]

$$F_{\text{peak}} \approx C(p) (1 - \cos\theta_j)^{\frac{p+3}{3}} \times D_{\text{L},26}^{-2} \epsilon_{\text{e},-1}^{p-1} \epsilon_{\text{B},-2}^{\frac{p+1}{4}} n^{\frac{1+p}{4}} \theta_{\text{obs}}^{-\frac{8p}{3}} E_{\text{iso},52} \nu_{9.7}^{\frac{1-p}{2}} \text{ mJy}, \quad (5.5)$$

Where θ_{obs} is in degrees and

$$C(p) \approx 7440(p - 0.04) \left(\frac{p - 2}{p - 1} \right)^{p-1} \left(1.13 \times 10^{-20} \right)^{-p} 10^{-14.96p}$$

These analytic estimates agree within a factor ~ 1.5 when compared to the light curves shown in Fig. 5.4. Criterion 2 requires F_{peak} to be larger than the detector sensitivity, in the case of radio we use $F_{\text{peak}} \gtrsim 0.01$ mJy. Substituting $\epsilon_{\text{e}} = 0.1$, $p = 2.17$, $\nu = 6$ GHz, $\theta_{\text{obs}} = 25^\circ$, $\theta_j = 5^\circ$, $D_{\text{L}} = 40$ Mpc, criterion 2 yields

$$E_{\text{iso},52} \gtrsim 0.4(n_{-4} \epsilon_{\text{B},-2})^{-0.79}. \quad (5.6)$$

This condition is shown by the dot-dashed line in the bottom panel of Fig. 5.2, where the different colors corresponds to different values of $\epsilon_{\text{B}} = 10^{-2}, 10^{-3}, 10^{-4}$ as indicated in the plot legend. The regions above the dot-dashed lines satisfy criterion 2 for the corresponding values of ϵ_{B} .

The final criterion for detectability requires that the flux at peak, F_{peak} is larger than the flux from the cocoon component. The latest observations show the afterglow of GW170817 has started to decline, and this decline follows a power law in time as $\propto t^{-\alpha}$ with $\alpha = 2.1_{-0.6}^{+1.6}$ [265]. Attributing this emission to the cocoon, we estimate the late time flux from it by extrapolating this power to later times. For example, taking the 6 GHz measurements we can model the decline in flux as

$$F_{\text{d}}(t) \approx 0.07 \left(\frac{t}{160} \right)^{-\alpha} \text{ mJy}, \quad (5.7)$$

with t in days. This extrapolation is shown by the solid lines in the top panel of Fig. 5.2 for multiple values of α within the range estimated by current detections. Criterion 3 requires $F_{\text{peak}} > F_{\text{d}}(t_{\text{peak}})$. Using the same parameter substitutions used to obtain equation 5.6, this condition yields

$$E_{\text{iso}} \gtrsim \left(5 \times 10^{47} \left(3.8 \times 10^{-19} \right)^{-\alpha} n^{\frac{\alpha-2.3775}{3}} \epsilon_{\text{B}}^{-0.7925} \right)^{\frac{3}{3+\alpha}}. \quad (5.8)$$

This equality is shown for $\alpha = 2$ by the solid lines in the bottom panel of Fig. 5.2 where different colors correspond to different values of ϵ_{B} color coded in the same way as for criterion 2 (the dot-dashed lines). Therefore the inequality 5.8 is satisfied for regions above the solid lines. So the regions in Fig. 5.2 which satisfy all three criteria must lie above the dashed black line (criterion 1), and above the dot-dashed and solid lines (criterion 2 and 3) corresponding to the same value of ϵ_{B} . These regions have been shaded for better visualization. In order for the second peak to be detectable, the parameters pertaining to the jet must lie in the shaded regions. The bottom panel of Fig. 5.2 is for a t^{-2} decline only, Fig. 5.3 shows a similar plot for varying power law declines (different values of α) that lie within the estimated range from latest observations [265], while fixing $\epsilon_{\text{B}} = 10^{-3}$. Like in Fig. 5.2, the shaded regions in Fig. 5.3 mark the parameters where the second peak is detectable, in general we find a shallower decline necessitates a higher energy for the jet in order for it to be detectable.

5.3.3 Second peak light curves using the ‘‘Afterglow library’’

In this Section we discuss the calculations of the afterglow light curves using the ‘‘Afterglow library’’ [268], which uses linear radiative transfer to calculate synchrotron light curves and spectra. Guided by observations [249]; [265] and analytic estimates above, we use a few different sets of parameters when calculating the afterglow. We fix the spectral slope, $p = 2.17$, the observing angle w.r.t jet axis, $\theta_{\text{obs}} = 25^\circ$, use a typical value of $\epsilon_e = 0.1$, which denotes the fraction of energy in the electrons of the shocked fluid, and a relatively narrow ‘top-hat’ jet with opening angle $\theta_j = 5^\circ$ and 10° . We vary the isotropic equivalent energy E_{iso} , the fraction of energy in the magnetic field of the shocked fluid ϵ_{B} , and number density of external medium $n \text{ cm}^{-3}$. The resulting light curves for these different sets of parameters are shown in

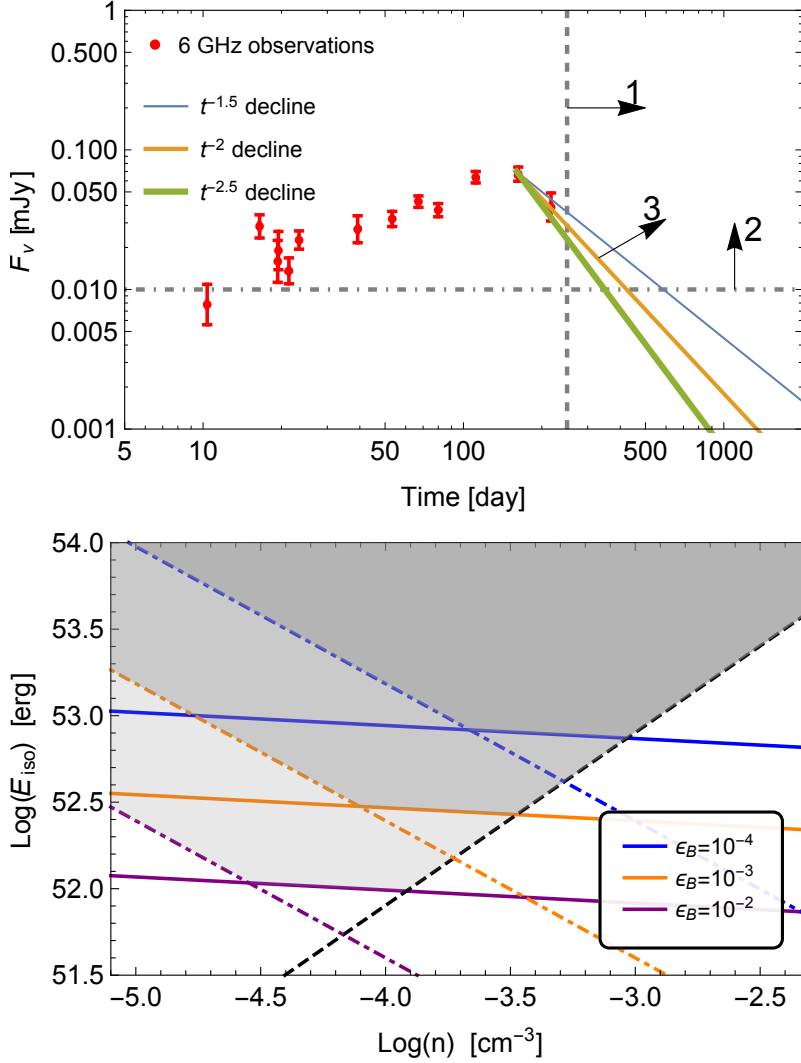


Figure 5.2. (Top) Depiction of the three criteria required for detectability of second peak. The plot shows observed radio data (red points) and multiple power law extrapolations for the observed decline (solid lines) (data taken from [249]; [265]). Vertical dashed line marks a time of 250 days and dot-dashed horizontal line indicates a radio detectability limit of $10 \mu\text{Jy}$. The numbered arrows point to the region where the second peak must lie in order to be detectable and the numbers label the criteria described in Section 5.3.2. In short, 1) requires peak time to be greater than 250d, 2) requires peak flux be above detector sensitivity and 3) requires peak flux be larger than cocoon emission. (Bottom) A figure exploring the parameter space in isotropic equivalent energy of the jet (E_{iso}) vs. external density (n). Shaded regions mark the parameter space where the second peak will be detectable (where all 3 criteria mention in top panel and Section 5.3.2 are satisfied) assuming a t^{-2} decline for current observations. Regions above dashed black line satisfy criterion 1, above dot-dashed lines satisfy criterion 2 and above solid lines satisfy criterion 3. Colors indicate the value of ϵ_B used for the solid and dot-dashed lines. See section 5.3.2 for analytic expressions of the lines, shaded regions and for relevant parameters used.

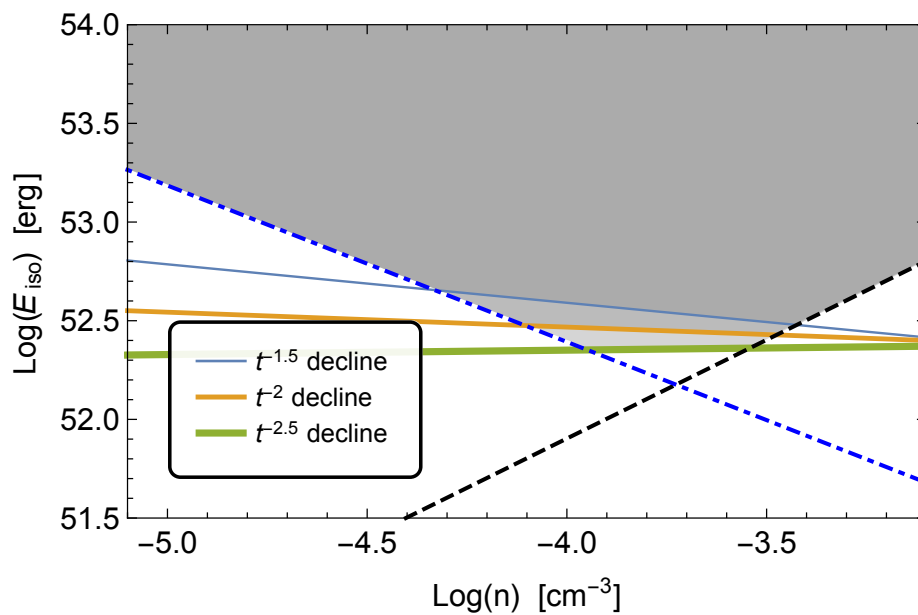


Figure 5.3. Same parameter space plot as in Fig. 5.2 except now we fix $\epsilon_B = 10^{-3}$ and vary the slope of the power law decline (shown in top panel of Fig. 5.2) to investigate how different declines will affect detectability of second peak. As in Fig. 5.2, shaded regions mark regions where the second peak would be detectable.

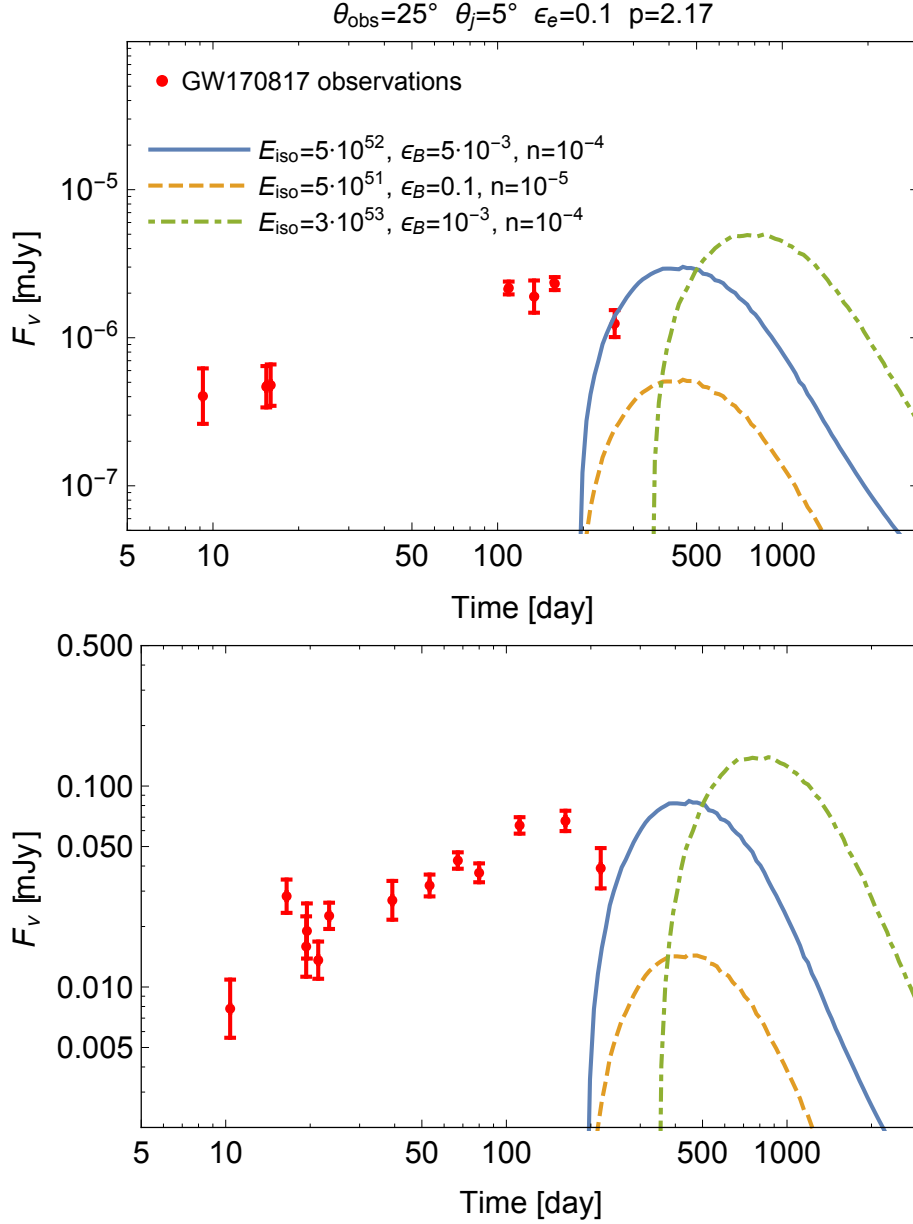


Figure 5.4. Light curves in X-ray at 1 keV (Top) and Radio at 6 GHz (Bottom) using the “Afterglow library”. Red points show observations of GW170817 [249], and lines show the afterglow from a jet calculated using the afterglow library [275] for two sets of parameters (see sec. for description of parameters). In a fast jet – cocoon model, the earlier time observations (red points) can be attributed to emission from the cocoon. The afterglow from a jet will peak at later times for off-axis observers, in this scenario, this peak can cause a second bump in the overall X-ray light curve of GW170817. For parameters used here, the second peak occurs at ~ 500 days.

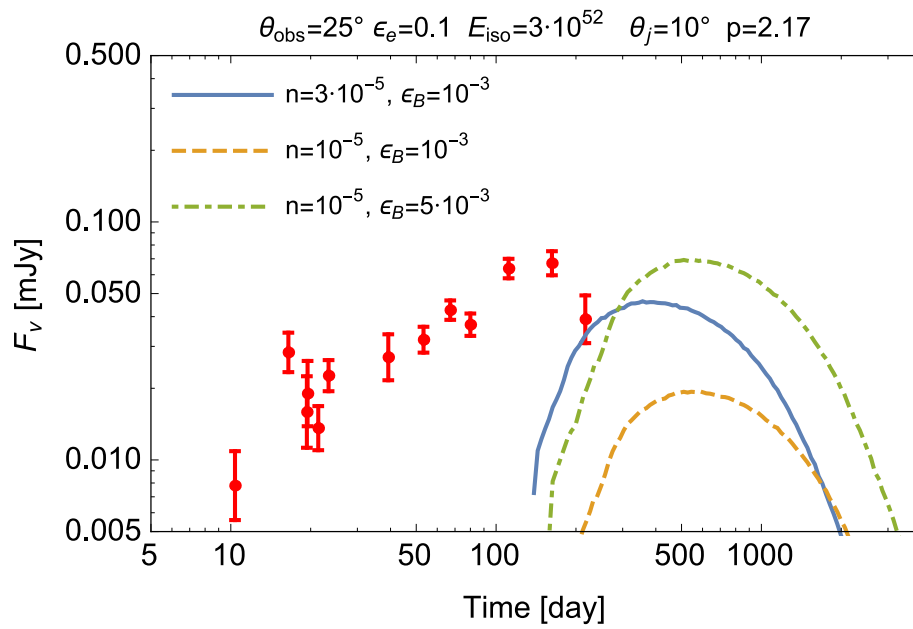


Figure 5.5. Radio (6 GHz) afterglow light curves, similar to bottom panel of Fig. 5.4 but with a jet of opening angle 10° .

Fig. 5.4 and 5.5, observations of GW170817 (taken from [249]; [265]) are also shown in the same plots for radio (6 GHz) and X-ray (1 keV). These plots demonstrate the possibility where the afterglow from the jet can cause a late time rise in the light curve of GW170817.

5.3.4 Emission from off-axis forward shock: numerical calculation of synchrotron emission

Next, we use the classic forward shock model of [276]; [110] to calculate the emission seen by an off-axis observer. As a novel feature, we calculate numerically the radiative and cooling losses of the particles. To do so, we first find Greens function for particles injected at some moment in time into the forward shock, then we integrate over different injections times, and allowing for time-of-flight delays we calculated the expected light curve.

We assume self-similar relativistic shock with $\Gamma \propto t^{-m/2}$ with $m = 3$ [107] (thus, we neglect lateral evolution of the shock - it is small [231]; [277]). The minimum Lorentz factor of accelerated electrons in the shock frame is then

$$\gamma'_{\min} \propto \epsilon_e (\Gamma - 1) \frac{m_p}{m_e}, \quad (5.9)$$

while the comoving magnetic field is

$$\frac{B'^2}{8\pi} = \epsilon_B n_p (\Gamma - 1) \Gamma m_p c^2 \propto t^{-m} \propto t'^{-\frac{2m}{2+m}} \quad (5.10)$$

(primed quantities are in the fluid frame and un-primed are in the coordinate frame.)

Thus, the magnetic field strength satisfies

$$B' = B'_0 \left(\frac{t'}{t'_0} \right)^{-\frac{m}{m+2}} \quad (5.11)$$

where the magnetic field is B_0 and Lorentz factor is $\Gamma = \Gamma_0$ at time $t' = t'_0$.

Particles are injected with distribution function f_{inj} at time t'_i through an area A . The Lorentz factor of particles evolves according to

$$\begin{aligned} \frac{d\gamma'}{dt'} &= -\frac{\tilde{C}_2 B_0^2 \gamma'^2}{t'^{\frac{2m}{2+m}}} - \frac{m\gamma'}{2t'(2+m)} \\ \tilde{C}_2 &= \frac{\sigma_T t_0^{\frac{2m}{2+m}}}{6\pi m_e c} \end{aligned} \quad (5.12)$$

where the first term describes radiative losses and the second the adiabatic expansion.

The evolution of the distribution function is then described by, first, solving for the Greens function $G(\gamma', t', t'_i)$

$$\begin{aligned} \frac{\partial G(\gamma', t')}{\partial t'} &= \frac{\tilde{C}_2 B_0^2}{t'^{\frac{2m}{2+m}}} \frac{\partial (\gamma'^2 G(\gamma', t'))}{\partial \gamma'} + \frac{m}{2t'(2+m)} \frac{\partial (\gamma' G(\gamma', t'))}{\partial \gamma'} \\ &\quad + f'_{inj}(\gamma', t'_i) \delta(t' - t'_i) \end{aligned} \quad (5.13)$$

with injection

$$f'_{inj}(\gamma', t'_i) = f'_i \gamma'^{-p} \Theta(\gamma' - \gamma'_{\min}(t'_i)) \quad (5.14)$$

where f'_i satisfies $f'_i \int_{\gamma'_{\min}}^{\infty} \gamma'^{-p} d\gamma' = nAc$. And, second, integrating with the injection rate

$$f(\gamma', t') = \int G(\gamma', t', t'_i) f'_i dt'_i, \quad (5.15)$$

where $f(\gamma', t')$ is the total distribution.

Consider a jet (actually, a shock) with opening angle θ_j viewed at an angle θ_{obs} . Emissivity at each moment is given by an integral over the shock surface

$$\begin{aligned} L'(\omega', t') &= \int \int \frac{f(\gamma', t')}{A} P(\omega') d\gamma' dA \\ &\approx \int_{\theta_{\text{obs}} - \theta_j}^{\theta_{\text{obs}} + \theta_j} \int_{\phi_{\min}(\theta)}^{\phi_{\max}(\theta)} \int_{\gamma'_{\min}}^{\infty} \frac{r^2 \sin \theta f(\gamma', t') P(\omega')}{2\pi r^2 (1 - \cos \theta_j)} d\gamma' d\phi d\theta \\ &= \int_{\theta_{\text{obs}} - \theta_j}^{\theta_{\text{obs}} + \theta_j} \int_{\gamma'_{\min}}^{\infty} \frac{(\phi_{\max}(\theta) - \phi_{\min}(\theta)) r^2 \sin \theta f(\gamma', t') P(\omega')}{2\pi r^2 (1 - \cos \theta_j)} d\gamma' d\theta \end{aligned} \quad (5.16)$$

where f is the distribution function, P is the synchrotron power per unit frequency emitted by each electron and we use spherical coordinate with the z axis oriented towards the observer and θ_{obs} is larger than θ_j .

The photons emitted by different parts of the jet at the same moment will arrive at different time due to time-of-flight effects. At an emission point (r, θ) , the relation between the time t measured in lab frame, t' measured in fluid frame and the corresponding observe time T_{obs} are

$$dt = \Gamma dt' \quad (5.17)$$

and

$$dT_{\text{obs}} = (1 - \beta \cos \theta) dt = \Gamma (1 - \beta \cos \theta) dt' \quad (5.18)$$

By solving the equations 5.17 and 5.18, we can find $\cos \theta = K(T_{\text{obs}}, t')$, where K is a function of T_{obs} and t' . So for a fixed T_{obs} , we find

$$\sin \theta d\theta = -d(\cos \theta) = -\frac{dK(T_{\text{obs}}, t')}{dt'} dt' \quad (5.19)$$

The geometric relation between θ and ϕ is

$$\phi_{\text{max}}(\theta) - \phi_{\text{min}}(\theta) = 2 \arccos \left(\frac{\cos(\theta_j) - \cos(\theta_{\text{obs}}) \cos(\theta)}{\sin(\theta_{\text{obs}}) \sin(\theta)} \right) \quad (5.20)$$

Substituting equations 5.19 and 5.20 into equation 5.16 and taking into account Doppler boosting, we finally arrive at the equation for the observed spectral luminosity as function of the observer time

$$L(T_{\text{obs}}) \approx \int_{t'(T_{\text{obs}})_{\theta'=\theta_{\text{obs}}+\theta_j}}^{t'(T_{\text{obs}})_{\theta'=\theta_{\text{obs}}-\theta_j}} \int_{\gamma'_{\text{min}}}^{\infty} \arccos \left(\frac{\cos(\theta_j) - \cos(\theta_{\text{obs}}) \cos(\theta(T_{\text{obs}}, t'))}{\sin(\theta_{\text{obs}}) \sin(\theta(T_{\text{obs}}, t'))} \right) \times \frac{\delta^3(T_{\text{obs}}, t') P(\frac{\omega}{\delta(T_{\text{obs}}, t')}) \int G(\gamma', t', t'_i) f'_i dt'_i}{\pi(1 - \cos(\theta_j))} \times \frac{dK(T_{\text{obs}}, t')}{dt'} d\gamma' dt' \quad (5.21)$$

Using the above procedure we calculate the light curve behavior at 1 keV and 6 GHz for the same set of parameters as in Fig. 5.4, see Fig.5.6. The slope of radio and X-ray are different at early times, because there is a spectra break due to γ_{min} in the radio region at early time. Within a factor of a few the two methods produce similar results.

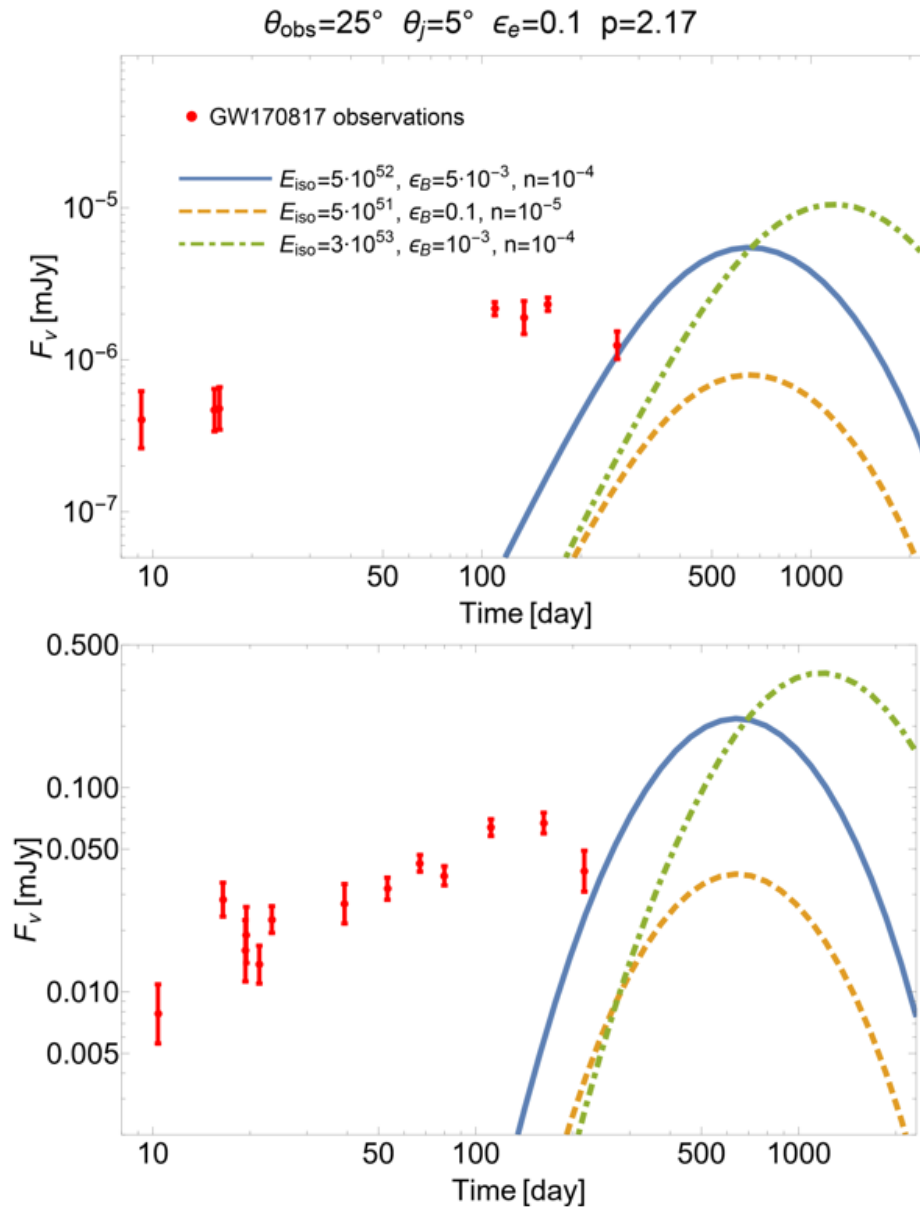


Figure 5.6. Light curves in X-ray at 1 keV and 6 GHz using the radiative calculations, see text for details. Red points show the observation of GW170817 at 1 KeV and 6 GHz [265]. All light curves have the same parameter value as Figure 3.

5.4 Conclusions

In this chapter, we argue that late afterglow of GRB/GW170817 may experience a second peak in brightness, as the fast primary jet, which avoided detection so far, becomes visible. Using three different approaches – basic analytic estimates, “Afterglow library” and new radiative calculations – we put constraints on the jet energetics and microphysical parameters for the second peak to be observable.

Detectability of the second peak depends on macroscopic parameter (energy of the primary jet E_{iso} and external density n), as well as microscopic parameters (ϵ_e and ϵ_B), as well as the viewing angle. Observations of the prompt emission and the corresponding GRB constrain the viewing angle to be $\sim 20 - 30^\circ$ (*e.g.* [278]; [237]; [265]). Thus, we are left with E_{iso} , n and ϵ_e , ϵ_B .

Our results indicate that even a mildly energetic jet, with $E_{\text{iso}} \sim \text{few} \times 10^{51}$ ergs may be detected even for low external density $n \sim 10^{-5} \text{ cm}^{-3}$ (if ϵ_e and ϵ_B are not too small). This compares favorably with the expected jet power (5.3). We should note, that in about 10% of cases the short GRBs with known red shift have $E_{\text{iso},\gamma} > 3 \times 10^{52}$ ergs, in particular GRB160410A [279], GRB090510A [280], GRB060801A and GRB090227B [281]. Taking into account the efficiency of kinetic energy gamma radiation conversion ~ 0.1 [282] the total energy budget of short GRBs $E_{\text{iso}} > 3 \times 10^{53}$ ergs can be significantly higher than the limitations of late afterglow visibility in Fig. (5.2).

We end our conclusions with general remark: if the jet has more energy than the cocoon, it should show up as a second distinct peak. This is because the other parameters (n , ϵ_e , and ϵ_B) should actually be the same for the 2 afterglow components. In the case of radiatively inefficient jet, the late time emission just tracks the total true energy of the jet. We can even argue that since the jet drives the cocoon, it is typically true that $E_{\text{jet}} > E_{\text{cocoon}}$, i.e. we should see a two bump structure on light curves from radio through X-ray.

6. SUMMARY

In modern astrophysics, we are heavily relying on the electromagnetic wave observations, which can span from radio to very high energy gamma-ray, to receive the information from the distant astrophysical objects. Many electromagnetic waves are produced from the radiation processes in relativistic astrophysical plasma, such as synchrotron and IC scattering. Thus, understanding the radiation processes in relativistic plasma is a crucially vital task to reveal the physics behind the observational data. In this dissertation, I have presented a systematic and comprehensive approach to treating radiation processes in relativistic astrophysical plasma, including synchrotron and IC scattering. I will summarize the results below.

Starting from the result of [226] which provides the standard formula used for the synchrotron power loss, I develop a program which takes account the effect of γ_{min} , the adiabatic losses, Doppler boosting, and finally extend the applicable conditions of my program to a general expansion (See §2). Taking the synchrotron emitted photons as the input seed photons, I develop a program to calculate the SSC spectra. The input seed photons are not necessary as synchrotron photons, but also could be CMB photons, thermal emission photons. The program can do calculations in both the Thomson regime and Klein-Nishina regime. Thus the IC spectra can be calculated from X-ray to very high energy γ ray. The full application of my program in radiation processes will provide opportunities to tackle many unsolved problems in astrophysics, three relevant applications are summarized below.

In chapter §3, I focus on the unsolved problems in Crab nebula, which are the sigma program, the spectrum of radio electrons, the high peak energy of gamma-ray flares, and the resolved spectral evolution. All problems are solved by using a two-component model. I applied my program to calculate the emission from the two-component model of Crab nebula. In this model, the broad-band spectrum of

crab nebula comes from two components: component-I is from terminate shock, and component-II is from turbulent. In this project, the broad-band spectrum (including synchrotron emission and IC emission) of Crab nebula is fitted very well, and the spectra index map of optical and IR are investigated.

In chapter §4, I focus on the GRB afterglow. I calculate the emission from an alternative GRB model, where afterglow is from RF instead of FS. The effect of the Lorentz factors of the bulk motion, jet angles, and cooling time scales is investigated. We can produce flares by giving a fluctuation to wind power since RS is in fast cooling and sensitive to wind properties. By applying the calculation, I could not only explain the steep drop in GRB 070110 afterglow but also explain the plateaus and flares within the GRB afterglows.

In chapter §5, as a part of collaborative work, I contribute the calculation of the emission from GRB/GW 170817 afterglow and explored different parameters setting based on a fast jet-cocoon model. In this model, the primary jet slows down and becomes visible, thus produce the rebrightening of the afterglow. In my calculation, we could see that there is a second bump in the afterglow, which could be used to test the fast jet-cocoon model from further observations.

In the end, I have a compelling program for calculating the synchrotron spectra and IC spectra, which can be applied to GRBs, PWNe, AGNs, and other relativistic processes.

REFERENCES

- [1] T. Piran. The physics of gamma-ray bursts. *Reviews of Modern Physics*, 76:1143–1210, October 2004.
- [2] P. Kumar and B. Zhang. The physics of gamma-ray bursts relativistic jets. , 561:1–109, February 2015.
- [3] C. Chiuderi and M. Velli. *Basics of Plasma Astrophysics*. 2015.
- [4] Gerard Belmont. *Introduction to plasma physics*. 2019.
- [5] H. C. Spruit. Essential Magnetohydrodynamics for Astrophysics. *arXiv e-prints*, page arXiv:1301.5572, January 2013.
- [6] Enrico Fermi. On the Origin of the Cosmic Radiation. *Physical Review*, 75(8):1169–1174, April 1949.
- [7] W. I. Axford, E. Leer, and G. Skadron. The Acceleration of Cosmic Rays by Shock Waves. In *International Cosmic Ray Conference*, volume 11 of *International Cosmic Ray Conference*, page 132, January 1977.
- [8] G. F. Krymskii. A regular mechanism for the acceleration of charged particles on the front of a shock wave. *Akademiia Nauk SSSR Doklady*, 234:1306–1308, June 1977.
- [9] A. R. Bell. The acceleration of cosmic rays in shock fronts - I. , 182:147–156, January 1978.
- [10] R. D. Blandford and J. P. Ostriker. Particle acceleration by astrophysical shocks. , 221:L29–L32, April 1978.
- [11] E. N. Parker. Sweet’s Mechanism for Merging Magnetic Fields in Conducting Fluids. , 62(4):509–520, December 1957.
- [12] H. E. Petschek. *Magnetic Field Annihilation*, volume 50, page 425. 1964.
- [13] Frank C. Jones. Calculated Spectrum of Inverse-Compton-Scattered Photons. *Physical Review*, 167(5):1159–1169, Mar 1968.
- [14] George R. Blumenthal and Robert J. Gould. Bremsstrahlung, Synchrotron Radiation, and Compton Scattering of High-Energy Electrons Traversing Dilute Gases. *Reviews of Modern Physics*, 42(2):237–271, Jan 1970.
- [15] F. A. Aharonian and A. M. Atoyan. Compton Scattering of Relativistic Electrons in Compact X-Ray Sources. , 79(2):321–336, Oct 1981.
- [16] P. S. Coppi and R. D. Blandford. Reaction rates and energy distributions for elementary processes in relativistic pair plasmas. , 245:453–507, Aug 1990.

- [17] George B. Rybicki and Alan P. Lightman. *Radiative Processes in Astrophysics*. 1986.
- [18] Gabriele Ghisellini. *Radiative Processes in High Energy Astrophysics*, volume 873. 2013.
- [19] J. J. Hester. The Crab Nebula : an astrophysical chimera. , 46:127–155, September 2008.
- [20] David H. Staelin and III Reifenstein, Edward C. Pulsating Radio Sources near the Crab Nebula. *Science*, 162(3861):1481–1483, December 1968.
- [21] R. B. E. Lovelace, J. M. Sutton, and H. D. Craft. Pulsar NP 0532 Near Crab Nebula. , 2113:1, January 1968.
- [22] M. Amenomori, Y. W. Bao, X. J. Bi, D. Chen, T. L. Chen, W. Y. Chen, Xu Chen, Y. Chen, Cirennima, S. W. Cui, Danzengluobu, L. K. Ding, J. H. Fang, K. Fang, C. F. Feng, Zhaoyang Feng, Z. Y. Feng, Qi Gao, Q. B. Gou, Y. Q. Guo, H. H. He, Z. T. He, K. Hibino, N. Hotta, Haibing Hu, H. B. Hu, J. Huang, H. Y. Jia, L. Jiang, H. B. Jin, F. Kajino, K. Kasahara, Y. Katayose, C. Kato, S. Kato, K. Kawata, M. Kozai, Labaciren, G. M. Le, A. F. Li, H. J. Li, W. J. Li, Y. H. Lin, B. Liu, C. Liu, J. S. Liu, M. Y. Liu, Y. Q. Lou, H. Lu, X. R. Meng, H. Mitsui, K. Munakata, Y. Nakamura, H. Nanjo, M. Nishizawa, M. Ohnishi, I. Ohta, S. Ozawa, X. L. Qian, X. B. Qu, T. Saito, M. Sakata, T. K. Sako, Y. Sengoku, J. Shao, M. Shibata, A. Shiomi, H. Sugimoto, M. Takita, Y. H. Tan, N. Tateyama, S. Torii, H. Tsuchiya, S. Udo, H. Wang, H. R. Wu, L. Xue, K. Yagisawa, Y. Yamamoto, Z. Yang, A. F. Yuan, L. M. Zhai, H. M. Zhang, J. L. Zhang, X. Zhang, X. Y. Zhang, Y. Zhang, Yi Zhang, Ying Zhang, Zhaxisangzhu, X. X. Zhou, and Tibet AS γ Collaboration. First Detection of Photons with Energy beyond 100 TeV from an Astrophysical Source. , 123(5):051101, Aug 2019.
- [23] Roberta Zanin. *Crab Observational Status: Nebulae, Pulsations, and Flares*, volume 446 of *Astrophysics and Space Science Library*, page 101. 2017.
- [24] M. J. Rees and J. E. Gunn. The origin of the magnetic field and relativistic particles in the Crab Nebula. , 167:1–12, Apr 1974.
- [25] C. F. Kennel and F. V. Coroniti. Confinement of the Crab pulsar’s wind by its supernova remnant. , 283:694–709, Aug 1984.
- [26] C. F. Kennel and F. V. Coroniti. Magnetohydrodynamic model of Crab nebula radiation. , 283:710–730, Aug 1984.
- [27] S. R. Kulkarni, S. G. Djorgovski, S. C. Odewahn, J. S. Bloom, R. R. Gal, C. D. Koresko, F. A. Harrison, L. M. Lubin, L. Armus, R. Sari, G. D. Illingworth, D. D. Kelson, D. K. Magee, P. G. van Dokkum, D. A. Frail, J. S. Mulchaey, M. A. Malkan, I. S. McClean, H. I. Teplitz, D. Koerner, D. Kirkpatrick, N. Kobayashi, I.-A. Yadigaroglu, J. Halpern, T. Piran, R. W. Goodrich, F. H. Chaffee, M. Feroci, and E. Costa. The afterglow, redshift and extreme energetics of the γ -ray burst of 23 January 1999. , 398:389–394, April 1999.
- [28] J. van Paradijs, C. Kouveliotou, and R. A. M. J. Wijers. Gamma-Ray Burst Afterglows. , 38:379–425, 2000.

- [29] J. E. Rhoads. The Dynamics and Light Curves of Beamed Gamma-Ray Burst Afterglows. , 525:737–749, November 1999.
- [30] R. Sari, T. Piran, and J. P. Halpern. Jets in Gamma-Ray Bursts. , 519:L17–L20, July 1999.
- [31] D. A. Frail, S. R. Kulkarni, R. Sari, S. G. Djorgovski, J. S. Bloom, T. J. Galama, D. E. Reichart, E. Berger, F. A. Harrison, P. A. Price, S. A. Yost, A. Diercks, R. W. Goodrich, and F. Chaffee. Beaming in Gamma-Ray Bursts: Evidence for a Standard Energy Reservoir. , 562:L55–L58, November 2001.
- [32] A. Panaitescu and P. Kumar. Fundamental Physical Parameters of Collimated Gamma-Ray Burst Afterglows. , 560:L49–L53, October 2001.
- [33] T. Piran, P. Kumar, A. Panaitescu, and L. Piro. The Energy of Long-Duration Gamma-Ray Bursts. , 560:L167–L169, October 2001.
- [34] E. Berger, S. R. Kulkarni, and D. A. Frail. A Standard Kinetic Energy Reservoir in Gamma-Ray Burst Afterglows. , 590:379–385, June 2003.
- [35] P. A. Curran, A. J. van der Horst, and R. A. M. J. Wijers. Are the missing X-ray breaks in gamma-ray burst afterglow light curves merely hidden? , 386:859–863, May 2008.
- [36] E.-W. Liang, J. L. Racusin, B. Zhang, B.-B. Zhang, and D. N. Burrows. A Comprehensive Analysis of Swift XRT Data. III. Jet Break Candidates in X-Ray and Optical Afterglow Light Curves. , 675:528–552, March 2008.
- [37] J. L. Racusin, E. W. Liang, D. N. Burrows, A. Falcone, T. Sakamoto, B. B. Zhang, B. Zhang, P. Evans, and J. Osborne. Jet Breaks and Energetics of Swift Gamma-Ray Burst X-Ray Afterglows. , 698:43–74, June 2009.
- [38] S. B. Cenko, D. A. Frail, F. A. Harrison, S. R. Kulkarni, E. Nakar, P. C. Chandra, N. R. Butler, D. B. Fox, A. Gal-Yam, M. M. Kasliwal, J. Kelemen, D.-S. Moon, E. O. Ofek, P. A. Price, A. Rau, A. M. Soderberg, H. I. Teplitz, M. W. Werner, D. C.-J. Bock, J. S. Bloom, D. A. Starr, A. V. Filippenko, R. A. Chevalier, N. Gehrels, J. N. Nousek, and T. Piran. The Collimation and Energetics of the Brightest Swift Gamma-ray Bursts. , 711:641–654, March 2010.
- [39] D. Band, J. Matteson, L. Ford, B. Schaefer, D. Palmer, B. Teegarden, T. Cline, M. Briggs, W. Paciesas, G. Pendleton, G. Fishman, C. Kouveliotou, C. Meegan, R. Wilson, and P. Lestrade. BATSE observations of gamma-ray burst spectra. I - Spectral diversity. , 413:281–292, August 1993.
- [40] C. Kouveliotou, C. A. Meegan, G. J. Fishman, N. P. Bhat, M. S. Briggs, T. M. Koshut, W. S. Paciesas, and G. N. Pendleton. Identification of two classes of gamma-ray bursts. , 413:L101–L104, August 1993.
- [41] C. A. Meegan, G. J. Fishman, R. B. Wilson, J. M. Horack, M. N. Brock, W. S. Paciesas, G. N. Pendleton, and C. Kouveliotou. Spatial distribution of gamma-ray bursts observed by BATSE. , 355:143–145, January 1992.

- [42] E. Rossi, D. Lazzati, and M. J. Rees. Afterglow Lightcurves, Viewing Angle and the Jet Structure of Gamma-Ray Bursts. In G. R. Ricker and R. K. Vanderspek, editors, *Gamma-Ray Burst and Afterglow Astronomy 2001: A Workshop Celebrating the First Year of the HETE Mission*, volume 662 of *American Institute of Physics Conference Series*, pages 335–337, April 2003.
- [43] B. Zhang and P. Mészáros. Gamma-Ray Bursts: progress, problems prospects. *International Journal of Modern Physics A*, 19:2385–2472, 2004.
- [44] P. Podsiadlowski, P. A. Mazzali, K. Nomoto, D. Lazzati, and E. Cappellaro. The Rates of Hypernovae and Gamma-Ray Bursts: Implications for Their Progenitors. , 607:L17–L20, May 2004.
- [45] R. W. Klebesadel, I. B. Strong, and R. A. Olson. Observations of Gamma-Ray Bursts of Cosmic Origin. , 182:L85, June 1973.
- [46] R. Margutti, E. Berger, W. Fong, B. A. Zauderer, S. B. Cenko, J. Greiner, A. M. Soderberg, A. Cucchiara, A. Rossi, S. Klose, S. Schmidl, D. Milisavljevic, and N. Sanders. The Afterglow and Environment of the Short GRB 111117A. , 756:63, September 2012.
- [47] F. J. Virgili, C. G. Mundell, V. Pal’shin, C. Guidorzi, R. Margutti, A. Melandri, R. Harrison, S. Kobayashi, R. Chornock, A. Henden, A. C. Updike, S. B. Cenko, N. R. Tanvir, I. A. Steele, A. Cucchiara, A. Gomboc, A. Levan, Z. Cano, C. J. Mottram, N. R. Clay, D. Bersier, D. Kopač, J. Japelj, A. V. Filippenko, W. Li, D. Svinkin, S. Golenetskii, D. H. Hartmann, P. A. Milne, G. Williams, P. T. O’Brien, D. B. Fox, and E. Berger. GRB 091024A and the Nature of Ultra-long Gamma-Ray Bursts. , 778:54, November 2013.
- [48] S. Mao and B. Paczynski. On the cosmological origin of gamma-ray bursts. , 388:L45–L48, April 1992.
- [49] T. Piran. The implications of the Compton (GRO) observations for cosmological gamma-ray bursts. , 389:L45–L48, April 1992.
- [50] E. E. Fenimore, R. I. Epstein, C. Ho, R. W. Klebesadel, C. Lacey, J. G. Laros, M. Meier, T. Strohmayer, G. Pendleton, G. Fishman, C. Kouveliotou, and C. Meegan. The intrinsic luminosity of γ -ray bursts and their host galaxies. , 366:40–42, November 1993.
- [51] B. Paczynski. How Far Away Are Gamma-Ray Bursters? , 107:1167, December 1995.
- [52] D. E. Reichart. The redshift of GRB970508. In C. A. Meegan, R. D. Preece, and T. M. Koshut, editors, *Gamma-Ray Bursts, 4th Huntsville Symposium*, volume 428 of *American Institute of Physics Conference Series*, pages 535–539, May 1998.
- [53] E. Costa, F. Frontera, J. Heise, M. Feroci, J. in’t Zand, F. Fiore, M. N. Cinti, D. Dal Fiume, L. Nicastro, M. Orlandini, E. Palazzi, M. Rapisarda#, G. Zavattini, R. Jager, A. Parmar, A. Owens, S. Molendi, G. Cusumano, M. C. Maccarone, S. Giarrusso, A. Coletta, L. A. Antonelli, P. Giommi, J. M. Muller, L. Piro, and R. C. Butler. Discovery of an X-ray afterglow associated with the γ -ray burst of 28 February 1997. , 387:783–785, June 1997.

- [54] J. van Paradijs, P. J. Groot, T. Galama, C. Kouveliotou, R. G. Strom, J. Telling, R. G. M. Rutten, G. J. Fishman, C. A. Meegan, M. Pettini, N. Tanvir, J. Bloom, H. Pedersen, H. U. Nørregaard-Nielsen, M. Linden-Vørnle, J. Melnick, G. Van der Steene, M. Bremer, R. Naber, J. Heise, J. in't Zand, E. Costa, M. Feroci, L. Piro, F. Frontera, G. Zavattini, L. Nicastro, E. Palazzi, K. Bennett, L. Hanlon, and A. Parmar. Transient optical emission from the error box of the γ -ray burst of 28 February 1997. , 386:686–689, April 1997.
- [55] F. Frontera, E. Costa, L. Piro, J. M. Muller, L. Amati, M. Feroci, F. Fiore, G. Pizzichini, M. Tavani, A. Castro-Tirado, G. Cusumano, D. Dal Fiume, J. Heise, K. Hurley, L. Nicastro, M. Orlandini, A. Owens, E. Palazzi, A. N. Parmar, J. i. Zand, and G. Zavattini. Spectral Properties of the Prompt X-Ray Emission and Afterglow from the Gamma-Ray Burst of 1997 February 28. , 493:L67–L70, February 1998.
- [56] M. Vietri and L. Stella. A Gamma-Ray Burst Model with Small Baryon Contamination. , 507:L45–L48, November 1998.
- [57] L. Wang and J. C. Wheeler. The Supernova-Gamma-Ray Burst Connection. , 504:L87–L90, September 1998.
- [58] K. Z. Stanek, T. Matheson, P. M. Garnavich, P. Martini, P. Berlind, N. Caldwell, P. Challis, W. R. Brown, R. Schild, K. Krisciunas, M. L. Calkins, J. C. Lee, N. Hathi, R. A. Jansen, R. Windhorst, L. Echevarria, D. J. Eisenstein, B. Pindor, E. W. Olszewski, P. Harding, S. T. Holland , and D. Bersier. Spectroscopic Discovery of the Supernova 2003dh Associated with GRB 030329. , 591(1):L17–L20, July 2003.
- [59] Jens Hjorth, Jesper Sollerman, Palle Møller, Johan P. U. Fynbo, Stan E. Woosley, Chryssa Kouveliotou, Nial R. Tanvir, Jochen Greiner, Michael I. Andersen, Alberto J. Castro-Tirado, José María Castro Cerón, Andrew S. Fruchter, Javier Gorosabel, Páll Jakobsson, Lex Kaper, Sylvio Klose, Nicola Masetti, Holger Pedersen, Kristian Pedersen, Elena Pian, Eliana Palazzi, James E. Rhoads, Evert Rol, Edward P. J. van den Heuvel, Paul M. Vreeswijk, Darach Watson, and Ralph A. M. J. Wijers. A very energetic supernova associated with the γ -ray burst of 29 March 2003. , 423(6942):847–850, June 2003.
- [60] L. Piro. GRB990123, BeppoSAX WFC detection and NFI planned follow-up. *GRB Coordinates Network*, 199:1, January 1999.
- [61] C. Akerlof, R. Balsano, S. Barthelmy, J. Bloch, P. Butterworth, D. Casperson, T. Cline, S. Fletcher, F. Frontera, G. Gisler, J. Heise, J. Hills, R. Kehoe, B. Lee, S. Marshall, T. McKay, R. Miller, L. Piro, W. Priedhorsky, J. Szymanski, and J. Wren. Observation of contemporaneous optical radiation from a γ -ray burst. , 398(6726):400–402, April 1999.
- [62] P. Meszaros and M. J. Rees. Gamma-Ray Bursts: Multiwaveband Spectral Predictions for Blast Wave Models. , 418:L59, December 1993.
- [63] P. Mészáros and M. J. Rees. Optical and Long-Wavelength Afterglow from Gamma-Ray Bursts. , 476:232–237, February 1997.
- [64] Re'em Sari and Tsvi Piran. Predictions for the Very Early Afterglow and the Optical Flash. , 520(2):641–649, August 1999.

- [65] B. Zhang. Gamma-Ray Burst Prompt Emission. In K. Rosquist, editor, *Thirteenth Marcel Grossmann Meeting: On Recent Developments in Theoretical and Experimental General Relativity, Astrophysics and Relativistic Field Theories*, pages 224–241, January 2015.
- [66] B. Paczynski. Gamma-ray bursters at cosmological distances. , 308:L43–L46, September 1986.
- [67] J. Goodman. Radio scintillation of gamma-ray-burst afterglows. , 2:449–460, November 1997.
- [68] D. A. Frail, S. R. Kulkarni, L. Nicastro, M. Feroci, and G. B. Taylor. The radio afterglow from the γ -ray burst of 8 May 1997. , 389:261–263, September 1997.
- [69] G. B. Taylor, D. A. Frail, E. Berger, and S. R. Kulkarni. The Angular Size and Proper Motion of the Afterglow of GRB 030329. , 609:L1–L4, July 2004.
- [70] B. Paczynski and J. E. Rhoads. Radio Transients from Gamma-Ray Bursters. , 418:L5, November 1993.
- [71] J. I. Katz. Two populations and models of gamma-ray bursts. , 422:248–259, February 1994.
- [72] D. Eichler, M. Livio, T. Piran, and D. N. Schramm. Nucleosynthesis, neutrino bursts and gamma-rays from coalescing neutron stars. , 340:126–128, July 1989.
- [73] R. Narayan, B. Paczynski, and T. Piran. Gamma-ray bursts as the death throes of massive binary stars. , 395:L83–L86, August 1992.
- [74] E. Berger. Short-Duration Gamma-Ray Bursts. , 52:43–105, August 2014.
- [75] J. A. van Paradijs. Gamma-Ray Bursts in Relation to Black-Hole Formation. In L. Kaper, E. P. J. V. D. Heuvel, and P. A. Woudt, editors, *Black Holes in Binaries and Galactic Nuclei*, page 316, 2001.
- [76] S. E. Woosley, A. I. MacFadyen, and A. Heger. Collapsars, gamma-ray bursts, and supernovae. In M. Livio, N. Panagia, and K. Sahu, editors, *Supernovae and Gamma-Ray Bursts: the Greatest Explosions since the Big Bang*, volume 13, pages 171–183, 2001.
- [77] J. C. Wheeler. Conference summary: Supernovae and gamma-ray bursts. In M. Livio, N. Panagia, and K. Sahu, editors, *Supernovae and Gamma-Ray Bursts: the Greatest Explosions since the Big Bang*, volume 13, pages 356–376, 2001.
- [78] K. W. Weiler, N. Panagia, M. J. Montes, and R. A. Sramek. Radio emission from supernovae and gamma ray-bursters. , 73:1144–1154, 2002.
- [79] P. Mészáros. Theories of Gamma-Ray Bursts. , 40:137–169, 2002.
- [80] J. B. Bloom, J. X. Prochaska, D. Pooley, C. W. Blake, R. J. Foley, S. Jha, E. Ramirez-Ruiz, J. Granot, A. V. Filippenko, S. Sigurdsson, A. J. Barth, H. W. Chen, M. C. Cooper, E. E. Falco, R. R. Gal, B. F. Gerke, M. D. Gladders, J. Greene, J. Hennanwi, L. C. Ho, K. Hurley, B. P. Koester, W. Li, L. Lubin, J. Newman, D. A. Perley, G. K. Squires, and W. M. Wood-Vasey. Closing in on

- a Short-Hard Burst Progenitor: Constraints from Early-Time Optical Imaging and Spectroscopy of a Possible Host Galaxy of GRB 050509b. In *American Astronomical Society Meeting Abstracts #206*, volume 37 of *Bulletin of the American Astronomical Society*, page 793, September 2005.
- [81] T. Matheson. The Supernovae Associated with Gamma-Ray Bursts. In M. Turatto, S. Benetti, L. Zampieri, and W. Shea, editors, *1604-2004: Supernovae as Cosmological Lighthouses*, volume 342 of *Astronomical Society of the Pacific Conference Series*, page 309, December 2005.
- [82] M. Della Valle. Supernovae shedding light on gamma-ray bursts. *Nuovo Cimento C Geophysics Space Physics C*, 28:563, July 2005.
- [83] P. Höflich, D. Baade, A. Khokhlov, L. Wang, and J. C. Wheeler. The Supernova/GRB Connection. In J.-M. Marcaide and K. W. Weiler, editors, *IAU Colloq. 192: Cosmic Explosions, On the 10th Anniversary of SN1993J*, page 403, 2005.
- [84] S. E. Woosley and J. S. Bloom. The Supernova Gamma-Ray Burst Connection. , 44:507–556, September 2006.
- [85] C. Wainwright, E. Berger, and B. E. Penprase. A Morphological Study of Gamma-Ray Burst Host Galaxies. , 657:367–377, March 2007.
- [86] J. Hjorth and J. S. Bloom. *The Gamma-Ray Burst - Supernova Connection*, pages 169–190. November 2012.
- [87] N. Gehrels. The Swift Gamma-Ray Burst Mission. In V. Schoenfelder, G. Lichti, and C. Winkler, editors, *5th INTEGRAL Workshop on the INTEGRAL Universe*, volume 552 of *ESA Special Publication*, page 777, October 2004.
- [88] N. Gehrels, C. L. Sarazin, P. T. O’Brien, B. Zhang, L. Barbier, S. D. Barthelmy, A. Blustin, D. N. Burrows, J. Cannizzo, J. R. Cummings, M. Goad, S. T. Holland, C. P. Hurkett, J. A. Kennea, A. Levan, C. B. Markwardt, K. O. Mason, P. Meszaros, M. Page, D. M. Palmer, E. Rol, T. Sakamoto, R. Willingale, L. Angelini, A. Beardmore, P. T. Boyd, A. Breeveld, S. Campana, M. M. Chester, G. Chincarini, L. R. Cominsky, G. Cusumano, M. de Pasquale, E. E. Fenimore, P. Giommi, C. Gronwall, D. Grupe, J. E. Hill, D. Hinshaw, J. Hjorth, D. Hullinger, K. C. Hurley, S. Klose, S. Kobayashi, C. Kouveliotou, H. A. Krimm, V. Mangano, F. E. Marshall, K. McGowan, A. Moretti, R. F. Mushotzky, K. Nakazawa, J. P. Norris, J. A. Nousek, J. P. Osborne, K. Page, A. M. Parsons, S. Patel, M. Perri, T. Poole, P. Romano, P. W. A. Roming, S. Rosen, G. Sato, P. Schady, A. P. Smale, J. Sollerman, R. Starling, M. Still, M. Suzuki, G. Tagliaferri, T. Takahashi, M. Tashiro, J. Tueller, A. A. Wells, N. E. White, and R. A. M. J. Wijers. A short γ -ray burst apparently associated with an elliptical galaxy at redshift $z = 0.225$. , 437(7060):851–854, October 2005.
- [89] A. Cucchiara, A. J. Levan, D. B. Fox, N. R. Tanvir, T. N. Ukwatta, E. Berger, T. Krühler, A. Küpcü Yoldaş, X. F. Wu, K. Toma, J. Greiner, F. E. Olivares, A. Rowlinson, L. Amati, T. Sakamoto, K. Roth, A. Stephens, Alexander Fritz, J. P. U. Fynbo, J. Hjorth, D. Malesani, P. Jakobsson, K. Wiersema, P. T. O’Brien, A. M. Soderberg, R. J. Foley, A. S. Fruchter, J. Rhoads, R. E. Rutledge, B. P. Schmidt, M. A. Dopita, P. Podsiadlowski, R. Willingale, C. Wolf,

- S. R. Kulkarni, and P. D'Avanzo. A Photometric Redshift of $z \sim 9.4$ for GRB 090429B. , 736(1):7, July 2011.
- [90] J. D. Gropp, J. A. Kennea, N. J. Klingler, H. A. Krimm, S. J. Laporte, A. Y. Lien, M. J. Moss, D. M. Palmer, B. Sbarufatti, and M. H. Siegel. GRB 190114C: Swift detection of a very bright burst with a bright optical counterpart. *GRB Coordinates Network*, 23688:1, January 2019.
- [91] W. B. Atwood, A. A. Abdo, M. Ackermann, W. Althouse, B. Anderson, M. Axelsson, L. Baldini, J. Ballet, D. L. Band, G. Barbiellini, and et al. The Large Area Telescope on the Fermi Gamma-Ray Space Telescope Mission. , 697:1071–1102, June 2009.
- [92] A. A. Abdo, M. Ackermann, M. Ajello, K. Asano, W. B. Atwood, M. Axelsson, L. Baldini, J. Ballet, G. Barbiellini, M. G. Baring, D. Bastieri, K. Bechtol, R. Bellazzini, B. Berenji, P. N. Bhat, E. Bissaldi, R. D. Blandford, E. D. Bloom, E. Bonamente, A. W. Borgland, A. Bouvier, J. Bregeon, A. Brez, M. S. Briggs, M. Brigida, P. Bruel, J. M. Burgess, D. N. Burrows, S. Buson, G. A. Calianandro, R. A. Cameron, P. A. Caraveo, J. M. Casand jian, C. Cecchi, Ö. Çelik, A. Chekhtman, C. C. Cheung, J. Chiang, S. Ciprini, R. Claus, J. Cohen-Tanugi, L. R. Cominsky, V. Connaughton, J. Conrad, S. Cutini, V. d'Elia, C. D. Dermer, A. de Angelis, F. de Palma, S. W. Digel, B. L. Dingus, E. do Couto e Silva, P. S. Drell, R. Dubois, D. Dumora, C. Farnier, C. Favuzzi, S. J. Fegan, J. Finke, G. Fishman, W. B. Focke, P. Fortin, M. Frailis, Y. Fukazawa, S. Funk, P. Fusco, F. Gargano, N. Gehrels, S. Germani, G. Giavitto, B. Giebels, N. Giglietto, F. Giordano, T. Glanzman, G. Godfrey, A. Goldstein, J. Granot, J. Greiner, I. A. Grenier, J. E. Grove, L. Guillemot, S. Guiriec, Y. Hanabata, A. K. Harding, M. Hayashida, E. Hays, D. Horan, R. E. Hughes, M. S. Jackson, G. Jóhannesson, A. S. Johnson, R. P. Johnson, W. N. Johnson, T. Kamae, H. Katagiri, J. Kataoka, N. Kawai, M. Kerr, R. M. Kippen, J. Knödseder, D. Kocevski, N. Komin, C. Kouveliotou, M. Kuss, J. Lande, L. Latronico, M. Lemoine-Goumard, F. Longo, F. Loparco, B. Lott, M. N. Lovellette, P. Lubrano, G. M. Madejski, A. Makeev, M. N. Mazziotta, S. McBreen, J. E. McEnery, S. McGlynn, C. Meegan, P. Mészáros, C. Meurer, P. F. Michelson, W. Mitthumsiri, T. Mizuno, A. A. Moiseev, C. Monte, M. E. Monzani, E. Moretti, A. Morselli, I. V. Moskalenko, S. Murgia, T. Nakamori, P. L. Nolan, J. P. Norris, E. Nuss, M. Ohno, T. Ohsugi, N. Omodei, E. Orlando, J. F. Ormes, W. S. Paciesas, D. Paneque, J. H. Panetta, V. Pelassa, M. Pepe, M. Pesce-Rollins, V. Petrosian, F. Piron, T. A. Porter, R. Preece, S. Rainò, R. Rando, A. Rau, M. Razzano, S. Razzaque, A. Reimer, O. Reimer, T. Reposeur, S. Ritz, L. S. Rochester, A. Y. Rodriguez, P. W. A. Roming, M. Roth, F. Ryde, H. F. W. Sadrozinski, D. Sanchez, A. Sander, P. M. Saz Parkinson, J. D. Scargle, T. L. Schalk, C. Sgrò, E. J. Siskind, P. D. Smith, P. Spinelli, M. Stamatikos, F. W. Stecker, G. Stratta, M. S. Strickman, D. J. Suson, C. A. Swenson, H. Tajima, H. Takahashi, T. Tanaka, J. B. Thayer, J. G. Thayer, D. J. Thompson, L. Tibaldo, D. F. Torres, G. Tosti, A. Tramacere, Y. Uchiyama, T. Uehara, T. L. Usher, A. J. van der Horst, V. Vasileiou, N. Vilchez, V. Vitale, A. von Kienlin, A. P. Waite, P. Wang, C. Wilson-Hodge, B. L. Winer, K. S. Wood, R. Yamazaki, T. Ylinen, and M. Ziegler. Fermi Observations of GRB 090902B: A Distinct Spectral Component in the Prompt and Delayed Emission. , 706(1):L138–L144, November 2009.

- [93] M. Ackermann, K. Asano, W. B. Atwood, M. Axelsson, L. Baldini, J. Ballet, G. Barbiellini, M. G. Baring, D. Bastieri, K. Bechtol, R. Bellazzini, B. Berenji, P. N. Bhat, E. Bissaldi, R. D. Blandford, E. D. Bloom, E. Bonamente, A. W. Borgland, A. Bouvier, J. Bregeon, A. Brez, M. S. Briggs, M. Brigida, P. Bruel, S. Buson, G. A. Caliandro, R. A. Cameron, P. A. Caraveo, S. Carrigan, J. M. Casand jian, C. Cecchi, Ö. Çelik, E. Charles, J. Chiang, S. Ciprini, R. Claus, J. Cohen-Tanugi, V. Connaughton, J. Conrad, C. D. Dermer, F. de Palma, B. L. Dingus, E. do Couto e. Silva, P. S. Drell, R. Dubois, D. Dumora, C. Farnier, C. Favuzzi, S. J. Fegan, J. Finke, W. B. Focke, M. Frailis, Y. Fukazawa, P. Fusco, F. Gargano, D. Gasparri, N. Gehrels, S. Germani, N. Giglietto, F. Giordano, T. Glanzman, G. Godfrey, J. Granot, I. A. Grenier, M. H. Grondin, J. E. Grove, S. Guiriec, D. Hadasch, A. K. Harding, E. Hays, D. Horan, R. E. Hughes, G. Jóhannesson, W. N. Johnson, T. Kamae, H. Katagiri, J. Kataoka, N. Kawai, R. M. Kippen, J. Knödseder, D. Kocevski, C. Kouveliotou, M. Kuss, J. Lande, L. Latronico, M. Lemoine-Goumard, M. Llena Garde, F. Longo, F. Loparco, B. Lott, M. N. Lovellette, P. Lubrano, A. Makeev, M. N. Mazziotta, J. E. McEnery, S. McGlynn, C. Meegan, P. Mészáros, P. F. Michelson, W. Mitthumsiri, T. Mizuno, A. A. Moiseev, C. Monte, M. E. Monzani, E. Moretti, A. Morselli, I. V. Moskalenko, S. Murgia, H. Nakajima, T. Nakamori, P. L. Nolan, J. P. Norris, E. Nuss, M. Ohno, T. Ohsugi, N. Omodei, E. Orlando, J. F. Ormes, M. Ozaki, W. S. Paciesas, D. Paneque, J. H. Panetta, D. Parent, V. Pelassa, M. Pepe, M. Pesce-Rollins, F. Piron, R. Preece, S. Rainò, R. Rando, M. Razzano, S. Razzaque, A. Reimer, S. Ritz, A. Y. Rodriguez, M. Roth, F. Ryde, H. F. W. Sadrozinski, A. Sander, J. D. Scargle, T. L. Schalk, C. Sgrò, E. J. Siskind, P. D. Smith, G. Spandre, P. Spinelli, M. Stamatikos, F. W. Stecker, M. S. Strickman, D. J. Suson, H. Tajima, H. Takahashi, T. Takahashi, T. Tanaka, J. B. Thayer, J. G. Thayer, D. J. Thompson, L. Tibaldo, K. Toma, D. F. Torres, G. Tosti, A. Tramacere, Y. Uchiyama, T. Uehara, T. L. Usher, A. J. van der Horst, V. Vasileiou, N. Vilchez, V. Vitale, A. von Kienlin, A. P. Waite, P. Wang, C. Wilson-Hodge, B. L. Winer, X. F. Wu, R. Yamazaki, Z. Yang, T. Ylinen, and M. Ziegler. Fermi Observations of GRB 090510: A Short-Hard Gamma-ray Burst with an Additional, Hard Power-law Component from 10 keV TO GeV Energies. , 716(2):1178–1190, June 2010.
- [94] M. Ackermann, M. Ajello, K. Asano, M. Axelsson, L. Baldini, J. Ballet, G. Barbiellini, D. Bastieri, K. Bechtol, R. Bellazzini, P. N. Bhat, E. Bissaldi, E. D. Bloom, E. Bonamente, J. Bonnell, A. Bouvier, T. J. Brand t, J. Bregeon, M. Brigida, P. Bruel, R. Buehler, J. Michael Burgess, S. Buson, D. Byrne, G. A. Caliandro, R. A. Cameron, P. A. Caraveo, C. Cecchi, E. Charles, R. C. G. Chaves, A. Chekhtman, J. Chiang, G. Chiaro, S. Ciprini, R. Claus, J. Cohen-Tanugi, V. Connaughton, J. Conrad, S. Cutini, F. D’Ammand o, A. de Angelis, F. de Palma, C. D. Dermer, R. Desiante, S. W. Digel, B. L. Dingus, L. Di Venere, P. S. Drell, A. Drlica-Wagner, R. Dubois, C. Favuzzi, E. C. Ferrara, G. Fitzpatrick, S. Foley, A. Franckowiak, Y. Fukazawa, P. Fusco, F. Gargano, D. Gasparri, N. Gehrels, S. Germani, N. Giglietto, P. Giommi, F. Giordano, M. Giroletti, T. Glanzman, G. Godfrey, A. Goldstein, J. Granot, I. A. Grenier, J. E. Grove, D. Gruber, S. Guiriec, D. Hadasch, Y. Hanabata, M. Hayashida, D. Horan, X. Hou, R. E. Hughes, Y. Inoue, M. S. Jackson, T. Jogler, G. Jóhannesson, A. S. Johnson, W. N. Johnson, T. Kamae, J. Kataoka, T. Kawano, R. M. Kippen, J. Knödseder, D. Kocevski, C. Kouveliotou, M. Kuss, J. Lande, S. Larsson, L. Latronico, S. H. Lee, F. Longo, F. Loparco, M. N. Lovellette, P. Lubrano, F. Massaro, M. Mayer, M. N. Mazziotta, S. McBreen, J. E. McEnery, S. McG-

- lynn, P. F. Michelson, T. Mizuno, A. A. Moiseev, C. Monte, M. E. Monzani, E. Moretti, A. Morselli, S. Murgia, R. Nemmen, E. Nuss, T. Nymark, M. Ohno, T. Ohsugi, N. Omodei, M. Orienti, E. Orlando, W. S. Paciesas, D. Paneque, J. H. Panetta, V. Pelassa, J. S. Perkins, M. Pesce-Rollins, F. Piron, G. Pivato, T. A. Porter, R. Preece, J. L. Racusin, S. Rainò, R. Rando, A. Rau, M. Razzano, S. Razzaque, A. Reimer, O. Reimer, T. Reposeur, S. Ritz, C. Romoli, M. Roth, F. Ryde, P. M. Saz Parkinson, T. L. Schalk, C. Sgrò, E. J. Siskind, E. Sonbas, G. Spandre, P. Spinelli, D. J. Suson, H. Tajima, H. Takahashi, Y. Takeuchi, Y. Tanaka, J. G. Thayer, J. B. Thayer, D. J. Thompson, L. Tibaldo, D. Tierney, M. Tinivella, D. F. Torres, G. Tosti, E. Troja, V. Tronconi, T. L. Usher, J. Vandenbroucke, A. J. van der Horst, V. Vasileiou, G. Vianello, V. Vitale, A. von Kienlin, B. L. Winer, K. S. Wood, M. Wood, S. Xiong, and Z. Yang. The First Fermi-LAT Gamma-Ray Burst Catalog. , 209(1):11, November 2013.
- [95] A. Goldstein, P. Veres, E. Burns, M. S. Briggs, R. Hamburg, D. Kocevski, C. A. Wilson-Hodge, R. D. Preece, S. Poolakkil, O. J. Roberts, C. M. Hui, V. Connaughton, J. Racusin, A. von Kienlin, T. Dal Canton, N. Christensen, T. Littenberg, K. Siellez, L. Blackburn, J. Broida, E. Bissaldi, W. H. Cleveland, M. H. Gibby, M. M. Giles, R. M. Kippen, S. McBreen, J. McEnery, C. A. Meegan, W. S. Paciesas, and M. Stanbro. An Ordinary Short Gamma-Ray Burst with Extraordinary Implications: Fermi-GBM Detection of GRB 170817A. , 848:L14, October 2017.
- [96] B. Grossan, I. H. Park, S. Ahmad, K. B. Ahn, P. Barrillon, S. Brandt, C. Budtz-Jørgensen, A. J. Castro-Tirado, P. Chen, H. S. Choi, Y. J. Choi, P. Connell, S. Dagoret-Campagne, C. De La Taille, C. Eyles, I. Hermann, M.-H. A. Huang, A. Jung, S. Jeong, J. E. Kim, M. Kim, S.-W. Kim, Y. W. Kim, J. Lee, H. Lim, E. V. Linder, T.-C. Liu, N. Lund, K. W. Min, G. W. Na, J. W. Nam, M. I. Panasyuk, J. Ripa, V. Reglero, J. M. Rodrigo, G. F. Smoot, J. E. Suh, S. Svertilov, N. Vedenkin, M.-Z. Wang, I. Yashin, and M. H. Zhao. A next generation Ultra-Fast Flash Observatory (UFFO-100) for IR/optical observations of the rise phase of gamma-ray bursts. In *Space Telescopes and Instrumentation 2012: Ultraviolet to Gamma Ray*, volume 8443 of , page 84432R, September 2012.
- [97] I. H. Park, S. Ahmad, P. Barrillon, S. Brandt, C. Budtz-Jørgensen, A. J. Castro-Tirado, P. Chen, Y. J. Choi, P. Connell, S. Dagoret-Campagne, C. Eyles, B. Grossan, M.-H. A. Huang, A. Jung, S. Jeong, J. E. Kim, M. B. Kim, S.-W. Kim, Y. W. Kim, A. S. Krasnov, J. Lee1, H. Lim, E. V. Linder, T.-C. Liu, N. Lund, K. W. Min, G. W. Na, J. W. Nam, M. I. Panasyuk, J. Ripa, V. Reglero, J. M. Rodrigo, G. F. Smoot, J. E. Suh, S. Svertilov, N. Vedenkin, M.-Z. Wang, and I. Yashin. Ultra-Fast Flash Observatory (uffo) for Observation of Early Photons from Gamma Ray Bursts. In *Towards Ultimate Understanding of the Universe*, pages 259–273, December 2013.
- [98] F.-J. Lu, S. Zhang, B.-B. Wu, Y. Chen, X.-L. Cao, Z. Zhang, J.-K. Deng, S.-N. Zhang, and T.-P. Li. The Hard X-ray modulation Telescope (HXMT) Mission. In N. Kawai, T. Mihara, M. Kohama, and M. Suzuki, editors, *Astrophysics with All-Sky X-Ray Observations*, page 368, March 2009.
- [99] D. A. Frail. The EVLA: A New Mission for High Energy Astrophysics. In *AAS/High Energy Astrophysics Division #11*, volume 42 of *Bulletin of the American Astronomical Society*, page 740, March 2010.

- [100] Y. Urata, K. Huang, and S. Takahashi. Gamma-Ray Burst Afterglows with ALMA. In D. Iono, K. Tatematsu, A. Wootten, and L. Testi, editors, *Revolution in Astronomy with ALMA: The Third Year*, volume 499 of *Astronomical Society of the Pacific Conference Series*, page 339, December 2015.
- [101] Lofar Transients Key Science Project, J. van Leeuwen, and LOFAR Transients Key Science Project. Neutron stars and gamma-ray bursts with LOFAR. *Advances in Space Research*, 47:1441–1443, April 2011.
- [102] F. Piron and SVOM Consortium. The SVOM Gamma-Ray Burst Mission. In *Eighth Huntsville Gamma-Ray Burst Symposium*, volume 1962 of *LPI Contributions*, page 4058, October 2016.
- [103] Amotz Shemi and Tsvi Piran. The Appearance of Cosmic Fireballs. , 365:L55, December 1990.
- [104] M. J. Rees and P. Meszaros. Relativistic fireballs - Energy conversion and time-scales. , 258:41P–43P, September 1992.
- [105] M. J. Rees and P. Meszaros. Unsteady Outflow Models for Cosmological Gamma-Ray Bursts. , 430:L93, August 1994.
- [106] T. Piran. Gamma-ray bursts and the fireball model. , 314:575–667, June 1999.
- [107] R. D. Blandford and C. F. McKee. Fluid dynamics of relativistic blast waves. *Physics of Fluids*, 19:1130–1138, August 1976.
- [108] R. Sari and T. Piran. Hydrodynamic Timescales and Temporal Structure of Gamma-Ray Bursts. , 455:L143, December 1995.
- [109] P. Mészáros. Gamma-ray bursts. *Reports on Progress in Physics*, 69:2259–2321, August 2006.
- [110] Re'em Sari, Tsvi Piran, and Ramesh Narayan. Spectra and Light Curves of Gamma-Ray Burst Afterglows. , 497(1):L17–L20, Apr 1998.
- [111] N. S. Kardashev. Nonstationarity of Spectra of Young Sources of Nonthermal Radio Emission. 39:393, 1962.
- [112] Poonam Chandra. Gamma-Ray Bursts: A Radio Perspective. *Advances in Astronomy*, 2016:296781, January 2016.
- [113] M. Lyutikov and J. Camilo Jaramillo. Early GRB Afterglows from Reverse Shocks in Ultra-relativistic, Long-lasting Winds. 835:206, February 2017.
- [114] A. M. Atoyan and F. A. Aharonian. On the mechanisms of gamma radiation in the Crab Nebula. , 278(2):525–541, Jan 1996.
- [115] R. Blandford and D. Eichler. Particle Acceleration at Astrophysical Shocks - a Theory of Cosmic-Ray Origin. , 154:1–+, October 1987.
- [116] S. S. Komissarov and Y. E. Lyubarsky. Synchrotron nebulae created by anisotropic magnetized pulsar winds. , 349(3):779–792, Apr 2004.

- [117] L. Del Zanna, E. Amato, and N. Bucciantini. Axially symmetric relativistic MHD simulations of Pulsar Wind Nebulae in Supernova Remnants. On the origin of torus and jet-like features. , 421:1063–1073, Jul 2004.
- [118] Oliver Porth, Serguei S. Komissarov, and Rony Keppens. Three-dimensional magnetohydrodynamic simulations of the Crab nebula. , 438(1):278–306, Feb 2014.
- [119] Oliver Porth, Rolf Buehler, Barbara Olmi, Serguei Komissarov, Astrid Lamberts, Elena Amato, Yajie Yuan, and Alexander Rudy. Modelling Jets, Tori and Flares in Pulsar Wind Nebulae. , 207(1-4):137–174, Jul 2017.
- [120] M. F. Bietenholz, N. Kassim, D. A. Frail, R. A. Perley, W. C. Erickson, and A. R. Hajian. The Radio Spectral Index of the Crab Nebula. , 490(1):291–301, Nov 1997.
- [121] Stephen P. Reynolds, George G. Pavlov, Oleg Kargaltsev, Noel Klingler, Matthieu Renaud, and Sandro Mereghetti. Pulsar-Wind Nebulae and Magnetar Outflows: Observations at Radio, X-Ray, and Gamma-Ray Wavelengths. , 207(1-4):175–234, Jul 2017.
- [122] Jonathan Arons. Pulsars: Progress, Problems and Prospects. *arXiv e-prints*, page arXiv:0708.1050, Aug 2007.
- [123] Jonathan Arons. Pulsar Wind Nebulae as Cosmic Pevatrons: A Current Sheet’s Tale. , 173(1-4):341–367, Nov 2012.
- [124] W. M. Fawley, J. Arons, and E. T. Scharlemann. Potential drops above pulsar polar caps: acceleration of nonneutral beams from the stellar surface. , 217:227–243, Oct 1977.
- [125] Alice K. Harding and Alexander G. Muslimov. Particle Acceleration Zones above Pulsar Polar Caps: Electron and Positron Pair Formation Fronts. , 508(1):328–346, Nov 1998.
- [126] Johann A. Hirsbman and Jonathan Arons. Pair Production Multiplicities in Rotation-powered Pulsars. , 560(2):871–884, Oct 2001.
- [127] F. V. Coroniti. Magnetically Striped Relativistic Magnetohydrodynamic Winds: The Crab Nebula Revisited. , 349:538, Feb 1990.
- [128] Y. Lyubarsky and J. G. Kirk. Reconnection in a Striped Pulsar Wind. , 547(1):437–448, Jan 2001.
- [129] Maxim Lyutikov and Roger Blandford. Gamma Ray Bursts as Electromagnetic Outflows. *arXiv e-prints*, pages astro-ph/0312347, Dec 2003.
- [130] M. Lyutikov. The electromagnetic model of gamma-ray bursts. *New Journal of Physics*, 8(7):119, Jul 2006.
- [131] O. Porth, S. S. Komissarov, and R. Keppens. Solution to the sigma problem of pulsar wind nebulae. , 431:L48–L52, Apr 2013.
- [132] Jonathan Zrake and Jonathan Arons. Turbulent Magnetic Relaxation in Pulsar Wind Nebulae. , 847(1):57, Sep 2017.

- [133] Shuta J. Tanaka, Kenji Toma, and Nozomu Tominaga. Confinement of the Crab Nebula with tangled magnetic field by its supernova remnant. , 478(4):4622–4633, Aug 2018.
- [134] M. Tavani, A. Bulgarelli, V. Vittorini, A. Pellizzoni, E. Striani, P. Caraveo, M. C. Weisskopf, A. Tennant, G. Pucella, A. Trois, E. Costa, Y. Evangelista, C. Pittori, F. Verrecchia, E. Del Monte, R. Campana, M. Pilia, A. De Luca, I. Donnarumma, D. Horns, C. Ferrigno, C. O. Heinke, M. Trifoglio, F. Gianotti, S. Vercellone, A. Argan, G. Barbiellini, P. W. Cattaneo, A. W. Chen, T. Contessi, F. D’Ammando, G. DeParis, G. Di Cocco, G. Di Persio, M. Feroci, A. Ferrari, M. Galli, A. Giuliani, M. Giusti, C. Labanti, I. Lapshov, F. Lazzarotto, P. Lipari, F. Longo, F. Fuschino, M. Marisaldi, S. Mereghetti, E. Morelli, E. Moretti, A. Morselli, L. Pacciani, F. Perotti, G. Piano, P. Picozza, M. Prest, M. Rapisarda, A. Rappoldi, A. Rubini, S. Sabatini, P. Soffitta, E. Vallazza, A. Zambra, D. Zanello, F. Lucarelli, P. Santolamazza, P. Giommi, L. Salotti, and G. F. Bignami. Discovery of Powerful Gamma-Ray Flares from the Crab Nebula. *Science*, 331(6018):736, Feb 2011.
- [135] A. A. Abdo, M. Ackermann, M. Ajello, A. Allafort, L. Baldini, J. Ballet, G. Barbiellini, D. Bastieri, K. Bechtol, R. Bellazzini, B. Berenji, R. D. Blandford, E. D. Bloom, E. Bonamente, A. W. Borgland, A. Bouvier, T. J. Brandt, J. Bregeon, A. Brez, M. Brigida, P. Bruel, R. Buehler, S. Buson, G. A. Calianandro, R. A. Cameron, A. Cannon, P. A. Caraveo, J. M. Casandjian, Ö. Çelik, E. Charles, A. Chekhtman, C. C. Cheung, J. Chiang, S. Ciprini, R. Claus, J. Cohen-Tanugi, L. Costamante, S. Cutini, F. D’Ammando, C. D. Dermer, A. de Angelis, A. de Luca, F. de Palma, S. W. Digel, E. do Couto e Silva, P. S. Drell, A. Drlica-Wagner, R. Dubois, D. Dumora, C. Favuzzi, S. J. Fegan, E. C. Ferrara, W. B. Focke, P. Fortin, M. Frailis, Y. Fukazawa, S. Funk, P. Fusco, F. Gargano, D. Gasparrini, N. Gehrels, S. Germani, N. Giglietto, F. Giordano, M. Giroletti, T. Glanzman, G. Godfrey, I. A. Grenier, M. H. Grondin, J. E. Grove, S. Guiriec, D. Hadasch, Y. Hanabata, A. K. Harding, K. Hayashi, M. Hayashida, E. Hays, D. Horan, R. Itoh, G. Jóhannesson, A. S. Johnson, T. J. Johnson, D. Khangulyan, T. Kamae, H. Katagiri, J. Kataoka, M. Kerr, J. Knödlseider, M. Kuss, J. Lande, L. Latronico, S. H. Lee, M. Lemoine-Goumard, F. Longo, F. Loparco, P. Lubrano, G. M. Madejski, A. Makeev, M. Marelli, M. N. Mazziotta, J. E. McEnery, P. F. Michelson, W. Mitthumsiri, T. Mizuno, A. A. Moiseev, C. Monte, M. E. Monzani, A. Morselli, I. V. Moskalenko, S. Murgia, T. Nakamori, M. Naumann-Godo, P. L. Nolan, J. P. Norris, E. Nuss, T. Ohsugi, A. Okumura, N. Omodei, J. F. Ormes, M. Ozaki, D. Paneque, D. Parent, V. Pelassa, M. Pepe, M. Pesce-Rollins, M. Pierbattista, F. Piron, T. A. Porter, S. Rainò, R. Rando, P. S. Ray, M. Razzano, A. Reimer, O. Reimer, T. Reposeur, S. Ritz, R. W. Romani, H. F. W. Sadrozinski, D. Sanchez, P. M. Saz Parkinson, J. D. Scargle, T. L. Schalk, C. Sgrò, E. J. Siskind, P. D. Smith, G. Spandre, P. Spinelli, M. S. Strickman, D. J. Suson, H. Takahashi, T. Takahashi, T. Tanaka, J. B. Thayer, D. J. Thompson, L. Tibaldo, D. F. Torres, G. Tosti, A. Tramacere, E. Troja, Y. Uchiyama, J. Vandenbroucke, V. Vasileiou, G. Vianello, V. Vitale, P. Wang, K. S. Wood, Z. Yang, and M. Ziegler. Gamma-Ray Flares from the Crab Nebula. *Science*, 331(6018):739, Feb 2011.
- [136] R. Buehler, J. D. Scargle, R. D. Blandford, L. Baldini, M. G. Baring, A. Belfiore, E. Charles, J. Chiang, F. D’Ammando, C. D. Dermer, S. Funk, J. E. Grove, A. K. Harding, E. Hays, M. Kerr, F. Massaro, M. N. Mazziotta, R. W. Romani,

- P. M. Saz Parkinson, A. F. Tennant, and M. C. Weisskopf. Gamma-Ray Activity in the Crab Nebula: The Exceptional Flare of 2011 April. , 749(1):26, Apr 2012.
- [137] Maxim Lyutikov. A high-sigma model of pulsar wind nebulae. , 405(3):1809–1815, Jul 2010.
- [138] E. Clausen-Brown and M. Lyutikov. Crab nebula gamma-ray flares as relativistic reconnection minijets. , 426(2):1374–1384, Oct 2012.
- [139] O. C. de Jager, A. K. Harding, P. F. Michelson, H. I. Nel, P. L. Nolan, P. Sreekumar, and D. J. Thompson. Gamma-Ray Observations of the Crab Nebula: A Study of the Synchro-Compton Spectrum. , 457:253, Jan 1996.
- [140] S. Zenitani and M. Hoshino. The Generation of Nonthermal Particles in the Relativistic Magnetic Reconnection of Pair Plasmas. , 562:L63–L66, November 2001.
- [141] Maxim Lyutikov and Dmitri Uzdensky. Dynamics of Relativistic Reconnection. , 589(2):893–901, Jun 2003.
- [142] Y. E. Lyubarsky. On the relativistic magnetic reconnection. , 358(1):113–119, Mar 2005.
- [143] Serguei S. Komissarov. Magnetic dissipation in the Crab nebula. , 428(3):2459–2466, Jan 2013.
- [144] Yuri Lyubarsky and Michael Liverts. Particle Acceleration in the Driven Relativistic Reconnection. , 682(2):1436–1442, Aug 2008.
- [145] M. Hoshino and Y. Lyubarsky. Relativistic Reconnection and Particle Acceleration. , 173(1-4):521–533, Nov 2012.
- [146] B. Cerutti, G. R. Werner, D. A. Uzdensky, and M. C. Begelman. Three-dimensional Relativistic Pair Plasma Reconnection with Radiative Feedback in the Crab Nebula. , 782(2):104, Feb 2014.
- [147] Maxim Lyutikov, Lorenzo Sironi, Serguei S. Komissarov, and Oliver Porth. Particle acceleration in relativistic magnetic flux-merging events. *Journal of Plasma Physics*, 83(6):635830602, Dec 2017.
- [148] Maxim Lyutikov, Lorenzo Sironi, Serguei S. Komissarov, and Oliver Porth. Explosive X-point collapse in relativistic magnetically dominated plasma. *Journal of Plasma Physics*, 83(6):635830601, Dec 2017.
- [149] Maxim Lyutikov, Serguei Komissarov, Lorenzo Sironi, and Oliver Porth. Particle acceleration in explosive relativistic reconnection events and Crab Nebula gamma-ray flares. *Journal of Plasma Physics*, 84(2):635840201, Apr 2018.
- [150] Stephen P. Reynolds. Synchrotron-Loss Spectral Breaks in Pulsar-Wind Nebulae and Extragalactic Jets. , 703(1):662–670, Sep 2009.
- [151] Maxim Lyutikov, Tea Temim, Sergey Komissarov, Patrick Slane, Lorenzo Sironi, and Luca Comisso. Interpreting Crab Nebula’s Synchrotron Spectrum: Two Acceleration Mechanisms. , page 2051, Aug 2019.

- [152] Luca Comisso and Lorenzo Sironi. Particle Acceleration in Relativistic Plasma Turbulence. , 121(25):255101, Dec 2018.
- [153] W. H. Matthaeus and S. L. Lamkin. Turbulent magnetic reconnection. *The Physics of Fluids*, 29(8):2513–2534, 1986.
- [154] L. Gratton. Source Models with Electron Diffusion. , 16(1):81–100, Apr 1972.
- [155] S. P. Reynolds and F. C. Jones. A Green’s Function Solution for the Spherical Diffusion Equation in the Presence of Energy Losses, and its Applications to Crablike Supernova Remnants. In *International Cosmic Ray Conference*, volume 2 of *International Cosmic Ray Conference*, page 400, Aug 1991.
- [156] Xiaping Tang and Roger A. Chevalier. Particle Transport in Young Pulsar Wind Nebulae. , 752(2):83, Jun 2012.
- [157] O. Porth, M. J. Vorster, M. Lyutikov, and N. E. Engelbrecht. Diffusion in pulsar wind nebulae: an investigation using magnetohydrodynamic and particle transport models. , 460(4):4135–4149, Aug 2016.
- [158] A. J. Dean, D. J. Clark, J. B. Stephen, V. A. McBride, L. Bassani, A. Bazzano, A. J. Bird, A. B. Hill, S. E. Shaw, and P. Ubertini. Polarized Gamma-Ray Emission from the Crab. *Science*, 321(5893):1183, Aug 2008.
- [159] M. Chauvin, H. G. Florén, M. Jackson, T. Kamae, T. Kawano, M. Kiss, M. Kole, V. Mikhalev, E. Moretti, G. Olofsson, S. Rydström, H. Takahashi, A. Iyudin, M. Arimoto, Y. Fukazawa, J. Kataoka, N. Kawai, T. Mizuno, F. Ryde, H. Tajima, T. Takahashi, and M. Pearce. Observation of polarized hard X-ray emission from the Crab by the PoGOLite Pathfinder. , 456(1):L84–L88, Feb 2016.
- [160] M. Chauvin, H. G. Florén, M. Friis, M. Jackson, T. Kamae, J. Kataoka, T. Kawano, M. Kiss, V. Mikhalev, T. Mizuno, N. Ohashi, T. Stana, H. Tajima, H. Takahashi, N. Uchida, and M. Pearce. Shedding new light on the Crab with polarized X-rays. *Scientific Reports*, 7:7816, Aug 2017.
- [161] M. Chauvin, H. G. Florén, M. Friis, M. Jackson, T. Kamae, J. Kataoka, T. Kawano, M. Kiss, V. Mikhalev, T. Mizuno, H. Tajima, H. Takahashi, N. Uchida, and M. Pearce. The PoGO+ view on Crab off-pulse hard X-ray polarization. , 477(1):L45–L49, Jun 2018.
- [162] A. Ritacco, J. F. Macías-Pérez, N. Ponthieu, R. Adam, P. Ade, P. André, J. Aumont, A. Beelen, A. Benoît, A. Bideaud, N. Billot, O. Bourrion, A. Bracco, M. Calvo, A. Catalano, G. Coiffard, B. Comis, A. D’Addabbo, M. De Petris, F. X. Désert, S. Doyle, J. Goupy, C. Kramer, G. Lagache, S. Leclercq, J. F. Lestrade, P. Mauskopf, F. Mayet, A. Maury, A. Monfardini, F. Pajot, E. Pascale, L. Perotto, G. Pisano, M. Rebolo-Iglesias, V. Revéret, L. Rodriguez, C. Romero, H. Roussel, F. Ruppim, K. Schuster, A. Sievers, G. Siringo, C. Thum, S. Triqueneaux, C. Tucker, H. Wiesemeyer, and R. Zylka. NIKA 150 GHz polarization observations of the Crab nebula and its spectral energy distribution. , 616:A35, Aug 2018.
- [163] Planck Collaboration, N. Aghanim, Y. Akrami, M. Ashdown, J. Aumont, C. Baccigalupi, M. Ballardini, A. J. Banday, R. B. Barreiro, N. Bartolo,

- S. Basak, K. Benabed, J. P. Bernard, M. Bersanelli, P. Bielewicz, J. R. Bond, J. Borrill, F. R. Bouchet, F. Boulanger, M. Bucher, C. Burigana, E. Calabrese, J. F. Cardoso, J. Carron, A. Challinor, H. C. Chiang, L. P. L. Colombo, C. Combet, F. Couchot, B. P. Crill, F. Cuttaia, P. de Bernardis, A. de Rosa, G. de Zotti, J. Delabrouille, J. M. Delouis, E. Di Valentino, J. M. Diego, O. Doré, M. Douspis, A. Ducout, X. Dupac, G. Efstathiou, F. Elsner, T. A. Enßlin, H. K. Eriksen, E. Falgarone, Y. Fantaye, F. Finelli, M. Frailis, A. A. Fraisse, E. Franceschi, A. Frolov, S. Galeotta, S. Galli, K. Ganga, R. T. Génova-Santos, M. Gerbino, T. Ghosh, J. González-Nuevo, K. M. Górski, S. Gratton, A. Gruppuso, J. E. Gudmundsson, W. Handley, F. K. Hansen, S. Henrot-Versillé, D. Herranz, E. Hivon, Z. Huang, A. H. Jaffe, W. C. Jones, A. Karakci, E. Keihänen, R. Keskitalo, K. Kiiveri, J. Kim, T. S. Kisner, N. Krachmalnicoff, M. Kunz, H. Kurki-Suonio, G. Lagache, J. M. Lamarre, A. Lasenby, M. Lattanzi, C. R. Lawrence, F. Levrier, M. Liguori, P. B. Lilje, V. Lindholm, M. López-Cañiego, Y. Z. Ma, J. F. Macías-Pérez, G. Maggio, D. Maino, N. Mandolese, A. Mangilli, P. G. Martin, E. Martínez-González, S. Matarrese, N. Mauri, J. D. McEwen, A. Melchiorri, A. Mennella, M. Migliaccio, M. A. Miville-Deschênes, D. Molinari, A. Moneti, L. Montier, G. Morgante, A. Moss, S. Mottet, P. Natoli, L. Pagano, D. Paoletti, B. Partridge, G. Patanchon, L. Patrizii, O. Perdereau, F. Perrotta, V. Pettorino, F. Piacentini, J. L. Puget, J. P. Rachen, M. Reinecke, M. Remazeilles, A. Renzi, G. Rocha, G. Roudier, L. Salvati, M. Sandri, M. Savelainen, D. Scott, C. Sirignano, G. Sirri, L. D. Spencer, R. Sunyaev, A. S. Suur-Uski, J. A. Tauber, D. Tavagnacco, M. Tenti, L. Toffolatti, M. Tomasi, M. Tristram, T. Trombetti, J. Valiviita, F. Vansyngel, B. Van Tent, L. Vibert, P. Vielva, F. Villa, N. Vittorio, B. D. Wandelt, I. K. Wehus, and A. Zonca. Planck 2018 results. III. High Frequency Instrument data processing and frequency maps. *arXiv e-prints*, page arXiv:1807.06207, Jul 2018.
- [164] Michael F. Bietenholz and Philipp P. Kronberg. Faraday Rotation and Physical Conditions in the Crab Nebula. , 368:231, Feb 1991.
- [165] Roger A. Chevalier. Young Core-Collapse Supernova Remnants and Their Supernovae. , 619(2):839–855, Feb 2005.
- [166] A. Lazarian and Ethan T. Vishniac. Reconnection in a Weakly Stochastic Field. , 517(2):700–718, Jun 1999.
- [167] V. Carbone, P. Veltri, and A. Mangeney. Coherent structure formation and magnetic field line reconnection in magnetohydrodynamic turbulence. *Physics of Fluids A*, 2(8):1487–1496, Aug 1990.
- [168] A. Mallet, A. A. Schekochihin, and B. D. G. Chandran. Disruption of sheet-like structures in Alfvénic turbulence by magnetic reconnection. , 468(4):4862–4871, Jul 2017.
- [169] Nuno F. Loureiro and Stanislav Boldyrev. Role of Magnetic Reconnection in Magnetohydrodynamic Turbulence. , 118(24):245101, Jun 2017.
- [170] L. Comisso, Y. M. Huang, M. Lingam, E. Hirvijoki, and A. Bhattacharjee. Magnetohydrodynamic Turbulence in the Plasmoid-mediated Regime. , 854(2):103, Feb 2018.
- [171] L. Comisso, M. Lingam, Y.-M. Huang, and A. Bhattacharjee. General theory of the plasmoid instability. *Physics of Plasmas*, 23(10):100702, October 2016.

- [172] D. A. Uzdensky and N. F. Loureiro. Magnetic Reconnection Onset via Disruption of a Forming Current Sheet by the Tearing Instability. *Physical Review Letters*, 116(10):105003, March 2016.
- [173] L. Comisso, M. Lingam, Y. M. Huang, and A. Bhattacharjee. Plasmoid Instability in Forming Current Sheets. , 850(2):142, Dec 2017.
- [174] Luca Comisso and Lorenzo Sironi. The Interplay of Magnetically Dominated Turbulence and Magnetic Reconnection in Producing Nonthermal Particles. , 886(2):122, Dec 2019.
- [175] V. Zhdankin, G. R. Werner, D. A. Uzdensky, and M. C. Begelman. Kinetic Turbulence in Relativistic Plasma: From Thermal Bath to Nonthermal Continuum. *Physical Review Letters*, 118(5):055103, February 2017.
- [176] L. Sironi and A. Spitkovsky. Relativistic Reconnection: An Efficient Source of Non-thermal Particles. , 783:L21, March 2014.
- [177] F. Guo, H. Li, W. Daughton, and Y.-H. Liu. Formation of Hard Power Laws in the Energetic Particle Spectra Resulting from Relativistic Magnetic Reconnection. *Physical Review Letters*, 113(15):155005, October 2014.
- [178] G. R. Werner, D. A. Uzdensky, B. Cerutti, K. Nalewajko, and M. C. Begelman. The Extent of Power-law Energy Spectra in Collisionless Relativistic Magnetic Reconnection in Pair Plasmas. , 816:L8, January 2016.
- [179] S. Zenitani, M. Hesse, and A. Klimas. Two-Fluid Magnetohydrodynamic Simulations of Relativistic Magnetic Reconnection. , 696:1385–1401, May 2009.
- [180] N. Bessho and A. Bhattacharjee. Fast Magnetic Reconnection and Particle Acceleration in Relativistic Low-density Electron-Positron Plasmas without Guide Field. , 750:129, May 2012.
- [181] B. Cerutti, G. R. Werner, D. A. Uzdensky, and M. C. Begelman. Beaming and Rapid Variability of High-energy Radiation from Relativistic Pair Plasma Reconnection. *The Astrophysical Journal*, 754(2):L33, Aug 2012.
- [182] D. Kagan, L. Sironi, B. Cerutti, and D. Giannios. Relativistic Magnetic Reconnection in Pair Plasmas and Its Astrophysical Applications. *Space Science Reviews*, 191:545, January 2015.
- [183] Y.-H. Liu, F. Guo, W. Daughton, H. Li, and M. Hesse. Scaling of Magnetic Reconnection in Relativistic Collisionless Pair Plasmas. *Physical Review Letters*, 114(9):095002, March 2015.
- [184] L. Sironi, D. Giannios, and M. Petropoulou. Plasmoids in relativistic reconnection, from birth to adulthood: first they grow, then they go. , 462:48–74, October 2016.
- [185] L. Comisso and A. Bhattacharjee. On the value of the reconnection rate. *Journal of Plasma Physics*, 82(6):595820601, Dec 2016.
- [186] G. R. Werner and D. A. Uzdensky. Nonthermal Particle Acceleration in 3D Relativistic Magnetic Reconnection in Pair Plasma. , 843:L27, July 2017.

- [187] Martin Lemoine. Generalized Fermi acceleration. , 99(8):083006, Apr 2019.
- [188] Maxim Lyutikov, Serguei Komissarov, Lorenzo Sironi, and Oliver Porth. Particle acceleration in explosive relativistic reconnection events and Crab Nebula gamma-ray flares. *Journal of Plasma Physics*, 84(2):635840201, Apr 2018.
- [189] R. Bandiera, R. Neri, and R. Cesaroni. The Crab Nebula at 1.3 mm. Evidence for a new synchrotron component. , 386:1044–1054, May 2002.
- [190] M. Meyer, D. Horns, and H. S. Zechlin. The Crab Nebula as a standard candle in very high-energy astrophysics. , 523:A2, Nov 2010.
- [191] B. Cerutti, G. R. Werner, D. A. Uzdensky, and M. C. Begelman. Gamma-ray flares in the Crab Nebula: A case of relativistic reconnection? a). *Physics of Plasmas*, 21(5):056501, May 2014.
- [192] T. Schweizer, N. Bucciantini, W. Idec, K. Nilsson, A. Tennant, M. C. Weisskopf, and R. Zanin. Characterization of the optical and X-ray properties of the north-western wisps in the Crab nebula. , 433(4):3325–3335, Aug 2013.
- [193] B. Olmi, L. Del Zanna, E. Amato, R. Bandiera, and N. Bucciantini. On the magnetohydrodynamic modelling of the Crab nebula radio emission. , 438(2):1518–1525, Feb 2014.
- [194] B. Olmi, L. Del Zanna, E. Amato, and N. Bucciantini. Constraints on particle acceleration sites in the Crab nebula from relativistic magnetohydrodynamic simulations. , 449(3):3149–3159, May 2015.
- [195] M. P. Veron-Cetty and L. Woltjer. Spectrophotometry of the continuum in the Crab Nebula. , 270:370–378, Mar 1993.
- [196] Felix A. Aharonian. *Very high energy cosmic gamma radiation : a crucial window on the extreme Universe*. 2004.
- [197] J. E. Baldwin. The Electromagnetic Spectrum of the Crab Nebula. In Rodney Deane Davies and Francis. Graham-Smith, editors, *The Crab Nebula*, volume 46 of *IAU Symposium*, page 22, Jan 1971.
- [198] J. W. M. Baars, R. Genzel, I. I. K. Pauliny-Toth, and A. Witzel. Reprint of 1977A&A...61...99B. The absolute spectrum of Cas A; an accurate flux density scale and a set of secondary calibrators. , 500:135–142, Oct 1977.
- [199] J. F. Macías-Pérez, F. Mayet, J. Aumont, and F. X. Désert. Global Spectral Energy Distribution of the Crab Nebula in the Prospect of the Planck Satellite Polarization Calibration. , 711(1):417–423, Mar 2010.
- [200] Edward P. Ney and Wayne A. Stein. Observations of the Crab Nebula at $\lambda = 5800 \text{ \AA}$ 2.2 μ , and 3.5 μ with a 4-MINUTE Beam. , 152:L21, Apr 1968.
- [201] G. L. Grasdalen. Near infrared observations of the Crab nebula. , 91:436–441, Aug 1979.
- [202] D. A. Green, R. J. Tuffs, and C. C. Popescu. Far-infrared and submillimetre observations of the Crab nebula. , 355(4):1315–1326, Dec 2004.

- [203] Tea Temim, Robert D. Gehrz, Charles E. Woodward, Thomas L. Roellig, Nathan Smith, Lawrence Rudnick, Elisha F. Polomski, Kris Davidson, Luning Yuen, and Takashi Onaka. Spitzer Space Telescope Infrared Imaging and Spectroscopy of the Crab Nebula. , 132(4):1610–1623, Oct 2006.
- [204] L. Kuiper, W. Hermsen, G. Cusumano, R. Diehl, V. Schönfelder, A. Strong, K. Bennett, and M. L. McConnell. The Crab pulsar in the 0.75-30 MeV range as seen by CGRO COMPTEL. A coherent high-energy picture from soft X-rays up to high-energy gamma-rays. , 378:918–935, Nov 2001.
- [205] F. Aharonian, A. G. Akhperjanian, A. R. Bazer-Bachi, M. Beilicke, W. Benbow, D. Berge, K. Bernlöhr, C. Boisson, O. Bolz, V. Borrel, I. Braun, F. Breitling, A. M. Brown, R. Bühler, I. Büsching, S. Carrigan, P. M. Chadwick, L. M. Chounet, R. Cornils, L. Costamante, B. Degrange, H. J. Dickinson, A. Djannati-Ataï, L. O’C. Drury, G. Dubus, K. Egberts, D. Emmanoulopoulos, P. Espigat, F. Feinstein, E. Ferrero, A. Fiasson, G. Fontaine, Seb. Funk, S. Funk, Y. A. Gallant, B. Giebels, J. F. Glicenstein, P. Goret, C. Hadjichristidis, D. Hauser, M. Hauser, G. Heinzlmann, G. Henri, G. Hermann, J. A. Hinton, W. Hofmann, M. Holleran, D. Horns, A. Jacholkowska, O. C. de Jager, B. Khélifi, Nu. Komin, A. Konopelko, K. Kosack, I. J. Latham, R. Le Gallou, A. Lemièrre, M. Lemoine-Goumard, T. Lohse, J. M. Martin, O. Martineau-Huynh, A. Marcowith, C. Masterson, T. J. L. McComb, M. de Naurois, D. Nedbal, S. J. Nolan, A. Noutsos, K. J. Orford, J. L. Osborne, M. Ouchrif, M. Panter, G. Pelletier, S. Pita, G. Pühlhofer, M. Punch, B. C. Raubenheimer, M. Raue, S. M. Rayner, A. Reimer, O. Reimer, J. Ripken, L. Rob, L. Rolland , G. Rowell, V. Sahakian, L. Saugé, S. Schlenker, R. Schlickeiser, U. Schwanke, H. Sol, D. Spangler, F. Spanier, R. Steenkamp, C. Stegmann, G. Superina, J. P. Tavernier, R. Terrier, C. G. Théoret, M. Tluczykont, C. van Eldik, G. Vasileiadis, C. Venter, P. Vincent, H. J. Völk, S. J. Wagner, and M. Ward. Observations of the Crab nebula with HESS. , 457(3):899–915, Oct 2006.
- [206] J. Albert, E. Aliu, H. Anderhub, P. Antoranz, A. Armada, C. Baixeras, J. A. Barrio, H. Bartko, D. Bastieri, J. K. Becker, W. Bednarek, K. Berger, C. Bigongiari, A. Biland, R. K. Bock, P. Bordas, V. Bosch-Ramon, T. Bretz, I. Britvitch, M. Camara, E. Carmona, A. Chilingarian, J. A. Coarasa, S. Comichau, J. L. Contreras, J. Cortina, M. T. Costado, V. Curtef, V. Danielyan, F. Dazzi, A. De Angelis, C. Delgado, R. de los Reyes, B. De Lotto, E. Domingo-Santamaría, D. Dorner, M. Doro, M. Errando, M. Fagiolini, D. Ferenc, E. Fernández, R. Firpo, J. Flix, M. V. Fonseca, L. Font, M. Fuchs, N. Galante, R. García-López, M. Garczarczyk, M. Gaug, M. Giller, F. Goebel, D. Hakobyan, M. Hayashida, T. Hengstebeck, A. Herrero, D. Höhne, J. Hose, C. C. Hsu, P. Jacon, T. Jogler, R. Kosyra, D. Kranich, R. Kritzer, A. Laille, E. Lindfors, S. Lombardi, F. Longo, J. López, M. López, E. Lorenz, P. Majumdar, G. Maneva, K. Mannheim, O. Mansutti, M. Mariotti, M. Martínez, D. Mazin, C. Merck, M. Meucci, M. Meyer, J. M. Miranda, R. Mirzoyan, S. Mizobuchi, A. Moralejo, D. Nieto, K. Nilsson, J. Ninkovic, E. Oña-Wilhelmi, N. Otte, I. Oya, D. Paneque, M. Panniello, R. Paoletti, J. M. Paredes, M. Pasanen, D. Pascoli, F. Pauss, R. Pegna, M. Persic, L. Peruzzo, A. Piccioli, M. Poller, E. Prandini, N. Puchades, A. Raymers, W. Rhode, M. Ribó, J. Rico, M. Rissi, A. Robert, S. Rügamer, A. Saggion, A. Sánchez, P. Sartori, V. Scalzotto, V. Scapin, R. Schmitt, T. Schweizer, M. Shayduk, K. Shinozaki, S. N. Shore, N. Sidro, A. Sillanpää, D. Sobczynska, A. Stamerra, L. S. Stark, L. Takalo, P. Temnikov, D. Tescaro, M. Teshima, N. Tonello, D. F. Torres, N. Turini,

- H. Vankov, V. Vitale, R. M. Wagner, T. Wibig, W. Wittek, F. Zandanel, R. Zanin, and J. Zapatero. VHE γ -Ray Observation of the Crab Nebula and its Pulsar with the MAGIC Telescope. , 674(2):1037–1055, Feb 2008.
- [207] A. A. Abdo, M. Ackermann, M. Ajello, W. B. Atwood, M. Axelsson, L. Baldini, J. Ballet, G. Barbiellini, M. G. Baring, D. Bastieri, K. Bechtol, R. Bellazzini, B. Berenji, R. D. Blandford, E. D. Bloom, E. Bonamente, A. W. Borgland, J. Bregeon, A. Brez, M. Brigida, P. Bruel, T. H. Burnett, G. A. Calianandro, R. A. Cameron, F. Camilo, P. A. Caraveo, J. M. Casandjian, C. Cecchi, Ö. Çelik, A. Chekhtman, C. C. Cheung, J. Chiang, S. Ciprini, R. Claus, I. Cognard, J. Cohen-Tanugi, L. R. Cominsky, J. Conrad, C. D. Dermer, A. de Angelis, A. de Luca, F. de Palma, S. W. Digel, E. do Couto e. Silva, P. S. Drell, R. Dubois, D. Dumora, C. Espinoza, C. Farnier, C. Favuzzi, S. J. Fegan, E. C. Ferrara, W. B. Focke, M. Frailis, P. C. C. Freire, Y. Fukazawa, S. Funk, P. Fusco, F. Gargano, D. Gasparrini, N. Gehrels, S. Germani, G. Giamittito, B. Giebels, N. Giglietto, F. Giordano, T. Glanzman, G. Godfrey, I. A. Grenier, M. H. Grondin, J. E. Grove, L. Guillemot, S. Guiriec, Y. Hanabata, A. K. Harding, M. Hayashida, E. Hays, R. E. Hughes, G. Jóhannesson, A. S. Johnson, R. P. Johnson, T. J. Johnson, W. N. Johnson, S. Johnston, T. Kamae, H. Katagiri, J. Kataoka, N. Kawai, M. Kerr, J. Knödseder, M. L. Kocian, M. Kramer, F. Kuehn, M. Kuss, J. Lande, L. Latronico, S. H. Lee, M. Lemoine-Goumard, F. Longo, F. Loparco, B. Lott, M. N. Lovellette, P. Lubrano, A. G. Lyne, A. Makeev, M. Marelli, M. N. Mazziotta, J. E. McEnery, C. Meurer, P. F. Michelson, W. Mitthumsiri, T. Mizuno, A. A. Moiseev, C. Monte, M. E. Monzani, E. Moretti, A. Morselli, I. V. Moskalenko, S. Murgia, T. Nakamori, P. L. Nolan, J. P. Norris, A. Noutsos, E. Nuss, T. Ohsugi, N. Omodei, E. Orlando, J. F. Ormes, M. Ozaki, D. Paneque, J. H. Panetta, D. Parent, V. Pelassa, M. Pepe, M. Pesce-Rollins, M. Pierbattista, F. Piron, T. A. Porter, S. Rainò, R. Rando, P. S. Ray, M. Razzano, A. Reimer, O. Reimer, T. Reposeur, S. Ritz, L. S. Rochester, A. Y. Rodriguez, R. W. Romani, M. Roth, F. Ryde, H. F. W. Sadrozinski, D. Sanchez, A. Sander, P. M. Saz Parkinson, J. D. Scargle, C. Sgrò, E. J. Siskind, D. A. Smith, P. D. Smith, G. Spandre, P. Spinelli, B. W. Stappers, M. S. Strickman, D. J. Suson, H. Tajima, H. Takahashi, T. Tanaka, J. B. Thayer, J. G. Thayer, G. Theureau, D. J. Thompson, S. E. Thorsett, L. Tibaldo, D. F. Torres, G. Tosti, A. Tramacere, Y. Uchiyama, T. L. Usher, A. Van Etten, V. Vasileiou, N. Vilchez, V. Vitale, A. P. Waite, E. Wallace, P. Wang, K. Waters, P. Weltevrede, B. L. Winer, K. S. Wood, T. Ylinen, and M. Ziegler. Fermi Large Area Telescope Observations of the Crab Pulsar And Nebula. , 708(2):1254–1267, Jan 2010.
- [208] A. M. Atoyan. Radio spectrum of the Crab nebula as an evidence for fast initial spin of its pulsar. , 346:L49–L52, Jun 1999.
- [209] Patrick Slane, David J. Helfand, Eric van der Swaluw, and Stephen S. Murray. New Constraints on the Structure and Evolution of the Pulsar Wind Nebula 3C 58. , 616(1):403–413, November 2004.
- [210] J. A. Nousek, C. Kouveliotou, D. Grupe, K. L. Page, J. Granot, E. Ramirez-Ruiz, S. K. Patel, D. N. Burrows, V. Mangano, S. Barthelmy, A. P. Beardmore, S. Campana, M. Capalbi, G. Chincarini, G. Cusumano, A. D. Falcone, N. Gehrels, P. Giommi, M. R. Goad, O. Godet, C. P. Hurkett, J. A. Kennea, A. Moretti, P. T. O’Brien, J. P. Osborne, P. Romano, G. Tagliaferri, and A. A.

- Wells. Evidence for a Canonical Gamma-Ray Burst Afterglow Light Curve in the Swift XRT Data. , 642(1):389–400, May 2006.
- [211] E. Troja, G. Cusumano, P. T. O’Brien, B. Zhang, B. Sbarufatti, V. Mangano, R. Willingale, G. Chincarini, J. P. Osborne, F. E. Marshall, D. N. Burrows, S. Campana, N. Gehrels, C. Guidorzi, H. A. Krimm, V. La Parola, E. W. Liang, T. Mineo, A. Moretti, K. L. Page, P. Romano, G. Tagliaferri, B. B. Zhang, M. J. Page, and P. Schady. Swift Observations of GRB 070110: An Extraordinary X-Ray Afterglow Powered by the Central Engine. , 665:599–607, August 2007.
- [212] Maxim Lyutikov. Gamma Ray Bursts: back to the blackboard. *arXiv e-prints*, page arXiv:0911.0349, November 2009.
- [213] B. Sbarufatti, V. Mangano, T. Mineo, G. Cusumano, and H. Krimm. GRB070110: Swift XRT team refined analysis. *GRB Coordinates Network*, 6008, 2007.
- [214] H. A. Krimm, P. Boyd, V. Mangano, F. Marshall, B. Sbarufatti, and N. Gehrels. GRB 070110 declared a “Burst of interest” by Swift team. *GRB Coordinates Network*, 6014, 2007.
- [215] H. A. Krimm, P. Boyd, V. Mangano, F. Marshall, D. M. Palmer, P. W. A. Roming, B. Sbarufatti, S. D. Barthelmy, D. N. Burrows, and N. Gehrels. Updates Swift observations of GRB 070110. *GCN Report*, 26, 2007.
- [216] N. Lyons, P. T. O’Brien, B. Zhang, R. Willingale, E. Troja, and R. L. C. Starling. Can X-ray emission powered by a spinning-down magnetar explain some gamma-ray burst light-curve features? , 402:705–712, February 2010.
- [217] A. Rowlinson, P. T. O’Brien, N. R. Tanvir, B. Zhang, P. A. Evans, N. Lyons, A. J. Levan, R. Willingale, K. L. Page, O. Onal, D. N. Burrows, A. P. Beardmore, T. N. Ukwatta, E. Berger, J. Hjorth, A. S. Fruchter, R. L. Tunnicliffe, D. B. Fox, and A. Cucchiara. The unusual X-ray emission of the short Swift GRB 090515: evidence for the formation of a magnetar? , 409:531–540, December 2010.
- [218] L. Resmi and B. Zhang. Gamma-ray Burst Reverse Shock Emission in Early Radio Afterglows. , 825:48, July 2016.
- [219] P. Beniamini and R. Mochkovitch. What can we learn from “internal plateaus”? The peculiar afterglow of GRB 070110. , 605:A60, September 2017.
- [220] A. Rowlinson, P. T. O’Brien, B. D. Metzger, N. R. Tanvir, and A. J. Levan. Signatures of magnetar central engines in short GRB light curves. , 430:1061–1087, April 2013.
- [221] H. van Eerten. Self-similar relativistic blast waves with energy injection. , 442:3495–3510, August 2014.
- [222] Maxim Lyutikov. Ultra-relativistic double explosions. *Physics of Fluids*, 29(4):047101, Apr 2017.
- [223] A. Bruce Langdon, Jonathan Arons, and Claire E. Max. Structure of relativistic magnetosonic shocks in electron-positron plasmas. , 61(7):779–782, August 1988.

- [224] Masahiro Hoshino, Jonathan Arons, Yves A. Gallant, and A. B. Langdon. Relativistic Magnetosonic Shock Waves in Synchrotron Sources: Shock Structure and Nonthermal Acceleration of Positrons. , 390:454, May 1992.
- [225] K. R. Lang. *Astrophysical formulae*. 1999.
- [226] N. S. Kardashev. Nonstationarity of Spectra of Young Sources of Nonthermal Radio Emission. , 6:317, Dec 1962.
- [227] E. E. Fenimore, C. D. Madras, and S. Nayakshin. Expanding Relativistic Shells and Gamma-Ray Burst Temporal Structure. , 473:998, December 1996.
- [228] Ehud Nakar, Tsvi Piran, and Jonathan Granot. Variability in GRB afterglows and GRB 021004. , 8(5):495–505, July 2003.
- [229] L. Vetere, D. N. Burrows, N. Gehrels, P. Meszaros, D. C. Morris, and J. L. Racusin. GRBs with no afterglow even in the Swift Era? In M. Galassi, David Palmer, and Ed Fenimore, editors, *American Institute of Physics Conference Series*, volume 1000 of *American Institute of Physics Conference Series*, pages 191–195, May 2008.
- [230] Jonathan Granot, Alin Panaitescu, Pawan Kumar, and Stan E. Woosley. Off-Axis Afterglow Emission from Jetted Gamma-Ray Bursts. , 570(2):L61–L64, May 2002.
- [231] Hendrik van Eerten, Weiqun Zhang, and Andrew MacFadyen. Off-axis Gamma-ray Burst Afterglow Modeling Based on a Two-dimensional Axisymmetric Hydrodynamics Simulation. , 722(1):235–247, Oct 2010.
- [232] G. Ghirlanda, R. Salvaterra, S. Campana, S. D. Vergani, J. Japelj, M. G. Bernardini, D. Burlon, P. D’Avanzo, A. Melandri, A. Gomboc, F. Nappo, R. Paladini, A. Pescalli, O. S. Salafia, and G. Tagliaferri. Unveiling the population of orphan γ -ray bursts. , 578:A71, Jun 2015.
- [233] B. P. Abbott, R. Abbott, T. D. Abbott, M. R. Abernathy, F. Acernese, K. Ackley, C. Adams, T. Adams, P. Addesso, R. X. Adhikari, and et al. Observation of Gravitational Waves from a Binary Black Hole Merger. *Physical Review Letters*, 116(6):061102, February 2016.
- [234] B. P. Abbott, R. Abbott, T. D. Abbott, F. Acernese, K. Ackley, C. Adams, T. Adams, P. Addesso, R. X. Adhikari, V. B. Adya, and et al. Gravitational Waves and Gamma-Rays from a Binary Neutron Star Merger: GW170817 and GRB 170817A. , 848:L13, October 2017.
- [235] B. P. Abbott, R. Abbott, T. D. Abbott, F. Acernese, K. Ackley, C. Adams, T. Adams, P. Addesso, R. X. Adhikari, V. B. Adya, and et al. GW170817: Observation of Gravitational Waves from a Binary Neutron Star Inspiral. *Physical Review Letters*, 119(16):161101, October 2017.
- [236] V. Savchenko, C. Ferrigno, E. Kuulkers, A. Bazzano, E. Bozzo, S. Brandt, J. Chenevez, T. J.-L. Courvoisier, R. Diehl, A. Domingo, L. Hanlon, E. Jourdain, A. von Kienlin, P. Laurent, F. Lebrun, A. Lutovinov, A. Martin-Carrillo, S. Mereghetti, L. Natalucci, J. Rodi, J.-P. Roques, R. Sunyaev, and P. Ubertini. INTEGRAL Detection of the First Prompt Gamma-Ray Signal Coincident with the Gravitational-wave Event GW170817. , 848:L15, October 2017.

- [237] A. S. Pozanenko, M. V. Barkov, P. Y. Minaev, A. A. Volnova, E. D. Mazareva, A. S. Moskvitin, M. A. Krugov, V. A. Samodurov, V. M. Loznikov, and M. Lyutikov. GRB 170817A Associated with GW170817: Multi-frequency Observations and Modeling of Prompt Gamma-Ray Emission. , 852:L30, January 2018.
- [238] O. Bromberg, A. Tchekhovskoy, O. Gottlieb, E. Nakar, and T. Piran. The γ -rays that accompanied GW170817 and the observational signature of a magnetic jet breaking out of NS merger ejecta. , 475(3):2971–2977, Apr 2018.
- [239] S. I. Blinnikov, I. D. Novikov, T. V. Perevodchikova, and A. G. Polnarev. Exploding Neutron Stars in Close Binaries. *Soviet Astronomy Letters*, 10:177–179, Apr 1984.
- [240] A. V. Tutukov and A. V. Fedorova. Late stages of the evolution of close compact binaries: Type I supernovae, gamma-ray bursts, and supersoft X-ray sources. *Astronomy Reports*, 51(4):291–307, Apr 2007.
- [241] Ariadna Murguia-Berthier, Gabriela Montes, Enrico Ramirez-Ruiz, Fabio De Colle, and William H. Lee. Necessary Conditions for Short Gamma-Ray Burst Production in Binary Neutron Star Mergers. , 788(1):L8, Jun 2014.
- [242] K. P. Mooley, E. Nakar, K. Hotokezaka, G. Hallinan, A. Corsi, D. A. Frail, A. Horesh, T. Murphy, E. Lenc, D. L. Kaplan, K. de, D. Dobie, P. Chand ra, A. Deller, O. Gottlieb, M. M. Kasliwal, S. R. Kulkarni, S. T. Myers, S. Nissanke, T. Piran, C. Lynch, V. Bhalerao, S. Bourke, K. W. Bannister, and L. P. Singer. A mildly relativistic wide-angle outflow in the neutron-star merger event GW170817. , 554(7691):207–210, Feb 2018.
- [243] M. M. Kasliwal, E. Nakar, L. P. Singer, D. L. Kaplan, D. O. Cook, A. Van Sistine, R. M. Lau, C. Fremling, O. Gottlieb, J. E. Jencson, S. M. Adams, U. Feindt, K. Hotokezaka, S. Ghosh, D. A. Perley, P. C. Yu, T. Piran, J. R. Allison, G. C. Anupama, A. Balasubramanian, K. W. Bannister, J. Bally, J. Barnes, S. Barway, E. Bellm, V. Bhalerao, D. Bhattacharya, N. Blagorodnova, J. S. Bloom, P. R. Brady, C. Cannella, D. Chatterjee, S. B. Cenko, B. E. Cobb, C. Copperwheat, A. Corsi, K. De, D. Dobie, S. W. K. Emery, P. A. Evans, O. D. Fox, D. A. Frail, C. Frohmaier, A. Goobar, G. Hallinan, F. Harrison, G. Helou, T. Hinderer, A. Y. Q. Ho, A. Horesh, W. H. Ip, R. Itoh, D. Kasen, H. Kim, N. P. M. Kuin, T. Kupfer, C. Lynch, K. Madsen, P. A. Mazzali, A. A. Miller, K. Mooley, T. Murphy, C. C. Ngeow, D. Nichols, S. Nissanke, P. Nugent, E. O. Ofek, H. Qi, R. M. Quimby, S. Rosswog, F. Rusu, E. M. Sadler, P. Schmidt, J. Sollerman, I. Steele, A. R. Williamson, Y. Xu, L. Yan, Y. Yatsu, C. Zhang, and W. Zhao. Illuminating gravitational waves: A concordant picture of photons from a neutron star merger. *Science*, 358(6370):1559–1565, Dec 2017.
- [244] O. Gottlieb, E. Nakar, and T. Piran. The cocoon emission - an electromagnetic counterpart to gravitational waves from neutron star mergers. , 473:576–584, January 2018.
- [245] Gavin P. Lamb and Shiho Kobayashi. GRB 170817A as a jet counterpart to gravitational wave triggerGW 170817. , 478(1):733–740, Jul 2018.

- [246] E. Troja, L. Piro, G. Ryan, H. van Eerten, R. Ricci, M. H. Wieringa, S. Lotti, T. Sakamoto, and S. B. Cenko. The outflow structure of GW170817 from late-time broad-band observations. , 478(1):L18–L23, Jul 2018.
- [247] P. D’Avanzo, S. Campana, O. S. Salafia, G. Ghirlanda, G. Ghisellini, A. Melandri, M. G. Bernardini, M. Branchesi, E. Chassande-Mottin, S. Covino, V. D’Elia, L. Nava, R. Salvaterra, G. Tagliaferri, and S. D. Vergani. The evolution of the X-ray afterglow emission of GW 170817/ GRB 170817A in XMM-Newton observations. , 613:L1, May 2018.
- [248] Xiaoyi Xie, Jonathan Zrake, and Andrew MacFadyen. Numerical Simulations of the Jet Dynamics and Synchrotron Radiation of Binary Neutron Star Merger Event GW170817/GRB 170817A. , 863(1):58, Aug 2018.
- [249] R. Margutti, K. D. Alexander, X. Xie, L. Sironi, B. D. Metzger, A. Kathirgamaraju, W. Fong, P. K. Blanchard, E. Berger, A. MacFadyen, D. Giannios, C. Guidorzi, A. Hajela, R. Chornock, P. S. Cowperthwaite, T. Eftekhari, M. Nicholl, V. A. Villar, P. K. G. Williams, and J. Zrake. The Binary Neutron Star Event LIGO/Virgo GW170817 160 Days after Merger: Synchrotron Emission across the Electromagnetic Spectrum. , 856:L18, March 2018.
- [250] A. Kathirgamaraju, R. Barniol Duran, and D. Giannios. Off-axis short GRBs from structured jets as counterparts to GW events. , 473:L121–L125, January 2018.
- [251] Davide Lazzati, Rosalba Perna, Brian J. Morsony, Diego Lopez-Camara, Matteo Cantiello, Riccardo Ciolfi, Bruno Giacomazzo, and Jared C. Workman. Late Time Afterglow Observations Reveal a Collimated Relativistic Jet in the Ejecta of the Binary Neutron Star Merger GW170817. , 120(24):241103, Jun 2018.
- [252] A. Murguia-Berthier, E. Ramirez-Ruiz, C. D. Kilpatrick, R. J. Foley, D. Kasen, W. H. Lee, A. L. Piro, D. A. Coulter, M. R. Drout, B. F. Madore, B. J. Shappee, Y. C. Pan, J. X. Prochaska, A. Rest, C. Rojas-Bravo, M. R. Siebert, and J. D. Simon. A Neutron Star Binary Merger Model for GW170817/GRB 170817A/SSS17a. , 848(2):L34, Oct 2017.
- [253] Milton Ruiz, Ryan N. Lang, Vasileios Paschalidis, and Stuart L. Shapiro. Binary Neutron Star Mergers: A Jet Engine for Short Gamma-Ray Bursts. , 824(1):L6, Jun 2016.
- [254] Albino Perego, David Radice, and Sebastiano Bernuzzi. AT 2017gfo: An Anisotropic and Three-component Kilonova Counterpart of GW170817. , 850(2):L37, Dec 2017.
- [255] Luciano Rezzolla, Bruno Giacomazzo, Luca Baiotti, Jonathan Granot, Chryssa Kouveliotou, and Miguel A. Aloy. The Missing Link: Merging Neutron Stars Naturally Produce Jet-like Structures and Can Power Short Gamma-ray Bursts. , 732(1):L6, May 2011.
- [256] Luis Lehner, Carlos Palenzuela, Steven L. Liebling, Christopher Thompson, and Chad Hanna. Intense electromagnetic outbursts from collapsing hypermassive neutron stars. , 86(10):104035, Nov 2012.
- [257] Ulf Torkelsson and Axel Brandenburg. Turbulent accretion disk dynamos ? , 283:677–692, Mar 1994.

- [258] R. Arlt and G. Rüdiger. Accretion-disk dynamo models with dynamo-induced alpha-effect. , 349:334–338, Sep 1999.
- [259] N. Bucciantini and L. Del Zanna. A fully covariant mean-field dynamo closure for numerical $3 + 1$ resistive GRMHD. , 428(1):71–85, Jan 2013.
- [260] Aleksander Sadowski, Ramesh Narayan, Alexander Tchekhovskoy, David Abarca, Yucong Zhu, and Jonathan C. McKinney. Global simulations of axisymmetric radiative black hole accretion discs in general relativity with a mean-field magnetic dynamo. , 447(1):49–71, Feb 2015.
- [261] R. D. Blandford and R. L. Znajek. Electromagnetic extraction of energy from Kerr black holes. , 179:433–456, May 1977.
- [262] Daniel Finstad, Soumi De, Duncan A. Brown, Edo Berger, and Christopher M. Biwer. Measuring the Viewing Angle of GW170817 with Electromagnetic and Gravitational Waves. , 860(1):L2, Jun 2018.
- [263] E. Troja, L. Piro, H. van Eerten, R. T. Wollaeger, M. Im, O. D. Fox, N. R. Butler, S. B. Cenko, T. Sakamoto, C. L. Fryer, R. Ricci, A. Lien, R. E. Ryan, O. Kobrin, S.-K. Lee, J. M. Burgess, W. H. Lee, A. M. Watson, C. Choi, S. Covino, P. D’Avanzo, C. J. Fontes, J. B. González, H. G. Khandrika, J. Kim, S.-L. Kim, C.-U. Lee, H. M. Lee, A. Kutyrev, G. Lim, R. Sánchez-Ramírez, S. Veilleux, M. H. Wieringa, and Y. Yoon. The X-ray counterpart to the gravitational-wave event GW170817. , 551:71–74, November 2017.
- [264] Dougal Dobie, David L. Kaplan, Tara Murphy, Emil Lenc, Kunal P. Mooley, Christene Lynch, Alessandra Corsi, Dale Frail, Mansi Kasliwal, and Gregg Hallinan. A Turnover in the Radio Light Curve of GW170817. , 858(2):L15, May 2018.
- [265] K. D. Alexander, R. Margutti, P. K. Blanchard, W. Fong, E. Berger, A. Hajela, T. Eftekhari, R. Chornock, P. S. Cowperthwaite, D. Giannios, C. Guidorzi, A. Kathirgamaraju, A. MacFadyen, B. D. Metzger, M. Nicholl, L. Sironi, V. A. Villar, P. K. G. Williams, X. Xie, and J. Zrake. A Decline in the X-Ray through Radio Emission from GW170817 Continues to Support an Off-axis Structured Jet. , 863(2):L18, Aug 2018.
- [266] Ehud Nakar, Tsvi Piran, and Jonathan Granot. The Detectability of Orphan Afterglows. , 579(2):699–705, Nov 2002.
- [267] Jonathan Granot, Ramandeep Gill, Dafne Guetta, and Fabio De Colle. Off-axis emission of short GRB jets from double neutron star mergers and GRB 170817A. , 481(2):1597–1608, Dec 2018.
- [268] Hendrik J. van Eerten and Andrew I. MacFadyen. Gamma-Ray Burst Afterglow Scaling Relations for the Full Blast Wave Evolution. , 747(2):L30, Mar 2012.
- [269] Roger D. Blandford and Mitchell C. Begelman. On the fate of gas accreting at a low rate on to a black hole. , 303(1):L1–L5, Feb 1999.
- [270] B. D. Metzger, A. L. Piro, and E. Quataert. Time-dependent models of accretion discs formed from compact object mergers. , 390(2):781–797, Oct 2008.

- [271] Maxim V. Barkov and Serguei S. Komissarov. Stellar explosions powered by the Blandford-Znajek mechanism. , 385(1):L28–L32, Mar 2008.
- [272] Maxim V. Barkov and Alexei S. Pozanenko. Model of the extended emission of short gamma-ray bursts. , 417(3):2161–2165, Nov 2011.
- [273] David Radice, Filippo Galeazzi, Jonas Lippuner, Luke F. Roberts, Christian D. Ott, and Luciano Rezzolla. Dynamical mass ejection from binary neutron star mergers. , 460(3):3255–3271, Aug 2016.
- [274] Luca Baiotti and Luciano Rezzolla. Binary neutron star mergers: a review of Einstein’s richest laboratory. *Reports on Progress in Physics*, 80(9):096901, Sep 2017.
- [275] Hendrik J. van Eerten and Andrew I. MacFadyen. Observational Implications of Gamma-Ray Burst Afterglow Jet Simulations and Numerical Light Curve Calculations. , 751(2):155, Jun 2012.
- [276] Re’em Sari, Ramesh Narayan, and Tsvi Piran. Cooling Timescales and Temporal Structure of Gamma-Ray Bursts. , 473:204, Dec 1996.
- [277] Maxim Lyutikov. On the sideways expansion of relativistic non-spherical shocks and gamma-ray burst afterglows. , 421(1):522–524, Mar 2012.
- [278]
- [279] A. Tsvetkova, D. Frederiks, S. Golenetskii, A. Lysenko, P. Oleynik, V. Pal’shin, D. Svinkin, M. Ulanov, T. Cline, K. Hurley, and R. Aptekar. The Konus-Wind Catalog of Gamma-Ray Bursts with Known Redshifts. I. Bursts Detected in the Triggered Mode. , 850(2):161, Dec 2017.
- [280] P. Yu. Minaev and A. S. Pozanenko. Precursors of short gamma-ray bursts in the SPI-ACS/INTEGRAL experiment. *Astronomy Letters*, 43(1):1–20, Jan 2017.
- [281] Yuan-Chuan Zou, Fei-Fei Wang, Reetanjali Moharana, Bin Liao, Wei Chen, Qingwen Wu, Wei-Hua Lei, and Fa-Yin Wang. Determining the Lorentz Factor and Viewing Angle of GRB 170817A. , 852(1):L1, Jan 2018.
- [282] Paz Beniamini, Lara Nava, Rodolfo Barniol Duran, and Tsvi Piran. Energies of GRB blast waves and prompt efficiencies as implied by modelling of X-ray and GeV afterglows. , 454(1):1073–1085, Nov 2015.

A. THE DERIVATION OF THE LIGHT CURVE FUNCTION OF THE RELATIVISTICALLY EXPANSION AT HARD X-RAY AND ABOVE

Here I want to derive the equation (2.80) from my dissertation.

The function $F(x)$ in equation (4.11) can be estimated as a Dirac-Delta function with a peak at $x = 0.29$, i.e. $F(x) = C\delta(x - 0.29)$, where C is a normalization factor with the value 1.61207 so that

$$\int_0^{\infty} F(x) dx = \int_0^{\infty} C\delta(x - 0.29) dx. \quad (\text{A.1})$$

Use the properties of Dirac-Delta function, we have

$$F\left(\frac{\omega}{D\omega_c}\right) = C\delta\left(\frac{\omega}{D\omega_c} - 0.29\right) = C\delta\left(\frac{2\omega mc}{D\gamma'^2(3Be)} - 0.29\right) \quad (\text{A.2})$$

$$= \frac{C\left(\frac{2\omega mc}{0.29 \times 3DB'e}\right)^{3/2} \delta\left(\gamma' - \sqrt{\frac{2\omega mc}{0.29 \times 3DB'e}}\right)}{\frac{4\omega mc}{3DB'e}} \quad (\text{A.3})$$

$$\frac{C\sqrt{\frac{2\omega mc}{3DB'e}} \delta\left(\gamma' - \sqrt{\frac{2\omega mc}{0.29 \times 3DB'e}}\right)}{2 \times (0.29)^{3/2}} \quad (\text{A.4})$$

we already known: $B' \propto t'^{\frac{m-1}{m+1}}$, $D \propto t'^{\frac{-m}{m+1}}$, so $\gamma' \propto \sqrt{\frac{1}{DB'}} \propto t'^{\frac{1}{2m+2}}$

The Green function can be written as

$$G = n\left(\frac{t'_i}{t'_0}\right)^{\frac{mp-2}{1+m}} \gamma'^{-p} \left(\frac{t'_i}{t'}\right)^{\frac{(p-1)(1-m)}{2+2m}} \left(1 - \frac{2+2m}{7m-3} \tilde{C}_2 B_0^2 \gamma' t'^{\frac{1-m}{2+2m}} \left(t'^{\frac{7m-3}{2+2m}} - t'_i^{\frac{7m-3}{2+2m}}\right)\right)^{p-2} \quad (\text{A.5})$$

$$\propto t_i^{\frac{mp-\frac{p}{2}-2}{1+m}} \left(1 - t'^{\frac{2-m}{2+2m}} \left(t'^{\frac{7m-3}{2+2m}} - t_i^{\frac{7m-3}{2+2m}}\right)\right)^{p-2} \quad (\text{A.6})$$

For high energy region, we only consider N_4 from equation (2.78). By using the definition of t'_i and mean value theorem, t'_i satisfies

$$t'^{\frac{7m-3}{2+2m}} - t_i^{\frac{7m-3}{2+2m}} = t'^{\frac{m-2}{2+2m}} = \frac{7m-3}{2+2m} \zeta^{\frac{5m-5}{2+2m}} (t' - t'_i) \quad (\text{A.7})$$

So

$$h = t' - t'_i = O\left(t'^{\frac{3-4m}{2+2m}}\right) \quad (\text{A.8})$$

Notice that

$$\left(1 - \frac{2+2m}{7m-3} \tilde{C}_2 B_0^2 \gamma' t'^{\frac{1-m}{2+2m}} \left(t'^{\frac{7m-3}{2+2m}} - t_i^{\frac{7m-3}{2+2m}}\right)\right)^{p-2} \leq 1 \quad (\text{A.9})$$

we have

$$\int_{t'_i}^{t'} G(\gamma', t', t'_i) dt'_i = \int_{t'-h}^{t'} G(\gamma', t', t'_i) dt'_i \quad (\text{A.10})$$

$$\leq t^{\frac{mp-\frac{p}{2}-2}{1+m}} h(t) \quad (\text{A.11})$$

$$\leq t^{\frac{2mp-p-1-4m}{2+2m}} \quad (\text{A.12})$$

Also

$$1 - t'^{\frac{2-m}{2+2m}} \left(t'^{\frac{7m-3}{2+2m}} - \left(t'' - \frac{h}{2}\right)^{\frac{7m-3}{2+2m}}\right) \quad (\text{A.13})$$

$$= \left(1 - t'^{\frac{2-m}{2+2m}} \left(t'^{\frac{7m-3}{2+2m}} - \left(t' - \frac{h}{2}\right)^{\frac{7m-3}{2+2m}}\right)\right) - \left(1 - t'^{\frac{2-m}{2+2m}} \left(t'^{\frac{7m-3}{2+2m}} - (t' - h)^{\frac{7m-3}{2+2m}}\right)\right) \quad (\text{A.14})$$

$$= t'^{\frac{2-m}{2+2m}} \left(t' - \frac{h}{2}\right)^{\frac{7m-3}{2+2m}} - t'^{\frac{2-m}{2+2m}} (t' - h)^{\frac{7m-3}{2+2m}} \quad (\text{A.15})$$

$$= O\left(t'^{\frac{2-m}{2+2m}} \left(\left(t' - \frac{h}{2}\right)^{\frac{7m-3}{2+2m}} - (t' - h)^{\frac{7m-3}{2+2m}}\right)\right) \quad (\text{A.16})$$

$$= O(t'^{\frac{2-m}{2+m}} t'^{\frac{5m-5}{2+2m}} h) \quad (\text{A.17})$$

$$= O(t'^{\frac{2-m}{2+m} + \frac{5m-5}{2+2m}} + \frac{3-4m}{2+2m}) \quad (\text{A.18})$$

$$= O(t'^0) = O(1) \quad (\text{A.19})$$

So there is a positive number c , which satisfies

$$c = \inf\{(1 - t'^{\frac{2-m}{2+2m}} (t'^{\frac{7m-3}{2+2m}} - (t'_i)^{\frac{7m-3}{2+2m}}))^{p-2} : t'_i \in [\frac{t+t_l}{2}, \frac{t}{2}]\} \quad (\text{A.20})$$

so we have

$$\int_{t'_i}^{t'} G(\gamma', t', t'_i) dt'_i = \int_{t'-h}^{t'} G(\gamma', t', t'_i) dt'_i \quad (\text{A.21})$$

$$\geq ct^{\frac{mp-\frac{p}{2}-2}{1+m}} \quad (\text{A.22})$$

$$\geq ct^{\frac{2mp-p-1-4m}{2+2m}} \quad (\text{A.23})$$

Now we can claim that

$$\int_{t'_i}^{t'} G(\gamma', t', t'_i) dt'_i = \int_{t'-h}^{t'} G(\gamma', t', t'_i) dt'_i \quad (\text{A.24})$$

$$\propto t^{\frac{2mp-p-1-4m}{2+2m}} \quad (\text{A.25})$$

then

$$L(\omega, t) = \int N(\gamma, t) P(\omega) d\gamma = \int_{\gamma_{\min}}^{\infty} N(\gamma, t) \frac{\sqrt{3} B^2 e^3}{2\pi mc^2} F\left(\frac{\omega}{\omega_c}\right) d\gamma \quad (\text{A.26})$$

$$\propto t'^{\frac{2mp-p-1-4m}{2+2m} + \frac{m-1}{m+1} + \frac{1}{2+2m} - \frac{2m}{1+m}} \quad (\text{A.27})$$

$$t' = t^{\frac{1+m}{1+2m}} \quad (\text{A.28})$$

so

$$L(\omega, t) = \int N(\gamma, t) P(\omega) d\gamma = \int_{\gamma_{\min}}^{\infty} N(\gamma, t) \frac{\sqrt{3} B^2 e^3}{2\pi mc^2} F\left(\frac{\omega}{\omega_c}\right) d\gamma \quad (\text{A.29})$$

$$\propto t^{\frac{2mp-p-6m}{2+4m}} \quad (\text{A.30})$$

VITA

Yonggang Luo

Department of Physics and Astronomy

Purdue University

525 Northwestern Avenue

West Lafayette, IN 47905 USA

Mobile: 765-479-5218

Email: ygluo@purdue.edu

Born: September 26, 1992—Changsha, China

Nationality: Chinese

Areas of specialisation

High energy astrophysics

Synchrotron and IC radiation

Shock wave

Education

2010-2014 BACHELOR OF SCIENCE in Physics, Taishan Colloge, Shandong University

Thesis: *Indirect detection of particle dark matter: theoretical and experimental aspects*

Supervisor: Shi-Yuan Li

2014-2020 PhD in Physics, Department of Physics and Astronomy, Purdue University

Thesis: *Radiative Processes in Relativistic Astrophysical Plasmas*

Supervisor: Maxim Lyutikov

Grants, honours & awards

2017,2018 Summer Research Grants

2019-2020 Purdue Research Foundation Grant

Articles

2018 Maxim Barkov, Adithan Kathirgamaraju, Yonggang Luo, Maxim Lyutikov, Dimitrios Giannios, “Prediction of the Ssecond Peak in the Afterglow of GW170817”, *arXiv* 1805.08338

2020 Yonggang Luo, Maxim Lyutikov, Tea Temim, Luca Comisso, “Turbulent Model of Crab Nebula Model”, *submitted to The Astrophysical Journal*

2020 Yonggang Luo, Maxim Lyutikov, Pulsar winds in GRBs afterglows: flares, plateaus and steep decays, *in preparation*

Teaching

2014 Modern Physics

2015 Stars And Galaxies

2016 Galaxies and Large Scale Universe

2016 Quantum Mechanics II

2017 Descriptive Astronomy: Stars and Galaxies

2017 Astroparticle Physics

2017 Galaxies and Large Scale Universe

2017 Introduction to Elementary Particle Physics I

2018 High Energy Astrophysics

2018 Astroparticle physics

Public Services

Judge, Lafayette Regional Science and Engineering Fair

Grant Reviewer, Purdue Graduate Student Government

Active Member, The Mars Society Purdue Chapter